
Processes with Weak Gauge Boson Pairs at Hadron Colliders

—
Precise Predictions and Future Prospects

LUKAS SALFELDER

EBERHARD KARLS
UNIVERSITÄT
TÜBINGEN



TÜBINGEN
2016

Processes with Weak Gauge Boson Pairs at Hadron Colliders

—
Precise Predictions and Future Prospects

DISSERTATION

der Mathematisch-Naturwissenschaftlichen Fakultät
der Eberhard Karls Universität Tübingen
zur Erlangung des Grades eines
Doktors der Naturwissenschaften
(Dr. rer. nat.)

vorgelegt von
LUKAS SALFELDER
aus Lörrach

TÜBINGEN
2016

GEDRUCKT MIT GENEHMIGUNG DER MATHEMATISCH-NATURWISSENSCHAFTLICHEN
FAKULTÄT DER EBERHARD KARLS UNIVERSITÄT TÜBINGEN

TAG DER MÜNDLICHEN QUALIFIKATION: 08.02.2017

DEKAN: PROF. DR. WOLFGANG ROSENSTIEL

1. BERICHTERSTATTER: PROF. DR. BARBARA JÄGER

2. BERICHTERSTATTER: PROF. DR. WERNER VOGELANG

Abstract

In the last years, scattering processes comprising pairs of the massive weak gauge bosons gain more and more attention. Those reactions provide particularly promising means to investigate the very mechanism responsible for electroweak symmetry breaking in the Standard Model of particle physics and to search for new physics entering via the weak sector of the theory. Precisely predicting the differential distributions of the final-state particles in realistic conditions is an essential prerequisite to potentially reveal tiny deviations induced by physics beyond the Standard Model.

In this thesis we present a calculation of the next-to-leading order (NLO) electroweak corrections to W-boson pair production at CERNs Large Hadron Collider (LHC), as well as a detailed analysis of vector-boson scattering (VBS) processes at a future high-energy proton–proton collider.

In particular, our calculation of the NLO electroweak corrections to the hadronic process $pp \rightarrow W^+W^- \rightarrow 4 \text{ leptons}$ takes the leptonic W-boson decays as well as all off-shell effects fully into account and, thus, is the first prediction providing NLO accuracy everywhere in phase space. Employing realistic event selection criteria, we study the influence of the corrections in situations that are typical for the experimental analyses in the high-energy region and for Higgs-boson precision studies in the channel $H \rightarrow WW^*$, to which direct W-boson pair production represents an important irreducible background. We observe non-trivial distortions of the differential distributions that, if not properly included in upcoming analyses, could easily be misidentified as first signs of new physics. Furthermore, we compare our predictions to previous results obtained by employing the so-called double-pole approximation. At small and intermediate scales the two approaches show the expected agreement at the level of fractions of a percent, while in the TeV range the differences may easily reach several tens of percent.

Due to the comparably small production cross sections and the generally large QCD backgrounds, studying VBS reactions at hadron colliders is an intricate task, and even with the target luminosity of several 100 fb^{-1} presumably collected at the end of LHC Run II, dedicated differential analyses will hardly be realizable. In our analysis we therefore investigate the opportunities of a potential follow-up project of the LHC which is proposed to operate at a center-of-mass energy of 100 TeV and assumed to deliver a total integrated luminosity of 30 ab^{-1} . For several decay modes we perform a detailed signal-to-background analysis, revealing the excellent possibilities for future measurements of VBS processes at yet unprecedented energy scales that such a machine facilitates. With process-specific event-selection criteria we manage to significantly reduce the background contribution, while due to the deep energy reach definitely sufficient events of the VBS signal remain for a detailed examination at the differential level.

Zusammenfassung

Seit einigen Jahren ist das Interesse an Streureaktionen, an denen Eichboson-Paare der schwachen Wechselwirkung beteiligt sind, stetig gestiegen. Diese Prozesse bieten besonders erfolgversprechende Möglichkeiten sowohl die elektroschwache Symmetriebrechung im Standardmodell der Teilchenphysik zu erforschen, als auch nach ersten Anzeichen schwach-wechselwirkender Neuer Physik zu suchen. Präzise Vorhersagen der differentiellen Verteilungen der Endzustandsteilchen unter möglichst realistischen Bedingungen sind eine Grundvoraussetzung um winzige Veränderungen, welche durch Physik jenseits des Standardmodells verursacht würden, als solche erkennen zu können.

In der vorliegenden Arbeit wird sowohl die Berechnung der elektroschwachen Korrekturen in nächst-zu-führender Ordnung (next-to-leading order, NLO) des W-Boson Paarproduktionsprozesses am Large Hadron Collider (LHC) als auch eine detaillierte Studie zur Untersuchung von Vektor-Boson-Streuung (VBS) an einem zukünftigen hochenergetischen Proton-Proton Beschleuniger vorgestellt.

Unsere Berechnung der elektroschwachen NLO Korrekturen des hadronischen Streuprozesses $pp \rightarrow W^+W^- \rightarrow 4 \text{ Leptonen}$ bezieht die leptonischen Zerfälle der W-Bosonen sowie alle off-shell Beiträge vollständig mit ein und ist somit die erste Vorhersage welche über den gesamten Phasenraum NLO Genauigkeit liefert. Mit Hilfe einer realistischen Ereignisauswahl wird der Einfluss der Korrekturen auf typische experimentelle Analysen untersucht. Hier konzentrieren wir uns zum einen auf die Hochenergie-Region und zum anderen auf den Bereich in dem Präzisionsstudien des Higgs-Bosons im Zerfallskanal $H \rightarrow WW^*$ durchgeführt werden, da hierzu die direkte W-Boson Paarproduktion einen wichtigen irreduziblen Untergrund darstellt. Wenn die vorhergesagten nicht-trivialen Änderungen der differentiellen Verteilungen nicht in geeigneter Weise in den bevorstehenden Analysen berücksichtigt werden, können diese leicht mit ersten Anzeichen Neuer Physik verwechselt werden. Zusätzlich werden unsere Vorhersagen mit früheren Ergebnissen verglichen, welche auf der sogenannten Doppelpol-Näherung basieren. Bei kleinen und mittleren Energieskalen bestätigt sich die erwartete Übereinstimmung im Promillebereich, während wir im Hochenergie-Bereich eine deutliche Diskrepanz zwischen den zwei Methoden von bis zu einigen zehn Prozent aufzeigen können.

Die Untersuchung von VBS Reaktionen an Hadron Beschleunigern ist durch die vergleichsweise geringen Produktions-Wirkungsquerschnitte und dem meist großen QCD Untergrund eine sehr komplizierte Aufgabe und selbst mit einer Luminosität von einigen 100 fb^{-1} , welche bis zum Ende von LHC Run II erreicht werden sollte, wird eine detaillierte Analyse auf differentieller Ebene kaum möglich sein. In unserer Studie untersuchen wir daher das Potenzial eines möglichen LHC-Nachfolgeprojektes, welches bei einer Schwerpunktsenergie von 100 TeV eine Luminosität von 30 ab^{-1} liefern soll.

Anhand einer detaillierten Signal-zu-Untergrund Studie verschiedener Zerfallskanäle zeigen wir die exzellenten Bedingungen unter denen zukünftige Messungen an bisher unerreichten Energieskalen an solch einer Maschine durchgeführt werden könnten. Durch prozessspezifische Ereignisselektionen können die Untergrundbeiträge erheblich verringert werden, während aufgrund des zugänglichen Hochenergiebereiches genügend Ereignisse des VBS Signales verbleiben würden um dieses eingehend auf differenzieller Ebene untersuchen zu können.

Contents

Abstract	vii
Zusammenfassung	ix
1. Introduction	1
I. Theoretical Background and Basic Concepts	7
2. The Standard Model of Particle Physics	9
2.1. The Electroweak Sector of the SM	11
2.2. The QCD Part of the SM	21
3. Quantum Corrections	23
3.1. Regularization of UV Divergences	27
3.2. Renormalization	29
3.2.1. On-Shell Renormalization	30
3.2.2. The Complex-Mass Scheme	32
3.2.3. $\overline{\text{MS}}$ Renormalization	33
3.3. Infrared Singularities	36
4. NLO Predictions at Hadron Colliders	41
4.1. Parton Model and Factorization Theorem	41
4.1.1. The QCD-Improved Parton Model	42
4.1.2. Factorization of QED Singularities	44
4.1.3. Hadron-Hadron Collisions	46
4.2. The Dipole Subtraction Formalism	47
4.2.1. Real Photon Radiation	49
4.2.2. Photon-Induced Processes	56
4.3. One-Loop Integrals	60
II. Phenomenological Applications	63
5. NLO EW Corrections to $pp \rightarrow W^+W^- \rightarrow 4$ Leptons	65
5.1. Theoretical and Experimental Status	66

5.2.	Outline of the Calculation	70
5.2.1.	Real Corrections and Factorization Terms	73
5.2.2.	Full Virtual Corrections	78
5.2.3.	Virtual Corrections in the Double-Pole Approximation	80
5.2.4.	Independent Checks of the Calculation	84
5.3.	Phenomenological Results	85
5.3.1.	Input Parameters and Computational Setup	86
5.3.2.	Event Selection	88
5.3.3.	Results on Integrated Cross Sections	90
5.3.4.	Differential Cross Sections in the ATLAS WW Setup	91
5.3.5.	Differential Cross Sections in the Higgs-Background Setup	96
5.3.6.	Collinear-Safe Versus Collinear-Unsafe Case	99
5.3.7.	Comparison to the Double-Pole Approximation	102
5.4.	Conclusions and Outlook	106
6.	Vector-Boson Scattering Processes at a 100 TeV Collider	107
6.1.	Vector-Boson Scattering at Hadron Colliders	107
6.2.	Studying VBS at 100 TeV	111
6.2.1.	Setup of the Analysis	112
6.2.2.	Input Parameter and Default Selection Cuts	113
6.3.	Phenomenological Results	116
6.3.1.	Same-sign W-pair Production via VBS	116
6.3.2.	$W^\pm Z$ Production via VBS	122
6.3.3.	Z-pair Production via VBS	125
6.3.4.	Opposite-sign W-pair Production via VBS	129
6.3.5.	Single Gauge-Boson Production via VBF	133
6.4.	Summary and Conclusions	136
7.	Summary and Outlook	139
	Appendices	141
A.	Group Theory	143
B.	Kinematics and Scattering	151
C.	Feynman Rules	155
	Bibliography	161
	List of Publications	175
	Acknowledgements	177

Chapter 1

Introduction

The main objective of particle physics is to reveal the fundamental constituents of matter and to explain the very principles governing their interaction. A major part of our present knowledge about these elementary particles is incorporated in the Standard Model of particle physics (SM), which exists in its present form for already 40 years.

The SM addresses three of the four known fundamental interactions of nature, namely the strong, the weak, and the well-known electromagnetic interaction. Describing these forces at the level of elementary particles, the SM is formulated as a quantized gauge theory, where the interactions are mediated by the exchange of associated force carriers, the gauge bosons. The strong interaction, which is responsible for the formation of hadrons, such as protons and neutrons, is described by Quantum Chromodynamics (QCD) [1] and the corresponding gauge bosons are called gluons. The weak and electromagnetic forces are collectively described by the so-called electroweak (EW) theory [2], incorporating the massless mediator of the electromagnetic force, the photon, and the three massive weak gauge bosons called W^+ , W^- , and Z boson. The very existence of these massive gauge bosons in the SM originates from an involved dynamical mechanism that breaks the gauge symmetry of the EW theory, the Higgs mechanism [3]. Since this procedure of electroweak symmetry breaking (EWSB) possesses an essential role in the SM, the experimental observation of the massive W^\pm and Z bosons in 1983 at the European Organisation for Nuclear Research (*Conseil Européen pour la Recherche Nucléaire*, CERN) [4] can be seen as one of the most important steps in establishing the SM. Indeed, after this discovery various collider experiments have been performed to further peruse the distinct structure of the theory, revealing an astonishing agreement with the SM predictions.

However, for many years the ultimate confirmation of the Higgs mechanism, the existence of the Higgs boson, was pending. For almost two decades the Higgs boson was the last missing particle predicted by the SM such that its experimental observation was already eagerly awaited when the Large Hadron Collider (LHC) at CERN began its operation in 2008. Eventually, in July 2012, the discovery of a particle has been announced by the two independent LHC experiments ATLAS [5] and CMS [6], that so far is entirely consistent with a 125 GeV SM Higgs boson [7] and, thus, completes the particle spectrum of the SM. Further determining the properties of this Higgs-like particle is one of the main tasks of the LHC Run II. Started in 2015, this run presently collects data at a centre-of-mass (c.m.) energy of 13 TeV, which is almost twice the

energy reached in Run I.

Irrespective of the outstanding success the SM experienced in the past decades, several experimental observations and theoretical arguments indicate that also physics beyond the SM (BSM) has to exist. Among the most pressing experimental evidences, there are the cosmological observations of *dark matter* and *dark energy*, which both can not be satisfactorily addressed within the SM. While the origin of dark energy, however, is still completely unknown, with dark matter we denote the preponderant part of the matter content of our universe ($\sim 85\%$), that, although gravitationally interacting, seems not to emit any kind of electromagnetic radiation like ordinary matter. Only the remaining $\sim 15\%$ are presently believed to account for the kind of matter that we try to describe within the SM. Although very massive unobserved objects made of ordinary matter (e.g. Massive Astrophysical Compact Halo Objects, MACHOs) can not be excluded with current astronomical data, another conceivable explanation would be that dark matter consists of particles which are not included in the SM, like for example additional Weakly Interacting Massive Particles (WIMPs).

Such a particle-physics-related explanation is further supported by some particular shortcomings of the SM. An explanation of the observed neutrino oscillations, for example, requires for non-zero neutrino masses, while neutrinos have to remain exactly massless in the SM. Another example is the distinct discrepancy between the predicted and measured value in one of the most precise measured quantities, the anomalous magnetic moment of the muon.

Various theories have been developed to account for these experimental evidences, extending the SM by additional particles and/or interactions. Justifying the considerable agreement of collider data with SM predictions observed so far, most of these theories include the SM as a low-energy approximation and new-physics effects are generally assumed to enter the theory at some higher, yet unprobed, energy scale. Attempts to include the fourth known fundamental interaction, the gravitational force, in such a more fundamental theory were, however, so far unsuccessful, as no consistent quantized theory of gravitation is known to date. Indeed, the strength of gravitation is tens of orders of magnitude weaker than the three remaining forces, and can therefore safely be neglected when searching for new-physics effects in the interaction of elementary particles at energy scales that are accessible in collider experiments.

Consequently, the prospects of the present LHC Run II, but especially of future collider experiments, should not be seen in further confirming the SM, but to eventually observe deviations from the SM predictions. A smoking gun signal of BSM physics would for example be a prominent peak in the differential distribution of the decay products of a new particle, similar to the resonance peak of the Higgs boson in the invariant di-photon mass that mainly led to its observation in 2012. At the end of 2015, such a signal has simultaneously been reported by ATLAS [8] and CMS [9], both observing a small excess at around 750 GeV in the di-photon mass. Although the experimentalists explicitly pointed to the limited statistical significance, this excess caused considerable interest especially in the theoretical community and was extensively discussed as the first sign of new physics. However, both experiments could not confirm

their observation in the analyses of the new datasets presented in August this year [10] and the alleged excess turned out to be only a statistical fluctuation.

It is therefore clear that the eventual detection of new particles not only requires a clean experimental environment, allowing for a proper identification of its decay products, but also sufficient statistics, especially in the tails of differential distributions reaching far into unprecedented energy regimes, is of utter importance. Under these aspects, processes with weak gauge bosons provide a particularly suitable testbed to search for BSM physics. Especially in the leptonic decay channels of the weak gauge bosons the SM processes exhibit very distinct and well detectable final states. Even at hadron colliders, where one is genuinely plagued by competing QCD-induced processes that lead to the same signature in the detector, so-called QCD backgrounds, the purely EW processes remain very well distinguishable and therefore allow for precise measurements. Moreover, the gauge-boson self-interaction is very sensitive to the exact realisation of EWSB. Possible new-physics effects entering via the EW sector could have large effects on the internal structure of the theory such that deviations from the SM predictions should already be detectable well below the production threshold of new particles.

In order to reveal such BSM effects above the large SM background, knowing the contributing SM processes to the highest possible accuracy is mandatory. The inclusion of quantum corrections, so-called higher-order corrections, may lead to considerable modifications of theoretical predictions performed at the lowest possible order (leading order, LO). For particular processes, these corrections may reach several 100 %, as they include additional contributions, which are, however, not separately detectable. Especially missing higher-order corrections of the EW theory may easily be misinterpreted as signs of new physics. Despite the fact that EW corrections are generally much smaller than the corresponding corrections in the strong force (QCD corrections), they have a particularly large influence in the tails of distributions, where new-physics searches are conventionally performed. However, also for present and upcoming precision studies at rather low or intermediate energy domains, including not only the dominant QCD corrections but additionally the effects of EW corrections becomes more and more important to fully exploit the potential of these analyses.

In this thesis, we concentrate on two slightly related process classes that both provide particularly promising means to further challenge the SM at hadron colliders, namely weak-boson pair production and vector-boson scattering (VBS) reactions. While for weak-boson pair production we focus on the particular process featuring two oppositely charged W bosons ($pp \rightarrow W^+W^-$), for VBS the genuine $2 \rightarrow 2$ scattering processes $VV \rightarrow VV$, with V denoting either a W^\pm boson or the Z boson, are considered.

Our objectives of studying these two process classes, however, fairly differ: For the W-pair production process we aim for predictions at the highest possible accuracy and present our calculation of the full next-to-leading order (NLO) corrections in the EW coupling [11]. For realistic LHC event-selection criteria we quantify the impact of the individual contributions by means of differential distributions of the final-state particles, as well as discuss the validity of EW corrections employing the so-called double-pole

approximation [12], which is partly based on an expansion about the W-resonance poles. With an envisaged integrated luminosity of several 100fb^{-1} at the end of LHC Run II, certainly enough statistics will be collected to probe this process in energy regions where a precise knowledge of the distinct effects of EW corrections possesses an essential part in the theoretical predictions.

Studying VBS processes at hadron colliders is unfortunately much more involved, since large irreducible backgrounds heavily complicate the extraction of the signal contribution. Although the techniques to efficiently suppress the background by imposing dedicated selection criteria are in principle very well known, their application unavoidably also reduces the signal cross section. Consequently, the dedicated search for new-physics effects in the EW sector via VBS processes is strongly limited by the very low cross sections in the remaining phase space. Despite the higher luminosity and deeper energy reach of LHC Run II compared to Run I, the investigation of VBS processes at the differential level will hardly be possible at the LHC.

Much more powerful means for studying VBS reactions would be provided by a future high-energy proton–proton collider operating at a c.m. energy of 100 TeV, that is currently discussed as a possible follow-up project of the LHC. In order to explore the prospects of probing VBS processes at such a machine, we perform a dedicated LO analysis, where we examine the signal and background contributions of several VBS processes. While present LHC studies definitely should be performed at the highest possible accuracy, the omission of higher-order corrections is, however, well justified at such an early stage of the project, where the possible experimental setup still represents the largest source of uncertainties.

This thesis is divided in two parts and organized as follows:

In the first part, we discuss the basic theoretical concepts needed to perform accurate predictions for scattering processes at hadron colliders. We begin with a detailed introduction to the SM in Chap. 2, where we separately discuss the EW and subsequently the QCD part of the theory. In Chap. 3 we comment in a general way on the problems one is confronted with in the calculation of higher-order corrections and present methods to handle those. After discussing the regularization procedure and different renormalization schemes in the first two sections of this chapter, in Sec. 3.3 we introduce the issue of infrared divergences, which occur in intermediate results of explicit higher-order calculations. The additional requirements to perform predictions at hadron colliders are then discussed in Chap. 4. Section 4.1 is dedicated to the introduction of the parton model and the necessary factorization properties of the scattering process. Subsequently, in Sec. 4.2 we present in detail the subtraction formalism that will be applied in our calculation of EW corrections to handle the infrared singularities appearing in the phase-space integration, and in Sec. 4.3 some details on the explicit calculation of one-loop integrals are given.

In the second part of this thesis, we turn to the explicit application of the presented theoretical foundations and discuss two particularly important processes for collider phenomenology. In Chap. 5 we outline our calculation of the EW correction to the W-

boson pair production process at the LHC and discuss our results by means of integrated and differential distributions for several event-selection setups. Chapter 6 comprises the details of our LO studies of vector-boson scattering processes at a future hadron collider operating at 100 TeV. In a detailed signal-to-background analysis of the SM processes we comment in particular on the prospects in the search for new physics. Finally, in the last chapter we summarize our main results and provide a short outlook.

Part I

Theoretical Background and Basic Concepts

Chapter 2

The Standard Model of Particle Physics

The Standard Model of particle physics (SM) describes all known elementary particles and their interactions. Its formulation as a relativistic quantum field theory combines the fundamental principles of special relativity and quantum mechanics with the well-known concepts and mathematical techniques of classical field theory.

As a field theory, the SM is most conveniently formulated within the Lagrangian formalism, where the Lagrangian density (*Lagrangian*) \mathcal{L} contains all relevant information on the fields and their interactions in form of kinetic, mass, and interaction terms. Within this formalism, the dynamics of the theory is derived by the principle of least action $\delta\mathcal{S} = 0$, where the action \mathcal{S} is defined as the four dimensional space-time integral over the Lagrangian,

$$\mathcal{S} = \int d^4x \mathcal{L}. \quad (2.1)$$

In the following, we work in natural units, i.e. we set $\hbar = c = 1$ throughout, which results in all quantities having dimensions of mass to some power. In particular, the action defined in Eq. (2.1) becomes a dimensionless quantity, which implies that the Lagrangian has to be of mass-dimension four.

Given the Lagrangian of a theory, it is in principle straightforward to derive the so-called *Feynman rules* which serve as building blocks for any calculation of physical observables, see e.g. Refs. [13–16]. The Lagrangian of the SM is, however, strongly constrained by the compliance with fundamental symmetry principles, such that we start with a detailed discussion of the Lagrangian in this section. Within the SM, we generally distinguish between two kinds of symmetries, namely *space-time symmetries* and *gauge symmetries*. Since these symmetries are described by means of groups and their associated algebras, we provide a short introduction to group theory and, in particular, discuss the relevant symmetry groups of the SM in App. A. Further details on the individual properties of the groups that we simply assume in the following can be found there.

The group associated with the space-time symmetries of the SM is the so called Poincaré group. This group generalizes the underlying group of special relativity, the Lorentz group, by incorporating beside Lorentz rotations and Lorentz boosts also the translation on the four-dimensional space-time, the Minkowski space. The fields appearing in the SM Lagrangian are objects belonging to a specific irreducible representation of the Poincaré group, which are characterised by their mass and spin. The requirement

of renormalizability¹ of the SM further restricts the fields that may appear in the Lagrangian to only three different kinds of spin values, namely bosonic spin-0 (scalars) and spin-1 fields (vectors) and fermionic spin- $\frac{1}{2}$ fields (spinors). Fields of a higher spin value may not enter the SM Lagrangian, since it is not possible to construct Lorentz-invariant operators of mass dimension four without spoiling renormalizability [17].

The second and completely distinct kind of symmetries are the gauge symmetries, or internal symmetries, that determine the interaction among the SM fields. In the SM these symmetries have to be respected at each individual space-time point, which further defines the so-called *local* gauge symmetries, where the spin-1 vector bosons, mediating the interactions among the SM fields, act as gauge bosons corresponding to a specific gauge group. The gauge group of the SM,

$$SU(3)_C \times SU(2)_W \times U(1)_Y, \quad (2.2)$$

is a product group of three fundamental Lie-groups. The colour group $SU(3)_C$ is the internal group of Quantum Chromodynamics (QCD) that describes the strong interaction. The eight gauge bosons of QCD are called gluons (g) and the fermions interacting with these gluons are called quarks (q). $SU(2)_W$ and $U(1)_Y$ are the symmetry groups of the weak isospin (I_W) and the weak hypercharge (Y), respectively, which together build the electroweak (EW) sector of the SM (EWSM). The four gauge bosons of the EWSM are usually denoted by W^i ($i = 1, 2, 3$) and B . Finally, the fermions of the SM that do not interact strongly are called leptons (ℓ), where we further differentiate between the electrically charged leptons (l) and the electrically neutral neutrinos (ν). With respect to their associated gauge group, all gauge bosons transform under the adjoint representation, while the fermionic fields either live in the fundamental representation if they take part in the respective interaction, or in the trivial representation if they do not.

The EWSM is for a particular reason much more involved than the strongly interacting part, namely the appearance of massive gauge bosons in the EW sector. Since explicit mass terms for gauge bosons would immediately violate gauge invariance, a dynamical mechanism is required to generate the experimentally observed gauge boson masses in the EW sector. The only known possibility for introducing gauge boson masses without spoiling gauge invariance, is the Englert-Brout-Higgs-Guralnik-Hagen-Kibble mechanism [3], or, shortly, the Higgs mechanism. The spontaneous breaking of the $SU(2)_W \times U(1)_Y$ symmetry (EWSB) via a complex scalar field eventually leads to gauge invariant mass terms for three of the four gauge bosons of the EW sector. The strongly interacting part of the SM, on the other hand, remains unbroken and therefore $SU(3)_C$ is an exact symmetry in the SM. The QCD Lagrangian, which exclusively describes quarks and massless gluons, will be discussed separately in Sec. 2.2.

For the quantization of the classical Lagrangian of the SM, usually the path-integral formalism [18] is applied, which allows for a clean treatment of the divergences appearing

¹ A theory is called renormalizable if all ultraviolet divergences that occur in higher orders of the perturbative expansion may be reabsorbed by a finite number of appropriate redefinitions of the input parameters and fields. The renormalization of the SM will be discussed in detail in Sec. 3.2.

in the quantization of non-Abelian gauge theories. These divergences appear, because the functional integral over the gauge fields automatically contains infinitely many physically equivalent field configurations, as they are related among each other by gauge transformations. The *Faddeev–Popov procedure* [19] allows to re-parametrize the classical Lagrangian such that the resulting effective Lagrangian reads

$$\mathcal{L}_{\text{SM, eff}} = \mathcal{L}_{\text{SM, cl.}} + \mathcal{L}_{\text{fix}} + \mathcal{L}_{\text{FP}}, \quad (2.3)$$

containing two additional terms, the gauge-fixing term (\mathcal{L}_{fix}) and the Faddeev–Popov term (\mathcal{L}_{FP}), respectively. The gauge-fixing term selects one configuration out of each set of fields that transform into each other, and therefore restricts the path-integral to physically non-equivalent field configurations. This allows to split off the divergence arising from the integration over the gauge group, which subsequently can be absorbed in the normalization of the functional integral. \mathcal{L}_{FP} introduces anti-commuting scalar fields, the Faddeev–Popov ghosts, to the theory, which by definition violate the spin-statistics theorem. This is, however, unproblematic as they are unphysical degrees of freedom that only appear as intermediate particles within higher-order corrections, but never as external particles.

Finally, from the effective Lagrangian (Eq. (2.3)) the Feynman rules of the SM can be derived in a straightforward way. These rules allow for a pictorial representation of the mathematical expressions describing the interaction among the different kinds of particles, which tremendously facilitates handling and description of reappearing building blocks in any calculation. The Feynman rules assign a set of symbols to the most fundamental building blocks, namely to external particles, the interaction among different particles (vertices), and the propagation of intermediate particles. The assignment for all SM particles is collected in App. C.

In the upcoming two sections we now discuss separately the Lagrangian of the EW sector and the QCD sector. We thereby closely follow the presentation of Ref. [14], which we also recommend for further insights.

2.1. The Electroweak Sector of the SM

In this section we discuss the Glashow–Weinberg–Salam (GWS) model [2], which governs the EW part of the SM, in detail. The GWS model describes the interaction among all fermionic fields of the SM, the four gauge bosons associated with the symmetry group $\text{SU}(2)_W \times \text{U}(1)_Y$, and the complex scalar Higgs field. Via the Higgs mechanism [3], the EW symmetry is spontaneously broken, which eventually leads to mass terms for the fermions as well as for three of the four gauge bosons of the theory. In the following, we first separately introduce the three gauge invariant terms of the classical Lagrangian,

$$\mathcal{L}_{\text{GWS, cl.}} = \mathcal{L}_{\text{Gauge}} + \mathcal{L}_{\text{Fermions}} + \mathcal{L}_{\text{Higgs}}, \quad (2.4)$$

before extracting the physical consequences following from the Lagrangian. The quantization of the classical Lagrangian will be discussed in Sec. 2.1.5.

2.1.1. Gauge Part

The gauge part of the Lagrangian (2.4) reads

$$\mathcal{L}_{\text{Gauge}} = -\frac{1}{4}B_{\mu\nu}(x)B^{\mu\nu}(x) - \frac{1}{4}W_{\mu\nu}^i(x)W^{i,\mu\nu}(x), \quad (2.5)$$

with the two field-strength tensors of the $U(1)_Y$ and $SU(2)_W$ symmetry groups

$$B_{\mu\nu}(x) = \partial_\mu B_\nu(x) - \partial_\nu B_\mu(x), \quad (2.6)$$

and

$$W_{\mu\nu}^i(x) = \partial_\mu W_\nu^i(x) - \partial_\nu W_\mu^i(x) + g_2 \epsilon^{ijk} W_\mu^j(x) W_\nu^k(x), \quad (2.7)$$

respectively. In Eqs.(2.5) and (2.7), the summation over the repeated Lorentz- and group-indices is implicitly understood. Here, g_2 is the coupling strength of the weak interaction and the structure constants of the $SU(2)_W$ are denoted by ϵ^{ijk} , the totally antisymmetric tensor in three dimensions. Since $U(1)_Y$ is an Abelian group, no self-interaction term and therefore also no structure constant appears in Eq.(2.6). Note again, that no explicit mass terms for the gauge bosons can be added to the Lagrangian, since such a term would immediately violate gauge invariance.

2.1.2. Fermionic Part

Already several years before the theoretical formulation of the GWS model, it was shown by Wu et al. [21] that the electroweak interaction is not invariant under the parity transformation (\mathcal{P}), which transforms right-handed and left-handed Weyl spinors into one another. Actually, it even turned out that only left-handed fermions take part in the radioactive processes that are nowadays distributed to the weak force, whereas both chiralities interact electromagnetically in a uniform way. Note, however, that the combined symmetry transformation of charge conjugation and parity (\mathcal{CP}) again is a symmetry of the unbroken EWSM, implying that right handed anti-fermions do interact weakly. Since direct mass-terms in the Lagrangian would spoil this $SU(2)_W$ gauge invariance, with respect to the Poincaré group, the fermion states of the EWSM are given as massless left- and right-handed Weyl spinors.

For the formulation of the GWS model as a gauge theory, these experimental observations imply that left-handed fermions transform under the two-dimensional fundamental representation ($I_W^a = \sigma^a/2$, with the Pauli matrices σ^a), whereas the right-handed fermions have to transform trivially under the $SU(2)_W$ part ($I_W^a = 0$), and, thus, could be omitted completely in purely weak processes. However, since both chiralities carry a weak hypercharge and therefore transform in a non-trivial way under the $U_Y(1)$ subgroup, the right-handed fermions have to be included as $SU(2)_W$ -singlets in the unified theory. According to the *Gell-Mann-Nishijima relation*,

$$Q = I_W^3 + \frac{Y}{2}, \quad (2.8)$$

Fermions of the EWSM		Generation			I_{W}^3	Y	Q
		1	2	3			
leptons ℓ	neutrinos ν_i	ν_e	ν_μ	ν_τ	$\frac{1}{2}$ 0	-1 0	0
	charged leptons l_i	e	μ	τ	$-\frac{1}{2}$ 0	-1 -2	-1
quarks q	up-type quarks u_i	u	c	t	$\frac{1}{2}$ 0	$\frac{1}{3}$ $\frac{4}{3}$	$\frac{2}{3}$
	down-type quarks d_i	d	s	b	$-\frac{1}{2}$ 0	$\frac{1}{3}$ $-\frac{2}{3}$	$-\frac{1}{3}$

Table 2.1.: The quantum numbers of the fermionic fields of the EWSM: I_{W}^3 , Y, and Q denote third component of the weak isospin, the weak hypercharge, and the electric charge, respectively. The upper part of each line belongs to the left-handed representation of the corresponding field, the lower part to the right-handed. The electric charge Q is independent of the chirality and is obtained accordingly to Eq. (2.8). For a more transparent presentation the primes indicating EW eigenstates are omitted in this arrangement. Adapted from [20].

the electric charge Q is calculated irrespective of the chirality from the generators I_{W}^3 and Y in the actual representation, thus setting the weak hypercharges for the right- and left-handed fermionic fields. In nature we observe three *generations* of quarks and leptons, which show exactly the same transformation properties under the EW gauge groups. In Tab. 2.1 we collect the quantum numbers of the left- and right-handed components of all fermionic fields of the EWSM. Note that since neutrinos are found to be electrically neutral, Eq. (2.8) implies that right-handed neutrinos must also transform trivially under $U_Y(1)$, and therefore can be completely removed from the particle spectrum, as they do not interact at all. As we will see below, this omission, in particular, prevents the neutrinos from receiving a mass-term in the same manner as the remaining fermions².

Finally, we can write the fermionic fields of the EWSM in the following manner

$$L_i^L = \begin{pmatrix} \nu_i^L \\ l_i^L \end{pmatrix}, \quad Q_i^L = \begin{pmatrix} u_i^L \\ d_i^L \end{pmatrix}, \quad l_i^R, \quad u_i^R, \quad d_i^R, \quad (i = 1, 2, 3), \quad (2.9)$$

where the superscripts L and R denote the chirality of the fields and the subscript i is the label for the three generations. The reason for the convention to label the eigenstates of the EW interaction with an additional prime, will become apparent in the discussion of the Higgs part of the EW Lagrangian. Introducing the covariant derivative of the

²From the observation of *neutrino oscillations* we know that non-zero neutrino masses have to exist, which—due to the omission of the right-handed component—cannot be explained within the SM.

EWSM,

$$D_\mu = \partial_\mu - ig_2 W_\mu^i I_W^i + ig_1 B_\mu \frac{Y}{2}, \quad \not{D} = \gamma^\mu D_\mu, \quad (2.10)$$

we can finally write down the Lagrangian of the fermionic part,

$$\mathcal{L}_{\text{Fermion}} = \sum_j i \left(\bar{L}_j^{\prime L} \not{D} L_j^{\prime L} + \bar{Q}_j^{\prime L} \not{D} Q_j^{\prime L} + \bar{l}_j^{\prime R} \not{D} l_j^{\prime R} + \bar{u}_j^{\prime R} \not{D} u_j^{\prime R} + \bar{d}_j^{\prime R} \not{D} d_j^{\prime R} \right), \quad (2.11)$$

that describes the kinematics of massless fermionic fields and the interaction with the gauge bosons of the EWSM. Here, the bar above a fermionic field denotes the corresponding anti-field, which shows exactly the opposite quantum numbers listed in Tab. 2.1. Note, that even though labeled equally, the covariant derivative \not{D} in Eq. (2.11) takes a different form, depending on the actual quantum numbers of the field it acts on. In Eq. (2.10) beside the coupling constant of the weak interaction, g_2 , we also introduced the coupling constant of the $U(1)_Y$ -part, which we denote by g_1 .

2.1.3. Higgs Part

The Higgs part of the classical Lagrangian of Eq. (2.4) describes the kinematics of a complex scalar $SU(2)_W$ doublet Φ , the Higgs doublet, and the interaction of this field with the gauge bosons and fermions introduced above. The self-interaction potential of the scalar $V(\Phi)$ is chosen in such a way that the ground state Φ_0 acquires a non-vanishing vacuum expectation value (vev) which spontaneously breaks the $SU(2)_W \times U(1)_Y$ symmetry into the conserved electromagnetic $U(1)_{\text{EM}}$ symmetry, and eventually leads to mass terms for three of the four gauge bosons as well as for the fermions. Note, that if we postulate a vacuum that is invariant under Poincaré transformations, only scalar fields can acquire non-vanishing vevs via the spontaneous breaking of a local symmetry. Additionally, since we demand the vacuum to be electrically uncharged, according to Eq. (2.8), this implies for the ground state Φ_0

$$Q\Phi_0 = \left(\frac{\sigma^3}{2} + \frac{1}{2}Y_\Phi \right) \Phi_0 = \frac{1}{2} \begin{pmatrix} Y_\Phi + 1 & 0 \\ 0 & Y_\Phi - 1 \end{pmatrix} \begin{pmatrix} \phi_{01} \\ \phi_{02} \end{pmatrix} \stackrel{!}{=} 0, \quad (2.12)$$

which restricts the weak hypercharge of the Higgs doublet to be $Y_\Phi = \pm 1$, in order to obtain one (electrically) neutral component that acquires the non-vanishing vev. By convention we choose the + sign for the weak hypercharge, such that an arbitrary Φ reads

$$\Phi(x) = \begin{pmatrix} \phi^+(x) \\ \phi^0(x) \end{pmatrix}, \quad (2.13)$$

with an (electrically) charged upper and a neutral lower component. The most general renormalizable Lagrangian for this Higgs doublet,

$$\mathcal{L}_{\text{Higgs}} = (D^\mu \Phi)^\dagger (D_\mu \Phi) - V(\Phi) - \mathcal{Y}(\Phi, Q', L', u', d', l'), \quad (2.14)$$

contains a kinetic term with the covariant derivative of Eq. (2.10), the Higgs self-interaction potential $V(\Phi)$, and the Yukawa interaction between Φ and the fermionic fields, $\mathcal{Y}(\Phi, \dots)$. The Higgs potential reads

$$V(\Phi) = -\mu^2 \Phi^\dagger \Phi + \frac{\lambda}{4} (\Phi^\dagger \Phi)^2, \quad (2.15)$$

where both, the mass-parameter μ^2 and the coupling constant λ have to be chosen positive, for the Higgs potential to be bounded from below and to acquire a non-vanishing vev, respectively. The Yukawa interaction,

$$\mathcal{Y}(\Phi, \dots, l') = \sum_{i,j} \left(\bar{L}'^L_i G_{ij}^{\text{lep}} l_j'^R \Phi + \bar{Q}'^L_i G_{ij}^{\text{up}} u_j'^R \Phi^c + \bar{Q}'^L_i G_{ij}^{\text{down}} d_j'^R \Phi + \text{h.c.} \right), \quad (2.16)$$

contains couplings of the Higgs doublet to the left- and right-handed fermion fields. Here, we introduced the Yukawa coupling matrices of the fermion fields, G_{ij}^{ferm} , that will be further specified below, and the charge conjugate of the Higgs doublet, $\Phi^c = i\sigma^2 \Phi^* = [(\phi^{0*}, -\phi^-)]^\top$, where $\phi^-(x) = [\phi^+(x)]^*$. We want to point out, that if we would not have removed the right-handed neutrino fields completely from the theory, an additional term of the form $\bar{L}'^L_i G_{ij}^\nu \nu_j'^R \Phi^c$ occurred in Eq. (2.16).

The energy of the ground state of the Higgs potential, i.e. the vev v , is given by $v = |\Phi_0| = \sqrt{2\mu^2/\lambda}$, which specifies the ground state up to an $U(1)_{\text{em}}$ phase to be

$$\Phi_0 = \begin{pmatrix} 0 \\ \sqrt{\frac{2\mu^2}{\lambda}} \end{pmatrix} =: \begin{pmatrix} 0 \\ \frac{v}{\sqrt{2}} \end{pmatrix}. \quad (2.17)$$

Expanded about the minimum this yields

$$\Phi(x) = \begin{pmatrix} \chi^+(x) \\ \frac{1}{\sqrt{2}} [v + H(x) + i\chi^0(x)] \end{pmatrix}, \quad \Phi^c(x) = \begin{pmatrix} \frac{1}{\sqrt{2}} [v + H(x) - i\chi^0(x)] \\ -\chi^-(x) \end{pmatrix}, \quad (2.18)$$

for Φ and its charge conjugate, respectively. Here, $H(x)$ is the real scalar Higgs field and the fields $\chi^0(x)$, $\chi^+(x)$ and $\chi^-(x)$ are called would-be Goldstone fields. Whereas the Higgs field corresponds to the neutral scalar Higgs particle H of the SM, the latter three fields are not related to physical particles and can be eliminated by a suitable gauge transformation (the *unitary gauge*)³. However, the three degrees of freedom do not simply disappear from the theory, but reappear as the additional longitudinal degrees of freedom of the gauge bosons, that have been rendered massive.

2.1.4. The Physical Content of the EW SM

The physical content of the SM can be extracted in the most transparent way in the unitary gauge (u.g.), where the unphysical would-be Goldstone fields completely decouple

³Details on the choice of gauges for the quantization procedure will be discussed in Sec. 2.1.5.

from the theory and the physical particles can be classified as eigenstates of the electric charge Q and the mass. In this gauge Eq. (2.18) reads $\Phi(x) = \frac{1}{\sqrt{2}}[(0, v + H(x))]^T$, which inserted into the Higgs Lagrangian of Eq. (2.14) yields

$$\begin{aligned} \mathcal{L}_{\text{Higgs}}^{\text{u.g.}} &= \frac{1}{2}(D^\mu(v + H))^\dagger(D_\mu(v + H)) \\ &\quad - \mu^2 H^2 + \frac{\mu^2}{v} H^3 + \lambda H^4 \\ &\quad - \frac{1}{\sqrt{2}}(v + H) \sum_{i,j} \left(\bar{l}_i^L G_{ij}^{\text{lep}} l_j^{\prime R} + \bar{u}_i^L G_{ij}^{\text{up}} u_j^{\prime R} + \bar{d}_i^L G_{ij}^{\text{down}} d_j^{\prime R} + \text{h.c.} \right). \end{aligned} \quad (2.19)$$

In the second line we can directly identify the trilinear and quartic self couplings of the Higgs field as well as the bilinear term, the so-called the mass term, yielding $M_H = \sqrt{2}\mu$. As we will explain in the following two sections, the first and last lines of Eq. (2.19), in particular, incorporate terms that are bilinear in the individual bosonic and fermionic fields, respectively, and, thus, define their masses.

Boson mass terms

Since all four gauge bosons of the EW sector have vanishing hypercharge, according to Eq. (2.8) the eigenstates of the electrical charge operator Q are simultaneously eigenstates of I_W^3 . Defining

$$W_\mu^\pm = \frac{1}{\sqrt{2}}(W_\mu^1 \mp iW_\mu^2), \quad (2.20)$$

yields

$$QW_\mu^3(x) = QB_\mu(x) = 0, \quad QW_\mu^\pm(x) = \pm W_\mu^\pm(x), \quad (2.21)$$

thus, beside the two uncharged gauge bosons W^3 and B , we have one positively and one negatively charged gauge boson, W^+ and W^- , respectively. Expressed in these fields the mass terms for the gauge fields contained in the first line of Eq. (2.19) read

$$\frac{1}{4}v^2 g_2^2 W_\mu^- W^{+\mu} + \frac{1}{8}v^2 (g_1 B_\mu + g_2 W_\mu^3)^2, \quad (2.22)$$

where we identify the mass of the charged W^\pm bosons

$$M_W = \frac{g_2 v}{2}. \quad (2.23)$$

The masses of the two neutral gauge fields follow from the diagonalization of the corresponding mass-squared matrix

$$(M_{B,W^3})^2 = \frac{v^2}{4} \begin{pmatrix} g_1^2 & g_1 g_2 \\ g_1 g_2 & g_2^2 \end{pmatrix}. \quad (2.24)$$

Since the determinant of this matrix vanishes, one eigenvalue has to be equal to zero, while the other one is given by its trace. The mass eigenstates are obtained through a rotation of the two uncharged fields

$$\begin{pmatrix} A_\mu \\ Z_\mu \end{pmatrix} = \begin{pmatrix} c_W & -s_W \\ s_W & c_W \end{pmatrix} \begin{pmatrix} B_\mu \\ W_\mu^3 \end{pmatrix}, \quad (2.25)$$

where we have defined the *weak mixing angle* θ_W ,

$$c_W = \cos \theta_W = \frac{g_2}{\sqrt{g_1^2 + g_2^2}}, \quad s_W = \sin \theta_W. \quad (2.26)$$

A_μ is the photon field, which we identify as the massless field corresponding to the unbroken $U(1)_{\text{em}}$ symmetry and Z_μ yields the Z boson with the mass

$$M_Z = \frac{v}{2} \sqrt{g_1^2 + g_2^2} = \frac{M_W}{c_W}. \quad (2.27)$$

Fermion mass terms

In the third line of Eq. (2.19) we notice a restriction of the left-handed $SU(2)_W$ doublets defined in Eq. (2.9) onto the upper or lower parts, respectively, caused by the Higgs field and its charge conjugate in the unitary gauge.

In principle we can directly read off the masses of the fermions (f), but since the mass eigenstates of the fermionic fields are not equal to the EW eigenstates, the mass matrices $M_{ij}^f = 1/\sqrt{2}G_{ij}^f v$ are not diagonal. Note again, that due to the complete removal of right-handed neutrinos from the theory and the omission of the associated term already in Eq. (2.16), no mass term for neutrinos is included in Eq. (2.19).

In order to diagonalize the mass matrices we define left- and right-handed mass eigenstates according to

$$f_i^L = \sum_j U_{ij}^{f,L} f_j'^L, \quad f_i^R = \sum_j U_{ij}^{f,R} f_j'^R, \quad (2.28)$$

with the unitary matrices $U^{f,L}$ and $U^{f,R}$. These matrices build bi-unitary transformations that diagonalize the mass matrices, resulting in the fermion masses

$$m_{f_i} = \frac{1}{\sqrt{2}} \sum_{j,l} U_{ij}^{f,L} G_{jl}^f U_{li}^{\dagger f,R} v. \quad (2.29)$$

Since all those masses can be chosen real, the Hermitian conjugate parts of Eqs. (2.16) and (2.19), and, thus, the anti-particles, receive the same masses. Defining $f_i = f_i^L + f_i^R$, the mass terms of the fermions can be written very compactly as

$$- \sum_{f_i} m_{f_i} \bar{f}_i f_i, \quad (2.30)$$

since terms of the form $\bar{f}_i^L f_i^L$ and $\bar{f}_i^R f_i^R$ vanish, leaving only the couplings defined in Eq. (2.16), namely $m_{f_i} \bar{f}_i^R f_i^L$ and $m_{f_i} \bar{f}_i^L f_i^R$.

The terms proportional to the Higgs field H in the last line of Eq. (2.19) can now be understood as the interaction of the Higgs field with the fermions, where the coupling strength m_{f_i}/v is proportional to the mass of the respective fermion.

The Standard Model Lagrangian

The complete classical part of the Lagrangian of the SM (Eq. (2.3)) can be expressed in terms of the physical fields, which we just defined in the previous sections as mass and charge eigenstates, and reads

$$\begin{aligned}
\mathcal{L}_{\text{SM, cl.}}^{\text{u.g.}} = & \sum_{f_i=l_i, q_i} \left[\bar{f}_i (i\not{\partial} - m_{f_i}) f_i - e Q_f \bar{f}_i \gamma^\mu f_i (A_\mu + \frac{s_W}{c_W} Z_\mu) + \frac{e I_{W, f}^3}{s_W c_W} \bar{f}_i \gamma^\mu f_i Z_\mu \right] \\
& + \sum_i \frac{e}{\sqrt{2} s_W} \left[\bar{\nu}_i^L \gamma^\mu l_i^L W_\mu^+ + \bar{l}_i^L \gamma^\mu \nu_i^L W_\mu^- \right] \\
& + \sum_{i, j} \frac{e}{\sqrt{2} s_W} \left[\bar{u}_i^L \gamma^\mu \mathbf{V}_{ij} d_j^L W_\mu^+ + \bar{d}_i^L \gamma^\mu \mathbf{V}_{ij}^\dagger u_j^L W_\mu^- \right] \\
& - \sum_{f_i=l_i, q_i} e \frac{m_{f_i}}{2 s_W M_W} \bar{f}_i f_i H \\
& - \frac{1}{4} \left| \partial_\mu A_\nu - \partial_\nu A_\mu - ie (W_\mu^- W_\nu^+ - W_\nu^- W_\mu^+) \right|^2 \\
& - \frac{1}{4} \left| \partial_\mu Z_\nu - \partial_\nu Z_\mu + ie \frac{c_W}{s_W} (W_\mu^- W_\nu^+ - W_\nu^- W_\mu^+) \right|^2 \\
& - \frac{1}{2} \left| \partial_\mu W_\nu^+ - \partial_\nu W_\mu^+ - ie (W_\mu^+ A_\nu - W_\nu^+ A_\mu) + ie \frac{c_W}{s_W} (W_\mu^+ Z_\nu - W_\nu^+ Z_\mu) \right|^2 \\
& + \frac{1}{2} \left| \partial_\mu H + i M_Z Z_\mu + i \frac{e}{2 c_W s_W} Z_\mu H \right|^2 + \left| i M_W W_\mu^+ + i \frac{e}{2 s_W} W_\mu^+ H \right|^2 \\
& - \frac{1}{2} M_H^2 H^2 - e \frac{M_H^2 H^3}{4 s_W M_W} - e^2 \frac{M_H^2 H^4}{32 s_W^2 M_W^2} \\
& + \sum_{q_i} \left[g_s \bar{q}_i \gamma^\mu G_\mu^a T^a q_i \right] - \frac{1}{4} G_{\mu\nu}^a G^{a, \mu\nu}. \tag{2.31}
\end{aligned}$$

In addition to the already discussed mass terms, in this form we can directly identify the couplings of the fermions to the (partly) massive vector bosons and the Higgs bosons, as well as all bosons self-interaction terms. For completeness, we added in the last line the gauge boson interaction terms of the QCD-Lagrangian, which will be discussed in Sec. 2.2. The electric charge e is defined as the coupling constant multiplying the photon-fermion vertex appearing in the first line and is given in terms of the fundamental gauge couplings as

$$e = \frac{g_1 g_2}{\sqrt{g_1^2 + g_2^2}}. \tag{2.32}$$

In the third line of Eq. (2.31), which describes the coupling between the quark mass eigenstates and the charged W^\pm bosons, we introduced the unitary matrix

$$\mathbf{V} = U^{u,L} U^{d,L,\dagger}, \quad (2.33)$$

the *Cabibbo–Kobayashi–Maskawa* (CKM) matrix [22]. This matrix parametrizes the mixing of the mass eigenstates of the three different quark generations in charged current processes. The analogous matrix in the lepton sector is not needed, since the transition matrix of the massless—and in particular mass degenerate—neutrino fields $U^{\nu,L}$ can be chosen such, that it diagonalizes the lepton– W -bosons interaction vertex⁴.

The Feynman rules that can be derived from the Lagrangian $\mathcal{L}_{\text{SM,cl.}}^{\text{u.g.}}$ are collected in App. C.

2.1.5. Quantization of the EWSM

The general form of the gauge fixing Lagrangian in any R_ξ gauge reads

$$\mathcal{L}_{\text{fix}} = -\frac{1}{2\xi^a} (C^a\{\mathcal{A}_\mu, \mathcal{X}; x\})^2, \quad (2.34)$$

with the arbitrary gauge parameters ξ^a and the local gauge fixing functionals C^a for every gauge boson. The gauge fixing functional depends on the gauge fields and—in a spontaneously broken theory—on the would-be Goldstone fields. The Faddeev–Popov Lagrangian in its most general form can be written as

$$\mathcal{L}_{\text{FP}} = -\int d^4z \bar{u}^a(x) \frac{\delta C^a\{\mathcal{A}_\mu, \mathcal{X}; x\}}{\delta A_\nu^c(z)} D_\nu^{cb} u^b(z), \quad (2.35)$$

with the covariant derivative in the adjoint representation of the particular gauge group, D_μ^{ab} , and the Grassmann-valued (anti-commuting) scalar ghost and anti-ghost fields, u^a and \bar{u}^a .

In a spontaneously broken theory like the EWSM, mixing terms between gauge-boson fields and the unphysical would-be Goldstone fields of the form $V_\mu \partial^\mu \chi$ may appear, which in general lead to non-diagonal propagator structures. However, if we choose the following four linear gauge-fixing functionals for the physical eigenstates defined in Eqs. (2.20) and (2.25),

$$\begin{aligned} C^A &= \partial^\mu A_\mu, \\ C^Z &= \partial^\mu Z_\mu - M_Z \xi'_Z \chi^0, \\ C^\pm &= \partial^\mu W_\mu^\pm \mp i M_W \xi'_W \chi^\pm, \end{aligned} \quad (2.36)$$

which depend on the five gauge parameters ξ_a ($a = A, Z, W$) and ξ'_a ($a = Z, W$), the special choice $\xi'_W = \xi_W$ and $\xi'_Z = \xi_Z$ cancels these mixing contributions, such that the

⁴On the other hand this means that the consideration of non-degenerate finite neutrino masses for example through the inclusion of right-handed neutrinos, would spoil this diagonalization. Instead, the same procedure as in the quark sector needed to be applied in the lepton sector.

terms quadratic in the gauge fields allow for well-defined gauge-boson propagators. This set of gauges is called *'t Hooft gauges* and the gauge-fixing Lagrangian can be written compactly as

$$\mathcal{L}_{\text{fix, GWS}} = -\frac{1}{2\xi_A}(C^A)^2 - \frac{1}{2\xi_Z}(C^Z)^2 - \frac{1}{\xi_W}C^+C^-. \quad (2.37)$$

From the chosen gauge-fixing functionals, the Faddeev–Popov Lagrangian can be evaluated according to Eq. (2.35) and reads in the physical basis of the gauge bosons

$$\mathcal{L}_{\text{FP, GWS}} = -\sum_X \int d^4y \, d^4z \, \bar{u}^a(x) \frac{\delta C^a(x)}{\delta X(y)} \frac{\delta X(y)}{\delta \theta^b(z)} u^b(z). \quad (2.38)$$

The sum over X extends all particles appearing in the gauge-fixing functionals, namely $A_\mu, Z_\mu, W_\mu^\pm, \chi^\pm$, and χ^0 , and with $\theta^a(x)$ we denote the space-time dependent group parameter of the underlying local gauge group. Expanding both Lagrangians we find that the three would-be Goldstone bosons and all ghost fields but one are rendered massive,

$$M_{\chi^\pm} = M_{u^\pm} = \sqrt{\xi_W} M_W, \quad M_{\chi^0} = M_{u^Z} = \sqrt{\xi_Z} M_Z, \quad M_{u^A} = 0, \quad (2.39)$$

and the corresponding propagators read

$$\mathcal{P}_{\chi^a}(k^2) = \mathcal{P}_{u^a}(k^2) = \frac{i}{k^2 - \xi_a M_a^2}. \quad (2.40)$$

Since the physical result of the calculation must not depend on the choice of the gauge, and therefore of ξ_a , the gauge dependence of the masses underlines once again the unphysical nature of the would-be Goldstones and the ghost field.

The unitary gauge corresponds to $\xi_a \rightarrow \infty$, such that the masses of all unphysical fields (but u^A) tend to infinity and therefore decouple from the rest of the theory (u^A becomes a free, non-interacting field). In this gauge, the Lagrangian of the quantized theory takes exactly the same form as the classical Lagrangian, which we discussed in the previous section, since all unphysical fields are absent. However, in the unitary gauge, the generic gauge-boson propagator takes the special form

$$\mathcal{P}_V(k^2) = \frac{-ig_{\mu\nu}}{k^2 - M_V^2} + \frac{i(1 - \xi_V)k_\mu k_\nu}{(k^2 - M_V^2)(k^2 - \xi_V M_V^2)} \xrightarrow{\xi_V \rightarrow \infty} \frac{-i \left(g_{\mu\nu} - \frac{k_\mu k_\nu}{M_V^2} \right)}{k^2 - M_V^2}, \quad (2.41)$$

approaching a constant value in the limit $k_\mu \rightarrow \infty$. In the explicit calculation of higher-order corrections, were we have to deal with internal loop-momenta going to infinity (see Chap. 3), this behaviour unnecessarily leads to additional complications.

The most convenient choice for higher-order calculations is the *'t Hooft–Feynman gauge*, $\xi_a = 1$, where the masses of all unphysical fields are equal to the corresponding physical fields. Although in this gauge the unphysical fields remain in the theory, the simple form of the gauge-boson propagator,

$$\mathcal{P}_V(k^2) \xrightarrow{\xi_V=1} \frac{-ig_{\mu\nu}}{k^2 - M_V^2}, \quad (2.42)$$

ensures the favourable high-energy behaviour

$$\mathcal{P}_{V,\chi,u^a} \underset{k^2 \gg 0}{\sim} \frac{1}{k^2} \xrightarrow{k^2 \rightarrow \infty} 0, \quad (2.43)$$

for the gauge bosons, the would-be Goldstone bosons, and the ghost fields.

2.2. The QCD Part of the SM

Quantum Chromodynamics is the unbroken local gauge theory that describes the interaction of the colour-charged quarks via the exchange of massless gauge bosons, the gluons. Since the underlying gauge group $SU(3)_C$ is a non-Abelian group, also the gluons carry colour-charge and interact among each other. In contrast to the EW interaction, the strong interaction does not distinguish between left- and right-handed fermions and parity is a conserved quantity in purely strong interactions. Another very distinct difference to the EW interaction is that colour-charged particles never appear isolated, but are always grouped together to build compound colour neutral objects, the hadrons. This feature is called *confinement* of quarks and gluons and we will come back to the consequences this property implies in the Secs. 3.2.3 and 4.1.

The classical Lagrangian of QCD reads

$$\mathcal{L}_{\text{QCD,cl.}} = \sum_{f=1}^{n_f} \sum_{i,j=1}^{N_c} \bar{q}_{f,i} (i\mathcal{D}_{ij} - m_{q_f} \delta_{ij}) q_{f,j} - \frac{1}{4} G_{\mu\nu}^a G^{a,\mu\nu}, \quad (2.44)$$

where $q_{f,i}$ is a massive Dirac spinor belonging to the fermionic quark field of flavour f and colour i . The first sum includes the three generations of up- and down-type quarks introduced in Sec. 2.1.2, such that we have $n_f = 6$ quark-flavours that only differ in their mass with respect to QCD, while the second sum runs over the $N_c = 3$ colours in which each quark exist. Note that in Eq. (2.31) we completely suppressed the colour degrees-of-freedom, and the sum over q_i of Eq. (2.31) corresponds to the flavour-sum of Eq. (2.44). \mathcal{D}_{ij} is the gamma-contracted covariant derivative in the fundamental representation,

$$\mathcal{D}_{ij} = \gamma_\mu D_{ij}^\mu = \gamma_\mu (\partial^\mu \delta_{ij} + ig_s T_{ij}^a G^{a,\mu}), \quad a = 1, \dots, 8, \quad (2.45)$$

with the kinetic term for the quark fields and the coupling to the eight gluon fields G^a , whose strength is given by the strong coupling constant g_s . The kinetic term of the gluon field is given in terms of the gluonic field-strength tensor,

$$G_{\mu\nu}^a = \partial_\mu G_\nu^a - \partial_\nu G_\mu^a - g_s f^{abc} G_\mu^b G_\nu^c, \quad (2.46)$$

with the structure constants of the $SU(3)_C$ -group f^{abc} that govern the self interaction among the gluon fields.

The quantization of the classical QCD Lagrangian proceeds in the same lines as in the EWSM, resulting in an effective Lagrangian including two additional terms. We

choose the gauge fixing functional for the massless gluons analogous to the one of the massless photon in Eq. (2.36). The gauge fixing Lagrangian therefore simply reads

$$\mathcal{L}_{\text{fix, QCD}} = -\frac{1}{2\xi} \left[\partial^\mu G_\mu^a(x) \right]^2, \quad (2.47)$$

and the Faddeev–Popov Lagrangian is given by

$$\mathcal{L}_{\text{FP, QCD}} = -\bar{u}^a(x) \partial^\mu D_\mu^{ab} u^b(x), \quad (2.48)$$

with the covariant derivative in the adjoint representation $D_\mu^{ab} = \partial_\mu \delta^{ab} - g_s f^{abc} G_\mu^c$ and the eight massless ghost fields of the QCD sector.

The Feynman rules that arise from the effective Lagrangian of QCD, are collected in App. C.

Chapter 3

Quantum Corrections

In the previous chapter, where we discussed the Lagrangian of the SM in great detail, we have already stated that this Lagrangian serves as foundation for every calculation of observables in high energy physics. In this chapter, we now first want to specify this statement and set the footing for precise theoretical predictions in particle physics. Subsequently we discuss in a general form the difficulties that arise when explicitly performing such a calculation. The next chapter will then be dedicated to the actual techniques used for the calculations presented in this thesis and the additional complication we are confronted with at hadron colliders.

As is comprehensively discussed in any textbook on relativistic quantum field theory, e.g. Refs. [13–16], via the S matrix,

$$\mathbf{S} = \text{T exp} \left[i \int d^4x \mathcal{L}_I \right], \quad (3.1)$$

the interaction Lagrangian \mathcal{L}_I is directly related to the probability $\mathcal{P} \propto |\langle f | \mathbf{S} | i \rangle|^2 = |\mathbf{S}_{fi}|^2$ for a given initial state $|i\rangle$ to evolve into a certain final state $|f\rangle$. In Eq. (3.1), T is the usual time-ordering operator acting on the field operators appearing after the series expansion of the exponential. The quantity that we finally calculate with the help of the Feynman rules is the *invariant matrix element* \mathcal{M}_{fi} , which is defined as the non-trivial part of the S matrix,

$$\mathbf{S}_{fi} = \langle f | \mathbf{S} | i \rangle = \langle f | i \rangle + i(2\pi)^4 \delta^4(\sum p_i - \sum p_f) \mathcal{M}_{fi}, \quad (3.2)$$

where we implicitly assume the initial- and final-state particles to be momentum eigenstates, such that we additionally extract the momentum conserving delta function from \mathcal{M}_{fi} . The relation of Eq. (3.2) is formally obtained by applying the Lehmann-Symanzik-Zimmermann (LSZ) reduction formula [23], which is discussed e.g. in Refs. [13, 14]. The full (partial) integration of the absolute square of the invariant matrix element¹ over the respective final-state phase space Φ finally defines the total (differential) cross section σ ($d\sigma/d\mathcal{O}$) of the process under consideration,

$$\sigma = \int d\mathcal{O} \frac{d\sigma}{d\mathcal{O}} = \frac{1}{F(p_a, p_b)} \int d\Phi |\mathcal{M}|^2 = \frac{1}{2s} \int d\Phi |\mathcal{M}|^2. \quad (3.3)$$

¹To keep the notation as clear as possible, additional labels corresponding to the summation and averaging over internal degrees of freedom are suppressed. See App. B for details.

\mathcal{O} denotes any experimentally measurable observable, like e.g. the transverse momentum of a charged lepton $p_{T,l}$, such that $d\sigma/d\mathcal{O}$ yields the differential cross section for the respective observable. In addition, the definition of Eq. (3.3) includes the flux-factor $F(p_a, p_b)$ which generally depends on the initial-state momenta p_a and p_b and the corresponding masses (c.f. Eq. (B.3) of App. B). For our purposes with massless initial-state particles the flux-factor always reduces to a simple function of the center-of-mass (c.m.) energy s and reads $F = 2(p_a + p_b)^2 = 2s$.

Still, we have not yet discussed one very important requirement for the applicability of this widely used method to calculate \mathbf{S}_{fi} , that we, however, already implicitly implied in writing Eq. (3.1), namely *perturbativity*. A theory is called perturbative if the observables may be approximated by a power series, where the strength of the interaction serves as expansion parameter. Obviously, only if the coupling parameter of a quantum field theory is much smaller than one, such a series expansion, and thus ultimately the utilization of the Feynman rules, is meaningful. This requirement is generally fulfilled for the EW sector, but, as we will discuss in Sec. 3.2.3, the application of perturbative methods in QCD is only possible in the high energy regime. The reason is the distinct running of the strong coupling $\alpha_s(Q^2) = \frac{g_s^2}{4\pi}$, which becomes weaker at higher scales Q , while towards lower scales we eventually reach the non-perturbative regime of QCD. We will discuss this very important feature of QCD in detail in the next chapter.

However, as long as perturbative methods are applicable, based on Eq. (3.1), the S-matrix can in principle be calculated to any order in the coupling constant, approximating the observable to arbitrarily high precision. In practise, on the other hand, the explicit calculations of higher-order corrections are very cumbersome already for rather simple processes, such that the practical calculation relies on a fast convergence of the series expansion.

For a given process, the lowest possible order in the coupling constant defines the leading order (LO) cross section, σ^{LO} , while the successive inclusion of additional interactions is regarded as additive correction, $\Delta\sigma$, defining the next-to-leading order (NLO), next-to-next-to-leading order (NNLO), etc. In the SM, with the strong force and the unified EW force, we have two different interactions, such that one further differentiates between QCD and EW LO processes and the corresponding corrections to those processes. In the energy regime we will be dealing with in the following, the coupling strengths are very roughly given by

$$\text{QCD} : \alpha_s \sim \mathcal{O}\left(\frac{1}{10}\right), \quad \text{EW} : \alpha \sim \mathcal{O}\left(\frac{1}{100}\right), \quad (3.4)$$

such that the LO process with the most strong and fewest EW couplings usually leads to the largest contribution. For example for the process $q\bar{q} \rightarrow q\bar{q}$, by applying the Feynman rules, we obtain diagrams with internal gluons as well as diagrams with internal photon and Z bosons, leading to contributions to the squared matrix elements, $|\mathcal{M}|^2 = \mathcal{M}\mathcal{M}^*$, of the orders $\mathcal{O}(\alpha_s^2)$, $\mathcal{O}(\alpha_s\alpha)$, and $\mathcal{O}(\alpha^2)$. In Fig. 3.1 we show the typical illustration of the three LO contributions representatively for one diagram each, where the dashed lines separate the two pieces contributing to $|\mathcal{M}|^2$.

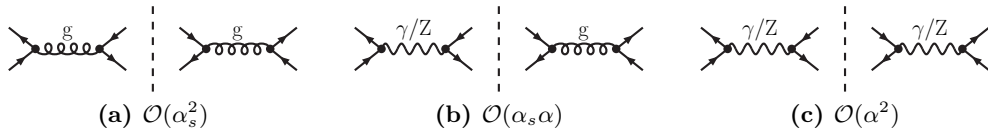


Figure 3.1.: Representative LO contributions to $|\mathcal{M}|^2$ for the process $q\bar{q} \rightarrow q\bar{q}$ at the lowest possible order in the strong- and EW-coupling constant. (a) shows the $\mathcal{O}(\alpha_s^2)$ contribution which generally leads to the largest contributions, while (b) and (c) show a mixed QCD-EW contribution and the purely EW contribution, respectively.

In general, the QCD corrections to a specific process turn out to be much larger and, thus, more important to be known than the EW corrections. However, already a naive comparison of the typical sizes of the two coupling constants given in Eq. (3.4), adumbrates that NLO_{EW} corrections are of similar size as the NNLO_{QCD} corrections, and therefore definitely have to be taken into account in order to reach the highest possible precision in theoretical predictions of cross sections. Additionally, for reasons that will be discussed below, EW corrections often show a much stronger kinematic dependence than QCD corrections. This may lead to significant distortions in the differential distributions of observables due to EW corrections, which makes their consideration often even more important than the inclusion of NNLO QCD corrections. In the following, however, we will only focus on the issues one is confronted with in the computation of NLO corrections, and will not address any additional complication arising in the computation of corrections exceeding this perturbative order.

On the basis of Eq. (3.3) we can generally define the NLO cross section as

$$\sigma^{\text{NLO}} = \sigma^{\text{LO}} + \Delta\sigma^{\text{NLO}}, \quad \Delta\sigma^{\text{NLO}} = \sigma^{\text{virt}} + \sigma^{\text{real}}, \quad (3.5)$$

where the NLO correction contribution, $\Delta\sigma^{\text{NLO}}$, is conveniently divided into two parts, namely a virtual and real contribution. The virtual contribution includes all (one-) loop diagrams, in which internally one additional (virtual) particle is produced and subsequently re-absorbed. Showing exactly the same final state as the LO process, experimentally there is no way of distinguishing higher-order virtual corrections from the LO, which is the reason why we need to consider their effects in the first place. The second contribution defined in Eq. (3.5), however, the real corrections, contains one additional external (real) particle, which might be observed in the final state. Especially the additional radiation of massive particles would (almost) certainly be separately detected, thus, leading to a distinct signature in the detector. If, on the other hand, the additional particle is massless and becomes very soft or is emitted collinearly to another particle, the separate detection may become unfeasible, and consequently also parts of the real corrections can be mistaken for the associated LO process.

Based on these considerations, we notice that the most convenient definition of the real contribution only includes the additional radiation of massless particles, while an additional massive particle in the final state defines a distinct process. In Sec. 3.3 we

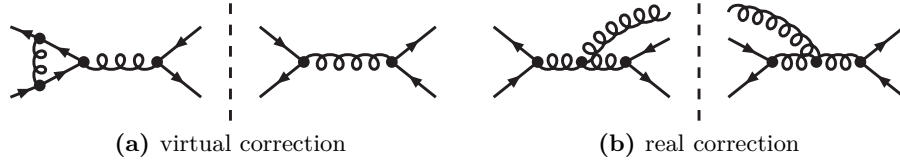


Figure 3.2.: Representative NLO_{QCD} contributions of $\mathcal{O}(\alpha_s^3)$ to $|\mathcal{M}|^2$ for the LO process $q\bar{q} \rightarrow q\bar{q}$.

will come back to this subtle point and discuss further implications of this definition.

When inspecting the vertices in the particular Feynman diagrams, we note that for every closed loop two additional couplings² are needed, while the real emission only yields one additional interaction. To stay in the same perturbative order, the virtual cross section is therefore defined as the interference of the one loop matrix element with the LO matrix element, yielding two times the real part of their product integrated over the LO phase space $\Phi = \Phi_{\text{LO}}$, while the real cross section is obtained by squaring the real emission diagrams,

$$\sigma^{\text{virt}} = \frac{1}{2s} \int d\Phi_{\text{LO}} 2\text{Re}[\mathcal{M}_{1\text{loop}}\mathcal{M}_{\text{LO}}^*], \quad \sigma^{\text{real}} = \frac{1}{2s} \int_{+1} d\Phi_{+1} |\mathcal{M}_{\text{real}}|^2. \quad (3.6)$$

Here, due to the additionally appearing particle in the final state, the phase-space integration for $|\mathcal{M}_{\text{real}}|^2$ needs to be extended accordingly. Figure 3.2 shows representative examples of the virtual and real NLO_{QCD} corrections to the process $q\bar{q} \rightarrow q\bar{q}$ at $\mathcal{O}(\alpha_s^3)$.

In tree-level diagrams, i.e. diagrams without loops, all internal momenta are fixed by the momenta of the external particles. The momentum flow in loops, however, can not be observed and has to be integrated over the entire Minkowski space. Typically, the LO process is a tree-level process³ and loop diagrams first enter via the virtual contributions at the NLO level of the calculation. This integration over the unconstrained loop momenta is a delicate task, since towards both integration boundaries, i.e. for very high, so-called *ultraviolet* (UV), loop momenta, as well as for very low loop momenta the integrand may diverge. Whereas UV divergences occur in any higher-order calculation, only if massless particles (e.g. photons with $m_\gamma = 0$) are involved, also in the low-momentum region singularities occur, which otherwise are regularized by the finite mass. For an arbitrarily soft photon momentum $q = |q_\mu|$, the fermion propagator \mathcal{P}_f inside an exemplary loop diagram takes the form

$$\mathcal{P}_f \sim \frac{1}{(k+q)^2 - m_f^2} \xrightarrow{k^2=m_f^2} \frac{1}{2k \cdot q + q^2}, \quad (3.7)$$

²Note that the quartic gauge boson couplings are quadratic in the respective coupling constant (see App. C), such that the number of vertices must not necessarily change.

³One of the rare, but very important counterexamples is Higgs production in gluon-gluon-fusion [24], where already at LO a heavy quark loop appears.

where we immediately see the divergent behaviour for $q = |q_\mu| \rightarrow 0$. However, for massless fermions ($m_f = 0$) Eq. (3.7) also diverges in the *collinear* limit,

$$q_\mu \parallel k_\mu \leftrightarrow k \cdot q \sim k^2 = m_f^2 \rightarrow 0, \quad (3.8)$$

such that we have to treat a third kind of divergence. Due to their similar behaviour, soft and collinear divergences will be treated in a combined manner and are commonly referred to as *infrared* (IR) singularities.


Note that in a (hypothetical) theory with *only* massive particles, no IR singularities would appear, since the physical mass acts as regulator in the respective soft and/or collinear limits, thus, leading to an (IR) finite result. As we have already seen in the previous chapter, the SM includes massless and massive particles, such that in concrete calculations we are confronted with both conditions, which we will further discuss in Sec. 3.3.

We want to emphasize, that both kinds of divergences, UV and IR divergences, are, however, completely unphysical as they only enter through our description and actual classification, while nature itself is finite. Nevertheless, for the calculation of predictions exceeding the LO, we need techniques to handle the occurring singularities in such a way, that we finally obtain a finite, well-defined result. The UV divergences can be isolated and finally reabsorbed by two consecutive procedures, namely *regularization* and *renormalization*, which we separately discuss in Secs. 3.1 and 3.2, respectively.

Possible IR singularities of the virtual contributions, however, are still present after the renormalization procedure. As we will discuss in Sec. 3.3, IR singularities also appear in the phase-space integration of the real matrix-element squared, if the additionally emitted massless particle becomes soft and/or collinear to its emitter. According to the well known Bloch–Nordsieck theorem [25], the soft singularities appearing in the virtual and real emission contribution exactly cancel in their sum at any order of the perturbative expansion. However, the same is not true in this general form for collinear singularities, such that further constraints and definitions have to be discussed in Sec. 3.3.

3.1. Regularization of UV Divergences

As we have already pointed out, one essential part of the calculation of higher-order corrections comprises the calculation of the loop diagrams. The integration over the internal loop momentum q_μ has to be performed over the entire Minkowski space, which might lead to a divergence, when the absolute value of the internal momentum $q = |q_\mu|$ becomes large, as for example in the fermionic one-loop correction to the photon propagator,



$$\sim \int d^4q \frac{1}{(q^2 + m^2)((q+k)^2 - m^2)}$$

$$\stackrel{q \gg k, m}{\sim} \int d^4q \frac{1}{q^4} \sim \int dq \frac{1}{q} \xrightarrow{q \rightarrow \infty} \infty. \quad (3.9)$$

In order to handle such a behaviour, we first need a regularization prescription, that allows us to separate the unphysical divergence from the finite, and thus physically relevant, contribution.

In the literature several regularization schemes have been discussed, as for example the hard cut-off, Pauli-Villars [26], lattice-regularization [27], or four dimensional regularization (FDR) [28] which, however, all have the major drawback of being either very cumbersome in practical applications or even do not respect gauge or Lorentz invariance. The most elegant regularization prescription known today respecting both of these fundamental principles of the SM is *dimensional regularization* [29], where the space-time is extended from four to $D = 4 - 2\epsilon$ dimensions. In principle, this regularization scheme may also be applied to treat possible IR divergences occurring in loop-integrations, but in the following we will limit the discussion to the treatment of UV divergences, while IR singularities will be discussed separately in Sec. 3.3.

After the integration over the D -dimensional solid angle Ω_D , the factor q^{D-1} may cure any pole in the remaining integration of the arbitrary integrand f , if D is chosen accordingly,

$$\int \frac{d^4q}{(2\pi)^4} f(q) \rightarrow \mu^{4-D} \int \frac{d^Dq}{(2\pi)^D} f(q) \sim \frac{2\pi^{D/2}}{\Gamma(D/2)} \mu^{2\epsilon} \int_0^\infty \frac{dq}{(2\pi)^D} q^{D-1} f(q). \quad (3.10)$$

Here, the arbitrary reference scale μ of mass dimension one is included in order to keep the mass dimension of the Lagrangian fixed. Γ denotes the Euler Gamma-function,

$$\Gamma(x) = \int_0^\infty dy y^{x-1} e^{-y}, \quad (3.11)$$

which can be regarded as the analytic continuation of the factorial as it fulfills the recursion relation

$$\Gamma(x+1) = x\Gamma(x), \quad \Gamma(1) = 1, \quad (3.12)$$

for arbitrary x . For negative integers the Γ -function exhibits simple poles, which, via Eq. (3.12), can be related to the pole at zero,

$$\Gamma(\epsilon) \underset{\epsilon \rightarrow 0}{\sim} \frac{1}{\epsilon} - \gamma_E + \frac{1}{2}(\gamma_E^2 + \frac{\pi^2}{6})\epsilon + \mathcal{O}(\epsilon^2) + \dots, \quad (3.13)$$

where $\gamma_E \approx 0.5772\dots$ is the irrational Euler-Mascheroni constant. For an arbitrary dimension $D = 4 - 2\epsilon$, the integration in Eq. (3.10) can always be performed yielding results that may still depend on ϵ . All terms appearing in the final result have to be carefully expanded in ϵ and possible divergences will ultimately show up as $\frac{1}{\epsilon}$ -poles in the limit $D \rightarrow 4$ ($\epsilon \rightarrow 0$).

Having separated the UV divergences for every one-loop diagram from the remaining finite part, we now turn to the renormalization of the parameters of the theory to absorb and remove those divergences from the calculation.

3.2. Renormalization

The basic idea of renormalization is to redefine the input parameters (masses, couplings, etc.) of the theory in such a way, that in well-defined relations between physical quantities no UV-divergent terms remain. If it is possible to obtain UV-finite results up to arbitrary loop-order with a finite amount of renormalization-conditions, we call the theory renormalizable. In particular, this means that only a finite number of loop integrals may lead to singularities, a fact to which we come back in Sec. 4.3.

In 1971 the renormalizability of non-Abelian gauge theories, also including spontaneous symmetry breaking, has been proven in a general form by 't Hooft [30], such that both gauge theories within the SM (the EWSM and QCD) are renormalizable theories. An important consequence of this proof is that no couplings with a negative mass dimension may appear in the SM Lagrangian.

Practically, in the counterterm approach, we obtain finite, renormalized, parameters from the originally divergent, bare, parameters by shifting the divergence into so-called *counterterms*. The renormalized parameters λ_r are defined from the bare parameters λ_0 by a multiplication with a (divergent) renormalization constant Z_λ , which, however, can be expanded in the respective coupling constant α_X ,

$$\lambda_0 = Z_\lambda \lambda_r = (1 + \delta Z_\lambda + \mathcal{O}(\alpha_X^2)) \lambda_r, \quad \delta Z_\lambda = \mathcal{O}(\alpha_X). \quad (3.14)$$

Although a renormalization of all (independent) masses and couplings of the theory is sufficient to obtain finite matrix elements [31], it is convenient to renormalize also the fields (Λ_i) appearing in the Lagrangian,

$$\Lambda_{i,0} = \sqrt{Z_{\Lambda_i}} \Lambda_{i,r}. \quad (3.15)$$

Since many terms of the Lagrangian are quadratic in the fields, it is common to include the squareroot in the definition. By inserting the properly expanded definitions, we can split the original, bare Lagrangian, \mathcal{L}_0 , depending on the bare fields and parameters, into a renormalized Lagrangian \mathcal{L}_r and the so-called counterterm Lagrangian $\delta\mathcal{L}$,

$$\mathcal{L}_0(\Lambda_{0,i}, \lambda_0) = \mathcal{L}_r(\Lambda_{r,i}, \lambda_r) + \delta\mathcal{L}(\Lambda_{r,i}, \lambda_r), \quad (3.16)$$

where \mathcal{L}_r shows the same dependence on the renormalized fields and parameters, as the bare Lagrangian on the bare quantities and $\delta\mathcal{L}$ contains all terms proportional to the renormalization constants δZ_i .

Note that the whole procedure does not change the original theory at all, but we only rearrange the elements appearing in the perturbative expansion, in order to separate the finite, renormalized, quantities. From $\delta\mathcal{L}$, new Feynman rules have to be derived, which for the EW part of the SM can be found, e.g., in App. A of Ref. [31]. Although the Feynman rules are already uniquely defined by this procedure, we still have to fix the renormalization constants by specifying a certain *renormalization scheme*, that finally fixes the definition of the physical parameters. For a reason that will become clear soon

enough, the fixing of the renormalization constants appearing in the EW part and in the QCD part is usually not performed in the same scheme. In the following we present the two schemes that are commonly used for explicit higher-order corrections in the respective coupling constants.

3.2.1. On-Shell Renormalization

The renormalization of the EW theory is most elegantly performed in the on-shell (OS) scheme [32], where the renormalized parameters equal the experimentally measured parameters in every order of the perturbative expansion. This means that we do not choose the original gauge couplings (g_1 and g_2 , induced in Eqs. (2.10) and (2.7), respectively) and the independent parameters of the Higgs Lagrangian (Eq. (2.14)), but the set

$$M_W, M_Z, M_H, m_{f_i}, \mathbf{V}_{ij}, e, \quad (3.17)$$

which consists of the physical parameters we have defined in Sec. 2.1.4. As we have seen there, these experimentally measurable parameters are directly related to the parameters of the underlying gauge theories extended by the requirements of EWSB, such that a renormalization of both sets is, in principle, equivalent. However, a renormalization of experimentally measurable parameters seems to be the most natural way. Additionally, in this physical basis, no renormalization of the unphysical ghost and would-be Goldstone fields needs to be performed to obtain finite results at the one-loop level.

Following the notation of Eqs. (3.14) and (3.15) the bare parameters and the bare fields of the SM-Lagrangian of Eq. (2.31) are expressed as product of the renormalized quantities and the renormalization constants [31],

$$\begin{aligned} e_0 &= Z_e e_r = (1 + \delta Z_e) e_r, \\ M_{W,0}^2 &= M_{W,r}^2 + \delta M_W^2, \\ M_{Z,0}^2 &= M_{Z,r}^2 + \delta M_Z^2, \\ M_{H,0}^2 &= M_{H,r}^2 + \delta M_H^2, \\ m_{f_i,0} &= m_{f_i,r} + \delta m_{f_i}, \\ \mathbf{V}_{ij,0} &= (U_1 \mathbf{V}_r U_2)_{ij} = \mathbf{V}_{ij,r} + \delta \mathbf{V}_{ij}, \\ W_0^\pm &= \sqrt{Z_W} W_r^\pm = (1 + \frac{1}{2} \delta Z_W) W_r^\pm, \\ \begin{pmatrix} A_0 \\ Z_0 \end{pmatrix} &= \begin{pmatrix} \sqrt{Z_{AA}} & \sqrt{Z_{AZ}} \\ \sqrt{Z_{ZA}} & \sqrt{Z_{ZZ}} \end{pmatrix} \begin{pmatrix} A_r \\ Z_r \end{pmatrix}, \\ &= \begin{pmatrix} 1 + \frac{1}{2} Z_{AA} & \frac{1}{2} Z_{AZ} \\ \frac{1}{2} Z_{ZA} & 1 + \frac{1}{2} Z_{ZZ} \end{pmatrix} \begin{pmatrix} A_r \\ Z_r \end{pmatrix}, \\ H_0 &= \sqrt{Z_H} H_r = (1 + \frac{1}{2} \delta Z_H) H_r, \\ f_{i,0}^L &= \sqrt{Z_{ij}^{f;L}} f_{j,r}^L = (\delta_{ij} + \frac{1}{2} \delta Z_{ij}^{f;L}) f_{j,r}^L, \end{aligned}$$

$$f_{i,0}^R = \sqrt{Z_{ij}^{f,R}} f_{j,r}^R = (\delta_{ij} + \frac{1}{2} \delta Z_{ij}^{f,R}) f_{j,r}^R. \quad (3.18)$$

In the OS scheme, the renormalization conditions for the masses M_W, M_Z, M_H and m_{f_i} identify the renormalized masses with the (measured) physical masses. They are defined as the real parts of the poles of the respective propagators, which are located at momenta $k^2 = M^2$, where M denotes the respective physical mass. It is worth noting that the radiative EW corrections generally yield non-diagonal corrections to the mass matrices, such that the bare fields are no longer mass eigenstates. With the above defined matrix valued field renormalization constants, however, it is possible to obtain the renormalized fields as mass eigenstates to all orders in perturbation theory.

At one-loop, the renormalized CKM matrix is directly connected to the renormalization constants of the left handed quark fields,

$$\mathbf{V}_{ij,r} = \mathbf{V}_{ij,0} - \frac{1}{2} \mathbf{V}_{0,il} \delta Z_{lj}^{d,AH} - \frac{1}{2} \delta Z_{ik}^{u,AH\dagger} \mathbf{V}_{0,kj}, \quad (3.19)$$

where we defined the anti-Hermitian part of the left-handed fermion field renormalization constant,

$$\delta Z_{ij}^{f,AH} = \frac{1}{2} (\delta Z_{ij}^{f,L} - \delta Z_{ij}^{f,L\dagger}). \quad (3.20)$$

For (mass-)degenerate up- and down-type quarks the anti-Hermitian part vanishes, such that in this case we obtain $\mathbf{V}_{ij,r} = \mathbf{V}_{ij,0}$. Actual calculations are often performed with the (light) quark masses set to zero, such that in these cases no renormalization of the CKM matrix elements needs to be performed [33].

The electric charge, e (c.f. Eq. (2.32)), is finally defined as the coupling of two on-shell external electrons (e) to a photon (γ) in the so-called *Thomson limit*. It is defined at vanishing photon momentum and implies that all corrections to the $ee\gamma$ -vertex vanish. When performing the renormalization, it turns out that its formulation is independent of the actual kind of fermion, which reflects the universality of the electric charge within the SM. In practical calculations, the electric charge will be substituted by the fine structure constant,

$$\alpha = \alpha(Q^2)|_{Q^2=0} = \frac{e^2}{4\pi}, \quad (3.21)$$

where the dependence on the scale Q reflects the dependence of the renormalization condition on the photon momentum, which is set to zero in the Thomson limit. The couplings of the massive EW vector bosons are typically defined at the so-called *EW-scale* $Q^2 = M_Z^2$, which, however, does not necessarily require a new renormalization. The running of the EW coupling can be expressed by

$$\alpha(Q^2) = \frac{\alpha}{1 - (\Delta\alpha(Q^2))_{\text{ferm}}}, \quad (3.22)$$

where $(\Delta\alpha(Q^2))_{\text{ferm}}$ are the universal fermionic contributions of the corrections appearing in the renormalization of α at non-zero momentum transfer.

The actual formulae for all renormalization constants at one-loop order are deduced and explicitly given in Chap. 4 of Ref. [31], such that we refrain from listing them here as well. These results are used to formulate the Feynman rules for the counterterms that allow for the cancellation of the UV divergences of EW one-loop diagrams already at the amplitude level.

3.2.2. The Complex-Mass Scheme

A particular consequence of the quantum-mechanical nature of the SM is that all massive particles tend to decay into lighter particles, whenever a decay is not forbidden due to the conservation of individual quantum numbers. Especially for the massive vector bosons W^\pm and Z , the Higgs boson H , and the heaviest quark, the top quark t , the *lifetimes* (τ) are very small, such that it is impossible to directly detect these particles. Only via the careful study of the possible decay products, conclusions about their properties, like e.g. mass, spin, charge, or even their actual lifetime, can be drawn.

On the theoretical side, the finite lifetime of a particle of mass M results in an additional imaginary part in the propagator,

$$\mathcal{P}(p^2) \sim \frac{1}{p^2 - M^2 + iM\Gamma}, \quad (3.23)$$

which means that the propagator follows a Breit-Wigner shape around the mass M of the decaying particle. Here, $\Gamma = 1/\tau$ is the inverse lifetime, called total decay width of the unstable particle. In a perturbative calculation, however, such an additional term naturally arises due to the inclusion of higher-order diagrams contributing to the self-energy of the massive particle, such that special care has to be taken when including a finite width already at the LO. Additionally, in gauge theories, such a mixing of perturbative orders may lead to gauge dependent results when truncating the expansion at a fixed order, which under certain conditions may lead to completely wrong results [34].

With the *complex-mass scheme* [35–37] a gauge independent formalism exists to include finite decay widths in theoretical predictions. In this scheme, the decay width does not only affect the propagator as defined in Eq.(3.23), but the masses of the unstable heavy particles are consistently replaced *everywhere* in the amplitude by the corresponding complex values,

$$M^2 \rightarrow \mu^2 = M^2 - iM\Gamma. \quad (3.24)$$

According to Eq.(2.27), this, in particular, leads to a complex weak mixing angle,

$$\cos^2 \theta_w = c_w^2 = 1 - s_w^2 = \frac{\mu_W^2}{\mu_Z^2}. \quad (3.25)$$

For calculations involving unstable particles only at tree-level, this strict complexification is already enough for a gauge independent inclusion of finite decay widths [35].

Also the calculation of NLO_{QCD}-corrections to processes involving unstable particles does not require any further modification. When it comes to virtual EW corrections involving massive vector bosons, however, the on-shell renormalization outlined in the previous section needs to be generalized resulting in complex renormalized masses for the unstable particles. Therefore, in the complex-mass scheme, the real-valued squared bare masses M_0^2 are decomposed into a complex-valued renormalized squared masses μ^2 and a complex counterterm $\delta\mu^2$. As before, the renormalized mass is obtained by subtracting the counterterm from the bare mass,

$$\mu^2 = M_0^2 - \delta\mu^2 = M^2 - i\Gamma M, \quad (3.26)$$

which now defines the real valued renormalized mass M and width Γ , to be extracted from the experiment. Additionally, the field renormalization of all SM fields has to be generalized to complex valued field renormalization constants, as is discussed in detail in Refs. [36] and [37], where also all renormalization conditions are explicitly given.

The renormalization in the complex-mass scheme finally leads to Feynman rules involving a complex coupling and, in particular, complex masses for all unstable particles, which are therefore excluded from being external particles.

3.2.3. $\overline{\text{MS}}$ Renormalization

As we have already stated in Sec.2.2, in contrast to the EW theory, within QCD the quarks and gluons can only be observed in colour-neutral compound states. This confinement makes the application of an on-shell renormalization procedure to QCD ambiguous, since we can neither measure the mass of an isolated quark, nor is there a meaningful way to define the Thomson limit in QCD.

The renormalization of QCD is therefore usually carried out in the so-called *modified Minimal Subtraction* ($\overline{\text{MS}}$) scheme [38]. In the *Minimal Subtraction* (MS) scheme [39] only the UV divergent terms, which appear as $\frac{1}{\epsilon}$ -poles in dimensional regularization, have been distributed to the renormalization constants, thus rendering the renormalized quantities finite. However, there obviously remains some arbitrariness in the inclusion of finite terms to the subtraction prescription. When it was realized that the $\frac{1}{\epsilon}$ -poles usually result from the term

$$(4\pi)^\epsilon \frac{\Gamma(1+\epsilon)}{\epsilon} = (4\pi)^\epsilon \Gamma(\epsilon) \underset{\epsilon \rightarrow 0}{\sim} \Delta_{\text{UV}} := \frac{1}{\epsilon} - \gamma_E + \ln 4\pi + \mathcal{O}(\epsilon), \quad (3.27)$$

the minimal subtraction prescription was extended to include also the finite contribution ($-\gamma_E + \ln 4\pi$) in the definition of the UV-divergent part Δ_{UV} , the subtraction of which, thus, defines the $\overline{\text{MS}}$ -scheme.

Using again the notation of Eqs. (3.14) and (3.15), the renormalized quantities of the QCD Lagrangian (c.f. Sec.2.2) and the corresponding renormalization constants are

defined as

$$\begin{aligned}
g_{s,0} &= Z_g g_{s,r}, \\
m_{q,0} &= Z_{m_q} m_{q,r}, \\
\xi_0 &= Z_\xi \xi_r, \\
G_0^a &= \sqrt{Z_G} G_r^a, \\
q_{i,0} &= \sqrt{Z_{q_i}} q_{i,r}, \\
u_0^a &= Z_u u_r^a.
\end{aligned} \tag{3.28}$$

For the renormalization at the one-loop order, we need the expansion of the renormalization constants up to the term linear in the strong-coupling constant,

$$Z_i = 1 + \delta Z_i + \mathcal{O}(\alpha_s^2), \quad \delta Z_i = \mathcal{O}(\alpha_s), \tag{3.29}$$

where in the $\overline{\text{MS}}$ -scheme δZ_i now only contains terms proportional to Δ_{UV} , defined in Eq. (3.27). By shifting the divergences into the counterterm Lagrangian, in the same manner as in the on-shell renormalization we obtain finite renormalized parameters. However, due to the lack of physical constraints fixing the renormalization, the dependence on the reference mass scale μ , that needed to be introduced in dimensional regularization, will not only remain in the renormalized coupling constant, but in general also in the renormalized quark masses,

$$\alpha_{s,r} \rightarrow \alpha_s(\mu), \quad m_{q,r} \rightarrow m_q(\mu), \tag{3.30}$$

defining the running coupling constant and the running quark masses. This dependence generally makes the proper treatment of quark masses and their renormalization a very delicate task, that, however, goes beyond the scope of the work presented in this thesis. For predictions at present high energy colliders, it is well justified to treat all quarks, but the top quark and, in some cases also the bottom quark, as massless particles. Then, the massless particles do not require a mass renormalization, while the mass renormalization of the massive quarks can consistently be performed in the on-shell scheme. Indeed, an on-shell renormalization for the top-quark mass is meaningful because of its short lifetime. In contrast to the light quarks, before the top-quark starts hadronizing, it rather decays weakly, such that a reconstruction of the top-quark mass can be performed. Therefore, for our purposes, after renormalization we are only left with a running coupling constant $\alpha_s(\mu)$, that depends on an arbitrary scale μ , while all masses are either zero or fixed by an OS renormalization condition. In the following we call this scale the *renormalization scale*, and identify $\mu = \mu_{\text{R}}$.

We already observed a certain scale dependence of the weak coupling constant α (Eq. (3.22)), but it turns out that the dependence of α_s on the arbitrary renormalization scale is much stronger. However, when measuring physical quantities in experiment, in the end all explicit and implicit dependences on the arbitrary scale μ_{R} have to cancel,

since observables are genuinely independent of arbitrarily introduced scales. For an observable \mathcal{R} this condition can mathematically be formulated as

$$\mu_{\text{R}}^2 \frac{\text{d}}{\text{d}\mu_{\text{R}}^2} \mathcal{R} = 0, \quad (3.31)$$

which is one of the so-called *renormalization group equations* (RGE), that are treated in great detail in Ref. [40]. If the series expansion is, however, truncated at a fixed order, the artificial dependence on the renormalization scale does not entirely cancel.

For the strong coupling α_s one defines the β -function,

$$\beta(\alpha_s) = \mu_{\text{R}}^2 \frac{\partial \alpha_s}{\partial \mu_{\text{R}}^2} = \frac{\partial \alpha_s}{\partial \ln \mu_{\text{R}}^2}, \quad (3.32)$$

that describes the running of α_s with the variation of μ_{R} . The perturbative expansion of β up to the one-loop order reads

$$\beta(\alpha_s) = -b_0 \alpha_s^2 + \mathcal{O}(\alpha_s^3), \quad b_0 = \frac{11C_{\text{A}} - 4n_f T_{\text{F}}}{12\pi}, \quad (3.33)$$

where $C_{\text{A}} = 3$ and $T_{\text{F}} = \frac{1}{2}$ denote the Casimir operator of the adjoint, and the Dynkin index of the fundamental representation of $\text{SU}(3)_{\text{C}}$ (cf. Eq. (A.16) ff.), respectively, while n_f is the number of active quark-flavours. Solving the differential equation of Eq. (3.32) at the one-loop order yields

$$\alpha_s(\mu_{\text{R}}^2) = \frac{1}{b_0 \ln(\frac{\mu_{\text{R}}^2}{\Lambda^2})}, \quad (3.34)$$

where we absorbed the integration constants in the constant mass scale $\Lambda = \Lambda_{\text{QCD}}$. In the SM, we can have maximally $n_f = 6$ active quark flavours, such that the parameter b_0 in Eq. (3.33) is always positive. Therefore Eq. (3.34) predicts

$$\alpha_s(\mu_{\text{R}}^2) \xrightarrow{\mu_{\text{R}} \rightarrow \infty} 0, \quad (3.35)$$

and we obtain a meaningful perturbative theory up to arbitrarily high scales μ_{R} .

This behaviour is called *asymptotic freedom* of the strong force, and allows for the perturbative description of QCD at sufficiently high energy scales, corresponding to very small distances. Note, that an analogous relation as Eq. (3.33) also holds within QED. There, however, we have $C_{\text{A}} = 0$ for the Abelian $\text{U}(1)$ -gauge group and consequently QED is not asymptotically free. When turning to smaller scales, i.e. larger distances, Eq. (3.34) also implies that for $\mu_{\text{R}} \simeq \Lambda$ the strong coupling becomes of the order of one and at some point perturbation theory will eventually break down. Empirically one finds $\Lambda_{\text{QCD}} \sim 100 - 400 \text{ MeV}$, which restricts the applicability of perturbative methods to energy regions $\gtrsim 1 \text{ GeV}$, as we will discuss in Sec. 4.1.

Finally, with Eq. (3.34) we can relate the strengths of α_s at two arbitrary scales μ_{R} and Q independently of the exact value of Λ_{QCD} , which defines the one-loop running of α_s ,

$$\alpha_s(Q^2) = \frac{\alpha_s(\mu_{\text{R}}^2)}{1 + \alpha_s(\mu_{\text{R}}^2) b_0 \ln(\frac{Q^2}{\mu_{\text{R}}^2})}. \quad (3.36)$$

3.3. Infrared Singularities

After we have removed all UV divergences of the one-loop amplitudes by applying a suitable renormalization procedure, we still have to take care of possible IR divergences. These divergences appear in the virtual as well as in the real contribution of any calculation that includes massless particles, whenever the momentum of the particle becomes soft or collinear to another particle.

Within the SM, the only truly massless particles are the photon, the gluons and the neutrinos. However, compared to the energies reachable with today's particle accelerators ($\mathcal{O}(\text{TeV})$), at least the masses of the electron ($m_e \sim 0.5 \text{ MeV}$), the muon ($m_\mu \sim 106 \text{ MeV}$) and the four lightest quarks ($m_{u,d,c,s} \lesssim \mathcal{O}(1 \text{ GeV})$) can safely be neglected in calculations of scattering matrix elements. With $m_\tau \sim 2 \text{ GeV}$ and $m_b \sim 4 \text{ GeV}$, the tau-lepton and the bottom-quark masses are already in an energy regime where either the massive or the massless treatment may be advantageous, depending on the available energy of the collider and the aim of the calculation.

In any case, a massless treatment of fermions tremendously facilitates the evaluation of matrix elements and, due to the omission of various different mass-scales, also stabilizes—and therefore speeds-up—a numerical phase-space integration. The drawback, on the other hand, are the additional IR divergences, that would not appear if we kept the masses of the particles finite.

The method that is commonly used in the calculation of high-energetic particle collisions at LHC energies is to treat all light fermions mentioned above as exactly massless for the evaluation of the matrix element and subsequently introduce a suitable regularization prescription to cure possible IR divergences appearing in the loop-momentum and phase-space integrations. If not stated otherwise, from now on we therefore will treat all SM particles, but the massive EW-gauge bosons (W^\pm, Z), the Higgs boson (H) and the top quark (t), as massless particles, which consequently all may appear in the real correction contribution.

As we have already mentioned above, the Bloch–Nordsieck (BN) theorem [25] guarantees the exact cancellation of the soft singularities stemming from the real contribution against their counterparts in the virtual correction. For the collinear singularities, on the other hand, according to the Kinoshita–Lee–Nauenberg (KLN) theorem [41], this cancellation only occurs in sufficiently inclusive regions.

For final-state radiation, the demand of inclusiveness is usually ensured by the application of a suitable recombination procedure of (nearly) collinear final-state particles. While such a procedure is easily realizable in calculations and, more importantly, respects the general experimental difficulty to separately resolve arbitrarily close final-state particles, an analogous treatment for the initial-state collinear radiation is not possible. Before we discuss the removal of these remaining IR-singular contributions by an appropriate redefinition of the initial state in Sec. 4.1, we now first focus on the exploration of the explicit cancellation of the remaining IR-singularities.

In particular, the light strongly interacting particles⁴ in the final state are impossible to individually detect as such, but, due to ongoing soft-particle emission, they rather lead to unfocused signatures in the detector, that are indistinguishable among each other. Consequently, in the final state, the light particles of QCD are collectively described as *jets*, and the IR safety is ensured by a recombination procedure, the *jet-algorithm*. While top-quarks are too heavy to appear as final-state particles (see Sec. 3.2.3), for the second heaviest quark, the bottom quark, elaborate experimental techniques exist to distinguish the so-called *b-jets* from jets produced by the remaining four quark flavours [42]. Due to the possibility of the separate detection of b-jets, also in theoretical predictions including external b quarks, these contributions can be treated separately from the remaining quark flavours, as we will also exploit in Part II of this thesis.

In contrast to QCD radiation, for the additional emission of photons off leptons, however, depending on the lepton flavour, it is experimentally possible to individually detect both particles even in the collinear configuration, since the particles are detected in different layers of the detector. To comply with this possibility also in a theoretical prediction, the application of a recombination procedure in the calculation has to be dropped, leading to so-called *collinear-unsafe* observables. As we will discuss in detail in Sec. 4.2, the inclusion of the non-collinear safe phase-space regions leads to additional contributions $\propto \alpha/\pi \ln(m_p)$, that are enhanced by the logarithm of the corresponding particles mass m_p . The remaining IR-singular contributions in the collinear region, however, also appear in the situation where inclusiveness is guaranteed by the application of a recombination procedure, such that, by virtue of the KLN theorem, these contributions always cancel in the sum of real and virtual contributions.

Prior to the introduction of a suitable treatment of the occurring IR divergences, we want to stress once more that the exclusion of massive particles from the real corrections does not give rise to uncanceled *singular* contributions in the virtual part of the calculation. However, although the particle mass acts as regulator, preventing the virtual contribution from a divergent behaviour, only the virtual corrections are affected by the logarithmic enhancement at energy scales that are much larger than the mass of the corresponding particle. Those *Sudakov-logarithms* [43], in particular, give rise to the aforementioned strong kinematic dependence of the EW corrections and will be subject to further discussion in Chap. 5 of this work.

In principle, the regularization of the IR-singular contributions could be performed in similar lines as the regularization of UV divergences, namely in dimensional regularization (see Sec. 3.1), where the phase-space and loop integrations are extended to $D = 4 - 2\epsilon$ dimensions and the cancellation of the divergent parts is performed analytically (see e.g. Ref. [44]). Another, yet easier, approach is to perform the phase-space integration consistently in four space-time dimensions and imply the BN and KLN theorems. Since the phase-space integrals over the real and virtual contributions

⁴That is, the massless gluon and the light quarks, which are treated as exactly massless particles in the calculation.

are, however, not only separately divergent, but are also of different dimensionalities (c.f. Eq. (3.6)), a dedicated *subtraction procedure* is required, that shifts the divergences from one phase space onto the other. This technique is particularly well suited if the phase-space integration is performed by Monte Carlo methods and slightly different realizations are broadly used in the community [45–52]. The underlying idea is to subtract a sufficiently simple auxiliary subtraction function $|\mathcal{M}_{\text{sub}}|^2$ from the real contribution that exhibits the same singular behaviour in the soft and collinear limits, such that the real phase-space integration can safely be performed in $D = 4$ dimensions,

$$\int d\Phi_{+1} (|\mathcal{M}_{\text{real}}|^2 - |\mathcal{M}_{\text{sub}}|^2) = \text{finite}, \quad (3.37)$$

without introducing a further regularization prescription. Subsequently, this subtraction function has to be re-added in a suitable form to the virtual contribution, which, by construction, cancels the IR singularities appearing in the loop integration. At that step, the dependence on the applied regularization scheme (R.S.) of the IR singularities becomes apparent. Very similarly to the procedure elaborated for the renormalization of the UV divergences, in QCD, the IR singularities are typically isolated from the respective finite parts of the amplitude by dimensional regularization. For the calculation of EW corrections, which in the real part reduces to massless QED corrections, it is very convenient to introduce small regulator masses for the (massless) fermions and the photon and regularize the IR singularities by mass regularization. Note, however, that this procedure is only applicable, because QED is an Abelian theory, while the introduction of a regulator mass for the gluons in QCD would immediately spoil the $SU(3)_C$ -gauge invariance⁵.

Independent of the actual regularization scheme applied, the explicit construction of the process independent subtraction functions, is not unique and in the literature many different subtraction methods to apply in NLO QCD corrections [45–50] and NLO EW corrections [51, 52] have been proposed and refined over the last decades.

However, all subtraction methods collectively rely on the universality of the IR singularities, which allows for the decomposition of the real phase-space integral into a non-radiative part with LO-kinematics, $\int d\tilde{\Phi}_{\text{LO}}$, and a part containing the IR region,

$$\int d\Phi_{+1} = \int d\tilde{\Phi}_{\text{LO}} \otimes \int d\Phi_{\text{IR}}. \quad (3.38)$$

As we will see, the subtraction function can be constructed in the same factorized form,

$$|\mathcal{M}_{\text{sub}}(\Phi_{+1})|^2 = f(\Phi_{\text{IR}}) \otimes |\mathcal{M}_{\text{LO}}(\tilde{\Phi}_{\text{LO}})|^2, \quad (3.39)$$

with an auxiliary function f that contains the IR singular part. If this function is chosen sufficiently simple, the integration over the IR region can be performed analytically, yielding

$$\int d\Phi_{+1} |\mathcal{M}_{\text{sub}}(\Phi_{+1})|^2 = \mathcal{F}_{\text{IR}}^{\text{R.S.}} \otimes \int d\tilde{\Phi}_{\text{LO}} |\mathcal{M}_{\text{LO}}(\tilde{\Phi}_{\text{LO}})|^2, \quad (3.40)$$

⁵If the real corrections do not include the non-Abelian three-gluon vertex, mass regularization may of course also be applied to regularize QCD corrections.

where all IR singularities are separated in the regularization scheme dependent functions $\mathcal{F}_{\text{IR}}^{\text{R.S.}} = \int d\Phi_{\text{IR}} f(\Phi_{\text{IR}})$.

The main advantage of the subtraction method is that the subtraction function $|\mathcal{M}_{\text{sub}}|^2$ can be constructed in a process independent way. The auxiliary functions may either be attributed to one single particle (soft divergence) or to a pair of two particles (collinear divergence) of the process under consideration. This feature makes the application of such a subtraction method especially suitable for processes with many particles in the final state, where the explicit elaboration of the singular behaviour otherwise becomes a very intricate procedure. Nevertheless, beside the actual form of the auxiliary function f , the appropriate mapping of all momenta from the real phase space onto the LO phase space $\tilde{\Phi}_{\text{LO}}$ is of utter importance for the realizability of such a subtraction procedure. In Sec. 4.2 we will discuss in detail the subtraction formalism that is commonly applied in the calculation of EW corrections and explicitly list all formulae relevant for the implementation of this method.

Owing to the BN and KLN theorems, for soft- and final-state collinear (fsc) singularities the integrated auxiliary functions $\mathcal{F}_{\text{soft}}$ and \mathcal{F}_{fsc} , respectively, now exhibit exactly the right singular behaviour in order to cancel the singular terms of the virtual contribution,

$$\int d\tilde{\Phi}_{\text{LO}} (|\mathcal{M}_{\text{virt}}|^2 + [\mathcal{F}_{\text{fsc}}^{\text{R.S.}} + \mathcal{F}_{\text{soft}}^{\text{R.S.}}] \otimes |\mathcal{M}_{\text{LO}}|^2) = \text{finite}, \quad (3.41)$$

thus yielding a finite result. As already mentioned above, the initial-state collinear (isc) singularities included in \mathcal{F}_{isc} do not entirely cancel against the virtual contributions. Nevertheless, by including them also in the subtraction formalism, we already isolated them from the finite part of real phase-space integration and, thus, prepared the further treatment. The final removal of these singularities will be discussed in Sec. 4.1.

Chapter 4

Next-to-Leading Order Predictions at Hadron Colliders

After the rather general discussion of the obstructions one is confronted with in the computation of quantum corrections in the previous chapter, we now turn to the explicit calculation of NLO corrections to processes studied at hadron colliders. In the first section we introduce the parton model and discuss the factorization theorem, which are two fundamental concepts that all predictions for scattering processes at hadron colliders strongly rely on. In Sec. 4.2 we discuss in detail the subtraction technique presented in Refs. [51, 52]. We explicitly list all subtraction terms and integrated counterparts as implemented in our calculation of EW corrections, which will be presented in Chap. 5 of this thesis. Subsequently, in Sec. 4.3 we shortly introduce the notation and the techniques used in the actual calculation of one-loop integrals.

4.1. Parton Model and Factorization Theorem

In Sec. 3.2.3 we have seen that the application of perturbative methods for the calculation of scattering processes within QCD is well justified due to the property of asymptotic freedom. As discussed there, this justification is, however, only limited to the high-energy region, while towards smaller energy scales the strong coupling becomes larger, and at a certain point a perturbative treatment is no longer possible. Additionally, as a result of this increasing coupling strength, quarks and gluons are at our disposal only confined in colour-neutral objects, the hadrons.

In order to investigate elementary particles via hadron collisions, one therefore first of all needs a prescription on how to extract objects from the hadrons to which the aforementioned perturbative techniques are applicable. The (naive) *parton model* [53] from the late 1960s was a first attempt towards such a prescription and a refined version is now the basis for the description of scattering processes involving hadrons.

In the parton model, a high-energetic scattering process of an elementary particle with a hadron is described in the so-called infinite momentum frame. In that frame, the hadron (H) moves very fast e.g. in the z -direction ($P_H^\mu = p_0(1, 0, 0, 1)$), and its mass becomes completely irrelevant ($p_0 \gg m_H$). The massless constituents of the hadron, the *partons*, all move in the same direction, and for the time of scattering, due to the time dilation, no interaction among the partons occurs. This implies that the parton

momenta will not show any component transverse to the hadron momentum and we can attribute a certain momentum fraction ($0 < \xi_a < 1$) of the momentum of the hadron to every parton a .

A single high-energetic scattering reaction of an elementary particle A with a hadron therefore turns out to be a *partonic scattering reaction* of A with exactly one of the partons of H , while the remaining partons remain unaffected. The probability of finding parton a with a specific momentum fraction $\xi_a \in (\xi, \xi + d\xi)$ is given by $g_{a|H}(\xi)d\xi$ and we call $g_{a|H}(\xi)$ the (naive) *parton distribution function* (PDF) of the parton a inside the hadron H .

In the infinite momentum frame, with the PDFs we therefore have objects at our disposal that encode the complete non-perturbative structure of the hadrons. Unfortunately, there is no way (yet?) to calculate the PDFs from first principles and their determination strongly relies on experimental input. Since the structure of a hadron is, however, obviously independent of the actual scattering reaction it is probed by, informations on PDFs can be extracted from basically every scattering experiment in which the actual kind of hadron, e.g. a proton or an anti-proton, is involved.

Historically, the structure of the proton has first been investigated in deep-inelastic scattering (DIS) experiments at the HERA collider at DESY, where in electron-proton (eP) collisions high-energetic virtual photons (γ^*) directly probed the electrically charged partons, the quarks. For an arbitrary hadron H , the cross section of such a scattering reaction into a certain final state F can then be expressed as

$$\sigma_{\gamma^*H \rightarrow F}(p_{\gamma^*}, P_H) = \sum_a \int_0^1 d\xi g_{a|H}(\xi) \hat{\sigma}_{\gamma^*a \rightarrow F}(p_{\gamma^*}, p_a). \quad (4.1)$$

Here, the sum extends over all partons a of H , $g_{a|H}(\xi)$ gives the probability to find the parton a carrying the momentum-fraction ξ of the momentum of H , $p_a = \xi P_H$, and $\hat{\sigma}_{\gamma^*a \rightarrow F}$ denotes the *partonic cross section* of the γ^*a initial state into the final state F .

4.1.1. The QCD-Improved Parton Model

Until now we have only discussed the naive parton model, which for precise calculations has to be refined upon including higher-order effects, leading to the so-called *QCD-improved parton model*. In Sec. 3.3 we indicated that the inclusion of higher-order corrections, in particular, introduces initial-state collinear singularities in the real part that will not entirely cancel against a virtual counterpart. However, the *factorization theorem* implies that those remaining singular contributions are process independent and can be absorbed into the naive PDFs by a suitable redefinition.

In dimensional regularization, the collinearly divergent part of the DIS cross section of Eq. (4.1) at NLO_{QCD} that can be attributed to the initial state takes the form

$$-\frac{\alpha_s}{2\pi} \frac{\Gamma(1+\epsilon)}{\epsilon} \int_0^1 d\xi \left(\frac{4\pi\mu_R^2}{\hat{s}} \right)^\epsilon \left(\sum_b \int_\xi^1 \frac{dz}{z} \mathcal{P}_{ab}(z) g_b \left(\frac{\xi}{z} \right) \right) \hat{\sigma}_{\gamma^*a \rightarrow F}(p_{\gamma^*}, p_a), \quad (4.2)$$

where we dropped for convenience the additional label H in the subscript of the PDFs. μ_R denotes the renormalization scale (c.f. Sec. 3.2.3) and $\hat{s} = (p_\gamma + p_a)^2$ is the c.m. energy of the partonic scattering reaction. The functions $\mathcal{P}_{ab}(z)$ are the regularized Altarelli-Parisi splitting functions in $D = 4$ dimensions, which can be interpreted as the probability of a parton a to emerge collinearly from parton b , carrying the momentum-fraction z . For a consistent calculation of NLO_{QCD} corrections, we require the four LO-splitting functions, \mathcal{P}_{qq} , \mathcal{P}_{qg} , \mathcal{P}_{gq} , \mathcal{P}_{gg} , that include exactly one splitting and can, for example, be found in App.C of Ref. [47]. Note that at LO, the two (anti-)quarks appearing in \mathcal{P}_{qq} always have to be of the same flavour, while at higher orders also non-flavour diagonal splittings $\mathcal{P}_{qq'}$ as well as splittings from quarks to anti-quarks (and vice versa) occur.

Similarly to the renormalization procedure of the UV divergences, the divergent part of Eq. (4.2) can now be absorbed into the bare naive PDFs $g_{a,0}$,

$$g_{a,0}(\xi) = f_a(\xi, \mu_F^2) + \frac{\alpha_s}{2\pi} \sum_b \int_\xi^1 \frac{dz}{z} f_b\left(\frac{\xi}{z}, \mu_F^2\right) \left[\frac{\Gamma(1+\epsilon)}{\epsilon} \left(\frac{4\pi\mu_R^2}{\mu_F^2} \right)^\epsilon \mathcal{P}_{ab}(z) - \mathcal{C}_{ab}^{\text{F.S.}}(z) \right], \quad (4.3)$$

defining the (factorized) PDFs $f_a(\xi, \mu_F^2)$ which now depend on the additionally introduced *factorization scale* μ_F . This scale can be interpreted as to separate the perturbative region (short-distance physics, α_s small, c.f. Sec. 3.2.3), where we can calculate the hard scattering cross section, from the non-perturbative region (long-distance physics, α_s large), which is completely attributed to the PDFs. As we have already seen in the $\overline{\text{MS}}$ -renormalization scheme, in such a renormalization procedure there always remains some arbitrariness in the treatment of finite terms, such that in Eq. (4.3) an additional factorization-scheme-dependent finite term $\mathcal{C}_{ab}^{\text{F.S.}}$ is included. After the renormalization of the PDFs, the previously divergent expression in Eq. (4.2) now takes the form of a finite *collinear factorization term*,

$$\frac{\alpha_s}{2\pi} \int_0^1 d\xi \hat{\sigma}_{\gamma a \rightarrow F}(p_\gamma, p_a) \sum_b \int_\xi^1 \frac{dz}{z} f_b\left(\frac{\xi}{z}, \mu_F^2\right) \left[\ln\left(\frac{\hat{s}}{\mu_F^2}\right) \mathcal{P}_{ab}(z) - \mathcal{C}_{ab}^{\text{F.S.}}(z) \right], \quad (4.4)$$

that explicitly depends on the factorization scale and has to be taken into account in any higher-order calculation if PDFs are involved.

The actual value of the PDFs at different scales can be determined by the *Dokshitzer-Gribov-Lipatow-Altarelli-Parisi* (DGLAP) evolution equations [54],

$$\frac{\partial}{\partial \ln \mu_F^2} f_a(\xi, \mu_F^2) = \frac{\alpha_s}{2\pi} \sum_b \int_\xi^1 \frac{dz}{z} f_b\left(\frac{\xi}{z}, \mu_F^2\right) \mathcal{P}_{ab}(z), \quad (4.5)$$

which directly follow from Eq. (4.3) and the fact that the bare PDFs, before the renormalization procedure, do not depend on μ_F ,

$$\mu_F^2 \frac{\partial g_{a,0}(\xi)}{\partial \mu_F^2} = 0. \quad (4.6)$$

In the form given here, Eq. (4.5) is a coupled integro-differential equation, which determines the evolution of the renormalized PDFs at NLO_{QCD} for all strongly interacting partons, namely the quarks and gluons. The process-independent collinear splittings of those particles have been absorbed into the respective PDFs, such that these PDFs now serve as basic ingredient for any NLO calculation for hadron-collision processes.

We want to stress once more that physical observables must not depend on any theoretically introduced scale like μ_F or μ_R . However, due to the truncation of the perturbative expansion at a fixed order, unavoidably a residual scale dependence remains. This fact is sometimes used as a indication of the so-called *theoretical uncertainty* of the calculation. By varying the unphysical scales of the process by a constant factor (e.g. 2) around a smartly chosen central scale¹, upper and lower bounds for (differential) cross sections may be obtained. If the inclusion of higher-order corrections does not only lead to narrower scale-variation bands, but this band is also entirely contained in the error estimate of the former order, in general, the theory uncertainty is said to be under control.

4.1.2. Factorization of QED Singularities

For the calculation of EW corrections to hadron collisions, the initial-state singularities in the calculation of the partonic scattering reaction stem from the collinear splitting of quarks and photons, which are proportional to the EW-coupling constant α . The proper factorization of these remaining singularities into the respective PDFs can be performed along the same lines as in QCD, but additionally requires the introduction of a photon PDF f_γ . A combined QCD and QED evolution for NLO PDFs then reads [55]

$$\frac{\partial}{\partial \ln \mu_F^2} f_a(\xi, \mu_F^2) = \sum_b \int_\xi^1 \frac{dz}{z} \left[\frac{\alpha_s}{2\pi} \mathcal{P}_{ab}^{\text{QCD}}(z) + \frac{\alpha}{2\pi} \mathcal{P}_{ab}^{\text{QED}}(z) \right] f_b\left(\frac{\xi}{z}, \mu_F^2\right), \quad (4.7)$$

where a and b can now stand for quarks, gluons and photons. While the relevant QCD splittings have only been mentioned above, we list the non-zero contributions to $\mathcal{P}_{ab}^{\text{QED}}$ for further applications. At LO the relevant splittings read [56]

$$\mathcal{P}_{qq}^{\text{QED}}(z) = \frac{1+z^2}{1-z}, \quad \mathcal{P}_{q\gamma}^{\text{QED}}(z) = z^2 + (1-z)^2, \quad \mathcal{P}_{\gamma q}^{\text{QED}}(z) = \frac{1+(1-z)^2}{z}. \quad (4.8)$$

Since QED splittings, however, may also occur in leptonic processes, showing exactly the same analytical form, for later applications we additionally identify

$$\mathcal{P}_{ff}(z) = \mathcal{P}_{qq}^{\text{QED}}(z), \quad \mathcal{P}_{f\gamma}(z) = \mathcal{P}_{q\gamma}^{\text{QED}}(z), \quad \mathcal{P}_{\gamma f}(z) = \mathcal{P}_{\gamma q}^{\text{QED}}(z), \quad (4.9)$$

defining the three general QED-splitting functions for any charged fermion f . It is worth noting that by going beyond the LO in the splitting functions, we not only

¹ The choice of the central scale is a delicate task, since no “right” scale exists. Usually it is fixed to a typical energy scale of the process (e.g. M_Z), but also *running scales* are used that have to be determined for every phase-space point, like e.g. the invariant mass of two final state particles. We will come back to this issue in Part II of this thesis.

receive the aforementioned non-flavour diagonal splittings for the quarks, $\mathcal{P}_{qq'}$, but also mixed QCD-QED splittings have to be included in Eq. (4.7). In addition, starting at the order α^2 , in $\mathcal{P}_{ab}^{\text{QED}}$ also photon-to-photon as well as quark-to-lepton and lepton-to-quark splittings in principle become possible [57].

As already indicated above, the calculation of EW corrections presented in this thesis has been performed by applying a mass regularization to treat the IR QED singularities. In this scheme, the redefinitions of the quark and photon PDFs necessary to absorb these initial-state collinear singularities are given by [56]

$$\begin{aligned}
g_{q,0}(\xi) &= f_q^{\text{QED}}(\xi, \mu_F^2) \\
&+ \frac{Q_q^2 \alpha}{2\pi} \int_{\xi}^1 \frac{dz}{z} f_q^{\text{QED}}\left(\frac{\xi}{z}, \mu_F^2\right) \\
&\times \left[\ln\left(\frac{m_q^2}{\mu_F^2}\right) \left[\mathcal{P}_{qq}^{\text{QED}}(z) \right]_+ + \left[\mathcal{P}_{qq}^{\text{QED}}(z) (2 \ln(1-z) + 1) \right]_+ - \mathcal{C}_{qq}^{\text{F.S.}}(z) \right] \\
&+ \frac{3Q_q^2 \alpha}{2\pi} \int_{\xi}^1 \frac{dz}{z} f_{\gamma}^{\text{QED}}\left(\frac{\xi}{z}, \mu_F^2\right) \left[\ln\left(\frac{m_q^2}{\mu_F^2}\right) \mathcal{P}_{q\gamma}^{\text{QED}}(z) - \mathcal{C}_{q\gamma}^{\text{F.S.}}(z) \right], \quad (4.10)
\end{aligned}$$

$$\begin{aligned}
g_{\gamma,0}(\xi) &= f_{\gamma}^{\text{QED}}(\xi, \mu_F^2) \\
&+ \frac{Q_q^2 \alpha}{2\pi} \sum_b \int_{\xi}^1 \frac{dz}{z} f_b^{\text{QED}}\left(\frac{\xi}{z}, \mu_F^2\right) \\
&\times \left[\ln\left(\frac{m_q^2}{\mu_F^2}\right) \mathcal{P}_{\gamma q}^{\text{QED}}(z) + \mathcal{P}_{\gamma q}^{\text{QED}}(2 \ln z + 1) - \mathcal{C}_{\gamma q}^{\text{F.S.}}(z) \right], \quad (4.11)
\end{aligned}$$

where Q_q and m_q denotes the charge and the (regulator-) mass of the respective quark q . In comparison to Eq. (4.3), here we explicitly list the full expression for the two relevant PDFs, while gluonic initial states do not yield any initial-state collinear singularity and, thus, the gluon PDF does not require a redefinition. Note that due to the structure of the QED-splitting functions (Eq. (4.8)) the sum of Eq. (4.3) yields two terms for the quark PDF ($b = q, \gamma$), while only one term ($b = q$) contributes for the photon PDF.

Based on the standard definitions of QCD, also in QED the factorization scheme dependent constants are usually defined either in the so-called $\overline{\text{MS}}$ or DIS-like scheme,

$$\mathcal{C}_{qq}^{\overline{\text{MS}}}(z) = \mathcal{C}_{q\gamma}^{\overline{\text{MS}}}(z) = \mathcal{C}_{\gamma q}^{\overline{\text{MS}}}(z) = 0, \quad (4.12)$$

$$\begin{aligned}
\mathcal{C}_{qq}^{\text{DIS}}(z) &= -\mathcal{C}_{\gamma q}^{\text{DIS}}(z) = \left[\mathcal{P}_{qq}^{\text{QED}}(z) \left(\ln\left(\frac{1-z}{z}\right) - \frac{3}{4} \right) + \frac{9+5z}{4} \right]_+, \\
\mathcal{C}_{q\gamma}^{\text{DIS}}(z) &= \mathcal{P}_{q\gamma}^{\text{QED}}(z) \ln\left(\frac{1-z}{z}\right) - 8z^2 + 8z - 1. \quad (4.13)
\end{aligned}$$

Here, and already in Eq. (4.10), we made use of the usual plus prescription $[\dots]_+$, which is defined via its action on a test function g within an integral,

$$\int_0^1 dx [f(x)]_+ g(x) = \int_0^1 dx f(x) [g(x) - g(1)]. \quad (4.14)$$

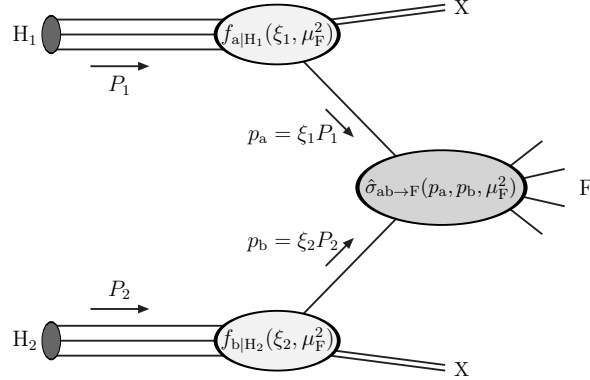


Figure 4.1.: Representation of the scattering reaction of two hadrons, H_1 and H_2 , into a specific final state F . X denotes the *hadron remnants*, including all partons that are not involved in the actual scattering reaction. Adapted from Ref. [20].

The actual form of the factorization constant needed for the collinear factorization term (c.f. Eq. (4.4)) may therefore differ, depending on the conventions applied in the experimental extraction of the PDF. More details on the factorization of photon PDFs in dimensional and mass regularization can be found in Ref. [56] and the references therein.

4.1.3. Hadron-Hadron Collisions

Now that we have absorbed QCD and QED initial-state singularities into the respective process-independent PDFs, we can finally turn to the theoretical description of hadron-hadron collisions. Following the same strategy as in Eq. (4.1), the scattering reaction of two hadrons (H_1 and H_2) can be written as sum over all possible partonic scattering reactions, which now simply have to be weighted by two PDFs, each corresponding to one of the hadrons. Integrating over the respective momentum fractions ξ_i of the partons i yields the hadronic cross section, which therefore reads

$$\begin{aligned} \sigma_{H_1 H_2 \rightarrow F}(P_1, P_2) &= \sum_{a,b} \int_0^1 d\xi_a \int_0^1 d\xi_b f_{a|H_1}(\xi_a, \mu_F) f_{b|H_2}(\xi_b, \mu_F) \hat{\sigma}_{ab \rightarrow F}(p_a, p_b, \mu_F), \\ &= \sum_{a,b} f_{a|H_1} f_{b|H_2} \otimes \hat{\sigma}_{ab \rightarrow F}(p_a, p_b, \mu_F). \end{aligned} \quad (4.15)$$

Here, the sums over a and b comprises all partons appearing as initial state in the respective partonic cross sections of the scattering reaction into the particular final state F , $\hat{\sigma}_{ab \rightarrow F}$. A schematic representation of this final formula is given in Fig. 4.1. Note that the short-hand notation defined in the second line of Eq. (4.15) suppresses the explicit

dependence of the PDFs on the factorization scale μ_F . In cases where the same partons of identical hadrons are considered (in particular proton–proton collisions), additionally the hadron labels in the subscripts of the PDFs may be dropped in future applications of Eq. (4.15).

As already mentioned above, the only part of the partonic cross section that depends on μ_F is the collinear factorization term. Additionally, we want to stress that our definition of the partonic cross section already implicitly includes all applied phase-space cuts via a so-called cut function Θ_{cut} , such that we may symbolically write

$$\hat{\sigma}_{ab \rightarrow F}(p_a, p_b, \mu_F) = \int d\Phi \frac{d\hat{\sigma}_{ab \rightarrow F}}{d\Phi} \Theta_{\text{cut}}(\Phi). \quad (4.16)$$

In addition to all phase-space cuts that define the particular *fiducial phase space*, also the possible recombination of final-state particles to collinear-safe objects, as well as the filling of histograms corresponding to particular observables is implemented via this function.

4.2. The Dipole Subtraction Formalism

In this section we discuss the details of the *dipole subtraction* technique which has been worked out in Refs. [51] and [52] and is widely used in the calculation of EW corrections. The method is based on the dipole formalism presented by Catani and Seymour for massless QCD [46, 47], which later has been refined to apply as well to massive strongly interacting particles [50]. Although the treatment of QCD is therefore to some extent very similar, we refrain from discussing the dipole subtraction formalism as well for QCD but refer the interested reader to the publications cited above. With the restriction to EW processes, we omit the discussion of any complication arising due to the colour structure, which would make the treatment a bit more complex than for the corresponding (electric) charge appearing in the EW theory. Additionally, following Refs. [51, 52], we will regularize the IR singularities with small regulator masses and avoid the less intuitive treatment of dimensional regularization, commonly applied in QCD calculations. As already indicated in Sec. 3.3, the dependence on the regulator masses will only explicitly appear in the integrated counterparts of the subtraction functions, while for the joint phase-space integration of the subtraction function and the real matrix element (c.f. Eq. (3.37)) all (light) fermion masses and the photon mass can be set exactly to zero.

In the dipole formalism, the subtraction function that cancels the singularities entailed by the radiation of an additional photon can be constructed from the auxiliary functions $g_{ff'}^{(\text{sub})}$, the so-called dipoles, and the LO matrix element [51],

$$|\mathcal{M}_{\text{sub}}(\Phi_{+1})|^2 = - \sum_{f \neq f'} Q_f \sigma_f Q_{f'} \sigma_{f'} e^2 g_{ff'}^{(\text{sub})}(p_f, p_{f'}, k) \left| \mathcal{M}_{\text{LO}}(\tilde{\Phi}_{\text{LO}}) \right|^2. \quad (4.17)$$

Here, the sum runs over all possible *emitter* and *spectator* fermions, f and f' , respectively, while σ_f and $Q_{f'e}$ denote their direction of movement in the diagram and their

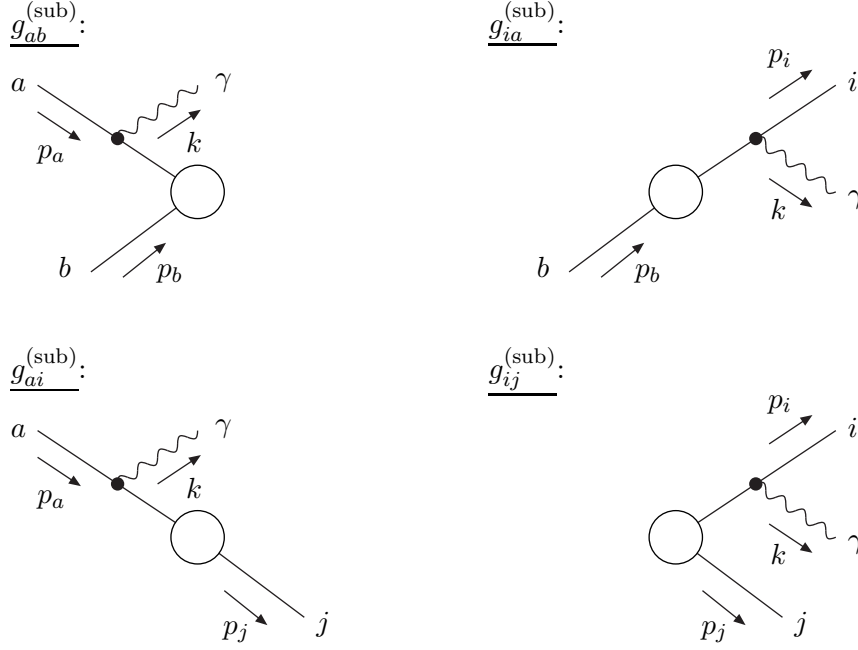


Figure 4.2.: Generic diagrams for the different emitter-spectator pairs for photonic radiation. Particles in the initial state are labeled with a and b , while i and j denote the final-state particles of the underlying LO scattering reaction. Adapted from Ref. [51].

charge, with e defined in Eq. (2.32). We set $\sigma_f = +1(-1)$ for incoming (outgoing) fermions and outgoing (incoming) anti-fermions, such that charge conservation implies

$$\sum_f Q_f \sigma_f = 0. \quad (4.18)$$

The kinematics of the singular configurations is fully transferred to the dipole splitting functions $g_{ff'}^{(\text{sub})}$ that depend only on the momentum of the photon, k , and the momenta of the corresponding emitter and spectator fermions, p_f and $p_{f'}$. Additionally, for the evaluation of \mathcal{M}_{LO} in Eq. (4.17), an appropriate mapping from the real phase space onto a Born-type phase space $\tilde{\Phi}_{\text{LO}}$, comprising one external particle less, has to be specified. Note that in contrast to the original publications, we may restrict the discussion to unpolarized splitting functions, since at the LHC no polarized proton-beams are used, such that no predictions for individual polarizations of the particles are necessary. The unpolarized splitting functions follow from the polarized splitting functions $g_{ff',\pm}^{(\text{sub})}$ in the obvious way,

$$g_{ff'}^{(\text{sub})} = g_{ff',+}^{(\text{sub})} + g_{ff',-}^{(\text{sub})}. \quad (4.19)$$

We distinguish between the four emitter-spectator pairs represented in Fig. 4.2, and here and in the following we consistently label initial-state particles with a and b , while i and j always correspond to final-state particles.

Conceptually, for final-state photon radiation, we further distinguish between emitting particles that have to be recombined with the photon at some point to obtain a meaningful, *collinear-safe* result, and particles that can be treated separately from the photon, even in the collinear region. In the former case, the final state is always treated fully inclusive, such that the KLN theorem applies and all IR singularities connected to final-state emission cancel in the sum of real and virtual contributions. The latter approach is referred to as *collinear-unsafe* treatment of nearly collinear photons and in general leads to additional contributions $\propto \alpha/\pi \ln(m_p)$ that are enhanced by the logarithm of the corresponding particle's mass m_p . As we will discuss below, the collinear-safe treatment follows in a certain well defined limit from the much more involved collinear-unsafe treatment.

Apart from singularities due to real photon radiation, also the collinear splitting of a photon into a fermion–anti-fermion pair, $\gamma \rightarrow f\bar{f}$, and the collinear emission of a fermion, $f \rightarrow f\gamma^*$, with the photon taking part in the hard scattering reaction, may appear in a calculation of EW corrections. In the latter splitting, the asterisk indicates the off-shellness of the photon connecting the splitting to the remaining amplitude. For the former splitting we further distinguish between the final-state photon splitting $\gamma^* \rightarrow f\bar{f}$, resulting in a collinear fermion–anti-fermion pair in the final state, and the initial-state photon splitting $\gamma \rightarrow f\bar{f}^*$, with the anti-fermion transferred to the hard scattering process and the fermion scattered into the direction of the incoming photon, i.e. the beam direction. Note that since σ_f and Q_f have already been factored out, the reversed splitting $\gamma \rightarrow f^*\bar{f}$ yields exactly the same splitting function and is therefore not considered separately.

While the singularities due to collinear final-state photon splittings $\gamma^* \rightarrow f\bar{f}$ can safely be neglected whenever the charged final-state fermions are required to be separately detectable, the same is not true for the singularities introduced by the two additional initial-state splittings, $\gamma \rightarrow f\bar{f}^*$ and $f \rightarrow f\gamma^*$. Both splittings only become relevant for a NLO prediction if the photon is consistently treated as parton, i.e. a LO photon PDF is taken into account. As already discussed in Sec. 4.1, their ultimate absorption requires the proper redefinition of the respective PDFs. However, in a similar manner as for the real photon radiation we additionally apply a dipole subtraction inspired method to facilitate the integration over the real phase space Φ_{+1} . The treatment of these additional splittings appearing only in photon-induced processes will be discussed in Sec. 4.2.2.

4.2.1. Subtraction Functions and Integrated Counterparts – Photon Radiation

In order to cancel all IR divergences appearing due to real photon radiation in the integration over the real phase space (Eq. (3.37)), in the soft and collinear limits the following asymptotic conditions must be fulfilled

$$|\mathcal{M}_{\text{sub}}|^2 \sim |\mathcal{M}_{\text{real}}|^2 \quad \text{for } k \rightarrow 0 \quad \text{or} \quad p_f \cdot k \rightarrow 0. \quad (4.20)$$

Obviously, these conditions do not uniquely specify the splitting functions $g_{ff'}^{(\text{sub})}$, but since the real matrix element shows a well known form in both of these limits (see, e.g., [51] and references therein), their analytic form is already strongly restricted.

Denoting the momenta corresponding to $\tilde{\Phi}_{\text{LO}}$ by a tilde, we generally require

$$\tilde{p}_f \xrightarrow[k \rightarrow 0]{} p_f, \quad \tilde{p}_i \xrightarrow[p_i \cdot k \rightarrow 0]{} p_i + k, \quad \tilde{p}_a \xrightarrow[p_a \cdot k \rightarrow 0]{} x_a p_a, \quad (4.21)$$

for the momentum of the (initial-/final-state) emitter in the respective limit and

$$\tilde{p}_{f'} \xrightarrow[\text{IR-limit}]{} p_{f'}, \quad \tilde{k}_n \xrightarrow[\text{IR-limit}]{} k_n, \quad (4.22)$$

for the momenta of the spectator fermion f' and the momenta of the remaining particles of the real phase space, k_n . In Eq. (4.21), $x_a = (p_a^0 - k^0)/p_a^0$ denotes the energy fraction of the fermion a after photon emission.

Additionally, the mapping will be constructed in such a way that the mass-shell conditions

$$\tilde{p}_f^2 = p_f^2 = m_f^2, \quad \tilde{p}_{f'}^2 = p_{f'}^2 = m_{f'}^2, \quad \tilde{k}_n^2 = k_n^2 = m_n^2, \quad (4.23)$$

are fulfilled for arbitrary photon momenta k .

In the following, we present the definitions of $g_{ff'}^{(\text{sub})}$ and the phase-space mappings for the individual emitter-spectator pairs, as well as the explicit form of the respective integrated counterpart as worked out in Refs. [51] and [52]. We list all formulae relevant for the implementation of the dipole subtraction method for non-collinear safe observables of massless, unpolarized fermions and refer the reader to the original publications for further details.

Initial-state emitter and initial-state spectator

For an emitter a and a spectator b in the initial state the unpolarized auxiliary function $g_{ab}^{(\text{sub})}$ is defined as

$$g_{ab}^{(\text{sub})}(p_a, p_b, k) = \frac{1}{(p_a \cdot k)x_{ab}} \left[\frac{2}{1 - x_{ab}} - 1 - x_{ab} \right], \quad (4.24)$$

where x_{ab} and y_{ab} are variables of scalar products of the relevant momenta in the singular region,

$$x_{ab} = \frac{p_a \cdot p_b - p_a \cdot k - p_b \cdot k}{p_a \cdot p_b}, \quad y_{ab} = \frac{p_a \cdot k}{p_a \cdot p_b}. \quad (4.25)$$

The modified momenta of the phase space $\tilde{\Phi}_{\text{LO}}$, satisfying the requirements of Eqs. (4.21)–(4.23), are chosen as

$$\tilde{p}_a^\mu = x_{ab} p_a^\mu, \quad \tilde{p}_b^\mu = p_b^\mu, \quad \tilde{k}_n^\mu = \Lambda^\mu{}_\nu k_n^\nu, \quad (4.26)$$

which means that the spectator momentum is kept fixed, while the remaining momenta are modified by the Lorentz transformation

$$\Lambda^\mu{}_\nu = g^\mu{}_\nu - \frac{(P_{ab} + \tilde{P}_{ab})^\mu (P_{ab} + \tilde{P}_{ab})_\nu}{P_{ab}^2 + P_{ab} \tilde{P}_{ab}} + \frac{2\tilde{P}_{ab}^\mu P_{ab,\nu}}{P_{ab}^2}, \quad (4.27)$$

with

$$P_{ab}^\mu = p_a^\mu + p_b^\mu - k^\mu, \quad \tilde{P}_{ab}^\mu = x_{ab} p_a^\mu + p_b^\mu. \quad (4.28)$$

These definitions are already sufficient to obtain a finite result in the real phase-space integration of Eq. (3.37). Due to the modification of the incoming momentum $p_a^\mu \rightarrow \tilde{p}_a^\mu$, however, via the (modified) squared partonic c.m. energy

$$\tilde{s} = 2(\tilde{p}_a \cdot p_b) = 2x_{ab}(p_a \cdot p_b) = x_{ab}s, \quad (4.29)$$

the non-radiative part of the phase-space measure $\tilde{\Phi}_{\text{LO}}$ also exhibits a dependence on x_{ab} , such that the complete analytic integration of the subtraction functions can not be performed, but an additional convolution over $x = x_{ab}$ remains,

$$\begin{aligned} \int d\Phi_{+1} |\mathcal{M}_{\text{sub},ab}(\Phi_{+1})|^2 &= -\frac{\alpha}{2\pi} Q_a \sigma_a Q_b \sigma_b \\ &\times \int_0^1 \frac{dx}{x} \mathcal{G}_{ab}^{(\text{sub})}(s, x) \int d\tilde{\Phi}_{\text{LO},ab}(x) \left| \mathcal{M}_{\text{LO}}(\tilde{\Phi}_{\text{LO},ab}(x)) \right|^2, \end{aligned} \quad (4.30)$$

where the additional argument s indicates that for the integration over x , the squared partonic c.m. energy is kept fixed to its original value. Note that since it would unnecessarily further complicate the notation, in this chapter we refrain from using the additional hat ($\hat{\cdot}$) to indicate partonic values. In order to perform the convolution numerically, it is convenient to separate the IR-singular endpoint part of $\mathcal{G}_{ab}^{(\text{sub})}$,

$$G_{ab}^{(\text{sub})}(s) = \int_0^1 dx \mathcal{G}_{ab}^{(\text{sub})}(s, x), \quad (4.31)$$

such that we can write Eq. (4.30) in the following form

$$\begin{aligned} \int d\Phi_{+1} |\mathcal{M}_{\text{sub},ab}(\Phi_{+1})|^2 &= -\frac{\alpha}{2\pi} Q_a \sigma_a Q_b \sigma_b \\ &\times \left\{ \int_0^1 dx \left[\mathcal{G}_{ab}^{(\text{sub})}(s, x) \right]_+ \frac{1}{x} \int d\tilde{\Phi}_{\text{LO},ab}(s, x) \left| \mathcal{M}_{\text{LO}}(\tilde{\Phi}_{\text{LO},ab}(x)) \right|^2 \right. \\ &\quad \left. + G_{ab}^{(\text{sub})}(s) \int d\tilde{\Phi}_{\text{LO},ab}(s, 1) \left| \mathcal{M}_{\text{LO}}(\tilde{\Phi}_{\text{LO},ab}(1)) \right|^2 \right\}, \end{aligned} \quad (4.32)$$

where the integration over x can now be safely performed due to the plus prescription (see Eq. (4.14)). The functions $\mathcal{G}^{(\text{sub})}(s, x)$ and $G^{(\text{sub})}(s)$ contain all remaining mass

singularities and are given by

$$\mathcal{G}_{ab}^{(\text{sub})}(s, x) = \mathcal{P}_{ff}(x) \left[\ln\left(\frac{s}{m_a^2}\right) - 1 \right] + 1 - x, \quad (4.33)$$

$$G_{ab}^{(\text{sub})}(s) = \mathcal{L}(s, m_a^2) - \frac{\pi^2}{3} + 2, \quad (4.34)$$

where $\mathcal{P}_{ff}(x)$ is the LO fermion-to-fermion splitting function defined in Eq. (4.9) and the singular terms of $G^{(\text{sub})}$ are contained in the function

$$\mathcal{L}(s, m^2) = \ln\left(\frac{m^2}{s}\right) \ln\left(\frac{m_\gamma^2}{s}\right) + \ln\left(\frac{m_\gamma^2}{s}\right) - \frac{1}{2} \ln^2\left(\frac{m^2}{s}\right) + \frac{1}{2} \ln\left(\frac{m^2}{s}\right). \quad (4.35)$$

As we can see, in Eq. (4.34) only the emitter mass m_a gives rise to logarithmic singularities, while the spectator mass can be set to zero everywhere in the calculation. Beside logarithmic singularities due to the regulator mass of the emitter, Eq. (4.35) also depends on logarithms of the photon regulator m_γ , which is required for the soft-photon regularization. The dependence on both regulator masses eventually drops out in the combination with the (mass-regulated) virtual contribution.

Initial-state emitter and final-state spectator

Although the case with an initial-state emitter a and a final-state spectator i shows some similarities with the reversed case (final-state emitter and initial-state spectator), for the sake of clarity we refrain from a joint treatment but discuss the reversed case separately below.

The unpolarized dipole splitting function for an initial-state emitter and a final-state spectator $g_{ai}^{(\text{sub})}$ is given by

$$g_{ai}^{(\text{sub})}(p_a, p_i, k) = \frac{1}{(p_a \cdot k)x_{ai}} \left[\frac{2}{2 - x_{ai} - z_{ai}} - 1 - x_{ai} \right], \quad (4.36)$$

with the variables

$$x_{ai} = \frac{p_a \cdot p_i + p_a \cdot k - p_i \cdot k}{p_a \cdot p_i + p_a \cdot k}, \quad z_{ai} = \frac{p_a \cdot p_i}{p_a \cdot p_i + p_a \cdot k}. \quad (4.37)$$

For this dipole, only the momenta of the emitter and spectator are modified to define the ingredients of the LO phase space $\tilde{\Phi}_{\text{LO}}$,

$$\tilde{p}_a^\mu = x_{ai} p_a^\mu, \quad \tilde{p}_i^\mu = p_i^\mu + k^\mu - (1 - x_{ai}) p_a^\mu, \quad (4.38)$$

while all other momenta of the process remain unchanged. As in the previous case, the necessary modification of the incoming momentum $p_a^\mu \rightarrow \tilde{p}_a^\mu$ implies a dependence of $\tilde{\Phi}_{\text{LO}}$ on the respective rescaling factor $x_{ai} = x$, which inhibits the full analytic

integration of the photonic phase space. As the fixed variable during the x -integration we choose the square of the conserved momentum,

$$P_{ai} = p_i + k - p_a = \tilde{p}_i - \tilde{p}_a, \quad (4.39)$$

such that we can finally write the subtraction function as

$$\begin{aligned} \int d\Phi_{+1} |\mathcal{M}_{\text{sub},ai}(\Phi_{+1})|^2 &= -\frac{\alpha}{2\pi} Q_a \sigma_a Q_i \sigma_i \\ &\times \left\{ \int_0^1 dx \left[\mathcal{G}_{ai}^{(\text{sub})}(P_{ai}^2, x) \right]_+ \frac{1}{x} \int d\tilde{\Phi}_{\text{LO},ai}(P_{ai}^2, x) \left| \mathcal{M}_{\text{LO}}(\tilde{\Phi}_{\text{LO},ai}(x)) \right|^2 \right. \\ &\left. + G_{ai}^{(\text{sub})}(P_{ai}^2) \int d\tilde{\Phi}_{\text{LO},ai}(P_{ai}^2, 1) \left| \mathcal{M}_{\text{LO}}(\tilde{\Phi}_{\text{LO},ai}(1)) \right|^2 \right\}, \end{aligned} \quad (4.40)$$

where we again make use of the plus prescription to enable a stable numerical integration over x and define the endpoint contributions as

$$G_{ai}^{(\text{sub})}(P_{ai}^2) = \int_0^1 dx \mathcal{G}_{ai}^{(\text{sub})}(P_{ai}^2, x). \quad (4.41)$$

Using again the function $\mathcal{L}(P^2, m^2)$ of Eq. (4.35) and $\mathcal{P}_{ff}(x)$ defined in Eq. (4.9), the explicit form of the IR-singular functions reads

$$\begin{aligned} \mathcal{G}_{ai}^{(\text{sub})}(P_{ai}^2, x) &= \mathcal{P}_{ff}(x) \left[\ln\left(\frac{|P_{ai}^2|}{m_a^2 x}\right) - 1 \right] \\ &\quad - \frac{2}{1-x} \ln(2-x) + (1+x) \ln(1-x) + 1 - x, \end{aligned} \quad (4.42)$$

$$G_{ai}^{(\text{sub})}(P_{ai}^2) = \mathcal{L}(|P_{ai}^2|, m_a^2) + \frac{\pi^2}{6} - 1. \quad (4.43)$$

Final-state emitter and final state-spectator

The unpolarized auxiliary function $g_{ij}^{(\text{sub})}$, corresponding to an emitter-spectator pair ij from the final state, is defined by

$$g_{ij}^{(\text{sub})}(p_i, p_j, k) = \frac{1}{(p_i \cdot k)(1 - y_{ij})} \left[\frac{2}{1 - z_{ij}(1 - y_{ij})} - 1 - z_{ij} \right], \quad (4.44)$$

with the variables of the corresponding momenta,

$$y_{ij} = \frac{p_i \cdot k}{p_i \cdot p_j + p_i \cdot k + p_j \cdot k}, \quad z_{ij} = \frac{p_i \cdot p_j}{p_i \cdot p_j + p_j \cdot k}. \quad (4.45)$$

For this case we choose the mapping onto the LO phase space $\tilde{\Phi}_{\text{LO}}$ as

$$\tilde{p}_i^\mu = p_i^\mu + k^\mu - \frac{y_{ij}}{1 - y_{ij}} p_j^\mu, \quad \tilde{p}_j^\mu = \frac{1}{1 - y_{ij}} p_j^\mu, \quad (4.46)$$

which only affects the corresponding final-state momenta, while, in particular, the entire initial state remains unaffected.

If the final-state photon-radiation is treated collinearly safe, the complete analytic integration of the subtraction function over the photonic part of the real $(N + 1)$ -particle phase space can be performed, without affecting the remaining momenta of the N -particle LO phase space $\tilde{\Phi}_{\text{LO}}$. As in the two cases discussed above, the evaluation of the real phase-space integral of Eq. (3.37) requires to assess the cut function Θ_{cut} twice, once for the real $(N + 1)$ -particle phase space Φ_{+1} corresponding to $|\mathcal{M}_{\text{real}}|^2$ and once for the integration of $|\mathcal{M}_{\text{sub}}|^2$ over the modified LO phase space $\tilde{\Phi}_{\text{LO}}$, respectively.

However, if the final-state fermion-photon system is not recombined to one quasi-particle in the collinear limit, the events associated with $|\mathcal{M}_{\text{sub},ij}|^2$ have to be treated as $(N + 1)$ -particle events. Still, the $(N + 1)$ momenta must reduce to the momenta used for the calculation of $|\mathcal{M}_{\text{LO}}(\tilde{\Phi}_{\text{LO}})|^2$ in the soft and collinear limit, which can be achieved by setting

$$p_i^\mu \rightarrow z\tilde{p}_i^\mu, \quad k^\mu \rightarrow (1 - z)\tilde{p}_i^\mu, \quad (4.47)$$

with \tilde{p}_i defined in Eq. (4.46) and $z = z_{ij}$ from Eq. (4.45). The spectator momentum, as well as the remaining momenta of the process k_n stay unaffected. Explicitly including the momentum and cut dependence, the final-state emitter cases of Eq. (3.37) read in the general collinear-unsafe treatment

$$\int d\Phi_{+1} \left[|\mathcal{M}_{\text{real}}(\Phi_{+1})|^2 \Theta_{\text{cut}}(\Phi_{+1}) - \sum_{x=a,j} |\mathcal{M}_{\text{sub},ix}|^2 \Theta_{\text{cut}}\left(z_{ix}\tilde{p}_i^{(ix)}, (1 - z_{ix})\tilde{p}_i^{(ix)}, \tilde{p}_x^{(ix)}, \{k_n\}\right) \right], \quad (4.48)$$

where x denotes the possible initial- and final-state spectators. While the modification in the subtraction part of the real phase-space integration reduces to an additional numerical integration over the z -variable that only affect the phase-space cuts, it considerably complicates the explicit calculation of the integrated counterpart. For the parametrization of the photonic phase space we make use of the conserved momentum

$$P_{ij} = p_i + p_j + k = \tilde{p}_i + \tilde{p}_j, \quad (4.49)$$

such that the subtraction function for a final-state emitter and final-state spectator in the collinear-unsafe case reads

$$\begin{aligned} \int d\Phi_{+1} |\mathcal{M}_{\text{sub},ij}(\Phi_{+1})|^2 &= -\frac{\alpha}{2\pi} Q_i \sigma_i Q_j \sigma_j \\ &\times \int d\tilde{\Phi}_{\text{LO},ij} \int_0^1 dz \left(G_{ij}^{(\text{sub})}(P_{ij}^2) \delta(1 - z) + [\bar{\mathcal{G}}_{ij}^{(\text{sub})}(P_{ij}^2, z)]_+ \right) \\ &\times |\mathcal{M}_{\text{LO}}(\tilde{\Phi}_{\text{LO}})|^2 \Theta_{\text{cut}}\left(z\tilde{p}_i, (1 - z)\tilde{p}_i, \tilde{p}_j, \{k_n\}\right). \end{aligned} \quad (4.50)$$

Here, the soft singularity of the function $\bar{\mathcal{G}}_{ij}^{(\text{sub})}(P_{ij}^2, z)$ has been isolated with the help of the plus prescription,

$$\bar{\mathcal{G}}_{ij}^{(\text{sub})}(P_{ij}^2, z) = G_{ij}^{(\text{sub})}(P_{ij}^2)\delta(1-z) + \left[\bar{\mathcal{G}}_{ij}^{(\text{sub})}(P_{ij}^2, z)\right]_+. \quad (4.51)$$

The given form of Eq. (4.51) allows for a direct transition to the collinear-safe case, where the full z -integration can be carried out and only the term proportional to $G_{ij}^{(\text{sub})}(P_{ij}^2)$ remains. The functions $G_{ij}^{(\text{sub})}$ and $\bar{\mathcal{G}}_{ij}^{(\text{sub})}(P_{ij}^2, z)$ are explicitly given by

$$G_{ij}^{(\text{sub})}(P_{ij}^2) = \mathcal{L}(P_{ij}^2, m_i^2) - \frac{\pi^2}{3} + \frac{3}{2}, \quad (4.52)$$

$$\bar{\mathcal{G}}_{ij}^{(\text{sub})}(P_{ij}^2, z) = \mathcal{P}_{ff}(z) \left[\ln\left(\frac{P_{ij}^2 z}{m_i^2}\right) - 1 \right] + (1+z)\ln(1-z) + 1-z, \quad (4.53)$$

with $\mathcal{L}(P^2, m^2)$ defined in Eq. (4.35). The aforementioned additional collinear singularity $\propto \ln m_i$ appearing in the collinear-unsafe treatment is contained in $\bar{\mathcal{G}}_{ij}^{(\text{sub})}(P_{ij}^2, z)$.

Final-state emitter and initial-state spectator

The case of an emitter i from the final state and a spectator a from the initial state is kinematically identical to the reversed emitter-spectator case, only that the roles of i and a are interchanged. The dipole splitting function $g_{ia}^{(\text{sub})}$ is defined as

$$g_{ia}^{(\text{sub})}(p_i, p_a, k) = \frac{1}{(p_i \cdot k)x_{ai}} \left[\frac{2}{2 - x_{ai} - z_{ai}} - 1 - z_{ai} \right], \quad (4.54)$$

where we use the variables x_{ai} and z_{ai} from Eq. (4.37). The modified momenta \tilde{p}_i and \tilde{p}_a are defined in the same way as in the reversed emitter-spectator case and are given in Eq. (4.38).

If the final-state emission is treated in a collinear-safe way, the analytic form of the integrated subtraction function can be obtained from Eq. (4.40) by simply exchanging i and a . The IR-singular functions to be inserted are given by

$$G_{ia}^{(\text{sub})}(P_{ai}^2) = \mathcal{L}(|P_{ai}^2|, m_i^2) - \frac{\pi^2}{2} + \frac{3}{2}, \quad (4.55)$$

$$\mathcal{G}_{ia}^{(\text{sub})}(P_{ai}^2, x) = \frac{1}{1-x} \left[2 \ln\left(\frac{2-x}{1-x}\right) - \frac{3}{2} \right], \quad (4.56)$$

where P_{ai} is the conserved momentum defined in Eq. (4.39) and $\mathcal{L}(P^2, m^2)$ is given in Eq. (4.35).

For a collinear-unsafe treatment of the final-state radiation, however, as discussed in the previous paragraph, the subtraction function has to be evaluated for an $(N+1)$ -particle phase space, where the momenta must behave as defined in Eq. (4.47) with $z = z_{ai}$. The additional numerical integration over z requires a further refinement

of Eq. (4.40) in order to isolate the soft singularities appearing at $z \rightarrow 1$. Thus, the collinear-unsafe generalization of the integrated subtraction function for an final-state emitter and initial-state spectator reads

$$\begin{aligned}
\int d\Phi_{+1} |\mathcal{M}_{\text{sub},ia}(\Phi_{+1})|^2 &= -\frac{\alpha}{2\pi} Q_a \sigma_a Q_i \sigma_i \quad (4.57) \\
&\times \left\{ \int_{(0,0)}^{(1,1)} d(x,z) \left([\mathcal{G}_{ia}^{(\text{sub})}(P_{ai}^2, x)]_+ \delta(1-z) + [\bar{g}_{ia}^{\text{sub}}(x,z)]_+^{(x,z)} \right) \right. \\
&\quad \times \frac{1}{x} \int d\tilde{\Phi}_{\text{LO},ia}(P_{ai}^2, x) \left| \mathcal{M}_0(\tilde{\Phi}_{\text{LO},ia}(x)) \right|^2 \Theta_{\text{cut}}(z\tilde{p}_i(x), \dots) \\
&\quad + \int_0^1 dz \left(G_{ia}^{(\text{sub})}(P_{ai}^2) \delta(1-z) + [\bar{\mathcal{G}}_{ia}^{(\text{sub})}(P_{ai}^2, z)]_+ \right) \\
&\quad \left. \times \int d\tilde{\Phi}_{\text{LO},ia}(P_{ai}^2, 1) \left| \mathcal{M}_0(\tilde{\Phi}_{\text{LO},ia}(1)) \right|^2 \Theta_{\text{cut}}(z\tilde{p}_i(1), \dots) \right\}.
\end{aligned}$$

In addition to the IR singular functions of Eqs. (4.55) and (4.56) here we defined

$$\bar{g}_{ia}^{\text{sub}}(x, z) = \frac{1}{1-x} \left(\frac{2}{2-x-z} - 1 - z \right), \quad (4.58)$$

$$\begin{aligned}
\bar{\mathcal{G}}_{ia}^{(\text{sub})}(P_{ai}^2, z) &= \mathcal{P}_{ff}(z) \left[\ln \left(\frac{-P_{ai}^2 z}{m_i^2} \right) - 1 \right] - \frac{2 \ln(2-z)}{1-z} \\
&\quad + (1+z) \ln(1-z) + 1 - z, \quad (4.59)
\end{aligned}$$

with the LO fermion-to-fermion splitting $\mathcal{P}_{ff}(x)$ defined in Eq. (4.9). Since $\bar{g}_{ia}^{\text{sub}}$ contains poles in x and z , to this function a *double plus prescription*,

$$\begin{aligned}
\int_{(0,0)}^{(1,1)} d(x,y) [f(x,y)]_+^{(x,y)} g(x,y) &= \\
\int_{(0,0)}^{(1,1)} d(x,y) f(x,y) [g(x,y) - g(1,y) - g(x,1) + g(1,1)] &, \quad (4.60)
\end{aligned}$$

is applied, while the collinear singularity $\propto \ln m_i$ is contained in $\bar{\mathcal{G}}_{ia}^{(\text{sub})}(P_{ai}^2, z)$.

4.2.2. Dipole Subtraction for Photon-Induced Processes

In contrast to the previous section, we now treat the collinear emission of an additional fermion in photon-induced processes. As mentioned in the beginning of this section, for our purpose the discussion can be limited to the additional fermions stemming from one of the two initial-state splittings $\gamma \rightarrow q\bar{q}^*$ or $q \rightarrow q\gamma^*$, depicted in Fig. 4.3. The reason for the further restriction to quarks is due to the fact that we require the charged final-state leptons to have a non-vanishing transverse momentum (p_T), such that no lepton can be emitted collinearly to the beam-pipe. Moreover, a $l \rightarrow l\gamma^*$ splitting would require a finite lepton content in the hadron already at the LO, which does not exist. It

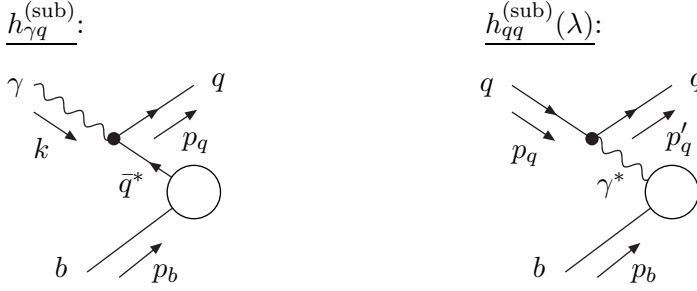


Figure 4.3.: Generic diagrams for the splittings $\gamma \rightarrow q\bar{q}^*$ and $q \rightarrow q\gamma^*$ with an initial-state spectator b . Adapted from Ref. [52].

is worth noting that in order for the calculation to apply also in the case of a vanishing lepton p_T , we would additionally need to include the photon-to-lepton splitting $\mathcal{P}_{\gamma l}^{\text{QED}}$ in Eq. (4.11) to properly cure the singularity due to the $\gamma \rightarrow l\bar{l}^*$ -splitting.

For both types of initial-state splittings depicted in Fig. 4.3, the appearing collinear singularities can be attributed to one single external leg and $|\mathcal{M}_{\text{sub}}|^2$ can be constructed from a single term $\propto Q_q^2$ with the spectator x being either the second particle b from the initial state (as shown in the figure) or any particle from the final state. The formulae for both cases are derived in great detail in Chap. 3 and 5 of Ref. [52], such that we restrict the discussion in this thesis to our actual implementation, where we choose the spectator from the final state, i.e. we set $x = b$.

Collinear singularities from $\gamma \rightarrow q\bar{q}^*$ splittings

For an initial-state spectator b , the subtraction function related to the $\gamma \rightarrow q\bar{q}^*$ splitting that has to be subtracted from the real amplitude is defined as

$$|\mathcal{M}_{\text{sub},\gamma b}(\Phi_{+1})|^2 = N_c Q_q^2 e^2 h_{\gamma q}^{(\text{sub})}(k, p_q, p_b) \left| \mathcal{M}_{\text{LO}}(\tilde{\Phi}_{\text{LO}}) \right|^2, \quad (4.61)$$

where $N_c = 3$ is the colour factor of the quark q with relative electric charge Q_q . The radiator function is given by

$$h_{\gamma q}^{(\text{sub})}(k, p_q, p_b) = \frac{1}{x_{q\gamma}(k \cdot p_q)} \mathcal{P}_{f\gamma}(x_{q\gamma}), \quad (4.62)$$

where we defined the auxiliary quantity,

$$x_{q\gamma} = x = \frac{k \cdot p_b - k \cdot p_q - p_q \cdot p_b}{k \cdot p_b}, \quad (4.63)$$

and used the LO photon-to-fermion splitting function $\mathcal{P}_{f\gamma}(x)$, which we already defined in Eq. (4.9). The modified incoming anti-quark momentum and the modified final-state momenta \tilde{k}_n defining $\tilde{\Phi}_{\text{LO}}$ are given by

$$\tilde{p}_q^\mu(x) = x k^\mu \quad \text{and} \quad \tilde{k}_n^\mu = \Lambda_\nu^\mu k_n^\nu, \quad (4.64)$$

which is exactly the same definition as in Eq. (4.26), with Λ_ν^μ defined in Eq. (4.27).

The integrated counterpart reads

$$\int d\Phi_{+1} |\mathcal{M}_{\text{sub},\gamma b}(\Phi_{+1})|^2 = \frac{\alpha Q_q^2 N_c}{2\pi} \times \int_0^1 dx \mathcal{H}_{\gamma q}^{(\text{sub})}(s, x) \int d\tilde{\Phi}_{\text{LO}}(x) \left| \mathcal{M}_{\text{LO}}(\tilde{\Phi}_{\text{LO}}(x)) \right|^2, \quad (4.65)$$

with all IR singularities contained in the function

$$\mathcal{H}_{\gamma q}^{(\text{sub})}(s, x) = \mathcal{P}_{f\gamma}(x) \ln\left(\frac{s(1-x)^2}{m_q^2}\right) + 2x(1-x), \quad (4.66)$$

where

$$s = (k + p_b)^2 = 2k \cdot p_b, \quad (4.67)$$

is again the squared partonic c.m. energy.

Collinear singularities from $q \rightarrow q\gamma^*$ splittings

In the case of an initial-state $q \rightarrow q\gamma^*$ splitting, with the photon of helicity $\lambda_\gamma = \pm$ taking part in the hard scattering reaction, the matrix element of the LO subprocess $\gamma b \rightarrow X$ can be written as

$$\mathcal{M}_{\text{LO}}(\tilde{\Phi}_{\text{LO}}) = \mathcal{M}_{\gamma b \rightarrow X}(\tilde{k}, p_b, \lambda_\gamma) = T_{\gamma b \rightarrow X}^\mu(\tilde{k}, p_b) \varepsilon_{\lambda_\gamma, \mu}(\tilde{k}), \quad (4.68)$$

where $T_{\gamma b \rightarrow X}^\mu(\tilde{k}, p_b)$ is the amplitude without the photon polarization vector $\varepsilon_{\lambda_\gamma, \mu}(\tilde{k})$, p_b the momentum of b , and \tilde{k} the momentum of the photon in the collinear limit,

$$\tilde{k}^\mu = \tilde{k}^\mu(x) = x \left(p_q^\mu - \frac{m_q^2}{\bar{s}} p_b^\mu \right), \quad (4.69)$$

with

$$x = x_{qq} = \frac{p_b \cdot p_q - p_q \cdot p'_q - p_b \cdot p'_q + m_q^2}{p_b \cdot p_q}, \quad (4.70)$$

and

$$\bar{s} = 2p_b \cdot p_q = (p_q + p_b)^2 - m_q^2 = s - m_q^2. \quad (4.71)$$

Due to the polarization of the photon, the squared real matrix element is not proportional to a polarization-summed squared LO amplitude $|\mathcal{M}_{\gamma b \rightarrow X}|^2$ as it was the case for all splittings discussed so far, with fermions connecting the splitting to the hard scattering reaction. Only after averaging over the azimuthal angle ϕ'_q of the $q \rightarrow q\gamma^*$ splitting plane around the collinear axis (i.e. the beam axis) the spin correlation drops out and the averaged squared real amplitude becomes proportional to a LO squared amplitude,

$$\langle |\mathcal{M}_{qb \rightarrow qX}(\Phi_{+1})|^2 \rangle_{\phi'_q} \widetilde{\bigg|}_{p_q p'_q \rightarrow 0} N_c Q_q^2 e^2 h_{qq}(p_q, p'_q) |\mathcal{M}_{\gamma b \rightarrow X}(\tilde{\Phi}_{\text{LO}})|^2, \quad (4.72)$$

where the collinear singularities are encoded in the function

$$h_{qq}(p_q, p'_q) = \frac{-1}{x(p_q - p'_q)^2} \left[\mathcal{P}_{\gamma f}(x) + \frac{2xm_q^2}{(p_q - p'_q)^2} \right], \quad (4.73)$$

which is valid in $D = 4$ space-time dimensions up to terms that are further suppressed by additional factors of m_q . $\mathcal{P}_{\gamma f}(x)$ is the splitting function defined in Eq. (4.9).

However, the subtraction functions can also be defined upon the spin-correlated squared Born amplitudes

$$\mathcal{B}_{\text{LO}}^{2\mu\nu}(\tilde{\Phi}_{\text{LO}}) = T_{\gamma b \rightarrow X}^\mu(\tilde{k}, p_b)^* T_{\gamma b \rightarrow X}^\nu(\tilde{k}, p_b), \quad (4.74)$$

with spin-dependent auxiliary functions $h_{qq,\mu\nu}^{(\text{sub})}$ that additionally depend on the helicity of the quark q , κ_q . For a massless initial-state spectator b the subtraction function can be defined as

$$|\mathcal{M}_{\text{sub}}(\kappa_q)|^2 = N_c Q_q^2 e^2 h_{qq,\mu\nu}^{(\text{sub})}(p_q, p'_q, p_b, \kappa_q) \mathcal{B}_{\text{LO}}^{2\mu\nu}(\tilde{\Phi}_{\text{LO}}), \quad (4.75)$$

with

$$h_{qq}^{(\text{sub}),\mu\nu}(p_q, p'_q, p_b, \kappa_q) = \frac{-1}{(p_q - p'_q)^2} \left[-g^{\mu\nu} - \frac{4(1-x)}{x^2} \frac{\tilde{k}_\perp^\mu \tilde{k}_\perp^\nu}{\tilde{k}_\perp^2 - x^2 m_q^2} \right. \\ \left. + \frac{\kappa_f}{x} \left(2 - x + \frac{2x^2 m_q^2}{(p_q - p'_q)^2} \right) \left(\varepsilon_+^\mu(\tilde{k})^* \varepsilon_+^\nu(\tilde{k}) - \varepsilon_-^\mu(\tilde{k})^* \varepsilon_-^\nu(\tilde{k}) \right) \right], \quad (4.76)$$

where we further used the auxiliary parameter x defined in Eq. (4.70) and the momenta of $\tilde{\Phi}_{\text{LO}}$ are given by

$$P^\mu = p_q^\mu + p_b^\mu - p'_q{}^\mu, \quad \tilde{P}^\mu = \tilde{P}^\mu(x) = \tilde{k}^\mu(x) + p_b^\mu, \\ \tilde{k}_\perp^\mu = p'_q{}^\mu - \frac{p'_q \tilde{k}}{p_b \tilde{k}} p_b^\mu, \quad \tilde{k}_n^\mu = \Lambda^\mu{}_\nu k_n^\nu, \quad (4.77)$$

where the Lorentz transformation matrix $\Lambda^\mu{}_\nu$ is again defined by P^μ and \tilde{P}^μ as in Eq. (4.27). In Eq. (4.76) we kept the dependence on m_q , but as before, we can set $m_q = 0$ in the numerical integration of $(|\mathcal{M}_{qb \rightarrow qX}|^2 - |\mathcal{M}_{\text{sub}}|^2)$ and the regulator dependence is only relevant in the integrated counterpart, which reads

$$\int d\Phi_{+1} |\mathcal{M}_{\text{sub},qb}(\Phi_{+1})|^2 = \frac{\alpha Q_q^2 N_c}{2\pi} \quad (4.78)$$

$$\times \int_0^1 dx \mathcal{H}_{qq}^{(\text{sub})}(s, x) \int d\tilde{\Phi}_{\text{LO}}(x) \left| \mathcal{M}_{\text{LO}}(\tilde{\Phi}_{\gamma b \rightarrow X}(x)) \right|^2, \quad (4.79)$$

with all IR singularities contained in the function

$$\mathcal{H}_{qq}^{(\text{sub})}(s, x) = \ln \left(\frac{\sqrt{s}(1-x)}{xm_q} \right) \left[\mathcal{P}_{\gamma f}(x) + \tau(2-x) \right] - \frac{1-x}{x}. \quad (4.80)$$

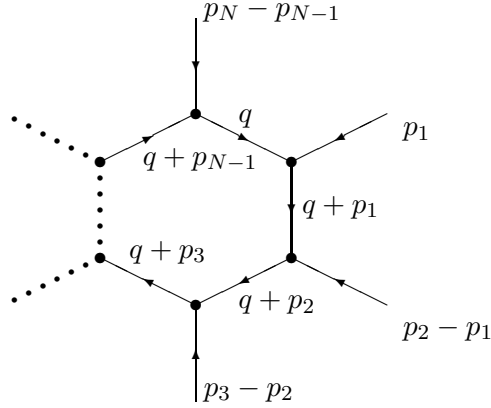


Figure 4.4.: Labeling convention for the relevant momenta of a N -point integral.

4.3. One-Loop Integrals

After having discussed the regularization and renormalization procedures in the previous chapter, we now turn to the actual calculation of one-loop diagrams. The additional integration over the loop momentum q in the virtual part can be decomposed into a finite number of one-loop N -point tensor integrals, where N denotes the number of vertices in the loop. The two illustrative examples from the previous chapter in Eqs. (3.7) and (3.9) therefore both show diagrams requiring the calculation of 2-point integrals, while in Fig. 3.2a an example diagram involving a 3-point integral is depicted.

In dimensional regularisation, the N -point tensor integrals are most conveniently defined in the form [31]

$$T_{\mu_1 \dots \mu_P}^N(p_1, \dots, p_{N-1}, m_0, \dots, m_{N-1}) = \frac{(2\pi\mu)^{4-D}}{i\pi^2} \int d^D q \frac{q_{\mu_1} \dots q_{\mu_P}}{\prod_{i=0}^{N-1} ((q + p_i)^2 - m_i^2 + i\varepsilon)}, \quad (4.81)$$

where the tensor rank P is given by the number of integration momenta in the numerator. The arguments p_i and m_i denote the relevant momenta and masses, where one conveniently labels the particles inside the loop clockwise, starting with the momentum q ($p_0 = 0$) and the mass m_0 , followed by the particle with momentum $q + p_1$ and mass m_1 , and so on, as depicted in Fig. 4.4. Consequently, the N external incoming momenta are labeled by $p_i - p_{i-1}$.

The possible number of external momenta connected to a loop can evidently not exceed the number of external legs, such that for a given process only a finite number of distinct N -point integrals may appear. Moreover, for renormalizable theories, such as the SM, we additionally have $P \leq N$ [31], which implies that for every N only a limited number of tensor structures P contributes to Eq. (4.81).

However, as already stated in Chap. 3, the loop integration may lead to UV-divergent results for a fixed space-time dimension. In the basis of tensor integrals, these divergent

contributions appear if $D \geq 2N - P$ and, consequently, in a renormalizable theory with $P \in (0, N)$, at most 4-point integrals may lead to UV-divergent contributions in $D = 4$ space-time dimensions. After renormalizing the input parameters of the theory, all occurring divergences are reabsorbed and we finally obtain a UV-finite result.

For the analytic evaluation of the tensor integrals, we can exploit the fact that every N -point tensor integral of rank P can be decomposed into a linear combination of all symmetric rank- P tensors that can be constructed from $g^{\mu\nu}$ and the external momenta p_i^μ . The coefficients of this decomposition can be expressed in terms of scalar N -point integrals T_0^N , where we conveniently label the N -point tensor integral by the N -th character of the alphabet, e.g. $T_0^1 = A$ or $T_{\mu\nu\rho}^3 = C_{\mu\nu\rho}$. It turns out, that the UV-divergent contributions are attributed to only eight of the tensor coefficients, which are explicitly given in Eq. (4.55) of Ref. [31].

The Passarino–Veltman reduction algorithm [58] is based on the above mentioned decomposition to scalar integrals. However, this numerical reduction algorithm becomes unstable in certain regions of phase space and in particular for N -point integrals where $N \geq 5$. The reason is that the reduction algorithm is based on the external momenta which, in intermediate steps, may appear in so-called inverse Gram determinants,

$$\left[\det Z^{(N)}\right]^{-1} = \begin{vmatrix} 2p_1p_1 & \dots & 2p_1p_N \\ \vdots & \ddots & \vdots \\ 2p_Np_1 & \dots & 2p_Np_N \end{vmatrix}^{-1}, \quad (4.82)$$

that get large if two momenta become collinear to each other. For linearly dependent momenta (i.e. in the collinear limit) the Gram determinant even vanishes, which makes a further reduction impossible.

For a stable and efficient calculation of one-loop integrals over the full phase space, however, a method that is not spoiled by small or vanishing Gram determinants is required. The one-loop library COLLIER [59] is based on a smart algorithm that ensures a fast and numerically stable calculation of the tensor coefficients. Mainly based on the results of Refs. [60, 61], depending on the actual N -point integral to calculate, different methods are exploited in COLLIER. While for $N = 1, 2$ directly explicit numerically stable expressions are used, for $N = 3, 4$ a reduction to scalar integrals is performed. Per default, this reduction relies on the Passarino–Veltman reduction algorithm [58], but is superseded by a more involved method if the former does not provide sufficient numerical accuracy (which typically results from the aforementioned small/vanishing Gram determinants). The tensor integrals with $N > 4$ are directly reduced to lower rank and lower N integrals by exploiting the dedicated methods of Refs. [60].

In addition, since COLLIER supports the complex-mass scheme for unstable particles as well as provides the results either in dimensional or mass regularization, it can be applied to calculations of loop-integrals appearing in QCD and EW corrections.

Part II

Phenomenological Applications

Chapter 5

Next-to-leading-order Electroweak Corrections to $pp \rightarrow W^+W^- \rightarrow 4$ Leptons at the LHC

In this chapter we discuss in detail the calculation of the NLO EW corrections to the proton–proton collision process

$$pp \rightarrow \nu_\mu \mu^+ e^- \bar{\nu}_e + X, \quad (5.1)$$

which has recently been published in Ref. [11]. This process is dominated by the intermediate state of a pair of resonant W bosons decaying leptonically via $W^+ \rightarrow \nu_\mu \mu^+$ and $W^- \rightarrow e^- \bar{\nu}_e$, which is why the process is commonly referred to as W-boson pair production. In Fig. 5.1 we show a representative LO diagram of the hadronic scattering reaction of Eq. (5.1), containing, in thicker lines, a particular partonic subprocess with two resonant W bosons.

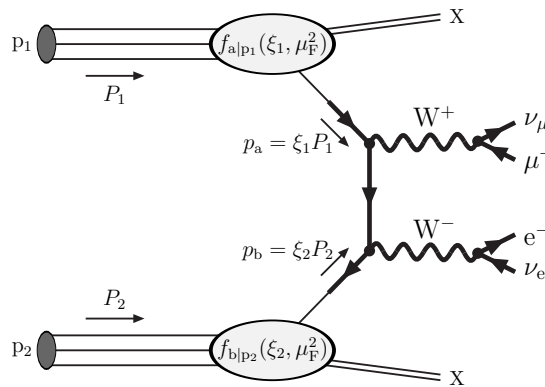


Figure 5.1.: Representative diagram of the hadronic scattering reaction of Eq. (5.1). The partonic scattering reaction is emphasized by thick lines, while the remaining part is identical to Fig. 4.1.

The restriction on the fully leptonic final state avoids the inclusion of additional QCD background diagrams, which considerably facilitates the theoretical prediction and, even more importantly, also gives rise to the cleanest signatures in experiments. We further focus on a final state with charged fermions of different generations to avoid mixing with the $pp \rightarrow ZZ \rightarrow l^-l^+\nu\bar{\nu}$ production process.

As already mentioned in the main introduction, the W-boson pair production process is particularly suited for probing the EW sector of the SM, since, for reasons that will be discussed below, the production cross section is very sensitive to the non-Abelian structure of the EWSM. A potential deviation of measured (differential) cross sections from the values predicted by the SM could consequently directly be interpreted as sign of physics beyond the SM. To unambiguously reveal such a deviation and clearly distinguish it from the effect of unknown higher-order corrections, theoretical predictions at the highest possible accuracy are mandatory. In order to reach such an accuracy for W-pair production at the LHC, radiative corrections of both, the strong and the EW interactions need to be considered and properly combined. In particular, the decay and off-shell effects of the W bosons, including fully differential kinematics and the phase-space regions below the W-pair threshold, have to be carefully taken into account.

In the following we first shortly review the theoretical and experimental status of the W-pair production process, and motivate why precise predictions, including EW corrections, are particularly important for this process. In Sec. 5.2, we present the details of our calculation and prepare the discussion of the phenomenological results. Those are discussed subsequently in Sec. 5.3 for several realistic event-selection setups, before Sec. 5.4 finally provides our conclusions.

5.1. Theoretical and Experimental Status

Beginning at the LO, W-pair production at the LHC is a purely EW process of $\mathcal{O}(\alpha^4)$ dominated by quark–antiquark annihilation, $(\bar{q}q/q\bar{q}) \rightarrow WW \rightarrow 4\text{fermions}$. However, as most of the processes at hadron colliders, due to the strongly interacting particles in the initial state, also the purely EW W-pair production process is plagued by large QCD corrections. The NLO QCD corrections are known since the 1990s, first for on-shell W bosons [62], followed by calculations also including leptonic W decays [63, 64]. The latter subsequently has been implemented in the public available Monte Carlo program MCFM [65]. For LHC energies of 8 TeV (13 TeV) the NLO QCD corrections increase the inclusive WW cross section by about 54% (58%) [66], making their inclusion in phenomenological studies obviously indispensable. The matching of the fixed-order NLO QCD predictions to parton-shower programs of the calculation without [67] and including [68] leptonic W decays as well as the inclusion of QCD resummation effects [69] helped to further diminish the dependence on the unphysical renormalization and factorization scales.

However, with the production of W-boson pairs in gluon–gluon scattering via quark

loops, $gg \rightarrow WW$, starting at NNLO QCD, an entirely new partonic channel opens up, which prevents the perturbative expansion from a fast convergence. Although this channel is of the order $\mathcal{O}(\alpha_s^2\alpha^4)$, and therefore naively strongly suppressed, due to the large gluon flux at the LHC its contribution amounts to more than 10% of the LO ($\bar{q}q/q\bar{q}$)-induced process [66]. At its LO, which solely comprises one-loop amplitudes, this channel was first considered for on-shell W bosons in Ref. [70] and later refined by including leptonic W decays [71], additional jet production, $gg \rightarrow WWg \rightarrow 4\ell g$ [72], and non-standard couplings [73].

The complete NNLO QCD corrections for inclusive W-pair production are known since 2014 [66], supplementing and improving upon previous partial results for the two-loop [74] and the one-loop squared [74] virtual corrections in the high-energy limit, as well as fully taking into account all double-real corrections. Recently, this calculation has been extended to predict also fiducial cross sections and arbitrary kinematical distributions [75]. The NNLO correction increase the inclusive W-pair cross section at the LHC by another 9% (12%) at a c.m. energy of 8 TeV (13 TeV) with respect to NLO QCD and show a residual theoretical uncertainty of about $\sim 3\%$ in the ($\bar{q}q/q\bar{q}$)-induced channel.

Since this year, also the full NLO QCD prediction for $gg \rightarrow WW$ with leptonic W-boson decays are known [76], which, depending on the exact phase-space definition, give rise to another percent correction, with respect to the LO ($\bar{q}q/q\bar{q}$) cross section.

Experimental analyses of the LHC data on W-boson pairs recorded during Run I, that have been independently performed by the ATLAS [77] and the CMS collaboration [78], definitely confirmed that the reached experimental precision requires to include all above mentioned QCD corrections in theoretical predictions. At the time the first Run I analyses were performed, the full NNLO result of Refs. [66, 75] was not yet available and the reported deviation of the data from the theory prediction was already mistakenly discussed as a first sign of new physics. Eventually, taking the missing higher-order correction into account, however, resolved the tension between the SM prediction and measured data. As was pointed out in Ref. [79], parts of the discrepancy also have been caused by an inappropriate extrapolation of the experimental result from the fiducial to the inclusive cross section, needed to compare to the theoretical prediction. This once more demonstrates the additional value of flexible Monte Carlo generators, which allow to supply any differential distribution for arbitrary cut-selection criteria and therefore render such vague extrapolations redundant. The first results on W-pair production from LHC Run II [80, 81], which have been directly compared to predictions for the fiducial phase space, do not show any serious deviation from the SM.

In addition, with the Run I data-set the constraints on non-standard γWW and ZWW couplings, so-called *anomalous trilinear gauge couplings* (aTGC), already became competitive with the constraints obtained at the predecessor experiments at the $p\bar{p}$ collider Tevatron and the e^+e^- collider LEP. The analyses of the upcoming LHC Run II data, which is presently recorded at a so far unprecedented c.m. energy of $\sqrt{s_{pp}} = 13$ TeV, will certainly further tighten these limits on aTGCs.

W-pair production is, however, not only important as signal process and as back-

ground in new-physics-searches, but also represents a very important irreducible background in precision studies of the Higgs-boson properties. The Higgs boson decay channel to two W bosons, $H \rightarrow WW^*$, already played an essential role in the Higgs boson discovery [5, 6], and the data presently recorded in Run II will allow to perform further precision studies focussing on the Higgs-to-W-boson coupling. For such a study, both, the Higgs signal process, $pp \rightarrow H \rightarrow WW^*$, and the irreducible direct production of two W bosons, the $pp \rightarrow WW^*$ background, have to be precisely known. In particular, this requires predictions at an invariant mass of the W-boson system around the Higgs-boson mass, $M_{WW} \sim M_H$, which lies below the W-pair production threshold, such that at least one of the W bosons is produced far off its mass shell.

So far, we have only mentioned and encouraged the importance of QCD corrections to the W-pair production process of Eq. (5.1). However, to provide theoretical predictions at the level of accuracy that is required to fully exploit the potential of the present and, especially, of the upcoming experimental measurements, certainly also the EW corrections have to be considered.

It is well known for many years, that the leading EW corrections above the EW scale $\mathcal{O}(M_W)$ are given by single as well as double logarithms (Sudakov logarithms [43]). As we already shortly mentioned in Sec. 3.3, these logarithms occur because the real radiation of (truly) massive particles is never considered as part of the real corrections, while their counterpart in the virtual contribution can not be excluded. Depending on the squared ratio of the relevant energy scale Q to the EW scale M_W , the uncompensated logarithms of the virtual contribution increase with the energy, and for $Q = 1$ TeV their relative contribution to the LO is given by [82]

$$\frac{\alpha}{4\pi s_W^2} \log\left(\frac{Q^2}{M_W^2}\right) \simeq 1.3\%, \quad \frac{\alpha}{4\pi s_W^2} \log^2\left(\frac{Q^2}{M_W^2}\right) \simeq 6.6\%. \quad (5.2)$$

Depending on the process and the exact setup, based on these logarithms, EW corrections at LHC energies may therefore easily grow to some 10% in the high-energy region.

The EW corrections for on-shell W-pair production at the LHC were first considered in logarithmic approximation at NLO and NNLO in Refs. [83, 84], confirming the global statement about their size made in Eq. (5.2). Those predictions, however, are only valid in the *Sudakov regime* where the absolute values of the Mandelstam variables

$$\hat{s} = (p_1 + p_2)^2, \quad \hat{t} = (p_1 - k_1)^2, \quad \hat{u} = (p_1 - k_2)^2, \quad (5.3)$$

of the W bosons have to be much larger than the square of the W-boson mass M_W , where p_i denote the momenta of the initial-state quarks and k_i are the momenta of the W bosons. Therefore, the logarithmic approximation neither applies at low and intermediate energies, nor in the dominant kinematical domain of forward-produced W bosons at high energies, the *Regge limit*, where \hat{s} is large, but \hat{t} and \hat{u} are both of the order of M_W^2 . This shortcoming was overcome by the complete NLO EW calculations for the production of on-shell W pairs [85, 86]. These calculations included

the quark–antiquark- and photon–photon-induced channels, revealing large and non-uniform corrections to kinematical distributions that go beyond the qualitative level based on logarithmic approximations. In Ref. [86] special emphasis was put on the photon–photon- and the quark–photon-induced channels, which both turned out to be quite sizable at TeV scales. However, it should be noticed that the quark–photon-induced subprocess leads to an additional jet in the final state, which, compared to the effects of NLO QCD corrections exhibiting the same final state, strongly diminishes the importance of this channel. Moreover, precise predictions for channels including initial-state photons are presently limited by the large uncertainties in current photon distribution functions, especially at large momentum fractions of the photon ($\xi_\gamma > 0.1$), where the PDF uncertainties can be as large as 100% [55]. The photon-PDF is, however, subject to present investigations (e.g. Refs. [87,88]), such that this situation should certainly improve in the near future.

In order to further improve the accuracy of radiative EW corrections to W-boson pair production at the LHC all off-shell effects and decay correlations of the W bosons have to be fully taken into account. Only such a calculation allows to accurately address the additional EW corrections stemming from soft and/or collinear photon emission off the final-state leptons and reveal the importance of the aforementioned phase-space region below the W-pair threshold at $2M_W$ for LHC predictions.

In Ref. [12] the leptonic W decays have been fully taken into account in a calculation employing the so-called *double-pole approximation* (DPA), which is based on an expansion of the loop amplitudes about the poles of the W resonances and will be discussed in more detail below. For the lepton-induced process $e^+e^- \rightarrow W^+W^- \rightarrow 4$ fermions, this approximation has been shown to be very accurate for predictions that are dominated by two resonant W bosons, such as total cross sections or observables only depending on the angular components of the final-state leptons. To be more precise, the comparison of the full off-shell NLO corrections for $e^+e^- \rightarrow 4$ fermions [36,89] to results obtained in the DPA, as delivered by the Monte Carlo program RACOONWW [90–92], revealed an accuracy of the total cross section of $\sim 0.5\%$ ($\sim 2\%$) for leptonic centre-of-mass energies $\lesssim 500$ GeV ($\lesssim 2$ TeV).

The increasing deviation towards larger energies together with the fact that it is genuinely impossible at hadron colliders to fix the partonic c.m. energy to a specific value, makes a simple transfer of this estimation to the LHC ambiguous. On the one hand, for observables that are dominated by two resonant W bosons, we still expect good agreement, while especially for high scattering energies in the TeV range and in regions of phase space where diagrams without intermediate WW states become important, much larger deviations are possible.

To unambiguously quantify the effect of the EW corrections to non-doubly-resonant contributions at the LHC, we therefore require to refine the former calculation of Ref. [12] and include in addition also all corrections to the non-resonant contributions.

The calculation we present in this thesis, in particular, is the first that accounts for EW corrections at partonic c.m. energies around the Higgs mass $\sqrt{\hat{s}} \sim M_H < 2M_W$, which lies below the WW threshold at $2M_W$, where the DPA, by construction, is not

applicable. As mentioned above, this region is particularly interesting for precision studies of the Higgs boson via the decay channel $H \rightarrow WW^*$, to which direct W-pair production represents a very important irreducible background.

5.2. Outline of the Calculation

The LO partonic channels contributing to the W-pair production process of Eq. (5.1) are of the order $\mathcal{O}(\alpha^4)$ and read

$$\bar{q}q/q\bar{q}/\gamma\gamma \rightarrow \nu_\mu\mu^+e^-\bar{\nu}_e, \quad (5.4)$$

where the antiquark–quark ($\bar{q}q/q\bar{q}$) annihilation channel, to which we refer in following as $\bar{q}q$, comprises the five (massless) down-type ($q = d, s, b$) and up-type ($q = u, c$) quarks, while the massive top quarks are not considered as active quarks in the proton at LHC energies.

In Fig. 5.2 we show the complete set of tree-level diagrams for the $\bar{d}d$ initial state, while analogous diagrams exist for all other quarks, and Fig. 5.3 shows some representative diagrams of the $\gamma\gamma$ channel. As can be seen from the figures, both production modes include diagrams with two W-boson propagators that possibly become on-shell (first row in Figs. 5.2 and 5.3), but also singly- and non-resonant *background* graphs. The first diagram of Fig. 5.2 includes the trilinear gauge coupling between two W bosons and a Z boson/ γ in the lowest accessible order, which makes the W-pair production process particularly sensitive to the exact realization of EWSB in the SM. Additionally, new physics entering via the weak sector of the SM could result in deviations from the SM coupling strength of this vertex, and parametrized as aTGC, such deviations are heavily search for at the LHC.

We neglect the extremely small CKM mixing of the third generation with the first two generations, such that the massive top quark only appears as internal particle in $\bar{b}b$ -induced subprocesses. Consequently, due to the top mass, we require slightly adapted LO matrix elements for the $\bar{b}b$ -induced channels. Owing to the unitarity of the CKM matrix, in the squared amplitude for a particular partonic initial state ij also the dependence on the quark mixing of the first two generations drops out after summing over the possible intermediate quarks,

$$|\mathcal{M}_{ij}|^2 \propto \sum_k \mathbf{V}_{q_i q_k}^\dagger \mathbf{V}_{q_k q_j} = (\mathbf{V}^\dagger \mathbf{V})_{q_i q_j} = \delta_{ij}, \quad (5.5)$$

and, consequently, the calculation may be performed with the CKM matrix set to the unit matrix straight away. Since we treat all partons as being exactly massless, the partonic cross sections of the s- and c-quark induced processes are completely identical to the d- and u-quark initiated processes, respectively. For the LO calculation we therefore require the partonic matrix elements for the subprocesses,

$$\bar{u}u/\bar{d}d/\bar{b}b/\gamma\gamma \rightarrow \nu_\mu\mu^+e^-\bar{\nu}_e, \quad (5.6)$$

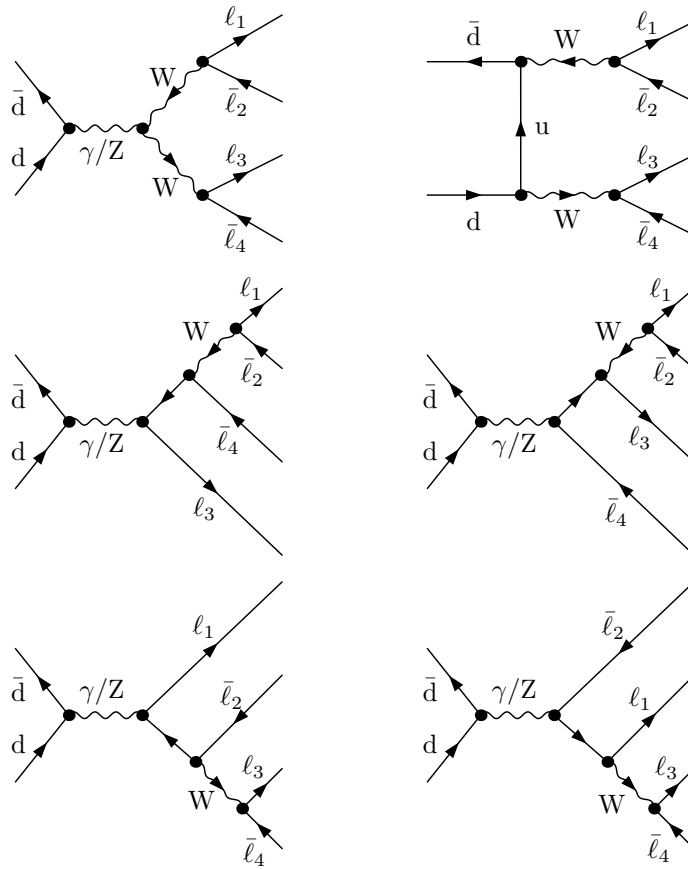


Figure 5.2.: Tree-level diagrams for the partonic (charged-current) process $\bar{d}d \rightarrow 4$ leptons.

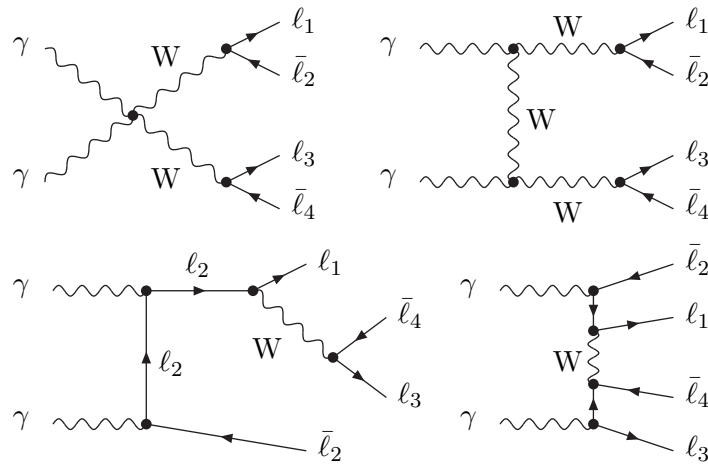


Figure 5.3.: A representative set of tree-level diagrams for the $\gamma\gamma$ induced process.

which easily follow from the LO matrix elements of the processes $e^+e^-/\gamma\gamma \rightarrow 4$ fermions that have been presented in the Weyl-van-der-Waerden spinor formalism [93] in Refs. [90] and [94], respectively. Applying the notation of Eq. (4.15), the hadronic cross section at LO finally follows upon convoluting the partonic LO cross sections $\hat{\sigma}_{ab}^{\text{LO}}$ with the respective PDFs and reads

$$\sigma_{\text{LO}} = f_\gamma f_\gamma \otimes \int_4 d\hat{\sigma}_{\gamma\gamma}^{\text{LO}} + \sum_{q,\bar{q}} f_{\bar{q}} f_q \otimes \int_4 d\hat{\sigma}_{\bar{q}q}^{\text{LO}} \Big|_{+(q\leftrightarrow\bar{q})}, \quad (5.7)$$

where the sum includes all five massless quark flavours. As indicated in the equation, in the following, only specific partonic contributions to the cross sections receive additional labels, while the two hadrons are implied to be two protons at the LHC.

As defined in Eq. (3.5) the NLO EW corrections, i.e. corrections including an additional order of α , require the calculation of the virtual part, including all one-loop diagrams, and a real part, composed of all diagrams with one additional external massless particle. For NLO corrections at hadron colliders, additionally, a finite factorization term has to be taken into account that eventually takes care of the remaining initial-state singularities, as discussed in detail in Sec. 4.1. Since the corrections to the clearly subdominant $\gamma\gamma$ induced LO channel have already been shown to be at the percent level in the accessible energy regime [94, 95], we see no reason for additionally including them in our NLO prediction.

The hadronic cross section of the NLO EW contribution for W -pair production is therefore given by

$$\begin{aligned} \Delta\sigma_{\text{NLOEW}} &= \sum_{\substack{q,\bar{q} \\ m_t=0}} f_{\bar{q}} f_q \otimes \left(\int_5 d\hat{\sigma}_{\bar{q}q}^{\text{real}} + \int_4 d\hat{\sigma}_{\bar{q}q}^{\text{virt}} + \int_0^1 dx \int_4 d\hat{\sigma}_{\bar{q}q}^{\text{fact}} \right) \Big|_{+(q\leftrightarrow\bar{q})} \\ &+ \sum_{\substack{q,\bar{q} \\ m_t=0}} f_q f_\gamma \otimes \left(\int_5 d\hat{\sigma}_{q\gamma}^{\text{real}} + \int_0^1 dx \int_4 d\hat{\sigma}_{q\gamma}^{\text{fact}} \right) \Big|_{+(q\leftrightarrow\gamma),(q\leftrightarrow\bar{q})}, \quad (5.8) \end{aligned}$$

comprising all corrections to the dominant $\bar{q}q$ -induced channels as well as additional real corrections with an (anti-)quark–photon-initial state, to which we refer in the following simply as $q\gamma$ -subprocess. As indicated, at the NLO, we completely neglect the effect of the top quark mass, which means that also the matrix elements with external bottom quarks internally include only massless up-type weak isospin partners and are, thus, identical to those with external down quarks. As will be discussed below, this approximation is well justified for the contributions with a $\bar{b}b$ initial state, while for the $b\gamma$ -induced channel the situation is more involved, and needs further clarification (see Sec. 5.2.4).

In the following we will separately discuss the individual contributions of Eq. (5.8) and, in particular, the cancellation of the individual IR singularities by the application of the dipole subtraction formalism of Sec. 4.2. Besides presenting the calculation of the full NLO EW corrections, in Sec. 5.2.3 we also briefly review the essential parts

of the calculation of the NLO EW corrections in the framework of the double-pole approximation (DPA), as presented in Ref. [12]. Note that this calculation is also based on full matrix elements for all tree-level contributions, such that differences to the full calculation are limited to the virtual contribution only. In Sec. 5.2.4 we finally shortly summarize the various checks that have been performed to ensure the correctness of the implementation.

5.2.1. Real Corrections and Factorization Terms

The real corrections comprise bremsstrahlung corrections to the $\bar{q}q$ -induced subprocesses, with one additional photon in the final state,

$$\bar{q}q \rightarrow \nu_\mu \mu^+ e^- \bar{\nu}_e + \gamma, \quad (5.9)$$

as well as the (anti-)quark-photon-induced contributions with an additional q/\bar{q} in the final state,

$$\begin{aligned} q\gamma/\gamma q &\rightarrow \nu_\mu \mu^+ e^- \bar{\nu}_e + q, \\ \bar{q}\gamma/\gamma \bar{q} &\rightarrow \nu_\mu \mu^+ e^- \bar{\nu}_e + \bar{q}. \end{aligned} \quad (5.10)$$

Considering the definitions of Eqs. (3.3), (3.6), and (3.37), we can divide the ab -induced partonic real-emission cross section into a finite and a singular term,

$$\int_5 d\hat{\sigma}_{ab}^{\text{real}} = \int_5 d\hat{\sigma}_{ab}^{\text{real,fin}} + \int_5 d\hat{\sigma}_{ab}^{\text{real,sing}}, \quad (5.11)$$

where the singular cross section corresponds to the situation in which the emitted particle becomes soft and/or collinear to another external particle. In the dipole subtraction formalism that has been discussed in detail in Sec. 4.2, the singular cross section is given as

$$\int_5 d\hat{\sigma}_{ab}^{\text{real,sing}} = \int_5 d\Phi_5 |\mathcal{M}_{\text{sub}}(\Phi_5)|^2, \quad (5.12)$$

with the subtraction functions $|\mathcal{M}_{\text{sub}}|^2$ that are defined for the considered initial states ($ab = \bar{q}q/q\gamma$) in Eqs. (4.17), (4.61), and (4.75). The factorization terms of Eq. (5.8) consist of two contributions for every partonic channel ab ,

$$d\hat{\sigma}_{ab}^{\text{fact}}(\mu_F) = d\hat{\sigma}_{ab}^{\text{fact},a}(\mu_F) + d\hat{\sigma}_{ab}^{\text{fact},b}(\mu_F), \quad (5.13)$$

which correspond to the redefinition of the associated initial-state distribution. Since the factorization contribution is the only partonic contribution of the cross section explicitly depending on an arbitrary scale, this dependence on μ_F is emphasized explicitly.

Real Photon Radiation

The diagrams contributing to the real photon radiation process of Eq. (5.9) are obtained by attaching a final-state photon to every charged particle of all diagrams of the LO

$\bar{q}q$ induced process. Consequently, in the phase-space integration of the real matrix elements we have to take care of initial- and final-state IR singularities. Applying the dipole subtraction formalism, all singularities can be isolated by means of a subtraction function and the numerical phase-space integration over the finite part of the real cross section,

$$\int_5 d\hat{\sigma}_{\bar{q}q}^{\text{real,fin}} = \int_{+1} d\Phi_5 \left[\left| \mathcal{M}_{\bar{q}q \rightarrow \nu\mu\mu^+e^-\bar{\nu}_e\gamma} \right|^2 \Theta_{\text{cut}}(\Phi_5) - \sum_{\substack{i,j=1 \\ i \neq j}}^6 |\mathcal{M}_{\text{sub},ij}|^2 \Theta_{\text{cut}}(\tilde{\Phi}_{ij}(x,z)) \right], \quad (5.14)$$

can safely be performed. As in Eq. (4.48), Θ_{cut} denotes the application of phase-space cuts that depend on the particular real phase-space point (Φ_5) and its actual mapping onto the LO phase space ($\tilde{\Phi}_{ij}(x,z)$), respectively. The definitions of the individual contributions $\mathcal{M}_{\text{sub},ij}$, as well as the mappings of real momenta that are necessary for the evaluation of the subtraction part and the phase-space cuts for all emitter-spectator pairs are listed in Sec. 4.2.1.

The integrated counterpart of the subtraction function, where (parts of) the one-particle phase space containing the IR singularities have been integrated out analytically, can schematically be written as

$$\int_5 d\hat{\sigma}_{\bar{q}q}^{\text{real,sing}} = \int_{\bar{4}} d\sigma_{\bar{q}q}^{\text{real,endpoint}} + \int_{(0,0)}^{(1,1)} d(x,z) \int_{\bar{4}(x,z)} d\hat{\sigma}_{\bar{q}q}^{\text{real,conv}}. \quad (5.15)$$

While the *endpoint part* $d\hat{\sigma}_{\bar{q}q}^{\text{real,endpoint}}$ includes all real-emission IR singularities with 4-particle kinematics ($\tilde{\Phi}_{\text{LO}}$), in the *convolution part* the LO phase space can not be fully factorized and the integration over x and/or z still has to be performed numerically. To be more precise, the endpoint part reads

$$d\hat{\sigma}_{\bar{q}q}^{\text{real,endpoint}} = -\frac{\alpha}{2\pi} \sum_{\substack{i,j=1 \\ i \neq j}}^6 (-1)^{i+j} Q_i Q_j G_{ij}^{(\text{sub})}(s) \cdot d\hat{\sigma}_{\bar{q}q}^{\text{LO}}, \quad (5.16)$$

with the functions $G_{ij}^{(\text{sub})}$ for the emitter-spectator-pairs ij defined in the Eqs. (4.34), (4.43), (4.52), and (4.55), respectively. By construction, this contribution shows exactly the same IR singular behaviour as the virtual corrections, such that their sum results in an IR finite expression (see Sec. 5.2.2).

Also the convolution part in Eq. (5.15) still contains IR singular contributions, which belong to the integrated subtraction functions of an initial-state emitter $\mathcal{G}_{ab}^{(\text{sub})}$ and $\mathcal{G}_{ai}^{(\text{sub})}$ that are defined in Eqs. (4.33) and (4.42), respectively. Finally, these singularities are compensated due to the inclusion of the factorization term $d\hat{\sigma}_{\bar{q}q}^{\text{fact}}$. Exemplary, we give the factorization contribution of the u quark for the specific initial-state $\bar{u}u$ that,

according to the PDF redefinition of Eq. (4.10), reads

$$\begin{aligned}
& f_{\bar{u}|H_1} f_{u|H_2} \otimes \int_0^1 dx \int_4 d\hat{\sigma}_{\bar{u}u}^{\text{fact},u}(\mu_F) \\
&= \frac{\alpha Q_u^2}{2\pi} \int_0^1 d\xi_{\bar{u}} f_{\bar{u}|H_1}(\xi_{\bar{u}}, \mu_F) \int_0^1 d\xi_u \int_{\xi_u}^1 \frac{dz}{z} f_{u|H_2}\left(\frac{\xi_u}{z}, \mu_F\right) \\
&\quad \times \left[\ln\left(\frac{m_u^2}{\mu_F^2}\right) \left[\mathcal{P}_{qq}^{\text{QED}}(z) \right]_+ - \left[\mathcal{P}_{qq}^{\text{QED}}(z) (2 \ln(1-z) + 1) \right]_+ + \mathcal{C}_{qq}^{\text{F.S.}}(z) \right] \\
&\quad \times \int_4 d\hat{\sigma}_{\bar{u}u}^{\text{LO}}(\xi_{\bar{u}}, \xi_u), \tag{5.17}
\end{aligned}$$

while the contributions for the \bar{u} quark, as well as the contributions for all other flavours, follow analogously. Note that for all $\bar{q}q$ -induced processes only the (flavour-diagonal) quark-to-quark splitting function $\mathcal{P}_{qq}^{\text{QED}}$, defined in Eq. (4.8), is considered here, while the factorization term belonging to the photon-to-quark splitting $\mathcal{P}_{q\gamma}^{\text{QED}}$ of Eq. (4.10) will be treated along with the $q\gamma$ -induced processes in the next section. Additionally, we want to point out that since $\int_0^1 dx \int_x^1 \frac{dy}{y} f(x, y) = \int_0^1 dx \int_0^1 dz f(x, z)$ for any test function f , the integration over the z -variable in Eq. (5.17) and the integration over x in Eqs. (4.32) and (4.40) are indeed identical such that the dependence on the regulator mass m_u in the initial state exactly cancels.

The z -integration in Eq. (5.15), finally, gives rise to additional finite contributions that are, however, logarithmically enhanced by the mass of the final-state emitter m_i over some hard scale Q , as can be explicitly read off Eqs. (4.53) and (4.59). As discussed in detail in Sec. 4.2.1, the additional numerical integration over z has to be performed only for final-state leptons that can be fully isolated from collinear photons, i.e. if the radiation is treated collinear unsafe. In our calculation this will be only relevant for the final-state muon, while electrons and collinear photons are always recombined. This is necessary for a realistic treatment, since both, electrons and photons, are detected as showers in the electromagnetic calorimeter, while the muon detection is realized in a geometrically separated part of the detector, the muon chamber, which, thus, allows for a separate detection even in the collinear region. The difference between treating the radiation off final-state muons collinearly unsafe or collinearly safe will be discussed in Sec. 5.3.6.

Photon Induced Processes

In Fig. 5.4 we show two representative diagrams contributing to the $q\gamma$ -induced process, which, however, already include all possible types of splittings that give rise to IR singularities in the real phase-space integration. In order to obtain an additional final-state quark, either a $\gamma \rightarrow q\bar{q}^*$ or a $q \rightarrow q\gamma^*$ splitting has to take place in the initial state, while the particles indicated with the asterisks connect to all possible LO diagrams showing the respective particle in the initial state.

The finite part of the real $q\gamma$ -induced cross section could in principle be defined in the same manner as for the $\bar{q}q$ process in Eq. (5.14). The subtraction terms and the

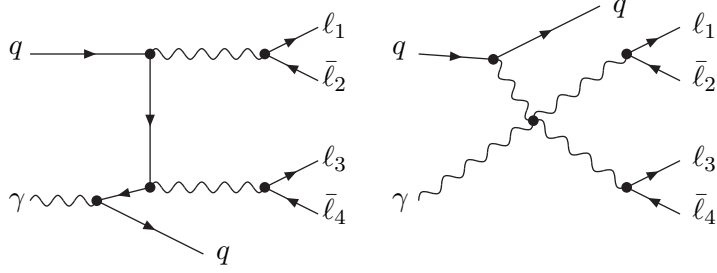


Figure 5.4.: Two representative diagrams for the partonic $q\gamma$ -induced subprocess.

necessary mapping of the momenta, as well as the associated integrated counterparts, have already been worked out in Sec. 4.2.2. As pointed out there, in the case of the $q \rightarrow q\gamma^*$ splitting, the subtraction function has to be defined upon the spin-correlated squared Born amplitudes $\mathcal{B}_{\text{LO}}^{2\mu\nu}$ for the underlying $\gamma\gamma$ -induced process.

However, as discussed e.g. in Ref. [12], the singularities related to this splitting can also be tackled by applying a so-called *effective collinear factor* (ECF). In this approach, the entire real part of the $q\gamma$ -induced cross section, including the subtraction terms related to the $\gamma \rightarrow q\bar{q}^*$ splittings, is multiplied by a factor that restores the correct leading quark-mass dependence in the collinear region of the $q \rightarrow q\gamma^*$ splitting, while for the remaining phase space it reduces to a factor of one up to mass-suppressed, and therefore negligible, terms. Since no spin-correlated amplitudes have to be additionally calculated when applying the ECF, we decided to implement this approach in our calculation.

By taking the ratio of Eq. (4.73) to its massless version we obtain a function that shows the desired kinematical dependence over the real phase space. In the partonic c.m. frame the ECF explicitly reads [12]

$$f_{\text{ECF}}(E_q, m_q, x, \theta) = \frac{\sin^2 \frac{\theta}{2}}{\left(\sin^2 \frac{\theta}{2} + \frac{m_q^2 x^2}{4E_q^2(1-x)^2}\right)^2} \left\{ \sin^2 \frac{\theta}{2} + \frac{\frac{m_q^2 x^4}{4E_q^2(1-x)^2}}{1 + (1-x)^2} \right\}, \quad (5.18)$$

where E_q is the energy of the incoming quark of mass m_q , $x = k_\gamma^0/E_q$ denotes the momentum fraction of the incoming quark that is passed to the photon taking part in the hard scattering reaction, and θ is the angle between the incoming and the outgoing quark. The mass m_q acts as regulator mass for the collinear singularity and is supposed to be much smaller than E_q .

In contrast to an approach which exclusively applies the subtraction method, now, due to $f_{\text{ECF}}(m_q)$, the finite part of the real cross section explicitly depends on the

regulator mass m_q ,

$$\int_5 d\hat{\sigma}_{q\gamma}^{\text{real,fin}}(m_q) = \int_{+1} d\Phi_5 f_{\text{ECF}}(m_q) \times \left[\left| \mathcal{M}_{q\gamma \rightarrow \nu_\mu \mu^+ e^- \bar{\nu}_e q} \right|^2 \Theta_{\text{cut}}(\Phi_5) - \left| \mathcal{M}_{\text{sub},\gamma \rightarrow q\bar{q}^*} \right|^2 \Theta_{\text{cut}}(\tilde{\Phi}_{\text{LO}}) \right], \quad (5.19)$$

while the subtraction function $\mathcal{M}_{\text{sub},\gamma \rightarrow q\bar{q}^*}$ ($\mathcal{M}_{\text{sub},\gamma b}$ in Eq.(4.61)), taking care of the $\gamma \rightarrow q\bar{q}^*$ splitting, is regulator independent. For this contribution, the regulator dependence is fully shifted to the integrated counterpart, Eq.(4.65), that only comprises a mass singular convolution term. Similar to the procedure for the $\bar{q}q$ -induced subprocesses, by including the appropriate photon-factorization term, the regulator dependence of this part eventually exactly cancels,

$$\int_0^1 \left[\int d\hat{\sigma}_{q\gamma(\gamma \rightarrow q\bar{q}^*)}^{\text{real,conv}} + \int d\hat{\sigma}_{q\gamma}^{\text{fact},\gamma} \right] \neq \mathcal{F}(m_q), \quad (5.20)$$

which we here symbolically write as not being a function \mathcal{F} of m_q .

Since the factorization term corresponding to the $q \rightarrow q\gamma^*$ splitting, $\hat{\sigma}_{u\gamma}^{\text{fact},u}$, by construction shows exactly the same dependence on the regulator mass m_q as the finite real part (Eq.(5.19)), the entire $q\gamma$ -induced contribution to the NLO cross section will not exhibit any regulator dependence anymore,

$$\begin{aligned} \int_5 d\hat{\sigma}_{q\gamma}^{\text{real}} + \int_0^1 dx \int_4 d\hat{\sigma}_{q\gamma}^{\text{fact}} = & \quad (5.21) \\ \underbrace{\int_5 d\hat{\sigma}_{q\gamma}^{\text{real,fin}}}_{=\mathcal{F}(m_q)[\text{Eq. (5.19)}]} + \underbrace{\int_0^1 \left[\int d\hat{\sigma}_{q\gamma(\gamma \rightarrow q\bar{q}^*)}^{\text{real,conv}} + \int d\hat{\sigma}_{q\gamma}^{\text{fact},\gamma} \right]}_{\neq \mathcal{F}(m_q)[\text{Eq. (5.20)}]} + \underbrace{\int_0^1 \int d\hat{\sigma}_{q\gamma}^{\text{fact},q}}_{=\mathcal{F}(m_q)} \neq \mathcal{F}(m_q). \end{aligned}$$

For completeness, we list the two factorization contributions of Eq.(5.21) for the specific initial-state $u\gamma$,

$$\begin{aligned} f_{u|H_1} f_{\gamma|H_2} \otimes \int_0^1 dx \int_4 d\hat{\sigma}_{u\gamma}^{\text{fact},\gamma}(\mu_F) & \\ = \frac{3\alpha Q_u^2}{2\pi} \int_0^1 d\xi_u f_{u|H_1}(\xi_u, \mu_F) \int_0^1 d\xi_\gamma \int_{\xi_\gamma}^1 \frac{dz}{z} f_{\gamma|H_2}\left(\frac{\xi_\gamma}{z}, \mu_F\right) & \\ \times \left[\ln\left(\frac{m_q^2}{\mu_F^2}\right) \mathcal{P}_{q\gamma}^{\text{QED}}(z) + \mathcal{C}_{q\gamma}^{\text{F.S.}}(z) \right] & \\ \times \int_4 d\hat{\sigma}_{u\bar{u}}^{\text{LO}}(\xi_u, \xi_\gamma), & \quad (5.22) \end{aligned}$$

for the factorization of the photon, corresponding to the redefinition of the quark PDF

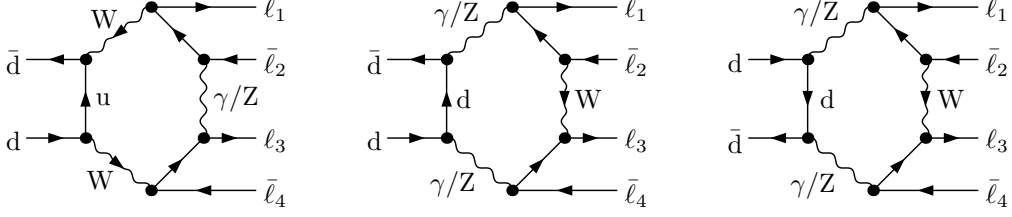


Figure 5.5.: 10 Hexagon diagrams for the partonic process $\bar{d}d \rightarrow 4\text{leptons}$. The remaining 30 hexagon diagrams are obtained by reversing the fermion flow in one or both of the fermion lines of the outgoing fermions and by exchanging $\ell_1 \leftrightarrow \bar{\ell}_2$ and/or $\ell_3 \leftrightarrow \bar{\ell}_4$.

(Eq. (4.10)) and

$$\begin{aligned}
& f_{u|H_1} f_{\gamma|H_2} \otimes \int_0^1 dx \int_4 d\hat{\sigma}_{u\gamma}^{\text{fact},u}(\mu_F) \\
&= \frac{\alpha Q_u^2}{2\pi} \int_0^1 d\xi_\gamma f_{\gamma|H_2}(\xi_\gamma, \mu_F) \int_0^1 d\xi_u \int_{\xi_u}^1 \frac{dz}{z} f_{u|H_1}\left(\frac{\xi_u}{z}, \mu_F\right) \\
&\quad \times \left[\ln\left(\frac{m_q^2}{\mu_F^2}\right) \mathcal{P}_{\gamma q}^{\text{QED}}(z) + \mathcal{P}_{\gamma q}^{\text{QED}}(2 \ln z + 1) + \mathcal{C}_{\gamma q}^{\text{F.S.}}(z) \right] \\
&\quad \times \int_4 d\hat{\sigma}_{\gamma\gamma}^{\text{LO}}(\xi_u, \xi_\gamma). \tag{5.23}
\end{aligned}$$

for the factorization of the quark, corresponding to the redefinition of the photon PDF in Eq. (4.11). For the other quarks and the reversed partonic channel evidently equivalent contributions have to be taken into account to eventually obtain the complete cancellation of the regulator dependence.

5.2.2. Full Virtual Corrections

The calculation of the virtual EW corrections to the full $\bar{q}q \rightarrow \nu_\mu \mu^+ e^- \bar{\nu}_e$ process requires the evaluation of $\mathcal{O}(10^3)$ different one-loop diagrams per $\bar{q}q$ channel, which comprise self-energy (2-point), vertex (3-point), box (4-point), pentagon (5-point), and hexagon (6-point) diagrams. In all these loop diagrams, up to three loop propagators may belong to one of the massive gauge bosons W^\pm or Z , while, as pointed out before, all fermions, including the top-quark, are treated massless at NLO. With six loop propagators, the hexagon diagrams shown in Fig. 5.5 exhibit the most complicated topology.

The calculation of the one-loop contributions proceeds along the same lines as for the related e^+e^- -induced process, which has been discussed in great detail in Ref. [36]. In the following, we therefore only sketch the calculation of the one-loop contributions, and refer to Ref. [36] for further details.

For the four-particle final-state, we assign the external momenta q_i and p_j in the following way

$$\bar{q}(q_1) q(q_2) \rightarrow \nu_\mu(p_1) \mu^+(p_2) e^-(p_3) \bar{\nu}_e(p_4), \quad (5.24)$$

and further define the kinematic invariants,

$$\hat{s} = (q_1 + q_2)^2, \quad s_{jk} = (p_j + p_k)^2, \quad t_{ij} = (q_i - p_j)^2, \quad \begin{matrix} i = 1, 2, \\ j, k = 1, \dots, 4. \end{matrix} \quad (5.25)$$

The amplitudes for all diagrams have been generated with FEYNARTS [96] and further algebraically reduced with in-house MATHEMATICA routines. The final result for the one-loop matrix element is most conveniently expressed in terms of form factors F_n^σ and so-called *standard matrix elements* (SME) $\hat{\mathcal{M}}_n^\sigma$, only depending on the spin structure (σ) and the momenta of the external particles [36],

$$\mathcal{M}_{1\text{loop}}^\sigma = \sum_{n=1}^{10} F_n^\sigma(\{\hat{s}, s_{jk}, t_{ij}\}) \hat{\mathcal{M}}_n^\sigma(q_1, q_2, p_1, p_2, p_3, p_4). \quad (5.26)$$

Due to the chiral coupling structure of the W bosons, it turns out that only two spin combinations of the external fermions yield a non-vanishing result for the one-loop amplitude, which we label with $\sigma = \pm$. The 20 possible SMEs are explicitly given in Eq. (3.48) of Ref. [36], while for the form factors F_n no closed form exists. They are composed of the N -point tensor integrals T^N , which require a numerical evaluation for every phase-space point, and the respective counterterms, needed to cancel the occurring UV divergences.

As discussed in Sec. 4.3, the numerical evaluation of N -point tensor integrals requires a very stable and efficient reduction algorithm to obtain sufficient accuracy over the entire phase space. For our calculation we applied the Denner-Dittmaier reduction-algorithm, via choosing the DD branch in the one-loop library COLLIER [59]. This one-loop library supports complex masses for all unstable particles, which is of utter importance for a consistent application of the complex-mass scheme (see Sec. 3.2.2). After the tensor reduction, the finite, UV, and IR-divergent parts of the loop-integration are separately calculated, which allows for the cancellation of the UV divergence via the counterterm approach directly at the amplitude level. The required counterterms in the complex-mass scheme are explicitly derived in Sec. 4 of Ref. [36].

The remaining IR-singularities, which in our calculation are regularized in mass regularization, eventually cancel after including the endpoint part of the real correction, $d\hat{\sigma}_{\bar{q}q}^{\text{real, endp}}$ (Eq. (5.16)),

$$\int_4 d\hat{\sigma}_{\bar{q}q}^{\text{virt, fin}} = \int_4 d\hat{\sigma}_{\bar{q}q}^{\text{virt}} + \int_4 d\hat{\sigma}_{\bar{q}q}^{\text{real, endp}}, \quad (5.27)$$

thus defining the finite part of the virtual corrections.

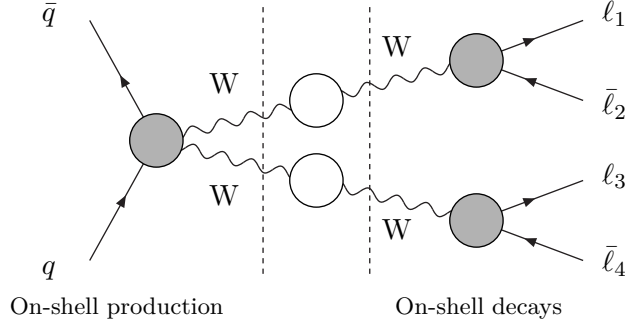


Figure 5.6.: Generic diagram for virtual factorizable corrections to $\bar{q}q \rightarrow WW \rightarrow 4\ell$ appearing in DPA, where the blobs stand for tree-level or one-loop insertions.

5.2.3. Virtual Corrections in the Double-Pole Approximation

In this section we briefly review the application of the DPA for the calculation of the virtual corrections for W -pair production, which has been presented in Ref. [12], and discuss the most important differences to the calculation employing full virtual corrections. For a general introduction to pole approximations or more details on the DPA for W -pair production in particular, we refer the interested reader to Refs. [12, 83, 90, 95, 97–99].

Generally, for W -pair production in the DPA, one only considers diagrams with two resonant W bosons. However, following the approach of Ref. [92] we can consistently restrict the application of the DPA to the virtual part only and employ full matrix elements for all tree-level contributions. To be more precise, the doubly-resonant loop contributions can be classified into two gauge-invariant categories, known as *factorizable* and *non-factorizable* corrections.

The former comprise all corrections that can be attributed either to the production or to the decays of the resonant W bosons, as depicted in the corresponding generic diagram of Fig. 5.6, while the latter includes all diagrams connecting these two parts. The calculation of the factorizable corrections in principle proceeds along the same lines as the calculation of the full virtual corrections, by simply restricting Eq. (5.26) to include only the aforementioned corrections to either the production or the decay of two resonant W bosons. The factorizable corrections in the DPA only comprise 14 SMEs and explicitly read [12, 91]

$$\mathcal{M}_{1\text{loop}}^{\sigma\text{fact,DPA}} = \sum_{n=1}^7 F_n^\sigma(\hat{s}, \hat{r}) \mathcal{M}_n^\sigma(q_1, q_2, \hat{k}_+, \hat{k}_-, k_+^2, k_-^2). \quad (5.28)$$

Here we denote the momenta of the two resonant W bosons by

$$k_+ = p_1 + p_2, \quad k_- = p_3 + p_4, \quad (5.29)$$

while \hat{k}_+ and \hat{k}_- are their on-shell projections, fulfilling $\hat{k}_+^2 = \hat{k}_-^2 = M_W^2$. In the on-shell projection, which is mandatory to maintain gauge invariance, each phase-space

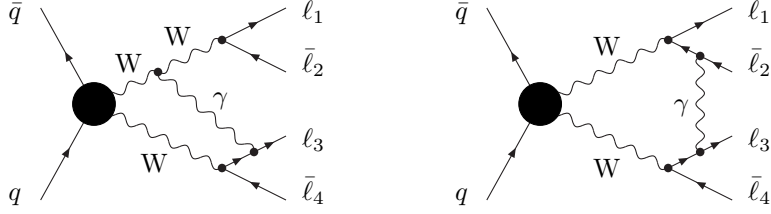


Figure 5.7.: Typical diagrams contributing to the virtual non-factorizable corrections to $\bar{q}q \rightarrow WW \rightarrow 4\text{leptons}$ appearing in DPA, where the blobs stand for any tree-level subdiagram.

point is identified with a phase-space point with on-shell W bosons, such that for each component μ the difference $|k_{\pm}^{\mu} - \hat{k}_{\pm}^{\mu}|^2$ is of the order $\mathcal{O}(k_{\pm}^2 - M_W^2)$. In the actual definition of such a projection some ambiguities remain, but all these variants only differ by effects beyond the DPA accuracy. We use the definition applied in Ref. [91] (see App. A therein), where in Eq. (3.1) also the explicit form of the 14 SMEs is given. In the DPA the form factors of Eq.(5.28) now just include $2 \rightarrow 2$ and $1 \rightarrow 2$ loop contributions and therefore only depend on two invariants, which we choose as

$$\hat{s} = (q_1 + q_2)^2 = (\hat{k}_+ + \hat{k}_-)^2, \quad \hat{r} = (q_1 - \hat{k}_+)^2 = (q_2 - \hat{k}_-)^2, \quad (5.30)$$

where \hat{s} is defined identically as in Eq.(5.25). Since the considered loop corrections do not involve unstable-particle effects, the loop-integration can well be performed with real masses and the less intricate OS-renormalization (see Sec.3.2.1) can be applied to define the counterterms to cancel the occurring UV divergences.

Owing to the fact that the exchange of a massive particle between the various production and decay subprocesses would shift at least one of the W bosons off its mass shell, the non-factorizable corrections comprise only contributions where a soft photon is exchanged, as illustrated in Fig.5.7. Note that here the terminology “non-factorizable” refers to the non-trivial off-shell behaviour of the correction, which is not a simple product of resonant propagators, and *not* to the factorization of the result. Indeed, the non-factorizable corrections factorize into a single correction factor times the lowest-order amplitude, such that the virtual corrections in DPA read

$$\int_4 d\hat{\sigma}_{\bar{q}q}^{\text{virt,DPA}} = \int_4 d\Phi_4 \left\{ 2 \text{Re} \left[\mathcal{M}_{1\text{loop}}^{\text{fact,DPA}} \left(\mathcal{M}_{\text{LO}}^{\text{DPA}} \right)^* \right] + \left| \mathcal{M}_{\text{LO}}^{\text{DPA}} \right|^2 \delta_{\text{non-fact}}^{\text{virt}} \right\}. \quad (5.31)$$

The LO DPA matrix element $\mathcal{M}_{\text{LO}}^{\text{DPA}}$ comprises only double-resonant contributions, like the ones shown in the first row of Fig.5.2, and the correction factor reads

$$\delta_{\text{non-fact}}^{\text{virt}} = \sum_{a=1,2} \sum_{b=3,4} (-1)^{a+b+1} \frac{\alpha Q_a Q_b}{\pi} \text{Re} \left(\Delta^{\text{virt}}(q_1, q_2; k_+, p_a; k_-, p_b) \right), \quad (5.32)$$

with Δ^{virt} defined as in Eq. (2.20) of Ref. [12]. In this final result for the non-factorizable correction factor all UV and IR-singularities cancel [91]¹, such that no renormalization procedure has to be applied additionally.

However, since the virtual corrections in DPA by definition do not comprise any corrections to the single-resonant diagrams (see Fig. 5.2), in particular, the IR divergent parts stemming from those contributions are not contained in Eq. (5.31). Therefore, in the form of Eq. (5.16), the endpoint contribution adds additional, uncompensated, IR singularities to the virtual contributions. However, the DPA version of the endpoint contribution,

$$d\hat{\sigma}_{\bar{q}q}^{\text{real, endp, DPA}} = -\frac{\alpha}{2\pi} \sum_{\substack{i,j=1 \\ i \neq j}}^6 (-1)^{i+j} Q_i Q_j G_{ij}^{(\text{sub})}(\hat{s}) \cdot d\hat{\sigma}_{\bar{q}q}^{\text{LO, DPA}}, \quad (5.33)$$

which is obtained from Eq. (5.16) by simply replacing all momenta in $G_{ij}^{(\text{sub})}$ with their respective on-shell expressions and considering the DPA LO cross section, $d\hat{\sigma}_{\bar{q}q}^{\text{LO, DPA}}$, does not include these additional contributions. Therefore, in the same manner as for the full virtual correction (Eq. (5.27)), the finite part of the virtual corrections in DPA is defined as

$$\int_4 d\hat{\sigma}_{\bar{q}q}^{\text{virt, DPA, fin}} = \int_4 d\hat{\sigma}_{\bar{q}q}^{\text{virt, DPA}} + \int_4 d\hat{\sigma}_{\bar{q}q}^{\text{real, endp, DPA}}. \quad (5.34)$$

As mentioned already several times, the DPA is by construction restricted to regions in phase space where two resonant W bosons dominate the cross section. In particular, this prevents its application in the region close to and below the W-pair threshold at $M_{4\ell} = 2M_W$. Following Ref. [12], we therefore apply an *improved Born approximation* in the region of phase space where $M_{4\ell} < 2M_W + 5 \text{ GeV}$. This approximation is based on the leading universal corrections of the coupling constant α and includes additional contributions stemming from photon exchange near the threshold, which have been worked out in Refs. [100, 101]. Note, however, that for all meaningful applications of the DPA, the influence of this phase-space region will be strongly suppressed due to the application of realistic phase-space cuts on the final state leptons.

In the following we briefly summarize the two most important differences between the DPA and the calculation solely based on the full four-fermion ($4f$) matrix elements, namely in complexity and validity.

- From the practical point of view, the DPA is simpler to work out, since the multiplicities of the underlying loop amplitudes for production and decays of resonant W bosons are much smaller. The complexity of the DPA loop calculations is the one of $2 \rightarrow 2$ production and $1 \rightarrow 2$ decay processes, which comprises about $\mathcal{O}(10^2)$ diagrams per partonic channel and mostly real particle masses, while the

¹ Δ^{virt} can be expressed in terms of the scalar coefficients B_0 , C_0 , D_0 , and E_0 , the only of which containing a UV divergent part (B_0) exclusively appears in the finite combination ($B_0(\dots) - B_0(\dots)$).

full $2 \rightarrow 4$ particle loop calculation involves $\mathcal{O}(10^3)$ diagrams up to hexagon topology with complex internal masses.

As a result of this difference and due to the possibility of an efficient numerical expansion of $2 \rightarrow 2$ loop amplitudes into tree-level-like form factors [90,95], the numerical evaluation of the DPA can become almost comparable in speed to a tree-level calculation, while the full $4f$ calculation is CPU intensive.

- The strength of the full off-shell calculation rests in its NLO accuracy everywhere in phase space, i.e. the intrinsic perturbative uncertainty Δ_{4f} of this approach is generically given by the size of the higher-order corrections that are not yet calculated. For the purely EW corrections, we thus expect $\Delta_{4f} \sim \delta_{\text{EW}}^2$ with the relative NLO EW correction factor

$$\delta_{\text{EW}} = \frac{\Delta\sigma_{\text{NLOEW}}}{\sigma_{\text{LO}}}. \quad (5.35)$$

As just pointed out, the validity of the DPA, is restricted to regions in phase space where the double resonance of the W-boson pair dominates the cross section. Taken literally, this restricts the DPA to four-lepton final states with invariant masses $M_{4\ell} > 2M_W + n\Gamma_W$ and $|M_{l_i\bar{\nu}_i} - M_W| \lesssim n\Gamma_W$, where $n \sim 2-3$ is some small number and $l_i\bar{\nu}_i$ generically stands for the two lepton–neutrino pairs from the W-boson decays. In practice this means that the DPA is applicable if the contributions from regions below the W-pair threshold and also the off-shell regions are sufficiently suppressed.

The theoretical uncertainty Δ_{DPA} of the DPA is, thus, not only based on the typical size of missing higher-order corrections, but also influenced by the intrinsic uncertainty of the pole expansion. Assuming that all LO contributions are based on full matrix elements and that the relative correction in DPA, $\delta_{\text{EW}}^{\text{DPA}}$, is normalized to the full LO cross section σ_{LO} , i.e.

$$\sigma_{\text{NLOEW}}^{\text{DPA}} = \sigma_{\text{LO}} + \Delta\sigma_{\text{EW}}^{\text{DPA}} = \sigma_{\text{LO}} \left(1 + \delta_{\text{EW}}^{\text{DPA}} \right), \quad \delta_{\text{EW}}^{\text{DPA}} = \frac{\Delta\sigma_{\text{EW}}^{\text{DPA}}}{\sigma_{\text{LO}}}, \quad (5.36)$$

we estimate Δ_{DPA} to

$$\Delta_{\text{DPA}} \sim \max \left\{ \left(\delta_{\text{EW}}^{\text{DPA}} \right)^2, \underbrace{\frac{\alpha}{\pi} \frac{\Gamma_W}{M_W} \ln(\dots)}_{\lesssim 0.5\%}, \left| \delta_{\text{EW}}^{\text{DPA}} \right| \times \frac{|\sigma_{\text{LO}} - \sigma_{\text{LO}}^{\text{DPA}}|}{\sigma_{\text{LO}}^{\text{DPA}}} \right\}. \quad (5.37)$$

The first term on the right-hand side (r.h.s.) of Eq. (5.37) corresponds to the missing higher-order EW corrections, similar to the NLO limitation of Δ_{4f} . The second term indicates the size of the off-shell contributions to the EW corrections in regions where the DPA applies. This estimate is based on the typical size of the respective effects: the off-shell contributions amounting to a fraction $\sim \Gamma_W/M_W$,

and the EW corrections being of order $\sim \alpha/\pi$ times some moderate logarithmic factor (see also Refs. [12, 36, 89, 90]). The last term on the r.h.s. of Eq. (5.37) mimics the failure of the DPA upon blowing up the relative correction δ_{EW}^{DPA} by the factor $|\sigma_{LO} - \sigma_{LO}^{DPA}|/\sigma_{LO}^{DPA}$ that is deduced from the LO cross sections based on the full $4f$ or DPA matrix elements.² As we will discuss in Sec. 5.3.7, the last term in Δ_{DPA} is surprisingly large in some transverse-momentum distributions in the TeV range.

5.2.4. Independent Checks of the Calculation

In order to guarantee reliable and accurate results, in addition to the calculation presented in this thesis, within our collaboration a completely independent, and to some extent orthogonal, calculation of all contributions has been performed. We find mutual agreement of the squared amplitudes at individual phase-space points, and all cross sections agree within statistical uncertainties of the final Monte Carlo phase-space integration.

While the implementation presented in this thesis closely follows the diagrammatic approach of Refs. [36, 89], where NLO EW corrections to $e^+e^- \rightarrow 4$ fermions via W -boson pairs were calculated, and builds on Ref. [12] for the real corrections and the Monte Carlo integration, the second calculation is based on the program RECOLA [102] that provides the automated generation of NLO EW amplitudes. For the explicit evaluation of the one-loop tensor integrals, the two calculations employ the two different branches of the one-loop library COLLIER [59], DD and COLI.

For the treatment of the IR singularities, both implementations resort to the dipole subtraction approach that we discussed in detail in Sec. 4.2 employing mass regularization. Technically, the IR singularities can also be treated in dimensional regularization, and we have checked numerically that the sum of virtual and real corrections is, independently of the regularization scheme, infrared finite. As discussed above, the final result only depends on the factorization scale μ_F and, in the case of collinear unsafe photon radiation off final-state muons, on the physical muon mass m_μ . While our diagrammatic calculation employed the ECF of Eq. (5.18) to treat the $q \rightarrow q\gamma^*$ splitting (see Sec. 5.2.1), the second calculation used the dipole approach throughout. For the sum of the real contribution and the factorization term of the $q\gamma$ -induced process (Eq. (5.21)), both procedures yield identical results, which, thus, comprises a stringent check of both approaches.

The calculation based on RECOLA fully includes the top mass at the NLO, while our calculation approximates all NLO matrix elements with external bottom quarks by those with external down quarks. For the $\bar{q}q$ -induced channels we find the difference

²The last uncertainty factor in Eq. (5.37) can also be written as $\Delta\sigma_{EW}^{DPA}/\sigma_{LO}^{DPA} \times |\sigma_{LO} - \sigma_{LO}^{DPA}|/\sigma_{LO}$, where $\Delta\sigma_{EW}^{DPA}/\sigma_{LO}^{DPA}$ would then be interpreted as the intrinsic relative EW correction of the DPA and $|\sigma_{LO} - \sigma_{LO}^{DPA}|/\sigma_{LO}$ is the relative deviation of the DPA LO from the full $4f$ LO cross section. However, we chose the form of Eq. (5.37) to be compatible with the definition of δ_{EW}^{DPA} made in Ref. [12] and the earlier e^+e^- references such as Ref. [89].

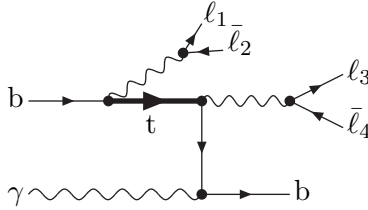


Figure 5.8.: Representative diagram for a $b\gamma$ induced subprocess, showing an intermediate massive top quark that leads to an on-shell resonance.

between these two approaches on the relative correction δ_{qq}^{NLO} to be below 0.02% in all three phenomenological setups (c.f. Secs. 5.3.1 and 5.3.2). Therefore, the approximation can safely be applied, without any notable loss in precision. Note, moreover, that the additional separate computation of the $\bar{b}b$ -induced matrix elements for all contributions unnecessarily prolongs the evaluation of the matrix element by roughly a factor of 1.5 compared to the entirely massless treatment, where the phase-space pointwise calculation of the partonic channels $\bar{u}u$ and $\bar{d}d$ is sufficient.

For the $b\gamma$ -induced subprocesses, however, the situation is very different, since these contributions are enhanced by the presence of top-quark resonances, as depicted in Fig. 5.8, which is simply a slightly distinct representation of the left diagram of Fig. 5.4. The approximation with massless top quarks obviously fails in this case, especially in our inclusive setup, where no jet veto is applied to the final state bottom quark. In this setup, the $b\gamma$ -contribution is of the same size as the genuine EW corrections. However, single top production is an entirely different process and can also experimentally be well separated from our signal process, such that we decided to additionally apply a b-jet veto, i.e. we identify $\delta_{q\gamma} \equiv \delta_{q\gamma}^{q \neq b}$.

To verify the correctness of the RECOLA result we additionally compared the massive matrix element for several phase-space points to a matrix elements generated with Madgraph [103] and found perfect agreement.

5.3. Phenomenological Results

In this section we present the results of our calculation for three phenomenologically relevant event-selection setups. Therefore, after listing the exact values of the input parameters we used and presenting our default setup in Sec. 5.3.1, we define the three event-selection setups in Sec. 5.3.2.

By means of integrated results and differential distributions the separate contributions to the cross section are presented in the Secs. 5.3.3–5.3.5. In Sec. 5.3.6 we discuss the difference between the two possible treatments of the photon radiation off muons, while in Sec. 5.3.7 we examine the quality of the DPA with respect to the full off-

shell calculation. Note that large parts of this section have recently been published in Ref. [11].

5.3.1. Input Parameters and Computational Setup

For our numerical studies we consider proton–proton collisions at the LHC at hadronic c.m. energies of $\sqrt{s_{pp}} = 8 \text{ TeV}$ and 13 TeV . We use the SM input parameters

$$\begin{aligned}
G_\mu &= 1.1663787 \times 10^{-5} \text{ GeV}^{-2}, & \alpha(0) &= 1/137.035999, \\
M_W^{\text{OS}} &= 80.385 \text{ GeV}, & \Gamma_W^{\text{OS}} &= 2.085 \text{ GeV}, \\
M_Z^{\text{OS}} &= 91.1876 \text{ GeV}, & \Gamma_Z^{\text{OS}} &= 2.4952 \text{ GeV}, \\
M_H &= 125.9 \text{ GeV}, & m_\mu &= 0.1057 \text{ GeV}, \\
m_t &= 173.07 \text{ GeV}, & \Gamma_t &= 2 \text{ GeV},
\end{aligned} \tag{5.38}$$

following Ref. [104]. The finite value of the top mass m_t is exclusively applied at the LO, and the muon mass m_μ only becomes relevant in the case of a collinear-unsafe treatment of photon emission off final-state muons. All the remaining fermions are considered as massless everywhere in the calculation. As discussed in Sec. 5.2, the CKM matrix is set to the unit matrix, without restricting the validity of our calculation.

Throughout, we apply the complex-mass scheme for the W and Z resonances, which also leads to a complex weak mixing angle θ_w and complex couplings, as discussed in Sec. 3.2.2. The complex vector-boson masses μ_V are given by

$$\mu_V^2 = M_V^2 - iM_V\Gamma_V, \quad V = W, Z, \tag{5.39}$$

with the real mass values M_V and constant vector-boson decay widths Γ_V . The gauge-boson mass and width values given in Eq. (5.38), however, correspond to the “on-shell” (OS) masses and widths, that have been measured at the former particle accelerators LEP and Tevatron using a running-width prescription. Consequently, we convert these OS values M_V^{OS} and Γ_V^{OS} ($V = W, Z$) to the “pole values” denoted by M_V and Γ_V according to [105],

$$M_V = M_V^{\text{OS}} / \sqrt{1 + (\Gamma_V^{\text{OS}}/M_V^{\text{OS}})^2}, \quad \Gamma_V = \Gamma_V^{\text{OS}} / \sqrt{1 + (\Gamma_V^{\text{OS}}/M_V^{\text{OS}})^2}, \tag{5.40}$$

which leads to

$$\begin{aligned}
M_W &= 80.357 \dots \text{ GeV}, & \Gamma_W &= 2.0842 \dots \text{ GeV}, \\
M_Z &= 91.153 \dots \text{ GeV}, & \Gamma_Z &= 2.4942 \dots \text{ GeV}.
\end{aligned} \tag{5.41}$$

Although the tiny difference in the phenomenological results between using M_V^{OS} and M_V would hardly be visible, for consistency we use the latter as input for our numerical results.

In the $\bar{q}q$ -induced contributions we determine all couplings in the G_μ scheme, where α is defined in terms of the input parameters given in Eqs. (5.38) and (5.41),

$$\alpha_{G_\mu} = \frac{\sqrt{2} G_\mu M_W^2}{\pi} \left(1 - \frac{M_W^2}{M_Z^2} \right). \tag{5.42}$$

This setting minimizes universal weak corrections beyond NLO in the high-energy tails of distributions where high-energy logarithms due to soft/collinear W/Z bosons dominate the EW corrections. However, we set $\alpha = \alpha(0)$ for the couplings of the incoming photons in the photon-induced ($q\gamma$ and $\gamma\gamma$) channels, since $\alpha(0)$ is the relevant electromagnetic coupling for real (external) photons. Therefore, the squared matrix elements for the $q\gamma \rightarrow 2l2\nu + q$ and $\gamma\gamma \rightarrow 2l2\nu$ subprocesses scale like $\alpha(0)\alpha_{G_\mu}^4$ and $\alpha(0)^2\alpha_{G_\mu}^2$, respectively.

For the calculation of the hadronic cross section, we use the $\mathcal{O}(\alpha)$ -corrected PDF set NNPDF2.3QED [55], which also includes a distribution function for the photon. Since the considered LO cross section and the EW corrections do not depend on the strong coupling, our result show no dependence on the renormalization scale μ_R and only a very weak dependence on the factorization scale μ_F . As has been explicitly shown in Ref. [12], the dependence basically vanishes when considering only the relative corrections such that we see no benefit in introducing a specific dynamical scale, but choose the fixed value

$$\mu_F = M_W. \quad (5.43)$$

Following the arguments of Ref. [106], we employ a DIS-like factorization scheme for the QED corrections, because EW corrections are not taken into account in the fit of the PDFs to data.

In subprocesses with a final-state quark or antiquark, a parton i is only considered as a jet, if its transverse momentum $p_{T,i}$ and its rapidity $|y_i|$ allow for a proper detection in experiment. For a parton i we require

$$p_{T,i} > p_{T,\text{jet}}^{\text{def}} = 25 \text{ GeV}, \quad |y_i| < |y_{\text{jet}}^{\text{def}}| = 5, \quad (5.44)$$

for being treated as a jet. If the parton does not meet these two requirements, it is treated as *invisible jet*, which means that no additional jet-related cuts are applied and its momentum contributes to the missing transverse momentum \vec{p}_T^{miss} . Note that our real matrix elements exhibit at most one final-state parton which either leads to a jet or remains undetected, such that no dedicated jet-algorithm has to be applied.

Similarly to the jets, final-state photons with rapidities outside the range accessible to the detector,

$$|y_\gamma| > 5, \quad (5.45)$$

are considered as *invisible photons*, and the corresponding momentum is part of the missing momentum.

As mentioned above, we provide two different setups concerning the treatment of nearly collinear photons: In the collinear-safe setup, nearly collinear photons are recombined with either of the two charged final-state leptons, whereas in the collinear-unsafe setup, we apply the photon recombination procedure only to final-state electrons while photons collinear to muons remain unrecombined. This recombination procedure mimics the experimental concept of “dressed leptons” used by ATLAS (see e.g. Ref. [107]), which avoids the experimental problem to separately resolve an electron and a nearly

collinear photon. As measure for the collinearity of photons and leptons, their distance R_{ij} in the rapidity–azimuthal-angle plane is used, where

$$R_{ij} = \sqrt{(y_i - y_j)^2 + \Delta\phi_{ij}^2}, \quad (5.46)$$

with $y_{i,j}$ denoting the rapidities of particle i and j and $\Delta\phi_{ij}$ their azimuthal angle difference, respectively. Whenever this separation is smaller than

$$R_{\gamma l}^{\text{recomb}} = 0.1, \quad (5.47)$$

we add the photon momentum to the respective lepton momentum and subsequently discard the photon from the event, while the momenta of all other particles in the event remain unaffected.

5.3.2. Event Selection

We compare results for three different event-selection setups: (i) defined by basic particle identification only (“inclusive setup”), (ii) designed by ATLAS for relatively enhancing the WW signal (“ATLAS WW setup”), and (iii) inspired by Higgs-boson analyses in the decay channel $H \rightarrow WW^*$ (“Higgs-background setup”), where direct W -pair production comprises an irreducible background. For the latter two setups we present results for fully integrated and differential cross sections, while for the inclusive setup only fully integrated numbers are given.

(i) Inclusive Setup

After a potential photon recombination we define an event for the process $pp \rightarrow \nu_\mu \mu^+ e^- \bar{\nu}_e + X$ by requiring the μ^+ and e^- to have transverse momenta

$$p_{T,l} > 20 \text{ GeV}, \quad (5.48)$$

in the central rapidity region of the detector,

$$|y_l| < 2.5. \quad (5.49)$$

For final states with an identified jet (cf. Eq. (5.44)) we demand this jet to be well separated from the lepton system, by rejecting any event with

$$R_{\text{jet},l} < 0.4. \quad (5.50)$$

In order to suppress overwhelmingly large QCD corrections from additional jet radiation, we employ a jet veto, i.e. we reject any event with

$$p_{T,\text{jet}} > 100 \text{ GeV}. \quad (5.51)$$

(ii) ATLAS WW Setup

Moreover, we consider an event selection that is inspired by the analyses of the 7 TeV dataset for $pp \rightarrow W^+W^- + X$ performed by the ATLAS collaboration [77]. In addition to the aforementioned lepton cuts we impose a stronger transverse-momentum cut on the hardest charged lepton (the leading lepton) and require the two charged leptons to be well separated from each other by imposing the cuts

$$p_{T,l}^{\text{leading}} > 25 \text{ GeV}, \quad R_{e-\mu^+} > 0.1, \quad M_{e-\mu^+} > 10 \text{ GeV}, \quad (5.52)$$

where $M_{e-\mu^+}$ denotes the invariant mass of the charged lepton system,

$$M_{e-\mu^+} = \sqrt{p_{e^-}^2 + p_{\mu^+}^2}. \quad (5.53)$$

For a cleaner signature we further demand a non-vanishing missing transverse momentum,

$$|\vec{p}_T^{\text{miss}}| > 25 \text{ GeV}, \quad (5.54)$$

and remind the reader that, according to the discussion in the previous section, undetected jets and photons do also contribute to this quantity. To further suppress the influence of QCD corrections, we veto all events with hard final-state jets obeying

$$p_{T,\text{jet}} > 25 \text{ GeV}. \quad (5.55)$$

Note that according to Eq. (5.44), all events with a detected jet are discarded due to this cut.

(iii) Higgs-Background Setup

Inspired by the recent analyses of the decay of the Higgs boson to WW^* independently performed by ATLAS [108] and CMS [109] we study the influence of EW corrections on the main irreducible background, namely $pp \rightarrow WW^* \rightarrow \nu_\mu \mu^+ e^- \bar{\nu}_e + X$, in a realistic cut scenario. Essentially following Ref. [108], we extend the ATLAS WW setup of Eqs. (5.52)–(5.55) by two additional cuts,

$$10 \text{ GeV} < M_{e-\mu^+} < 55 \text{ GeV}, \quad \Delta\phi_{e-\mu^+} < 1.8, \quad (5.56)$$

which are designed to favour the signal topology of the $H \rightarrow WW^*$ analysis and therefore significantly suppress direct WW^* production. Additionally, we adjust the threshold of the transverse-momentum cut to the value used in the experimental analysis,

$$|\vec{p}_T^{\text{miss}}| > 20 \text{ GeV}. \quad (5.57)$$

LHC		$\sigma_{\bar{q}q}^{\text{LO}}$ [fb]	$\delta_{\bar{q}q}^{\text{NLO}}$ [%]	$\delta_{q\gamma}^{q\neq b}$ [%]	$\delta_{\gamma\gamma}$ [%]	δ_{EW} [%]
Inclusive	8 TeV	238.65(3)	-3.28	0.44	0.84	-2.01
	13 TeV	390.59(3)	-3.41	0.49	0.73	-2.20
ATLAS WW	8 TeV	165.24(1)	-3.56	-0.26	1.01	-2.81
	13 TeV	271.63(1)	-3.71	-0.27	0.87	-3.11
Higgs bkg	8 TeV	31.59(2)	-2.52	-0.21	0.60	-2.13
	13 TeV	49.934(2)	-2.54	-0.22	0.52	-2.25

Table 5.1.: LO cross sections and relative EW corrections to $pp \rightarrow \nu_\mu\mu^+e^-\bar{\nu}_e + X$ at the LHC at 8 TeV and 13 TeV, in the inclusive setup (top), the ATLAS WW setup (middle), and the Higgs-background setup (bottom). The numbers in parentheses represent the Monte Carlo uncertainty on the last given digit.

5.3.3. Results on Integrated Cross Sections

In Tab. 5.1 we present the integrated cross section of the quark-initiated LO process, $\sigma_{\bar{q}q}^{\text{LO}}$, for $pp \rightarrow \nu_\mu\mu^+e^-\bar{\nu}_e + X$ at the LHC for the energies $\sqrt{s_{\text{pp}}} = 8$ TeV and $\sqrt{s_{\text{pp}}} = 13$ TeV within the three different setups defined in Sec. 5.3.2. The numbers include the five $\bar{q}q$ -initiated contributions induced by the light quarks. Due to the small bottom-quark PDFs, the $\bar{b}b$ channel comprises less than 2% of this LO cross section in all considered setups.

According to our definition of Eq. (5.8), the NLO corrections of $\mathcal{O}(\alpha)$ consist of virtual one-loop and photonic real-emission contributions to the $\bar{q}q$ -induced processes, as well as additional $q\gamma$ -initiated tree-level subprocesses. Note that the $b\gamma$ -contributions have been explicitly excluded from $q\gamma$ (see Sec. 5.2.4). Since the LO $\gamma\gamma$ -induced subprocess gives rise to a (sub-)percent correction to $\sigma_{\bar{q}q}^{\text{LO}}$, in the following we treat $\delta_{\gamma\gamma} = \sigma_{\gamma\gamma}^{\text{LO}}/\sigma_{\bar{q}q}^{\text{LO}}$ as part of the EW corrections δ_{EW} , which are, thus, given by

$$\delta_{\text{EW}} = \delta_{\bar{q}q}^{\text{NLO}} + \delta_{q\gamma}^{q\neq b} + \delta_{\gamma\gamma} \quad (5.58)$$

Similarly to the situation at LO, the corrections stemming from subprocesses with initial-state bottom-quark pairs account for less than 2% of the full NLO correction. As stated above, the effect of the finite top mass is therefore entirely negligible in this per mill correction. As default setup for the photonic real-emission contributions we choose the collinear-unsafe setup, as defined in Sec. 5.3.1. The difference to the collinear-safe setup is discussed in detail in Sec. 5.3.6 below.

The omission of virtual and photonic real-emission corrections of $\mathcal{O}(\alpha)$ to the $\gamma\gamma$ -induced contributions is justified by their small size already at LO. In Tab. 5.1, besides

the LO cross sections, we list the relative contributions of the different types of corrections normalized to $\sigma_{\bar{q}q}^{\text{LO}}$. The generally negative $\mathcal{O}(\alpha)$ corrections ($\delta_{\bar{q}q}^{\text{NLO}}$ and $\delta_{q\gamma}$) are somewhat reduced by the positive LO $\gamma\gamma$ correction, so that their sum (δ_{EW}) leads to a small negative correction of roughly $-(2-3)\%$ on the integrated cross section for all investigated setups. However, as is already well known from previous studies of W-boson pair production at hadron colliders [12, 83–86], the EW corrections become very important in differential distributions where they lead to significant distortions.

5.3.4. Differential Cross Sections in the ATLAS WW Setup

In this section we inspect some important differential cross sections evaluated in the ATLAS WW setup for the collinear-unsafe photon scenario. Here and in the following sections, we show, for an LHC energy of $\sqrt{s_{\text{pp}}} = 13$ TeV, absolute predictions for $d\sigma/d\mathcal{O}$ as histograms binned in the observable \mathcal{O} in the upper panel, followed by the relative corrections of type i ,

$$\delta_i(\mathcal{O}) = \frac{d\sigma^i}{d\mathcal{O}} / \frac{d\sigma_{\bar{q}q}^{\text{LO}}}{d\mathcal{O}}, \quad (5.59)$$

directly below.

In Fig. 5.9, we display the transverse-momentum distribution of the electron. We first concentrate on the left-hand side (l.h.s.) of the figure. In the upper panel, LO refers to $\sigma_{\bar{q}q}^{\text{LO}}$ induced by $\bar{q}q$ channels only, $\gamma\gamma$ to $\sigma_{\gamma\gamma}^{\text{LO}}$ induced by photon–photon collisions, and EW to the full NLO EW prediction, i.e. the sum of the LO cross section with all considered corrections. The $\bar{b}b$ -induced contribution to $\sigma_{\bar{q}q}^{\text{LO}}$ (not shown separately) is only relevant at low p_{T,e^-} , dropping below 2% already at $p_{\text{T},e^-} \sim 300$ GeV. The lower panel compares the relative corrections induced by the $\bar{q}q$, $q\gamma$, and $\gamma\gamma$ channels as well as their sum (EW, c.f. Eq. (5.58)). The corrections in the $\bar{q}q$ channels dominate and exhibit their known negative logarithmic increase due to weak Sudakov high-energy logarithms $\propto \alpha/(\pi s_W^2) \ln^2(p_{\text{T},e^-}/M_W)$, reaching $\sim -45\%$ at $p_{\text{T},e^-} = 1$ TeV. This huge negative correction is only partly compensated by the positive contribution of the $\gamma\gamma$ -induced tree-level process, whose impact steadily grows from about 1% at small transverse momentum to more than 10% at 1 TeV. The contribution of the $q\gamma$ -induced channel is completely insignificant within the ATLAS WW setup.

The behaviour of the $q\gamma$ contribution is enforced by the jet-identification criterion and the specific choice of the jet veto within the ATLAS WW setup, Eqs. (5.44) and (5.55), respectively. Both only affect the $q\gamma$ -induced contribution, since it is the only contribution that can give rise to a jet. On the r.h.s. of Fig. 5.9 we illustrate the dependence on the jet veto (JV) by means of the transverse-momentum distribution of the electron, where we show the $q\gamma$ -induced contribution together with the full EW correction for three different values of the jet veto. If we loosen the cut of Eq. (5.55) to only reject jets with $p_{\text{T,jet}} > 100$ GeV (the value within our inclusive setup, Eq. (5.51)), the $q\gamma$ -induced contribution becomes positive and leads to a correction of +0.62% for the integrated cross section, resembling the situation in the inclusive setup. However, the complete omission of a jet veto results in a positive correction of almost 70% at $p_{\text{T},e^-} = 1$ TeV,

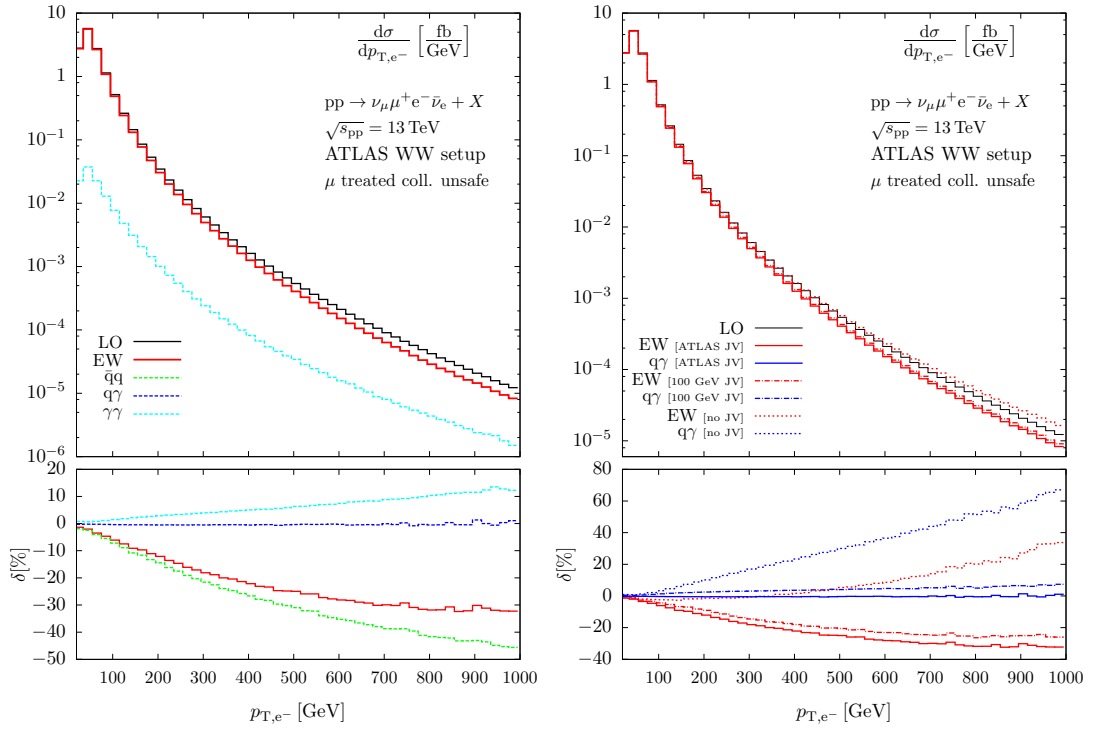


Figure 5.9.: Individual contributions to the differential cross section with the default ATLAS jet veto of $p_{T,\text{jet}} > 25$ GeV (left) and jet veto (JV) dependence (right) of the transverse-momentum distribution of the electron in $pp \rightarrow \nu_\mu \mu^+ e^- \bar{\nu}_e + X$ in the ATLAS WW setup. The lower panels show the relative size of the various corrections.

even rendering the total EW correction δ_{EW} positive for $p_{\text{T},e^-} \gtrsim 400$ GeV. In the latter case we obtain a positive correction of $\sigma_{q\gamma} = 3.914(2)\text{fb}$ ($\delta_{q\gamma} = +1.44\%$) to the integrated cross section from the $q\gamma$ channel alone, leading to a total EW correction of only $\delta_{\text{EW}} = -1.40\%$. The reason for this immense increase is a known mechanism, referred to as “giant K factor” [110], which was already discussed for $q\gamma$ -induced corrections to W-pair production in the literature [12, 86]. In such processes, topologies that first occur at NLO introduce kinematic configurations in which one massive gauge boson may become quasi-soft, leading to large double-logarithmic corrections for large transverse momenta. In QCD, such corrections may grow to several 100%. For $q\gamma$ collisions the size is mitigated by the smallness of α and the photon PDF with respect to α_s and the gluon PDF, respectively, in spite of some enhancement due to diagrams with incoming photons coupling to W bosons, which do not have a QCD counterpart. Note also that overwhelmingly large QCD corrections (as a consequence of a missing jet veto) would force us to calculate EW corrections for W-pair production in association with hard jets, a task that goes beyond the scope of this work.

In the following we always apply the jet veto in order to suppress configurations with hard jets and soft W bosons, which are less interesting for the investigation of W-boson pairs. For the ATLAS WW and Higgs-background setups, the jet veto actually implies that $q\gamma$ -induced events may only contribute to the zero-jet cross section, so that any potential final-state jet must remain undetected (cf. Eq. (5.44)). This eventually leads to a small negative contribution of the $q\gamma$ -induced processes in the ATLAS WW setup of $\sigma_{q\gamma} = -0.744(2)\text{fb}$ ($\delta_{q\gamma} = -0.27\%$), the value quoted in Tab. 5.1.

In Fig. 5.10 we turn to distributions in the transverse invariant masses of four or two leptons. Owing to the incomplete information about the momenta of the two neutrinos at a hadron collider, it is experimentally not possible to fully reconstruct the invariant mass of the W^+W^- system (M_{WW}) in leptonic final states. However, in the transverse plane the sum of the neutrino momenta can be inferred from the missing transverse momentum ($\vec{p}_{\text{T}}^{\text{miss}}$), motivating the following definition of the transverse mass of the four-lepton decay system [111],

$$M_{\text{T,WW}} = \sqrt{(E_{\text{T},e^-\mu^+} + E_{\text{T}}^{\text{miss}})^2 - (\vec{p}_{\text{T},e^-\mu^+} + \vec{p}_{\text{T}}^{\text{miss}})^2}, \quad (5.60)$$

with the vector sum $\vec{p}_{\text{T},e^-\mu^+}$ of the transverse momenta of the final-state charged leptons, the missing transverse momentum $\vec{p}_{\text{T}}^{\text{miss}}$ and the corresponding transverse energies given by

$$E_{\text{T},e^-\mu^+} = \sqrt{(\vec{p}_{\text{T},e^-\mu^+})^2 + M_{e^-\mu^+}^2} \quad \text{and} \quad E_{\text{T}}^{\text{miss}} = |\vec{p}_{\text{T}}^{\text{miss}}|. \quad (5.61)$$

The various contributions to the observable $M_{\text{T,WW}}$ are shown in Fig. 5.10 (l.h.s.) together with the invariant mass $M_{e^-\mu^+}$ of the charged-lepton system (r.h.s.). In the high-energy regions, the relative corrections to the two observables exhibit a very similar quantitative behaviour: As for the transverse momentum of the electron, the EW correction is dominated by the negative correction to the $\bar{q}q$ -induced contribution. The positive contribution of the $\gamma\gamma$ -induced tree-level process partly compensates for the

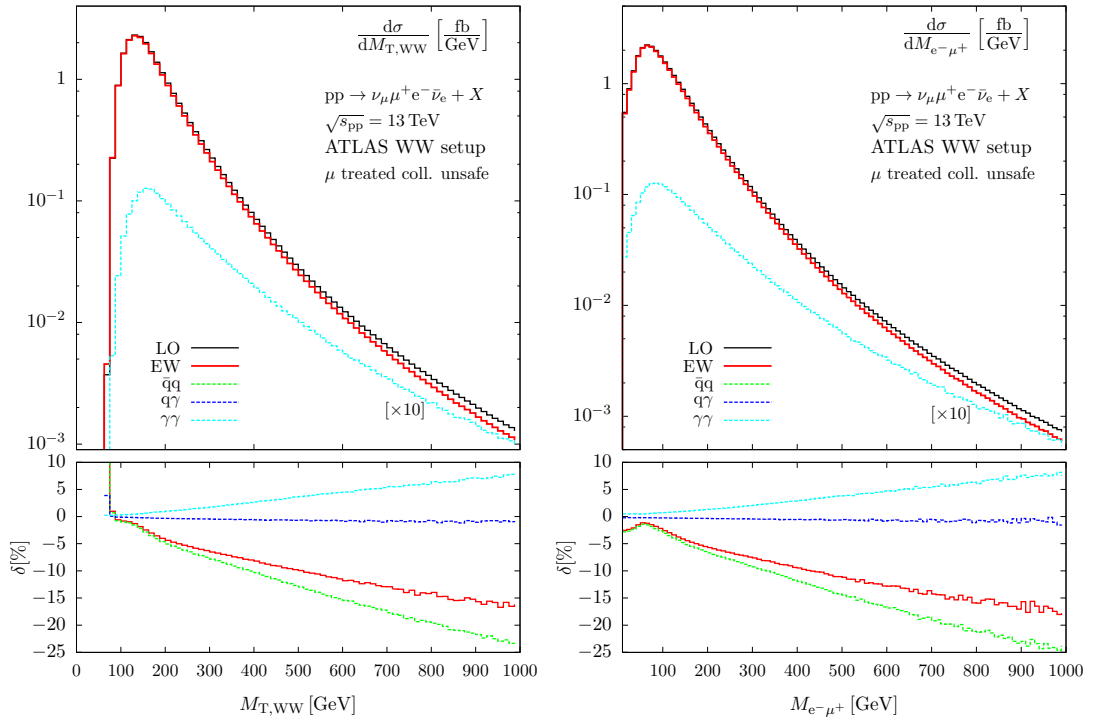


Figure 5.10.: Transverse-mass distribution of the four-lepton system (left) and invariant-mass distribution of the charged-lepton system (right) in $pp \rightarrow \nu_\mu \mu^+ e^- \bar{\nu}_e + X$ in the ATLAS WW setup (upper panels), together with the relative impact of the individual corrections (lower panels). Note that the $\gamma\gamma$ contribution is scaled by a factor of ten only in the upper panels.

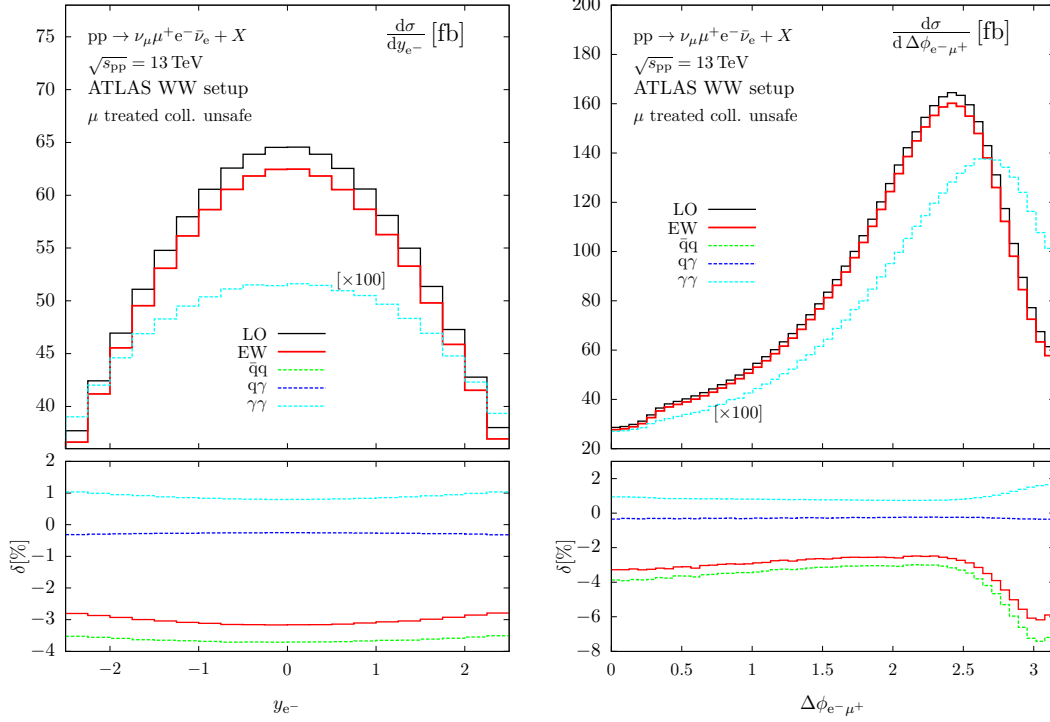


Figure 5.11.: Rapidity distribution of the electron (left) and distribution in the azimuthal-angle separation of the two charged leptons (right) in $pp \rightarrow \nu_\mu \mu^+ e^- \bar{\nu}_e + X$ in the ATLAS WW setup. The lower panels show the relative impact of the various contributions. Note that the $\gamma\gamma$ contribution is scaled by a factor of hundred only in the upper panels.

strong negative correction, while the contribution from $q\gamma$ initial states remains insignificant due to the jet veto. At the scale of 1 TeV, we observe a negative total EW correction of about -15% for both observables, i.e. about half the size as in the p_{T,e^-} distribution at the same scale. Note, however, that $d\sigma/dp_{T,e^-}$ falls off much steeper with p_{T,e^-} than the shown invariant-mass distributions with increasing masses.

In Fig. 5.11 we show rapidity and angular distributions of the charged leptons within the ATLAS WW setup. The corrections to the rapidity distribution of the electron (left) are uniformly distributed and resemble the corrections to the integrated cross sections given in Tab. 5.1. The azimuthal-angle separation of the two charged leptons (right), on the other hand, receive some distortion due to the EW corrections towards a separation of $\Delta\phi_{e^-\mu^+} = \pi$ of the two charged leptons. This back-to-back configuration in the transverse plane is favoured by events with W-boson pairs with large transverse momenta, which explains the tendency to receive more negative EW corrections in the $\bar{q}q$ channels.

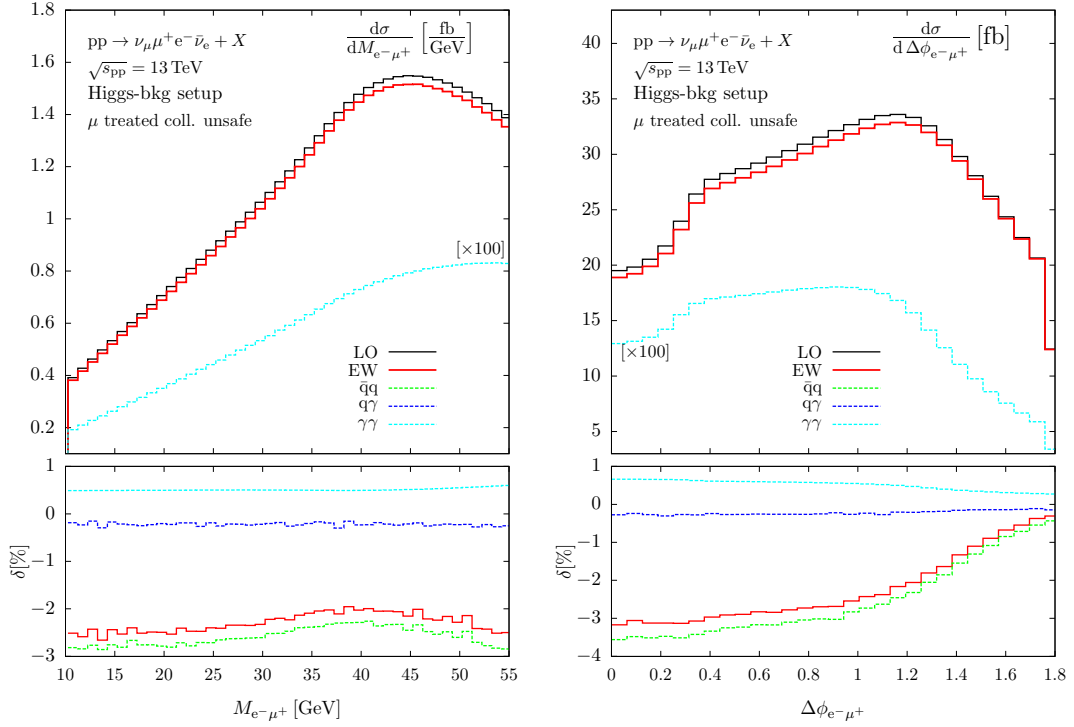


Figure 5.12.: Distributions in the invariant mass of the charged-lepton system (left) and in the azimuthal-angle separation of the two charged leptons (right) in $pp \rightarrow \nu_\mu\mu^+e^-\bar{\nu}_e + X$ in the Higgs-background setup. The lower panels show the relative impact of the various contributions. Note that the $\gamma\gamma$ contribution is scaled by a factor of hundred only in the upper panels.

5.3.5. Differential Cross Sections in the Higgs-Background Setup

A very important irreducible background to the decay of a Higgs boson to a W-boson pair, $H \rightarrow WW^*$, originates from the direct W-pair production process $pp \rightarrow WW^* \rightarrow \nu_\mu\mu^+e^-\bar{\nu}_e + X$. In the following, we study the influence of the EW corrections on this dominant background in the Higgs signal region defined by the additional cuts of Eq. (5.56) and Eq. (5.57). Since this setup is meant to favour the Higgs signal and to suppress any background as much as possible, we observe a reduction of σ_{qq}^{LO} by almost a factor of six compared to the ATLAS WW setup (cf. Tab. 5.1). We also observe some reduction of all relative corrections, resulting in a total EW correction of only -2.25% for the 13 TeV prediction (we again provide results for 13 TeV in the collinear-unsafe photon scenario). This reduction can be explained by looking at the differential distributions of the two observables to which the cuts of Eq. (5.56) are applied.

In Fig. 5.12 we show these observables, namely the invariant mass (left) and the azimuthal-angle separation (right) of the two charged leptons, within the Higgs-background setup. As discussed above, the large relative corrections to the invariant-mass

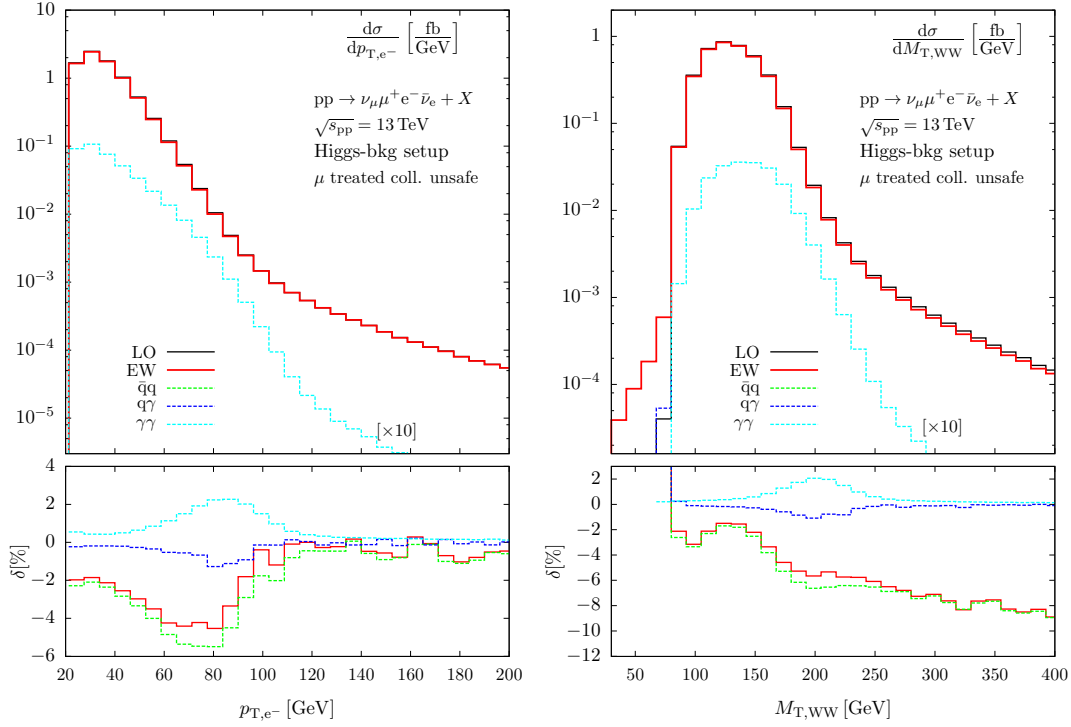


Figure 5.13.: Transverse-momentum distribution of the electron (left) and transverse-mass distribution of the four-lepton system (right) in $pp \rightarrow \nu_\mu \mu^+ e^- \bar{\nu}_e + X$ in the Higgs-background setup. The lower panels show the relative impact of the various contributions. Note that the $\gamma\gamma$ contribution is scaled by a factor of ten only in the upper panels.

distribution of the two charged leptons in the ATLAS WW setup were observed for large $M_{e-\mu^+}$, a region that is completely removed by the additional cuts, so that smaller EW corrections are expected. In the allowed range of the invariant mass of the charged-lepton system we now observe quite uniformly distributed corrections from all contributions (Fig. 5.12, left). For the azimuthal-angle separation (Fig. 5.12, right), the region of phase space exhibiting the most pronounced EW corrections in the ATLAS WW setup has been cut away, but the cuts affect the LO distribution and the corrections in the allowed range in a non-trivial way. Towards the new maximal value of $\Delta\phi_{e-\mu^+}^{\text{cut}} = 1.8$ we observe a strong decrease of the cross section and a reduction of the EW corrections.

The transverse-momentum distribution of the electron and the transverse-mass distribution of the W-pair in the Higgs-background setup are shown in Fig. 5.13. We point out that both observables exhibit a much steeper decrease of the LO cross section in the shown kinematic range than within the ATLAS WW setup (cf. Figs. 5.9 and 5.10): The distributions in the Higgs setup drop faster with increasing scales by roughly a factor of 100 compared to the situation in the ATLAS WW setup. The corrections induced by the $q\gamma$ and $\gamma\gamma$ channels almost cancel each other at low scales and are suppressed

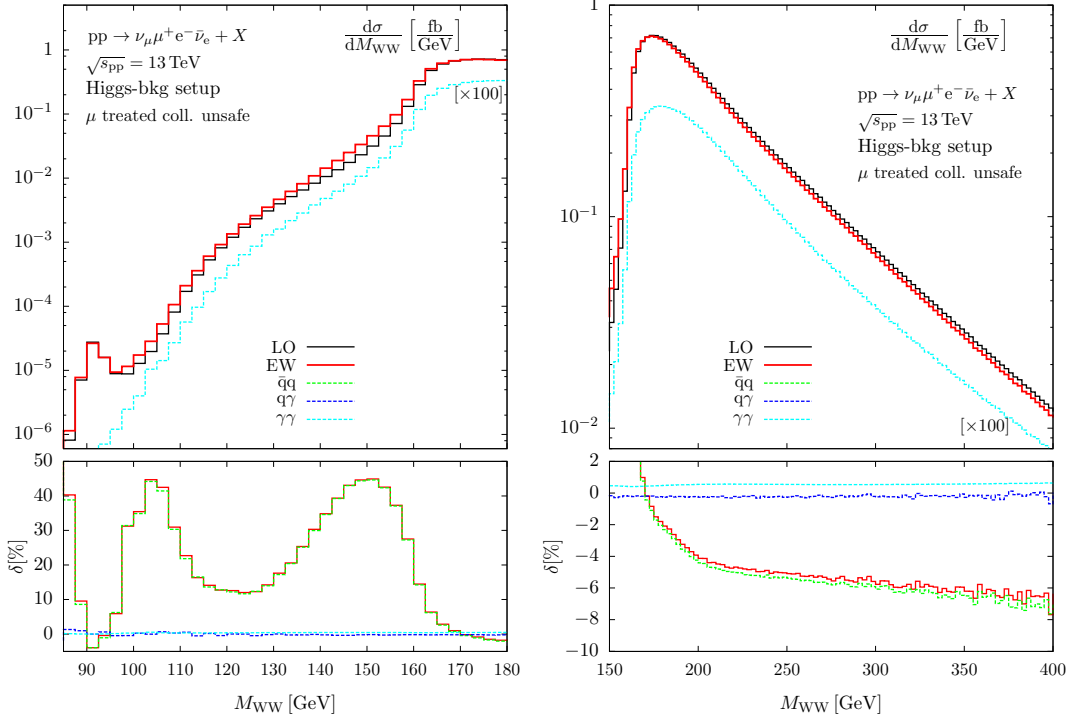


Figure 5.14.: Invariant-mass distribution of the four-lepton system in two different plot ranges in $pp \rightarrow \nu_\mu \mu^+ e^- \bar{\nu}_e + X$ in the Higgs-background setup. The lower panels show the relative impact of the various contributions. Note that the $\gamma\gamma$ contribution is scaled by a factor of hundred only in the upper panels.

at high scales. The EW corrections are, thus, almost entirely due to corrections to the $\bar{q}q$ channels. They distort the shapes of the distributions significantly in a non-trivial way. While the EW corrections to the $M_{T,WW}$ distribution (Fig. 5.13, right) show the onset of the typical decrease towards larger scales, the EW corrections to the p_{T,e^-} distribution are significant only for $p_{T,e^-} \lesssim 100$ GeV.

In Fig. 5.14 we investigate the (experimentally unobservable) invariant-mass distribution of the four-lepton system, where the Higgs-boson resonance is located at $M_{WW} = M_H \approx 125$ GeV. Between $M_{WW} = 80$ GeV and the on-shell W-pair threshold at $M_{WW} = 2M_W \approx 160$ GeV, we observe a very strong increase by almost five orders of magnitude in the M_{WW} distribution. Although we clearly see that the direct production of a W-boson pair within the Higgs-background setup is still dominated by on-shell W-pairs with $M_{WW} \gtrsim 2M_W$, it is still interesting to look into the region below this threshold, where at least one of the W bosons is forced to be off-shell. At $M_{WW} = M_Z$, the Z-boson resonance is visible, though very strongly suppressed, since at least one of the W bosons has to be far off shell there. The distinct structures and the strong positive enhancement of the EW corrections below the W-pair threshold can be attributed to the kinematic redistribution of events by collinear final-state

LHC 13 TeV	$\sigma_{\bar{q}q}^{\text{LO}}$ [fb]	$\delta_{\bar{q}q}^{\text{coll. unsafe}}$ [%]	$\delta_{\bar{q}q}^{\text{coll. safe}}$ [%]
inclusive	390.59(3)	-3.41	-2.91
ATLAS WW	271.63(1)	-3.71	-3.18
Higgs bkg	49.934(2)	-2.54	-1.95

Table 5.2.: LO cross sections for $pp \rightarrow \nu_{\mu}\mu^{+}e^{-}\bar{\nu}_{e} + X$ at the LHC running at 13 TeV in the inclusive cut scenario (top line), the ATLAS WW setup (middle line), and the Higgs-background setup (bottom line). In the last two columns we list the relative corrections to the $\bar{q}q$ -induced contributions in our default setup (collinear unsafe) and the collinear-safe setup. The numbers in parentheses represent the numerical error on the last given digit.

radiation of photons off the charged leptons. This effect systematically shifts events to lower values of M_{WW} , leading to pronounced positive corrections where the spectrum falls off steeply with decreasing values of M_{WW} . This well-known feature near kinematical thresholds has recently also been discussed in a similar setup for the EW corrections to off-shell Z-pair production [112]. At the invariant W-pair mass close to the Higgs-boson mass of 125 GeV we observe a positive EW correction of about +15%, but we remind the reader that M_{WW} is not an observable for purely leptonically decaying W-boson pairs, in contrast to the respective situation for Z-boson pairs, where the invariant mass M_{ZZ} is fully reconstructible if the decay into four charged leptons is considered. Above the WW threshold, where resonant W bosons dominate, the EW correction shows again the tendency to become more negative with increasing M_{WW} . We point out, however, that this negative increase is much slower than observed in the transverse-momentum and transverse-mass distributions (in particular in the ATLAS WW setup, cf. Figs. 5.9 and 5.10), because the region of large invariant mass M_{WW} is dominated by forward-scattered W bosons owing to t -channel diagrams, and thus not by the Sudakov regime where all momentum invariants have to be large. Finally, we note that within the Higgs-background setup the corrections due to the photon-induced channels do not play a significant role for this observable.

5.3.6. Collinear-Safe Versus Collinear-Unsafe Case

In this section we discuss the impact of the recombination of nearly collinear photons with final-state leptons on total and differential cross sections. In all results shown up to now, the recombination procedure described at the end of Sec. 5.3.1 was applied only to electrons, while muons were treated in a collinear-unsafe way. In Tab. 5.2 we list $\sigma_{\bar{q}q}^{\text{LO}}$ for our three phenomenological cut scenarios at the LHC operating at an energy of $\sqrt{s_{\text{pp}}} = 13$ TeV, together with the corrections from the $\bar{q}q$ -induced channels for our

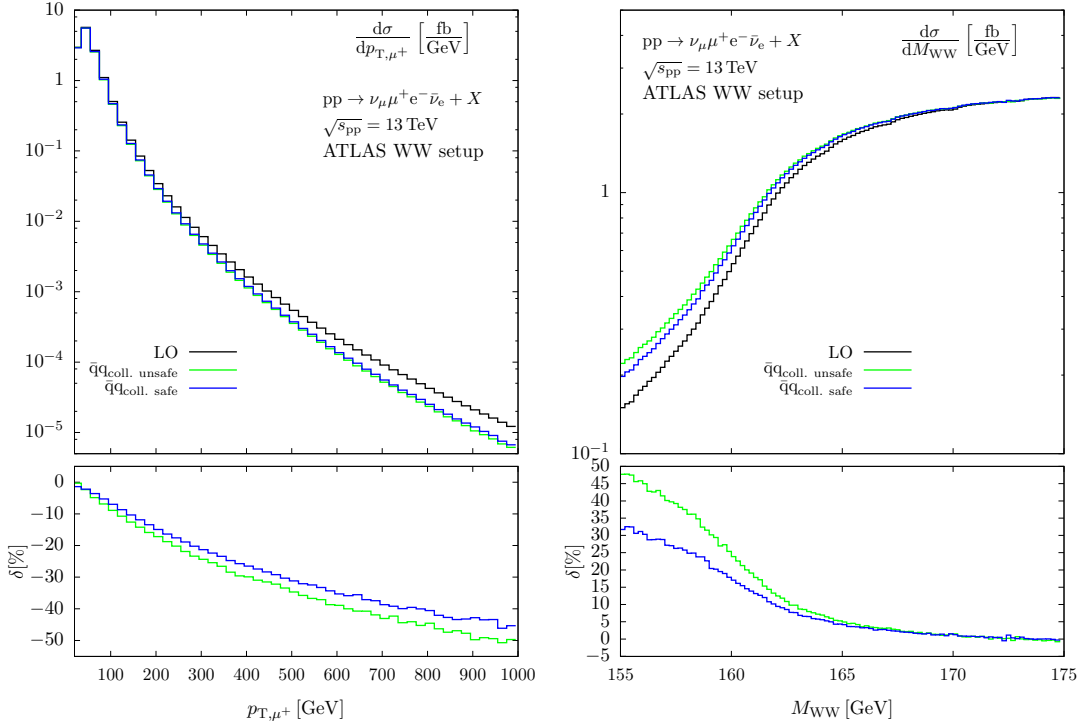


Figure 5.15.: Transverse-momentum distribution of the muon (left) and invariant-mass distribution of the four-lepton system (right) in $pp \rightarrow \nu_\mu \mu^+ e^- \bar{\nu}_e + X$ in the ATLAS WW setup. The lower panels show the relative size of the $\bar{q}q$ contribution within our default (collinear-unsafe) setup compared to the collinear-safe case.

default setup (collinear-unsafe case) and for the case where we apply the recombination procedure to both charged leptons (collinear-safe case). For integrated cross sections we observe slightly reduced corrections (by about 0.5%) in all three cut scenarios in the fully collinear-safe setup. This is due to the missing enhancement of final-state radiation by the mass singularity that appears in the collinear-unsafe treatment of muons. In the fully collinear-safe treatment of the real radiation more muons pass the cuts (after recombination with photons), so that the correction tends to be less negative.

This effect can most directly be observed in the transverse-momentum distribution of the muon and in the W-pair invariant-mass distribution, which are both shown in Fig. 5.15 in the ATLAS WW setup. In the p_{T,μ^+} distribution, which is widely monotonically falling, the collinear-unsafe correction factor signals larger negative corrections than its collinear-safe counterpart over the entire plot range, apart from the first bins where the maximum of the distribution is located. In the M_{WW} distribution the converse situation is observed: For $M_{WW} \gtrsim 165\text{--}175$ GeV, where the distribution is rather flat, hardly any difference between collinear-unsafe and collinear-safe event selection is visible, because events are shifted more or less uniformly by photon recombination. For $M_{WW} \lesssim 2M_W$, however, much more events migrate from larger to smaller invariant

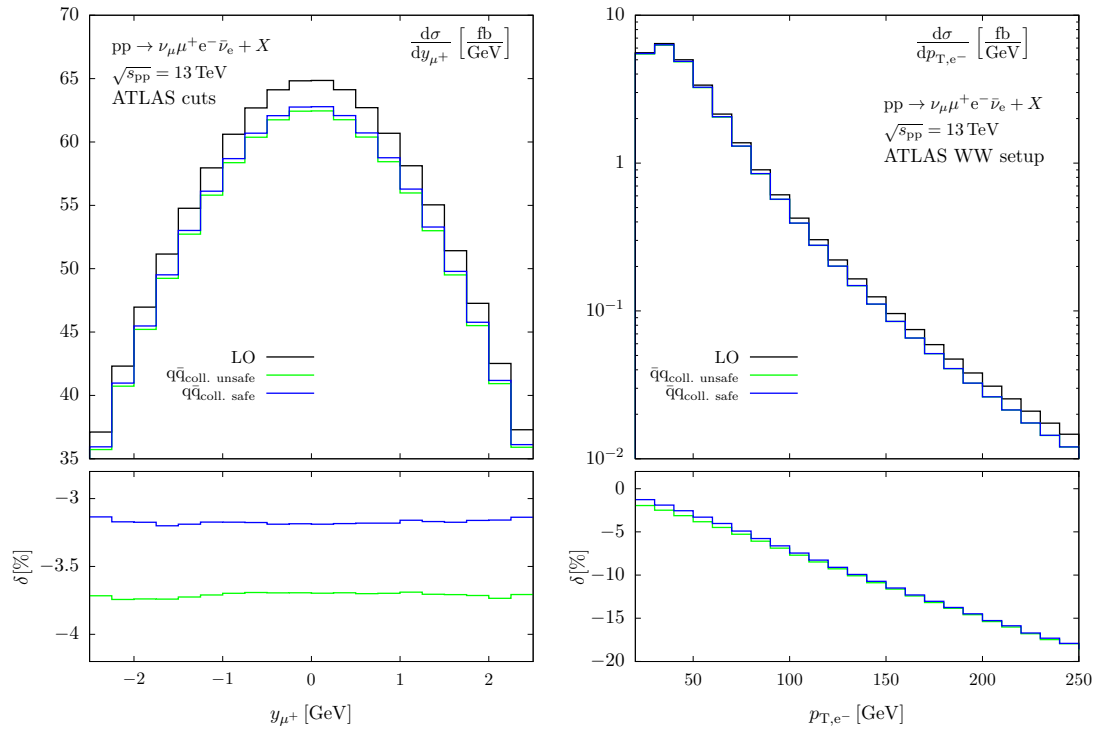


Figure 5.16.: Rapidity distribution of the muon (left) and transverse-momentum distribution of the electron (right) in the ATLAS WW setup. The lower panels show the relative size of the $\bar{q}q$ contribution within our default (collinear-unsafe) setup compared to the collinear-safe case.

LHC 13 TeV	$\sigma_{\bar{q}q}^{\text{LO}}$ [fb]	$\sigma_{\bar{q}q}^{\text{LO,DPA}}$ [fb]	$\delta_{\bar{q}q}$ [%]	$\delta_{\bar{q}q}^{\text{DPA}}$ [%]
inclusive	390.59(3)	384.96(9)	-3.41	-3.43
ATLAS WW	271.63(1)	265.31(3)	-3.71	-3.68
Higgs bkg	49.934(2)	48.88(2)	-2.54	-2.54

Table 5.3.: LO cross sections for $pp \rightarrow \nu_\mu\mu^+e^-\bar{\nu}_e + X$ at the LHC running at 13 TeV in the inclusive setup (top line), the ATLAS WW setup (middle line), and the Higgs-background setup (bottom line). In the last two columns we list the relative EW corrections to the $\bar{q}q$ -induced contributions including the full virtual corrections ($\delta_{\bar{q}q}$) and applying the DPA within the virtual contributions ($\delta_{\bar{q}q}^{\text{DPA}}$), both normalized to $\sigma_{\bar{q}q}^{\text{LO}}$. The numbers in parentheses represent the numerical error on the last given digit.

masses in the collinear-unsafe case because of the mass-singular enhancement of final-state radiation, leading to larger positive corrections as compared to the collinear-safe case.

As can be seen on the l.h.s of Fig. 5.16, the rapidity distribution of the final-state muon does not exhibit significant distortions when applying the recombination procedure, since recombining leptons and collinear photons does not systematically change the lepton direction. The difference between the two treatments directly reflects the difference observed in the integrated results over the full phase space. The r.h.s. of Fig. 5.16 finally shows the transverse-momentum distribution of the electron, where only towards very low momenta any deviation between the two approaches can be recognized. Since the electron itself is not directly affected by the change of the treatment, the small deviation at low p_{T,e^-} only reflects that events with high p_T muons are more likely to exhibit a low p_T electron, and vice versa.

5.3.7. Comparison to the Double-Pole Approximation

In this section we discuss the validity and quality of the DPA, by comparing integrated and differential results in DPA to results of our full $4f$ calculation. In Tab. 5.3 we list the LO cross sections $\sigma_{\bar{q}q}^{\text{LO}}$ and $\sigma_{\bar{q}q}^{\text{LO,DPA}}$ for our three setups at the LHC at an energy of $\sqrt{s_{pp}} = 13$ TeV. The difference of the LO results of approximately 2% indicates that non-doubly-resonant contributions only contribute at the expected level of $\mathcal{O}(\Gamma_W/M_W)$, which is, however, not good enough to achieve percent-level accuracy even after including higher-order corrections. Note that we include the DPA LO cross section $\sigma_{\bar{q}q}^{\text{LO,DPA}}$ in our discussion for illustration only, but that in the DPA version of Ref. [12] all tree-level contributions are fully taken into account. As discussed already in Sec. 5.2.3, we define the relative corrections of the full $4f$ prediction and the DPA upon normalizing

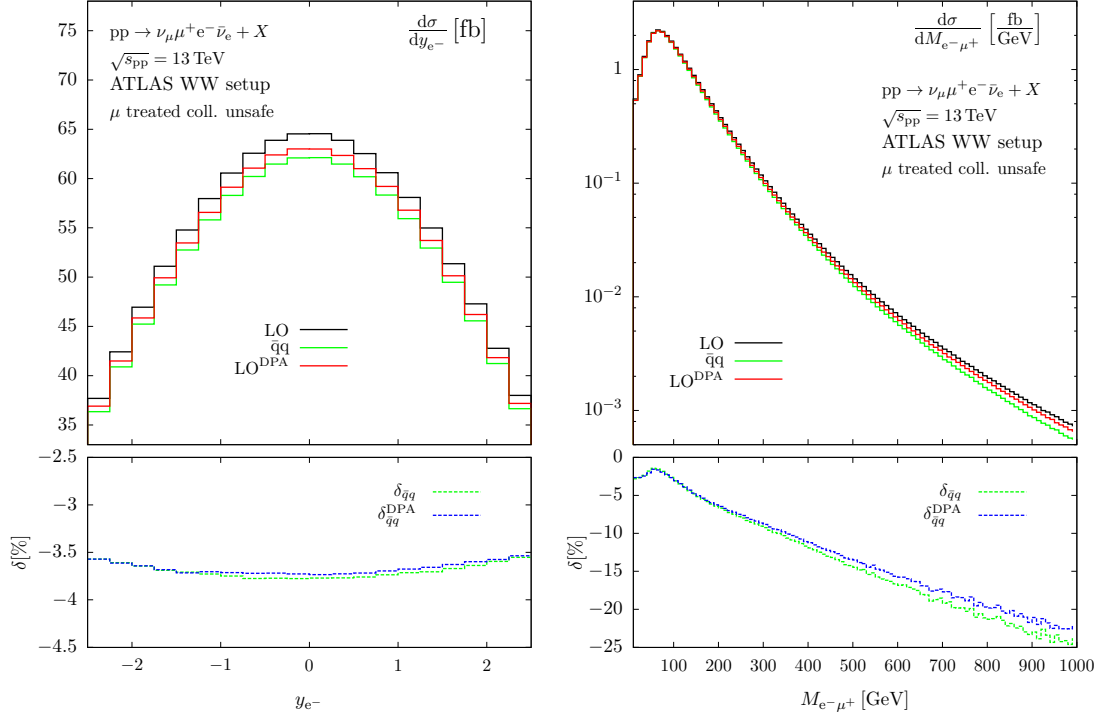


Figure 5.17.: Rapidity distribution of the electron (left) and invariant-mass distribution of the charged-lepton system (right) in $pp \rightarrow \nu_\mu \mu^+ e^- \bar{\nu}_e + X$ in the ATLAS WW setup. The lower panels show the relative size of the EW corrections to the $\bar{q}q$ channels in our default setup compared to the results based on the DPA.

to the full LO cross section,

$$\delta_{\bar{q}q}(\mathcal{O}) = \frac{d\sigma_{\bar{q}q}^{\text{NLO}}}{d\mathcal{O}} / \frac{d\sigma_{\bar{q}q}^{\text{LO}}}{d\mathcal{O}}, \quad \delta_{\bar{q}q}^{\text{DPA}}(\mathcal{O}) = \frac{d\sigma_{\bar{q}q}^{\text{NLO,DPA}}}{d\mathcal{O}} / \frac{d\sigma_{\bar{q}q}^{\text{LO}}}{d\mathcal{O}}, \quad (5.62)$$

so that they only differ within the virtual contributions of the NLO calculation. For integrated cross sections, the two corrections show very good agreement, as can be seen in the rightmost columns of Tab. 5.3.

A similar observation can be made for the rapidity distributions of the leptons, which is illustrated for the electron on the l.h.s. of Fig. 5.17 in the ATLAS WW setup. In the upper panel we observe the clear deviation of $\sigma_{\bar{q}q}^{\text{LO,DPA}}$ from the full LO prediction, being of the same order of magnitude as the EW corrections to the $\bar{q}q$ -induced processes. The lower panel shows the excellent agreement of the two versions for the relative corrections, with differences at the 0.1% level only.

The r.h.s. of Fig. 5.17 illustrates the same comparison for the invariant-mass distribution of the charged-lepton system in the ATLAS WW setup. For $M_{e-\mu^+} \lesssim 500$ GeV, the DPA is accurate within 1%, but the difference grows to about 2–3% in the TeV range. This increasing difference between the full $4f$ calculation and the DPA can

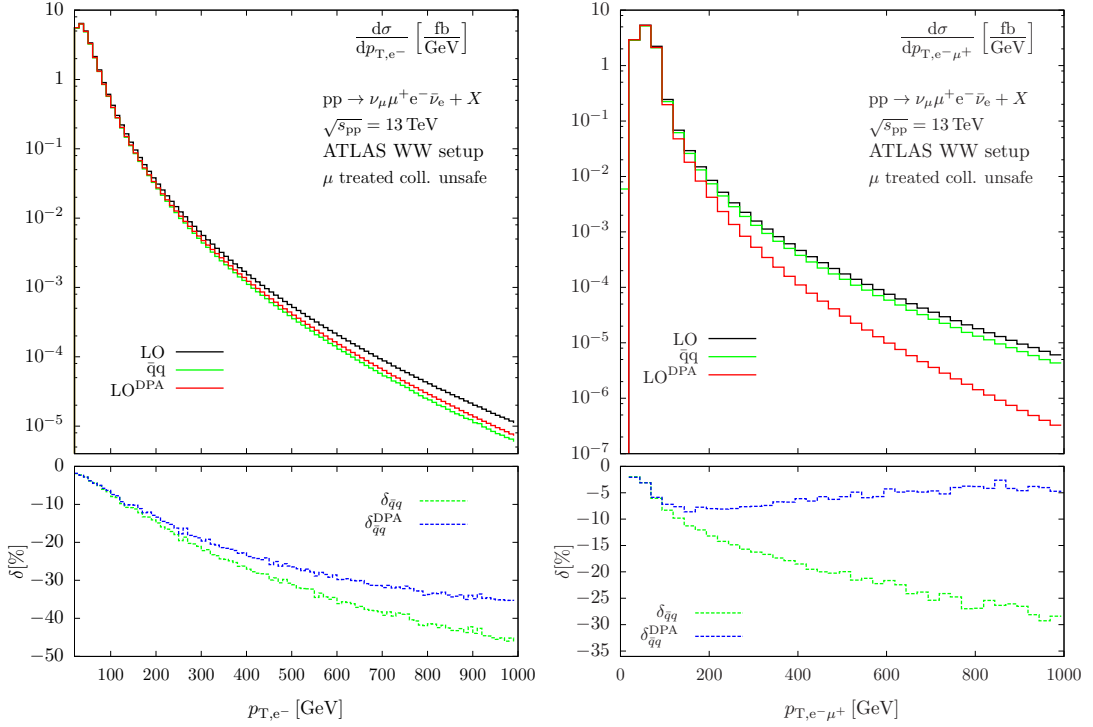


Figure 5.18.: Transverse-momentum distributions of the electron (left) and of the charged-lepton system (right) in $pp \rightarrow \nu_\mu \mu^+ e^- \bar{\nu}_e + X$ in the ATLAS WW setup. The lower panels show the relative size of the EW corrections to the $\bar{q}q$ channels in our default setup compared to the results based on the DPA.

already be inferred from the LO cross sections $\sigma_{\bar{q}q}^{\text{LO}}$ and $\sigma_{\bar{q}q}^{\text{LO,DPA}}$ in the upper panel, which signals the increasing impact of singly-resonant contributions not being included in the DPA. The difference between full and DPA NLO EW corrections is well covered by the last term of our estimate given in Eq. (5.37). In view of the typically expected accuracies in LHC data analyses, the DPA is certainly sufficient for this observable.

Finally, in Fig. 5.18 we turn to the transverse-momentum distributions of the electron (left) and the charged-lepton system (right): For the p_{T,e^-} distribution, the comparison between the full $4f$ and the DPA calculation reveals similar qualitative features as for the $M_{e^-\mu^+}$ distribution. The differences are, however, larger in size, reaching the 5% (10%) level for transverse momenta p_{T,e^-} of about 500 GeV (1 TeV). Again the deterioration of the DPA can already be seen at LO and attributed to an enhanced impact of the singly-resonant background diagrams shown in the second and third line of Fig. 5.2, which are not included in $\sigma_{\bar{q}q}^{\text{LO,DPA}}$. Schematically the relevant diagrams are illustrated on the l.h.s. of Fig. 5.19. The enhancement is due to events where one single lepton is recoiling against the other three in the final state. Thus, for large p_{T,e^-} the cross section $d\sigma_{\bar{q}q}^{\text{LO}}/dp_{T,e^-}$ receives large contributions from events where the electron is back-to-back to the three other leptons. For doubly-resonant diagrams (first

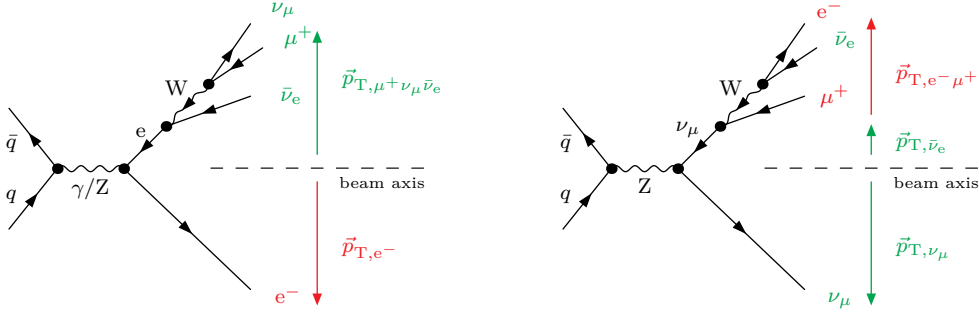


Figure 5.19.: Illustration of diagrammatic structures dominating the p_{T,e^-} (left) and $p_{T,e^-\mu^+}$ (right) distributions shown in Fig. 5.18 for high transverse momenta.

line in Fig. 5.2) this situation is less likely for large p_{T,e^-} , where the W-decay lepton pairs mostly appear back-to-back as a result of the boost from the W rest frames to the laboratory system. The comparison of $\sigma_{\bar{q}q}^{\text{LO}}$ with $\sigma_{\bar{q}q}^{\text{LO,DPA}}$ at high p_{T,e^-} shows that singly-resonant contributions dominate over doubly-resonant parts already for a p_{T,e^-} of some 100 GeV. Kinematically, it is, thus, easier to produce leptons with high transverse momenta directly rather than through the decay of W bosons. The difference between full and DPA NLO EW corrections is again reproduced quite well by the last term of our estimate of Eq. (5.37).

The difference between the full $4f$ and the DPA calculation is pushed to the extreme in the distribution of the transverse momentum of the charged-lepton system, $p_{T,e^-\mu^+}$. Here the enhancement of background diagrams is due to events where one neutrino recoils against the two charged leptons and the other neutrino, a situation that is supported by singly-resonant diagrams as illustrated on the r.h.s. of Fig. 5.19, but not by doubly-resonant graphs, where the two charged leptons tend to recoil against each other for high transverse momenta. Looking at equal sizes of transverse momenta on the horizontal axes of the two distributions in Fig. 5.18, the enhancement seems stronger in the case of the $p_{T,e^-\mu^+}$ distribution, but at the same time it should be realized that the spectrum on the r.h.s. drops much faster than the one of p_{T,e^-} on the l.h.s. for increasing p_T . This is due to the fact that $p_{T,e^-\mu^+}$ contains only part of the transverse momentum of the three-lepton system recoiling against the single neutrino and that it is very unlikely to produce a large $p_{T,e^-\mu^+}$ via the doubly-resonant contributions. In conclusion, we can state that transverse-momentum distributions are reproduced by the DPA only up to some 100 GeV owing to the growing influence of background diagrams that do not show two simultaneously resonant W bosons. For predictions of such p_T spectra in the TeV range, the calculation of EW corrections should be based on a full four-fermion calculation.

5.4. Conclusions and Outlook

Electroweak di-boson production processes represent a very interesting class of particle reactions at the LHC. They provide an ideal test-ground for the non-Abelian self-interactions among the electroweak gauge bosons, but also form an important class of backgrounds to many new-physics searches and to precision studies of the Higgs boson. Precise calculations for these processes, including radiative corrections of strong and electroweak interactions, are, thus, phenomenologically very important and have seen great progress in recent years. On the one hand, QCD predictions are being pushed to the next-to-next-to-leading-order level and are extended by including leading corrections beyond fixed orders. On the other hand, calculations of electroweak corrections become more and more refined by including decays of the unstable bosons and off-shell effects.

In this chapter we have presented the details of the first calculation of next-to-leading-order electroweak corrections to W-boson pair production at the LHC that fully takes into account leptonic W-boson decays and off-shell effects. This calculation is based on the complex-mass scheme for the treatment of the intermediate electroweak gauge bosons and provides next-to-leading-order precision over the entire phase space with resonant and/or non-resonant W bosons. Thus, it goes beyond previous calculations which are restricted to on-shell or nearly resonant W bosons.

We have discussed the electroweak corrections using different realistic event-selection setups, comprising one that is typical for the study of W-boson pairs as a signal process and another one that is typical for an analysis of Higgs-boson decays $H \rightarrow WW^*$, where W-boson pair production represents an irreducible background. In particular, we have compared the full off-shell results to previous results in the so-called double-pole approximation, which is based on an expansion of the loop amplitudes about the poles of the W resonances. At small and intermediate scales, i.e. in particular in angular and rapidity distributions, the two approaches show the expected agreement at the level of fractions of a percent, but larger differences appear for invariant-mass and transverse-momentum distributions in the TeV range. For transverse-momentum distributions, the differences can even exceed the 10% level in the TeV range where background diagrams with one instead of two resonant W bosons grow in importance because of the suppression of the doubly resonant contributions in these kinematical regimes.

To fully exploit our calculation in upcoming LHC data analyses, our state-of-the-art results on electroweak corrections should be combined with QCD-corrected cross sections. A possible way to achieve this, would be to apply differential reweighting factors for the electroweak corrections to differential distributions obtained in high-precision QCD-based predictions. Predictions obtained in this way would be accurate to the level of very few percent for integrated cross sections and distributions that are dominated by energy scales up to few 100 GeV. For transverse-momentum and invariant-mass distributions in the TeV range, the precision will deteriorate and most likely be limited by our knowledge of QCD corrections, while electroweak corrections are sufficiently well under control.

Chapter 6

Vector-Boson Scattering Processes at a 100 TeV Collider

This chapter is dedicated to the prospects of vector-boson scattering processes at a future high-energy hadron collider. After a short general introduction to vector-boson scattering reactions, in Sec. 6.2 we motivate their study at such a machine and present the details of our analysis. We want to stress already here that in contrast to the previous chapter, now the entire discussion will be restricted to the LO of all considered processes, since our goal is rather to examine the general capabilities of a future high-energy collider than to perform a precision study.

In Sec. 6.3 we discuss the main results of our studies of Refs. [113] and [114] and Sec. 6.4 contains our summary and conclusions.

6.1. Vector-Boson Scattering at Hadron Colliders

Weak vector-boson scattering (VBS) processes form a very important class of reactions to either further constrain the SM or alternatively find first signs of physics beyond the SM (BSM). Generally, we refer to VBS as the $2 \rightarrow 2$ scattering reaction of four massive EW gauge bosons,

$$V_1 V_2 \rightarrow V_3 V_4, \quad V_i = W^\pm, Z, \quad (6.1)$$

depicted in Fig. 6.1. At the LO, which is of $\mathcal{O}(\alpha^2)$, the subdiagrams contributing to a particular scattering reaction depend on the charges of the involved gauge bosons and may comprise quartic gauge couplings as well as t -, u -, and s -channel exchanges of the massive gauge bosons and the Higgs boson (c.f. Fig. 6.2).

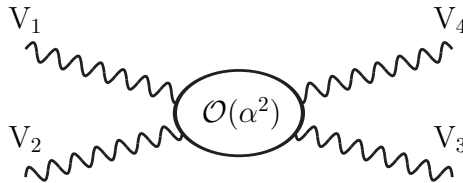


Figure 6.1.: Generic VBS diagram, where the blob includes all subdiagrams of $\mathcal{O}(\alpha^2)$ that are allowed by the charges of the four external gauge bosons.

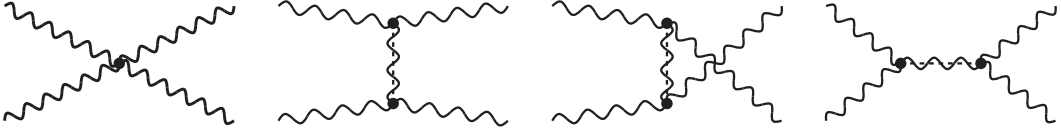


Figure 6.2.: Possible contributions to the generic diagram of Fig. 6.1. From left to right: the quartic gauge coupling and t -, u -, and s -channel exchanges of either an EW gauge boson (wavy line) or the Higgs boson (dashed line).

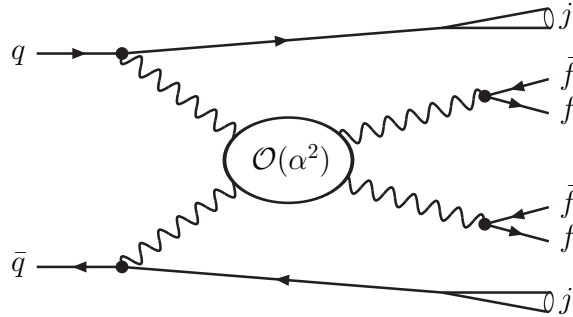


Figure 6.3.: Representative diagram of a VBS reaction at a hadron collider. Including the production and decay vertices this is at tree-level a purely EW process of $\mathcal{O}(\alpha^6)$.

The specific interplay between these contributions makes this process class particularly sensitive to the exact realization of EWSB in the SM as well as to possible new physics effects potentially entering via the EW gauge sector. It is for example well known, that the additional contributions involving the Higgs boson prevent the cross section of the longitudinal gauge-boson modes $V_L V_L \rightarrow V_L V_L$ from an unphysical growth with the scattering energy that would eventually even lead to unitarity violation in the TeV range.

We also want to stress that the s -channel production (i.e. the omission of the decay-vertex in the right-most diagram of Fig. 6.2) is also separately referred to as vector-boson fusion (VBF) into a weak boson or a Higgs boson, respectively. In the following discussion, however, we concentrate on the full VBS process of Eq. (6.1), from which the VBF processes are obtained straightforwardly by omitting particular subdiagrams.

As we already discussed in Sec. 3.2.2, the unstable massive EW gauge bosons are not experimentally accessible as external particles of scattering reactions, such that their study in collider experiments requires the inclusion of the incoming fermions and decay products, respectively. At hadron colliders, VBS is therefore studied in reactions of the type

$$qq \rightarrow VV + qq \rightarrow 4f + 2j, \quad V = W^\pm, Z, \quad (6.2)$$

where the initializing weak bosons are emitted from two (anti-)quarks (qq) that subsequently give rise to two jets (j) in the final state, as depicted in Fig. 6.3. Moreover, in order to perform a reliable prediction for this purely EW process, all diagrams of

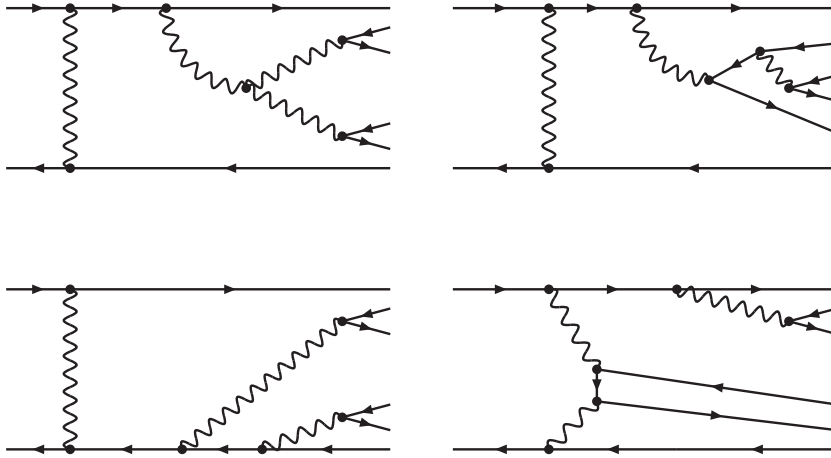


Figure 6.4.: Representative EW-background diagrams of $\mathcal{O}(\alpha^6)$.

$\mathcal{O}(\alpha^6)$ leading to the specific six-particle final-state $4f + 2j$, have to be taken into account. Beside the VBS topology, depicted in Fig. 6.3, this requires the inclusion of *EW-background* diagrams comprising also diagrams without any direct interaction of the weak bosons. In Fig. 6.4 we show some representative background diagrams of the genuine $\mathcal{O}(\alpha^6)$ process.

Since in the semi-leptonic ($4f = 2\ell 2q$) or even purely hadronic ($4f = 4q$) decay mode of the weak bosons the experimental distinction between the VBS topology and the background contributions is unnecessarily complicated due to the additional jets in the final state, we focus in the following exclusively on the purely leptonic decay mode ($4f = 4\ell$).

With this constraint, the jets emerging from the two quark lines can be used to suppress the background contributions and therefore restrict the phase space to regions that are dominated by the VBS topology. To be more precise, due to the recoil of the high momentum transfer to the VBS system, the two jets are typically located in the forward and backward regions of the detector, while in the central region only the leptonic decay products of the weak bosons are expected. The various background contributions, on the other hand, also give rise to jet activity in the central region of the detector and can therefore be considerably reduced by requiring widely separated jets in the final state, as we will explicitly show in our results.

Actually, the powerful suppression of the background becomes even more important as also QCD-induced contributions of the order $\mathcal{O}(\alpha_s^2 \alpha^4)$ exist, which lead to the same six-particle final-state $4\ell + 2j$. In Fig. 6.5 we show some representative *QCD-background* diagrams, where, depending on the total charge of the final-state leptons, also diagrams with external gluons may occur. Already the simple estimate of the two different coupling strengths of Eq. (3.4), and additionally the genuinely high gluon-luminosity at hadron colliders suggest that the cross section will be clearly dominated by the

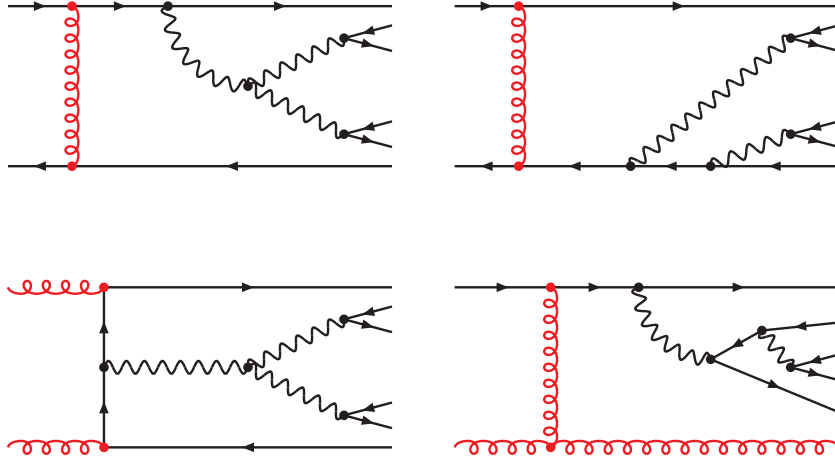


Figure 6.5.: Representative QCD-background diagrams of $\mathcal{O}(\alpha_s^2\alpha^4)$ for the purely leptonic decay mode.

QCD-induced contributions. Note, however, that a study of VBS in the semi-leptonic or hadronic decay mode would additionally require to take QCD-background graphs into account that are of the orders $\mathcal{O}(\alpha_s^4\alpha^2)$ and $\mathcal{O}(\alpha_s^6)$, respectively. The complication of both, the theoretical prediction as well as the possible measurement, is therefore reduced to a minimum by focusing on the fully leptonic decay channel of the weak gauge bosons, i.e. by considering the hadronic processes

$$pp \rightarrow 4\ell + 2j. \quad (6.3)$$

Note that these hadronic processes comprises beside the two aforementioned contributions of the order $\mathcal{O}(\alpha^6)$ and $\mathcal{O}(\alpha_s^2\alpha^4)$, to which we refer in the following as *EW-induced* and *QCD-induced* contributions, respectively, also interference contribution of the order $\mathcal{O}(\alpha^5\alpha_s)$. However, as has been explicitly shown in Ref. [115], these interference contributions become negligible in the regions of phase space where VBS processes are typically investigated, such that we can safely neglect them in our study.

By means of the final-state leptons, it is possible to differentiate between six processes which contribute to four distinct VBS process classes. In the following we refer to these process classes as same-sign W-pair production via VBS (W^+W^+jj and W^-W^-jj), W^\pm -Z production via VBS (W^+Zjj and W^-Zjj), Z-pair production via VBS ($ZZjj$), and opposite-sign W-pair production via VBS (W^+W^-jj). Note that although we refer to the processes only as massive vector-boson production (W^\pm, Z), the diagrams with the exchange of photons instead of Z bosons have to be fully taken into account in order not to violate EW-gauge invariance.

Among the four process classes, the same-sign W-pair process provides a particularly clean signature in the fully leptonic decay mode, since due to the conservation of the electric charge no gluon-induced contributions may appear in the QCD-background di-

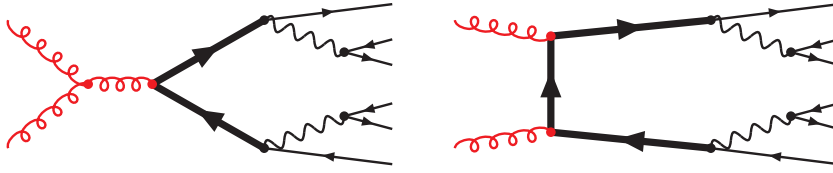


Figure 6.6.: Representative diagrams for $t\bar{t}$ -production decaying via $W^+bW^- \bar{b}$ to the $4\ell + 2j$ final state.

agrams. The opposite-sign W -pair process, on the other hand, is exceptionally plagued by a huge QCD background. Only for this process, the QCD contributions comprise diagrams with up to two resonant top quarks, as depicted in Fig. 6.6, which are additionally amplified by the genuinely large gluon flux at hadron colliders. In order to sufficiently suppress this overwhelming $t\bar{t}$ background, additional techniques have to be applied in order to study the corresponding VBS signal process, as will be discussed in Sec. 6.3.4.

6.2. Studying VBS at 100 TeV

In order to distinguish the specific signal of VBS reactions from the various background contributions one is unavoidably confronted with at hadron colliders, dedicated phase-space cuts for the different process classes are mandatory. Although the basic principles to improve on the signal-to-background ratio are very well known, at present colliders one is plagued by the relatively low cross sections in the remaining phase-space regions. The first experimental studies of VBS processes at the LHC at a c.m. energy of $\sqrt{s} = 8$ TeV by ATLAS [116–118] and CMS [119] for example, are based on merely a few events in the signal region, allowing only for very loose exclusion bounds for new physics.

While this situation will certainly improve with the higher luminosity and the higher energy reach of 13 TeV in LHC Run II, a dedicated study of differential distributions of the final-state particles will remain hardly performable. As already discussed in the previous chapter, this differential insight is, however, of particular importance, since possible deviations from the SM are expected to have a large impact in the tails of distributions, while total cross sections are considerably less sensitive to the effects of new physics. Since very recently, also a first calculation of the full NLO EW corrections to same-sign W -pair production via VBS is available [120], such that precise theoretical predictions, taking QCD and EW corrections into account, should be available very soon.

Therefore, the particle-physics community already discusses follow-up projects for future high-energy colliders, operating at even higher energies. For hadron-hadron colliders those are in particular the Future Circular hadron-hadron Collider (FCC-hh) [121] at CERN and the Chinese Super proton-proton Collider (SppC) [122], which were both envisaged operating at 100 TeV. For the sake of notation we refer to both

concepts in the following simply as FCC, meaning a 100 TeV proton-proton collider.

This year, various studies of SM [113, 123] and BSM [124] processes have been performed to obtain first insights on how and which kind of physics can be explored at the FCC. In Ref. [113], we have shown that, assuming an integrated luminosity of 30 ab^{-1} , the FCC delivers a sufficient amount of events to study differential distributions of all VBS processes up to very high energy scales with reasonable statistics.

In the remaining part of this chapter we present our study of VBS processes at 100 TeV performed in Ref. [113] as well as some results of our forthcoming analysis presented in Ref. [114].

6.2.1. Setup of the Analysis

In both our analyses [113, 114] we concentrate on the four VBS processes W^+W^+jj , W^+Zjj , $ZZjj$, and W^+W^-jj , each in a specific fully leptonic decay channel, such that no interference contributions among the process classes have to be taken into account. In the former study we additionally investigated single-vector boson production processes via VBF by means of the two processes Zjj and W^+jj , which will be presented in Sec. 6.3.5.

Apart from the QCD background for the opposite-sign W -boson channel, the treatment of which will be discussed separately below, all numerical calculations are performed with the VBFNLO Monte Carlo package [125]. The implementations of the VBS processes in VBFNLO are based on the NLO QCD calculations of Refs. [126–129] and Refs. [115, 130, 131] for the EW and QCD-induced processes, respectively.

In particular, these explicit calculations revealed that in the region of phase space where VBS is typically investigated, the impact of the NLO corrections can be strongly reduced by a specific choice of the renormalization and factorization scale. Although the corrections still show a certain kinematic dependence and obviously remain significant for precise predictions, this outcome also rectifies our restriction to the LO, especially at such an early stage of the FCC project. The recent elaborate review of Ref. [132] contains, among other topics, more details on the genuine size of QCD corrections to VBS and VBF processes. Our specific scale choices for the EW and QCD-induced contributions will be discussed in the next section.

Note that although we refer to the processes as $VVjj$ -production, the VBFNLO implementations on which our predictions are based, fully include all off-shell and finite-width effects of the EW gauge bosons in a modified version of the complex-mass scheme (see Sec. 3.2.2) where the weak mixing angle remains real [126]. For processes with intermediate Z bosons, also the photon contributions and the respective interference terms are considered throughout.

For all EW-induced contributions, two particular approximations have been exploited in order to considerably speed up the computation time of the matrix elements. On the one hand, they do not include any subprocesses where the incoming quarks directly fuse to an intermediate weak boson subsequently decaying to the considered final state. These s -channel contributions are regarded as part of the triple gauge-boson produc-

tion processes $pp \rightarrow VVV$, which populate completely different regions of phase space than VBS processes, and therefore can be safely neglected in studies concentrating on the VBS kinematics. Additionally, all interference contributions of t - and u -channel diagrams in processes with identical final-state (anti-)quarks are disregarded.

The general validity of these two approximations has been shown in Ref. [133] for the related Higgs production via VBF process ($pp \rightarrow Hjj$). After the application of VBS-specific phase-space cuts, the NLO QCD predictions applying the approximation agreed with the full results at the level of fraction of a percent. For the LO cross section of the W^+W^+jj process similar results have been obtained in Ref. [130]. In the predictions performed with the VBFNLO package we additionally disregard all contributions with external bottom quarks. While this common procedure can be well rectified due to the small b-quark PDF for initial-state b-quarks and motivated by a very efficient b-jet veto for final-state b's, a rigorous proof of this approximation is left to further studies.

The calculation of the QCD-induced background contribution for W^+W^-jj is performed with the HELAC-DIPOLES [134] package. As already mentioned in the previous section, this background in particular comprises gluon-induced contributions with on-shell top-quarks, decaying via W-boson emission into a $4\ell + 2b$ final state. Although disregarding all final-state b-quarks in the other contributions, for this $t\bar{t}$ -background we only neglect incoming bottom quarks, while a realistic b-jet veto is applied to the final-state b's, as will be discussed in Sec. 6.3.4. Moreover, in the same manner we also fully include $t\bar{t}$ contributions with one or two additional light jets, which are of the orders $\mathcal{O}(\alpha_s^3\alpha^4)$ and $\mathcal{O}(\alpha_s^4\alpha^4)$, respectively. Although suppressed due to their higher order in the strong coupling constant α_s , the resonant contributions of these processes give rise to very large cross sections and are therefore included in our study as part of the combined $t\bar{t}$ +jets sample. Note again, that these contributions also include all non-resonant diagrams, interference and off-shell effects of the top quarks as well as the W-bosons.

To ensure the correctness of our implementations we have cross-checked the results for the QCD-induced contributions calculated with the VBFNLO package against the results obtained with HELAC-DIPOLES and found full agreement within the numerical accuracy of the two codes on the integrated as well as on the differential level in all considered observables.

Our predictions for the single-vector boson production processes via VBF are also performed with the VBFNLO package and are based on the implementation of the NLO QCD calculation presented in Ref. [135].

6.2.2. Input Parameter and Default Selection Cuts

In this section we present the input parameters and a default set of selection cuts that are used in our numerical analysis. In addition to these selection criteria, for each considered process class dedicated cuts are applied, which will be derived process-

specifically in the next section. For all our results we use the SM masses and widths,

$$\begin{aligned}
M_W &= 80.385 \text{ GeV}, & \Gamma_W &= 2.097547 \text{ GeV}, \\
M_Z &= 91.1876 \text{ GeV}, & \Gamma_Z &= 2.508827 \text{ GeV}, \\
M_H &= 125.09 \text{ GeV}, & \Gamma_H &= 0.004066 \text{ GeV}, \\
m_t &= 172.5 \text{ GeV}, & \Gamma_t &= 1.340488 \text{ GeV}, \\
m_b &= 4.75 \text{ GeV}.
\end{aligned}
\tag{6.4}$$

Note that the mass and width of the top quark, as well as the mass of the bottom quark will only be relevant in the calculation of the top-background contributions of the W^+W^-jj -process.

The EW coupling constant is computed in the G_μ scheme from the above input parameters and the Fermi constant $G_\mu = 1.1663787 \times 10^{-5} \text{ GeV}^{-2}$, via

$$\alpha_{G_\mu} = \frac{\sqrt{2} G_\mu M_W^2}{\pi} \left(1 - \frac{M_W^2}{M_Z^2} \right).
\tag{6.5}$$

The CKM mixing of the quark generations (c.f. Eq.(2.33)) is neglected throughout, which means we assume a diagonal CKM matrix. For all contributions but the $t\bar{t}$ -background of the W^+W^-jj -process, we use the MMHT2014lo68cl set [136] and the corresponding values of α_s as provided by the LHAPDF6 repository [137]. The top-background contributions are consistently calculated in the 4-flavour scheme and we employ the MSTW2008lo68cl_{nf4} PDF set [138].

The factorization and renormalization scales, μ_F and μ_R , are set process-specifically: All EW-induced processes are of $\mathcal{O}(\alpha^6)$, and, thus, independent of μ_R . For μ_F , we use the momentum transfer Q_i from the incoming to the outgoing (anti-)quark on the upper and lower fermion lines, respectively,

$$\mu_F = Q_i,
\tag{6.6}$$

which has been shown reproduce the shapes of NLO distributions much better than a fixed scale. The same applies to the QCD-induced processes of $\mathcal{O}(\alpha_s^2\alpha^4)$, where we use the total transverse energy H_T^{VV} of each event as reference scale, such that

$$\mu_F = \mu_R = H_T^{\text{VV}}/2,
\tag{6.7}$$

with

$$H_T^{\text{VV}} = \sum_i p_{T,i} + E_T(V_1) + E_T(V_2).
\tag{6.8}$$

Here, the summation runs over the transverse momenta $p_{T,i}$ of all final-state partons i of the process. The transverse energy of each gauge boson is computed from its mass and the momenta of its leptonic decay products according to

$$E_T(V_i) = \sqrt{p_T^2(V_i) + M_{V_i}^2},
\tag{6.9}$$

where V_i is the corresponding weak gauge boson, W^\pm or Z .

Similarly, for the top-quark induced background processes of the orders $\mathcal{O}(\alpha_s^2\alpha^4)$, $\mathcal{O}(\alpha_s^3\alpha^4)$, and $\mathcal{O}(\alpha_s^4\alpha^4)$ we use

$$\mu_F = \mu_R = H_T^{\text{top}}/2, \quad (6.10)$$

with the transverse energy H_T^{top} being computed from the transverse energy of the top quarks or anti-quarks,

$$E_T(t) = \sqrt{p_T^2(t) + m_{\text{top}}^2}, \quad E_T(\bar{t}) = \sqrt{p_T^2(\bar{t}) + m_{\text{top}}^2}, \quad (6.11)$$

and the transverse momenta of all light partons in the final state of an event, yielding

$$H_T^{\text{top}} = \sum_i p_{T,i} + E_T(t) + E_T(\bar{t}). \quad (6.12)$$

For the reconstruction of jets from partons, we use the anti- k_T jet algorithm [139] with a cone radius of $R = 0.4$. In the final state we demand at least two jets with a minimum transverse momentum of

$$p_{T,\text{jet}} \geq 50 \text{ GeV}. \quad (6.13)$$

The two hardest jets fulfilling this cut are called *tagging jets* and are additionally required to reside in opposite hemispheres of the detector,

$$y_{j_1} \times y_{j_2} < 0. \quad (6.14)$$

In addition to the jet cuts, we impose cuts on the transverse momenta and the rapidities of the charged leptons,

$$p_{T,l} \geq 20 \text{ GeV}, \quad |y_l| \leq 5, \quad (6.15)$$

and require a jet-lepton separation in the rapidity-azimuthal angle plane,

$$\Delta R_{\text{jet},l} \geq 0.4. \quad (6.16)$$

Since the VBS topology favours two widely separated tagging jets and central decay products, a very powerful tool to further suppress the background is provided by requiring the charged leptons to be located between these two tagging jets in rapidity,

$$y_{j,\text{min}}^{\text{tag}} < y_l < y_{j,\text{max}}^{\text{tag}}. \quad (6.17)$$

In order to suppress contributions from virtual photons, $\gamma^* \rightarrow l^+l^-$, in processes with intermediate Z bosons, i.e. the process classes $ZZjj$ and W^+Zjj , we furthermore impose the minimal invariant-mass cut on oppositely charged leptons,

$$M_{l^+l^-} > 15 \text{ GeV}, \quad (6.18)$$

which we refined for our second study to apply only to same-flavour pairs, $M_{e^+e^-}$ and $M_{\mu^+\mu^-}$. This, however, only affects the $ZZjj$ process class and in the results we explicitly quote the difference between to two applied methods.

In addition to these minimal cuts, dedicated process-specific selection cuts are devised for each channel.

6.3. Phenomenological Results

In this section we present the results of our analyses of various VBS (Secs. 6.3.1-6.3.4) and VBF (Sec. 6.3.5) processes performed to explore the capabilities of a future 100 TeV proton-proton collider. For each process we devise specific selection cuts to improve on the signal-to-background (S/B) ratio by simultaneously reduce the cross section of the signal process as little as possible.

6.3.1. Same-sign W -pair Production via VBS

As already mentioned in the introduction, the same-sign W -pair-plus-dijet process, $pp \rightarrow W^\pm W^\pm jj$, provides the cleanest signature of all VBS processes, as due to charge conservation no gluon induced subprocesses contribute to the QCD-background. Moreover, since for the same reason each quark line has to be connected to at least one massive EW boson, the fully inclusive cross section, i.e. without applying any phase-space cuts, of both, the EW-induced and the QCD-induced, contributions is finite. These two properties make this process class particularly suitable to study the genuine properties of VBS reactions at hadron colliders.

In the following we concentrate on the $pp \rightarrow W^+ W^+ jj$ process, which, due to the positive charge of the proton, yields a slightly larger cross section than the production of two negatively charged W s, and consider the particular final state $\nu_e e^+ \nu_\mu \mu^+ jj$. Results for the related $W^- W^- jj$ process are obtained thereof by charge conjugation and parity reversal. Note, however, that these transformations also include the initial-state protons, requiring to change the respective proton PDFs to anti-proton PDFs.

In Fig. 6.7 we show the energy dependence of the EW- and QCD-induced contributions of the fully inclusive cross section, revealing a dominance of the EW-induced process above a hadronic c.m. energy of about 33 TeV. This demonstrates that kinematic properties of specific contributions might well become equally important as the size of the involved couplings, which would rather suggest an obviously larger QCD contribution independently of the energy regime.

By looking at the differential distribution of the invariant mass of the two tagging jets, m_{jj} , in the fully inclusive setup, depicted on the left-hand side (l.h.s.) of Fig. 6.8, the increasing dominance towards larger energies becomes apparent. While the region that is preferably populated by QCD contributions is also accessible with lower energies, the production of two jets with a large invariant mass, as favoured by the EW-induced process, only becomes competitive at more powerful colliders. However, even at 7 TeV, where the QCD-induced process exceeded the EW contributions by roughly a factor of 1.7 at the inclusive level, process-specific cuts allow to achieve a S/B ratio of ~ 27 , as explicitly shown in the NLO analysis of Ref. [140].

For such an efficient suppression of the QCD-background contributions, beside the invariant dijet mass, also the rapidity separation of the two jets,

$$\Delta y_{jj} = |y_{j1} - y_{j2}|, \quad (6.19)$$

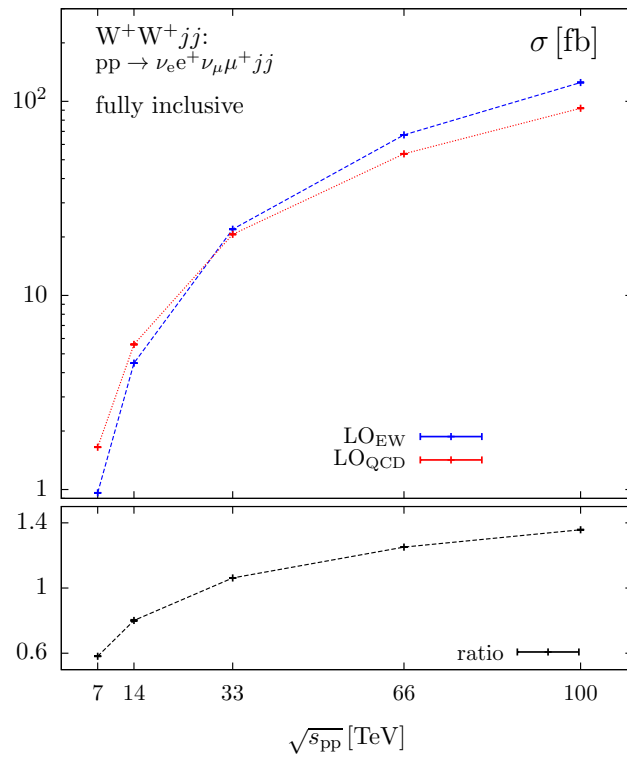


Figure 6.7.: Energy dependence of the EW-induced (blue line) and QCD-induced (red line) contributions to the fully inclusive cross section for $pp \rightarrow \nu_e e^+ \nu_\mu \mu^+ jj$. The lower panel shows the ratio of the EW- to the QCD-induced contribution.

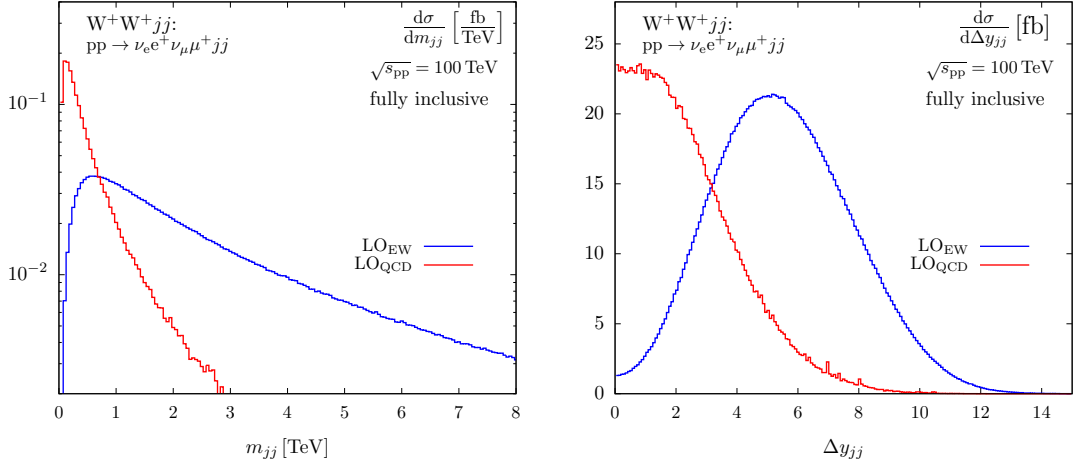


Figure 6.8.: Invariant mass (l.h.s.) and rapidity separation (r.h.s.) of the two tagging jets for the EW-induced (blue line) and QCD-induced (red line) contributions to $pp \rightarrow \nu_e e^+ \nu_\mu \mu^+ jj$, without any selection cuts.

plays a very important role, as it exhibits particularly distinctive shapes for the two production mechanisms. On the right-hand side (r.h.s.) of Fig. 6.8 we show the rapidity separation in the fully inclusive setup. From the two plots of Fig. 6.8 we observe that the two jets from the QCD-induced W^+W^+jj processes are mostly produced with a small invariant mass and close to each other in rapidity, while the VBS contribution to the EW-induced processes gives rise to a dijet system of large invariant mass and large rapidity separation.

We will use this distinct kinematic property of the VBS production mode as the most important ingredient for the efficient suppression of the QCD-background in all process classes. Although for the W^+W^+jj process already the application of our default selection cuts of Eqs. (6.13)–(6.17) yields a S/B ratio of 24, we additionally impose the specific selection cuts

$$m_{jj} > 500 \text{ GeV}, \quad \Delta y_{jj} > 1.5, \quad (6.20)$$

to define our VBS setup for the W^+W^+jj process. In Tab. 6.1 we list the cross sections for the two separate contributions together with the achieved S/B ratios for the three different selection criteria discussed so far. Since our result for the S/B ratio of 29 only slightly improved with respect to the 7 TeV analysis of Ref. [140] mentioned above, we want to stress that our VBS-specific cuts of Eq. (6.20) are very loose, especially compared to the applied VBS cuts of the 7 TeV analysis ($m_{jj} > 600$, $\Delta y_{jj} > 4$), which yield an EW-signal of only 0.2 fb [140]. In Fig. 6.9 we show the invariant mass distribution and rapidity separation of the two tagging jets, now after the application of our default cuts and the additional VBS-specific cuts of Eq. (6.20), respectively. Compared to Fig. 6.8 we recognize the huge impact due to the application of the default cuts,

FCC - W^+W^+jj	σ_{EW} [fb]	σ_{QCD} [fb]	S/B
fully inclusive	125.05(4)	92.1(1)	1.36
default cuts	49.936(8)	2.081(2)	24.00
VBS cuts	49.335(8)	1.683(1)	29.33

Table 6.1.: Cross-section contributions for the EW-induced W^+W^+jj production process together with the irreducible QCD background and the S/B ratio within the fully inclusive setup, our default selection cuts of Eqs. (6.13)–(6.17), and our VBS selection cuts, applying in addition to the default setup also the cuts of Eq. (6.20). The numbers in parentheses represent the Monte Carlo uncertainty on the last given digit.

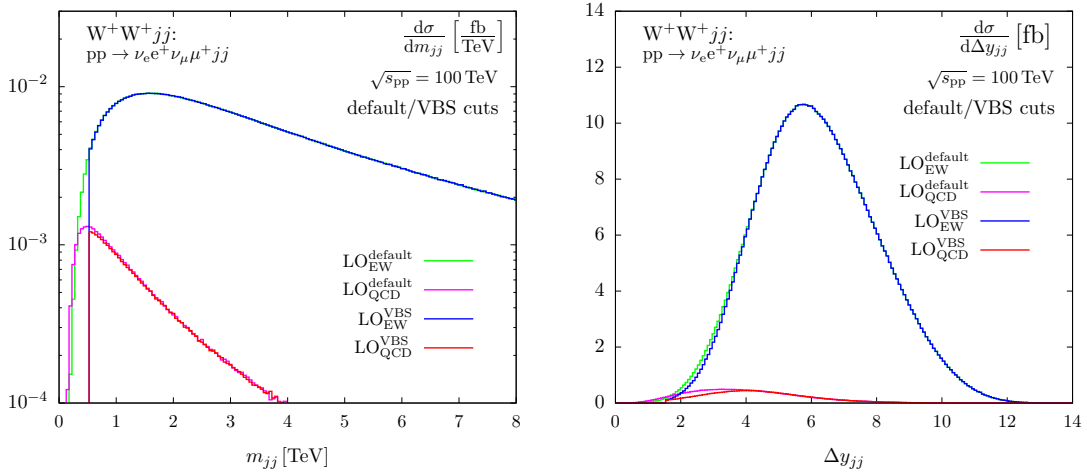


Figure 6.9.: Invariant mass (l.h.s.) and rapidity separation (r.h.s.) of the two tagging jets for the EW- and QCD-induced contributions to $pp \rightarrow \nu_e e^+ \nu_\mu \mu^+ jj$ within our default selection cuts of Eqs. (6.13)–(6.17) (green and purple line) and the additional VBS-specific cuts of Eq. (6.20) (blue and red line).

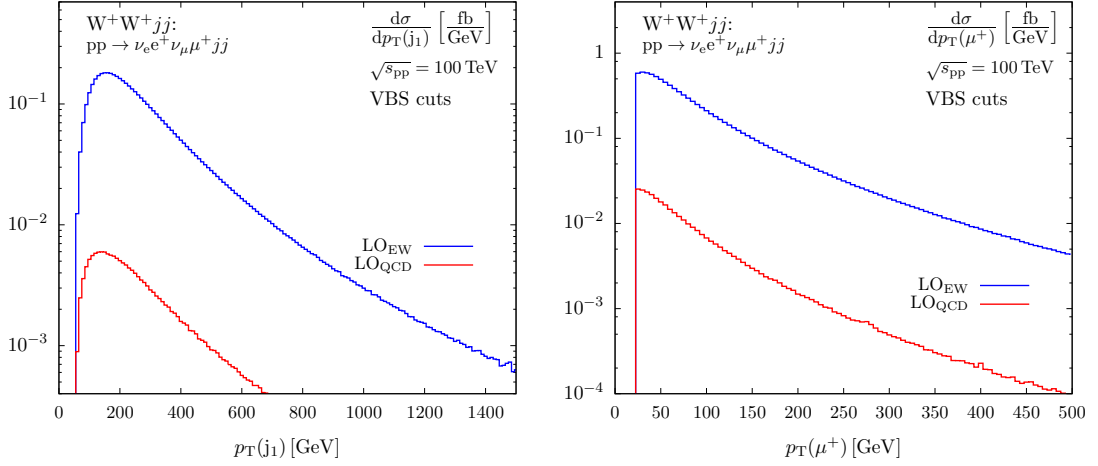


Figure 6.10.: Transverse-momentum distributions of the hardest tagging jet (l.h.s.) and the anti-muon (r.h.s.) for the EW-induced (blue line) and QCD-induced (red line) contributions to $pp \rightarrow \nu_e e^+ \nu_\mu \mu^+ jj$, within the selection cuts of Eqs. (6.13)–(6.17) and Eq. (6.20).

leading already to a dominance of the EW-induced contribution over almost the entire kinematic range. Our VBS-specific cuts of Eq. (6.20) are finally devised such that they eliminate the remaining QCD-dominated regions, as can be seen in Fig. 6.9.

While the EW-induced contribution is only marginally affected by the VBS-specific cuts ($-0.6 \text{ fb} \simeq -1\%$), they reduce the QCD background by 19% and, thus, improving the S/B ratio by another 5% compared to the default selection criteria. Due to the steep decrease of the m_{jj} -distribution in Fig. 6.9 it is obvious that much higher S/B -ratios can be easily achieved by simply increasing the cut value towards larger invariant dijet mass, which, however, would also significantly decrease our signal cross section.

In the final VBS setup, the impact of the QCD-background contributions on the differential distributions of the individual final-state particles is also very small, as we representatively demonstrate for the hardest tagging jet (j_1) and the anti-muon (μ^+). In the Figs. 6.10 and 6.11 we show their transverse-momenta and rapidity distributions, respectively, which are all clearly dominated by the EW-induced process over the entire kinematic range.

The transverse-momentum distribution of the hardest tagging jet in the EW-induced process exhibits a peak at about 170 GeV, while the QCD-induced contribution tends to produce slightly softer jets. The respective distribution of the anti-muon is less distinctive and only shows a slightly steeper decrease towards larger energy scales for the QCD-induced contribution.

In 6.11 we observe that the majority of the tagging jets in the QCD mode are typically produced at smaller rapidities than in the EW case, where the two peaks in $d\sigma/dy_{j_1}$ occur at values as large as ± 4 . The anti-muons, on the other hand, are mostly located

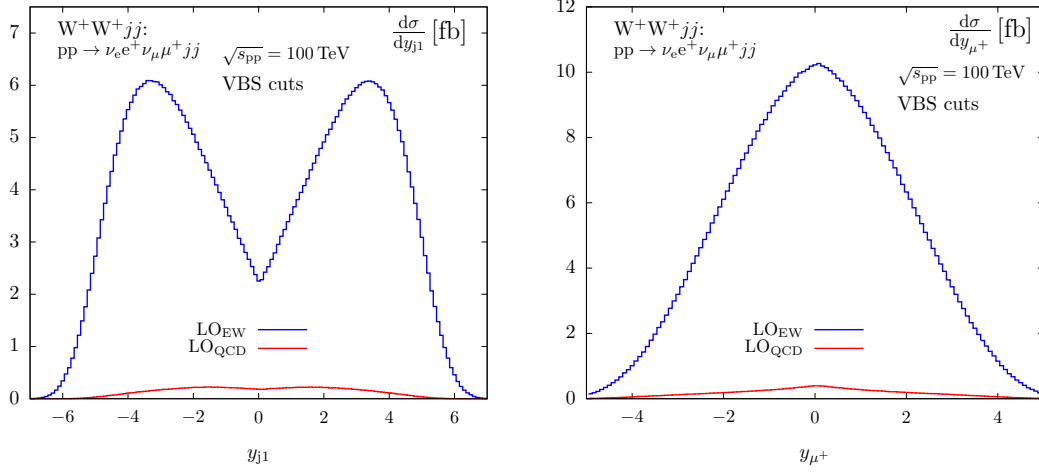


Figure 6.11.: Rapidity distributions of the hardest tagging jet (l.h.s.) and the anti-muon (r.h.s.) for the EW-induced (blue line) and QCD-induced (red line) contributions to $pp \rightarrow \nu_e e^+ \nu_\mu \mu^+ jj$, within the selection cuts of Eqs. (6.13)–(6.17) and Eq. (6.20).

at central rapidities in both production modes.

The tails of the invariant mass distributions of the gauge-boson system are most sensitive to the exact realization of EWSB in the SM or possible new physics effects. In the W^+W^+jj channel, however, this quantity is not fully reconstructible due to the presence of two final-state neutrinos, which escape the detector without observation. In this case, the transverse mass of the W^+W^+ system is considered instead, that is defined by

$$M_{T_{WW}} = \sqrt{(E_T^{ll} + E_T^{\text{miss}})^2 - (\vec{p}_T^{ll} + \vec{p}_T^{\text{miss}})^2}, \quad (6.21)$$

with

$$E_T^{ll} = \sqrt{(\vec{p}_T^{ll})^2 + M_{ll}^2}, \quad E_T^{\text{miss}} = |\vec{p}_T^{\text{miss}}|, \quad (6.22)$$

where, \vec{p}_T^{ll} denotes the transverse momentum of the charged-lepton system, and \vec{p}_T^{miss} is the total transverse momentum of the neutrino system.

The transverse-mass distribution depicted on the l.h.s of Fig. 6.12 clearly exhibits the dominance of the EW signal over the entire kinematic range. Thus, even after the application of a severe cut on $M_{T_{WW}}$ that might be necessary in new physics searches, the impact of the QCD-induced background on the VBS signal will remain small, or might even be further reduced. On the r.h.s. of Fig. 6.12 we show the number of events above a specific minimal value of $M_{T_{WW}}$, assuming an integrated luminosity of 30 ab^{-1} . Given the steep decrease of the $M_{T_{WW}}$ distribution towards larger energy scales of four orders of magnitude for a 6 TeV increase of the invariant mass, it is remarkable that above 10 TeV still $\mathcal{O}(10^2)$ signal events are delivered at the FCC. This explicitly reveals the potential of the FCC to test the SM via VBS reactions up to very high energy scales.

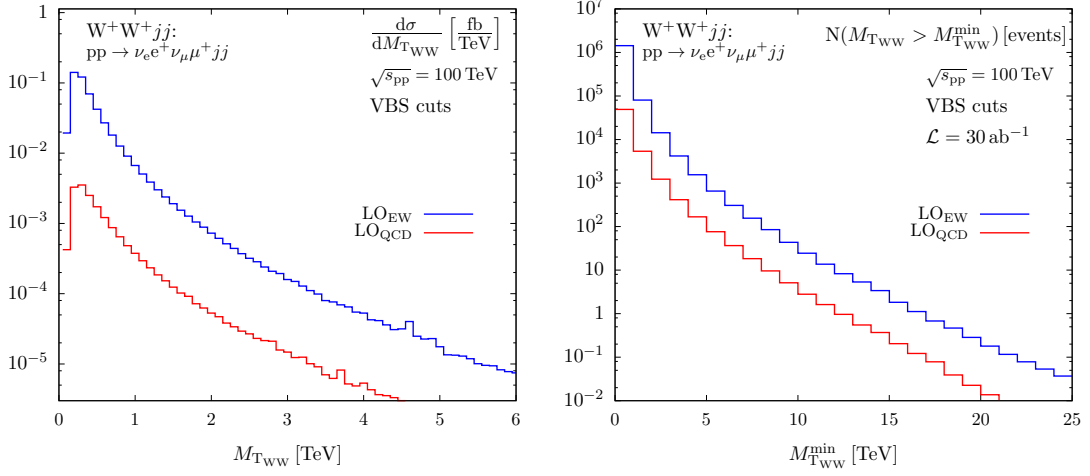


Figure 6.12.: Transverse-mass distribution of the gauge-boson system (l.h.s.) and total number of events (N) produced above a certain minimal value $M_{T_{WW}}^{\min}$ for the same observable (r.h.s.) for the EW-induced (blue line) and QCD-induced (red line) contributions to $pp \rightarrow \nu_e e^+ \nu_\mu \mu^+ jj$, within the selection cuts of Eqs. (6.13)–(6.17) and Eq. (6.20). For the computation of the number of events an integrated luminosity of 30 ab^{-1} is assumed.

6.3.2. $W^\pm Z$ Production via VBS

In contrast to the same-sign W-pair production channel that is free of gluon-induced background processes, the remaining VBS reactions are plagued by considerably larger QCD backgrounds. Additionally, the fully inclusive cross sections of all other processes are not by themselves finite. For this reason we begin our investigation after the application of our default cuts.

We concentrate again on the positively charged W-boson in the $W^\pm Z jj$ channel, which yields a slightly larger cross section than the $W^- Z jj$ mode, and consider the representative $pp \rightarrow e^+ \nu_e \mu^+ \mu^- jj$ process.

In Fig. 6.13 we show the invariant mass and rapidity separation of the two tagging jets after our default cuts have been applied. This illustrates clearly the different behaviour of the dijet system in the $W^\pm Z jj$ mode compared to the $W^+ W^+ jj$ channel considered in the same setup in Fig. 6.9. The invariant dijet mass is still dominated by QCD corrections up to around $m_{jj} \sim 4 \text{ TeV}$, and only for rapidity separations larger than roughly $\Delta y_{jj} = 7$ the EW-induced process begins to yield the largest contribution. However, due to the interplay between the two observables already the considerably looser process-specific selection criteria

$$m_{jj} > 2500 \text{ GeV}, \quad \Delta y_{jj} > 5, \quad (6.23)$$

lead to a reduction of the QCD-induced contribution of almost 90%, while actually 60%

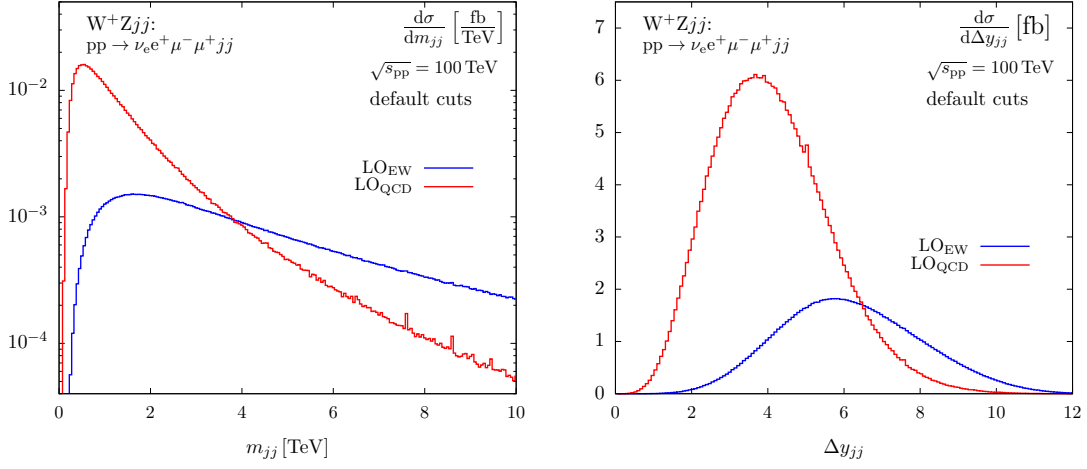


Figure 6.13.: Invariant mass (l.h.s.) and rapidity separation (r.h.s.) of the two tagging jets for the EW-induced (blue line) and QCD-induced (red line) contributions to $pp \rightarrow \nu_e e^+ \mu^- \mu^+ jj$, within our default selection cuts of Eqs. (6.13)–(6.18).

of the EW-induced process remains in our signal region, resulting in a S/B ratio of 1.8. In Tab. 6.2 we list the cross section of the two considered selection criteria including the corresponding S/B ratio.

Figure 6.14 shows the invariant mass and the rapidity separation of the two jets after our process-specific VBS cuts of Eq. (6.23) have been applied. As before, a better S/B ratio can be easily achieved by raising the cut on m_{jj} towards larger invariant masses since the QCD-induced process shows a much steeper decrease in this observable.

Even though the purely leptonic decay mode of the $W^\pm Zjj$ process class also contains a neutrino in the final state that is invisible to the detector, the invariant-mass distribution of the leptonic decay products, M_{WZ} , can be reconstructed. Following Ref. [141], the unknown longitudinal component of the neutrino momentum is constrained by the solution of the quadratic equation

$$M_{W^+}^2 = (p_{\nu_e} + p_{e^+})^2, \quad (6.24)$$

which physically means that we assume all neutrinos being produced by an on-shell decay of the W^+ -boson. For kinematic configurations that do not allow for a (real) solution of Eq. (6.24), the M_{WZ} histogram is not filled, thus resulting in a slightly reduced cross section for the corresponding observable. In our VBS setup this reduction amounts to $\sim 11\%$ for the EW- as well as for the QCD-induced contribution and hence does not change the S/B ratio. However, this effect has to be taken into account also in the theoretical prediction in order to accurately predict the outcome of a possible measurement, where the momentum of the neutrino always has to be reconstructed.

On the l.h.s of Fig. 6.15 we show the reconstructed invariant-mass distributions of

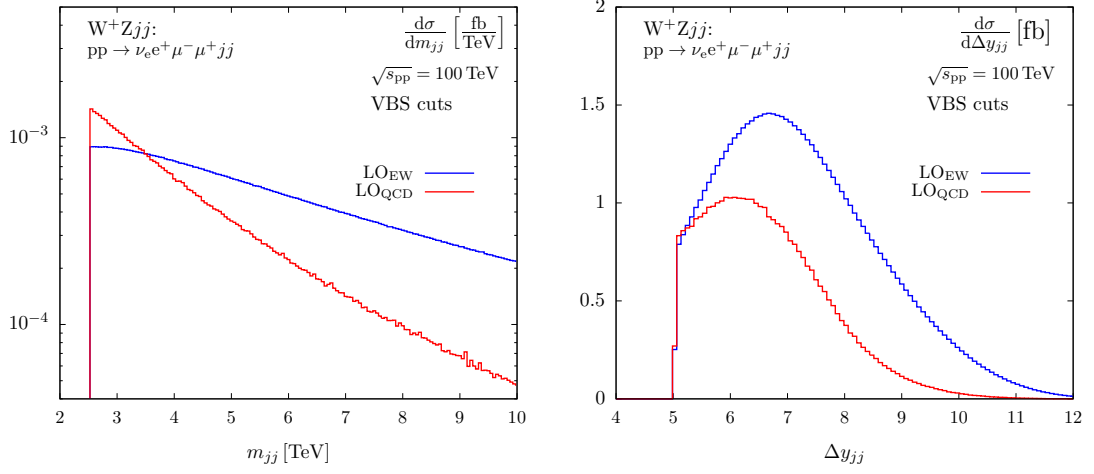


Figure 6.14.: Invariant mass (l.h.s.) and rapidity separation (r.h.s.) of the two tagging jets for the EW-induced (blue line) and QCD-induced (red line) contributions to $pp \rightarrow \nu_e e^+ \mu^- \mu^+ jj$, within our default selection cuts of Eqs. (6.13)–(6.18) and the process-specific VBS cuts of Eq. (6.23).

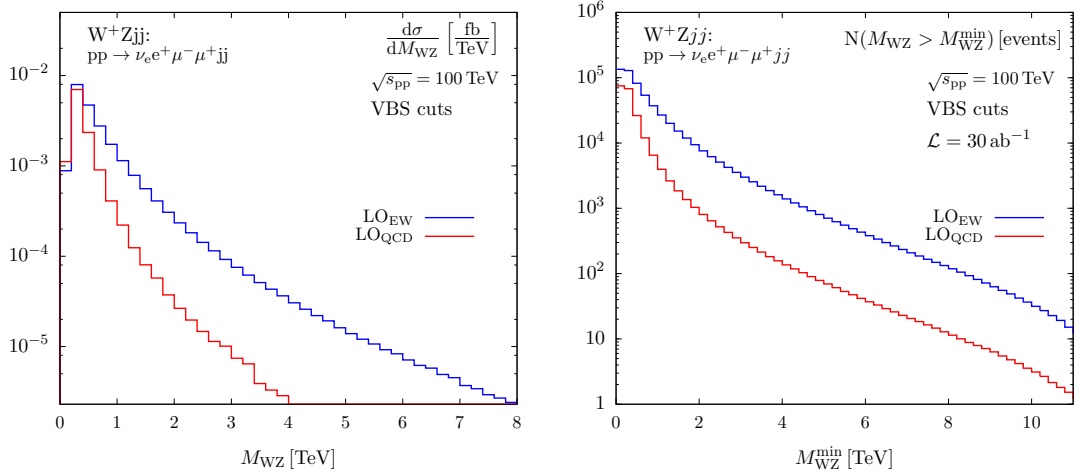


Figure 6.15.: Invariant-mass distribution of the WZ system reconstructed from the lepton momenta (l.h.s.) and total number of events (N) produced with $M_{WZ} > M_{WZ}^{\min}$ (r.h.s.) for the EW-induced (blue line) and QCD-induced (red line) contributions to $pp \rightarrow \nu_e e^+ \mu^- \mu^+ jj$, within the selection cuts of Eqs. (6.13)–(6.18) and Eq. (6.23). An integrated luminosity of 30 ab^{-1} is assumed.

FCC - W^+Zjj	σ_{EW} [fb]	σ_{QCD} [fb]	S/B
default cuts	8.464(2)	23.38(1)	0.36
VBS cuts	5.0771(7)	2.786(2)	1.82

Table 6.2.: Cross sections for the EW-induced W^+Zjj production process together with the irreducible QCD background and the signal-to-background ratio, S/B , within our default selection cuts of Eqs. (6.13)–(6.18) and the VBS selection criteria, with the additional cuts of Eq. (6.23). The numbers in parentheses represent the Monte Carlo uncertainty on the last given digit.

the leptonic decay products, for the EW- and QCD-induced contribution. Since there exists no particle within the SM exhibiting the appropriate quantum numbers and mass to resonantly produce an on-shell W^+Z system, both contributions are characterized by a broad continuum.

In particular BSM models, however, so-called W' bosons are predicted, potentially decaying into the WZ system which, thus, would lead to a clear signal above the SM continuum in the M_{WZ} distribution. Among the most prominent examples showing such a signature are Kaluza-Klein models, where the compactification of an additional space-time dimension leads to towers of gauge bosons with masses that would allow for a resonant decay into the $W^\pm Z$ -gauge boson system. The impact of such new resonances on VBS signatures was discussed, e.g., in [142].

On the r.h.s of Fig. 6.15 we show the number of events expected in the reconstructed M_{WZ} distribution above a specific value of M_{WZ} . Assuming an integrated luminosity of 30 ab^{-1} , within our VBS selection criteria this distribution would be experimentally accessible at least up to 8 TeV, where we still expect $\mathcal{O}(10^2)$ events in the EW-induced contribution.

6.3.3. Z-pair Production via VBS

The $ZZjj$ channel is of particular phenomenological importance, both, in the high energy region, where it is sensitive to new scalar resonances, but also in lower energy regions where this process comprises the most important background contribution to Higgs production via VBF in the $H \rightarrow ZZ$ decay mode.

From the experimental point of view, the $ZZjj$ channel provides the cleanest signature of all VBS processes in the fully leptonic decay channel, since the kinematics of the gauge-boson system is fully reconstructable, without any additional constraints. Note that this process with four charged leptons in the final state is slightly more affected by the lepton cuts of our default selection given in Eqs. (6.15)–(6.18). Much more importantly to consider, however, is the rather small branching fractions of $Z \rightarrow l^-l^+$ of merely 3.4%, compared to $\sim 11\%$ for $W^\pm \rightarrow l^\pm \bar{\nu}$ [104], as well as the smaller couplings

FCC - $ZZjj$	σ_{EW} [fb]	σ_{QCD} [fb]	S/B
default cuts	2.9575(9)	1.8773(8)	1.58
VBS cuts	2.1825(7)	0.2279(2)	9.58

Table 6.3.: Cross sections for the EW-induced $ZZjj$ production process together with the irreducible QCD background and the signal-to-background ratio, S/B , within our default selection cuts of Eqs. (6.13)–(6.18) and the VBS selection cuts, with the additional cuts of Eq. (6.25). The numbers in parentheses represent the Monte Carlo uncertainty on the last given digit.

of the Z bosons to the incoming quarks (see Tab. C.4 in App. C), which consequently results in much smaller cross sections for ZZ production via VBS than for the two process classes considered before.

Nevertheless, we concentrate in the following on the purely leptonic decay mode $ZZ \rightarrow e^-e^+\mu^-\mu^+$ and show that this process may be studied with sufficient statistics at the FCC. In Tab. 6.3 we list the EW- and QCD-induced contributions to the cross section within our default cut setup of Eqs. (6.13)–(6.18) and after the additional application of the process-specific VBS cuts of

$$m_{jj} > 2000 \text{ GeV}, \quad \Delta y_{jj} > 3, \quad (6.25)$$

which reduce the cross section of the QCD induced contribution by almost 90%, while 74% of the EW-signal cross section pass the additional cuts, resulting in a S/B ratio of almost 10.

Applying the cut of Eq. (6.18) to all pairs of oppositely charged leptons, i.e. additionally including a cut on the two pairs $e^-\mu^+$ and $e^+\mu^-$, result in the cross sections $\sigma_{\text{EW}} = 2.1506(7)$ and $\sigma_{\text{QCD}} = 0.2235(2)$. Since this corresponds to a difference to our default setting, where the cut is only applied to same-flavour pairs, listed in Tab. 6.3 of less than -2% for both production modes, we can safely state that such a treatment does not notably change the result.

Figure 6.16 illustrates the influence of the VBS-specific cuts of Eq. (6.25) on the two directly affected dijet observables m_{jj} and Δy_{jj} . While for invariant masses larger than roughly 1.5 TeV the EW-induced cross section already dominates without the additional cuts of Eq. (6.25) their application leads to a clear dominance over the whole kinematic range in both observables.

Within these selection criteria, the invariant mass of the ZZ system constructed from the four final-state leptons is shown in Fig. 6.17 for two different kinematic ranges. In the low energy region, on the l.h.s., we can identify the Z-boson peak at around 91 GeV, appearing in both production modes, while the Higgs resonance is only part of the purely EW process. Note, in particular, that the EW-induced process is more than three orders of magnitude larger at the Higgs resonance than the QCD-background

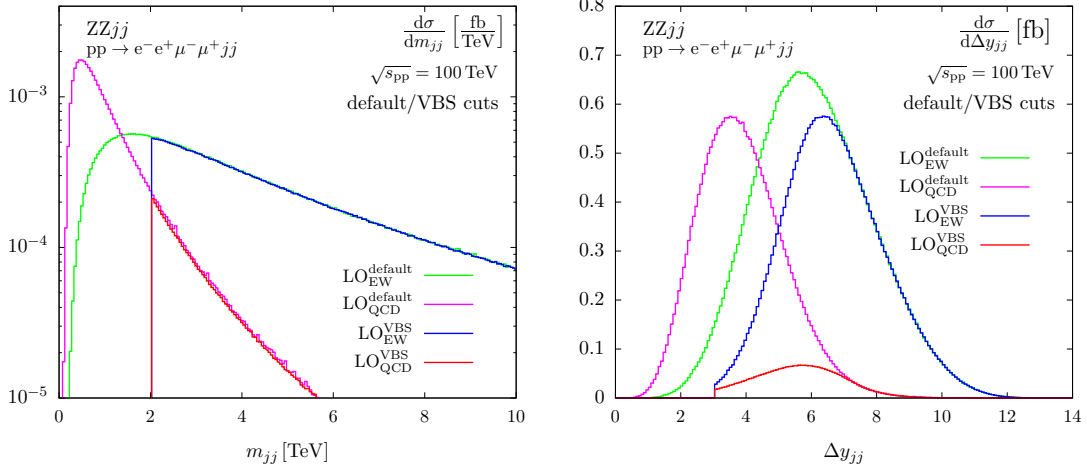


Figure 6.16.: Invariant mass (l.h.s.) and rapidity separation (r.h.s.) of the two tagging jets for the EW-induced and QCD-induced contributions to $pp \rightarrow e^-e^+\mu^-\mu^+jj$, within our default selection cuts of Eqs. (6.13)–(6.18) (green and purple line) and the additional application of the VBS-specific cuts of Eq. (6.25) (blue and red line).

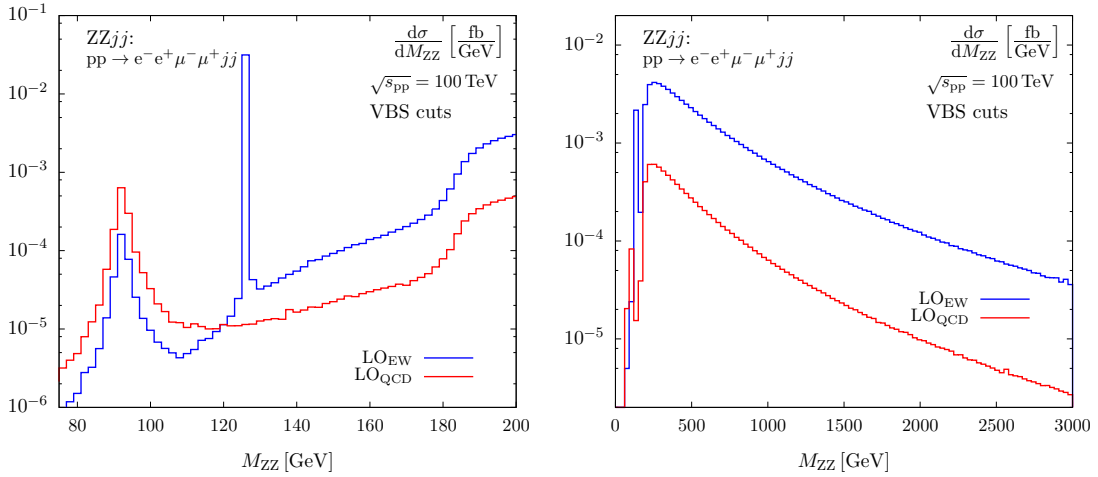


Figure 6.17.: Invariant-mass distribution of the four-lepton system for two different ranges of the EW-induced (blue line) and QCD-induced (red line) contributions to $pp \rightarrow e^-e^+\mu^-\mu^+jj$, within the selection cuts of Eqs. (6.13)–(6.18) and Eq. (6.25).

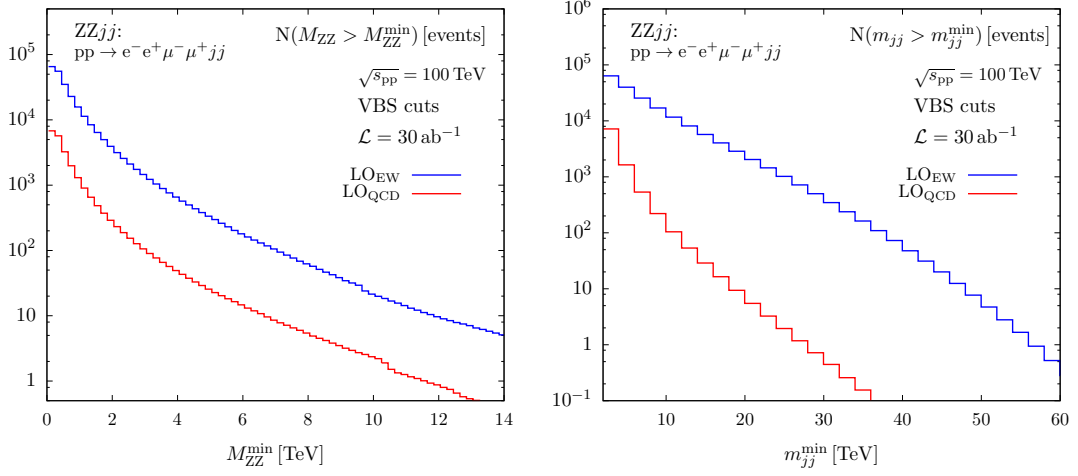


Figure 6.18.: Total number of events (N) produced with $M_{ZZ} > M_{ZZ}^{\min}$ (l.h.s.) and with $m_{jj} > m_{jj}^{\min}$ (r.h.s.) for the EW-induced (blue line) and QCD-induced (red line) contributions to $pp \rightarrow e^- e^+ \mu^- \mu^+ jj$, within the selection cuts of Eqs. (6.13)–(6.18) and Eq. (6.25). An integrated luminosity of 30 ab^{-1} is assumed.

contribution, although we did not even apply specific selection cuts to pronounce this region. Instead, our selection cuts of Eq. (6.25) are designed especially to suppress the QCD background in the high energy region, which is shown for the same observable on the r.h.s. of Fig. 6.17. The broad continuum above the Z-pair production threshold of $M_{ZZ} = 2M_Z \approx 180 \text{ GeV}$ is clearly dominated by the EW-induced contribution above which new physics effects entering via the EW-sector could be visible as distinct peaks, similar to the Higgs peak.

Compared to the fast decrease of the QCD-induced contribution in the m_{jj} distribution (l.h.s. of Fig. 6.16) the M_{ZZ} observable almost shows a constant differential S/B ratio above the Z-pair threshold. This becomes even more apparent if we consider the number of events above a specific minimal value for these two observables, depicted in Fig. 6.18. The number of events with an invariant four-lepton mass above M_{ZZ}^{\min} is shown on the left up to $M_{ZZ}^{\min} = 14 \text{ TeV}$, above which less than 10 events are expected if an integrated luminosity of 30 ab^{-1} is assumed. Every cut value on M_{ZZ} basically yields the same S/B ratio as our integrated result and for every 10 events of the EW-induced process one QCD-background event is expected. The situation is quite different in case of the invariant dijet mass, which we show on the r.h.s. of Fig. 6.18. Here, up to a cut value of $\sim 40 \text{ TeV}$ presumably sufficient events to perform differential measurements are predicted. As expected from the results for the W^+W^+jj and W^+Zjj process classes, the S/B ratio can most easily be improved by further raising the cut on m_{jj} , which is also apparent from Fig. 6.16. Based on Fig. 6.18 we can state that even for cut values on the invariant dijet mass as large as 10 TeV still $\mathcal{O}(10^4)$ events are expected for the EW-induced signal process, while the QCD-background is already suppressed by a least

two orders of magnitude and therefore of minor importance.

6.3.4. Opposite-sign W-pair Production via VBS

The purely EW opposite-sign W-pair production process via VBS exhibits the largest cross section of all VBS reactions. For the considered final state with different types of leptons, $\nu_e e^+ \mu^- \bar{\nu}_\mu j j$, within our default cut setup of Eqs. (6.13)–(6.17) we obtain with 99.38(8) fb almost twice the cross section of the W^+W^+jj process (c.f. Tab. 6.1).

However, in contrast to the same-sign W-pair VBS process, also the QCD backgrounds for the oppositely charged W-pair process are much larger. The aforementioned gluon-induced contributions are one reason, but additional contributions stemming from the top-quark pair production processes ($t\bar{t}$) account for the major part of the background. Considering the dominant decay mode of the top quarks into W bosons and bottom quarks, the latter may be misidentified as light-flavour tagging jets, thus leading to the same $4\ell 2j$ final state as the EW-signal process. Assuming an ideal (i.e. 100% efficient) b-tagging efficiency, these contributions obviously may be omitted entirely, but if realistic efficiencies are assumed for the b-jet veto, some events of this large background contribution will definitely remain in the sample. Additionally, modes where a $t\bar{t}$ pair is produced in association with one or two additional light-flavour jets that may mimic the tagging jets of a VBS event are even more problematic than $t\bar{t}$ -production without additional jets. As we will see, these modes will remain the major source of background.

For a realistic estimate of the background contribution, in addition to the genuine QCD background with two light-flavour jets in the final state, we therefore fully include a $t\bar{t} + \text{jets}$ sample in our analysis. This sample comprises of the three LO processes

$$pp \rightarrow 4\ell b\bar{b}, \quad pp \rightarrow 4\ell b\bar{b}j, \quad pp \rightarrow 4\ell b\bar{b}jj, \quad (6.26)$$

to which we refer in the following simply as $t\bar{t}$, $t\bar{t}j$, and $t\bar{t}jj$, respectively. The calculation of all QCD-background contributions is performed with the HELAC-DIPOLES [134] package in which all non-resonant diagrams, interference and off-shell effects of the top quarks as well as the W bosons are fully taken into account.

Considering the $t\bar{t}$ process, the two resulting tagging jets always stem from the two b quarks. We apply the realistic b-tagging efficiencies listed in Tab. 6.4 to both final-state b-quarks and discard any event in which at least one of them has been identified as such.

For the $t\bar{t}j$ process, only one of the two b quarks must be misidentified as light-flavour tagging jet, while the additional light jet mimics the second tagging jet and the second b-jet remains untagged and therefore entirely unconstrained (note that Eq. (6.13) only applies to the two tagging jets). Actually, this is even the only configuration we take into account for the $t\bar{t}j$ process, since the other possibility—two misidentified b-jets and an unconstrained light (i.e. massless) jet—is the real-correction contribution to the $t\bar{t}$ process, which is not well defined without the virtual contribution. Only due to the

p_{Tj}^{veto} [GeV]	$1.4 < \eta_j^{veto} $	$ \eta_j^{veto} < 1.4$
50 - 80	65%	75%
80 - 120	70%	80%
120 - 170	70%	80%
> 170	65%	75%

Table 6.4.: Assumed b-tagging efficiencies as functions of the transverse momentum of the jet for different rapidity ranges (adapted from Ref. [142]).

finite bottom-quark mass, the process with the unconstrained b-jet yields a finite and therefore well defined contribution.

The same procedure is applied to the $t\bar{t}jj$ process, where consequently both light jets have to mimic the tagging jets and the two b-jets remain unconstrained in the event.

In order to suppress the $t\bar{t}$ + jets background as much as possible we further apply a central-jet veto, which means we reject any event with an additional observed jet in the rapidity interval between the two tagging jets,

$$y_{j,\min}^{\text{tag}} < y_j^{\text{veto}} < y_{j,\max}^{\text{tag}}. \quad (6.27)$$

For this jet veto to apply, we require the additional jet to exhibit at least a transverse momentum of $p_{Tj}^{\text{veto}} \geq 50$ GeV to be well detectable. Note that the contributions of the EW VBS signal and the QCD-induced W^+W^-jj background never exhibit more than two jets and, thus, always pass the cut of Eq. (6.27). Additional jet activity would occur in these reactions only in higher-order corrections that include real-emission contributions. It is, however, a well-known feature of the VBS-signal processes, that extra parton emission typically occurs close to the tagging jets, see e.g. Ref. [143] and references therein. In contrast to $t\bar{t}$ production and the genuine QCD-induced background, even at NLO, the EW-signal contribution therefore exhibits hardly jet activity in the central-rapidity region, such that a central-jet veto is a very powerful tool to suppress these kind of background contributions.

In addition to the default cut setup of Eqs. (6.13)–(6.17), the realistic b-jet veto, as well as the central-jet veto of Eq. (6.27), the following process-specific cuts are imposed to define the VBS-cut setup,

$$m_{jj} > 2000 \text{ GeV}, \quad \Delta y_{jj} > 5. \quad (6.28)$$

Even with these rather stringent cuts on the dijet system, however, the $t\bar{t}$ + jets contribution clearly dominates the EW VBS signal. While the genuine QCD background is already reduced to less than half the signal contribution of about 58 fb, just the gluon–gluon-induced channels of the $t\bar{t}$ + jets background by far exceed the signal cross section,

FCC - W^+W^-jj	σ_{EW} [fb]	σ_{QCD} [fb]	$\sigma_{\text{t}\bar{\text{t}}+\text{jets}}$ [fb]	S/B
VBS cuts	58.27(2)	22.257(8)	~ 190 (gg-only)	> 0.25
+ $M_{\text{T}_{\text{WW}}} > 1 \text{ TeV}$	3.589(2)	0.3895(7)	4.23(3)	0.8

Table 6.5.: Cross sections for the EW-induced W^+W^-jj production process together with the irreducible backgrounds, comprising the QCD contribution and the $\text{t}\bar{\text{t}}+\text{jets}$ contribution, and the signal-to-background ratio, S/B . Results are given for our VBS selection setup (first row), which is defined by the default selection cuts of Eqs. (6.13)–(6.17) supplemented by the process-specific cuts of Eqs. (6.27) and (6.28), and the additional application of the $M_{\text{T}_{\text{WW}}}$ -cut of Eq. (6.29) (second row). The numbers in parentheses represent the Monte Carlo uncertainty on the last given digit.

as they account for already ~ 190 fb. In the first row of Tab. 6.5 the cross sections of the three considered contributions are listed.

In Fig. 6.19 we show the transverse mass of the diboson system, $M_{\text{T}_{\text{WW}}}$, constructed from the momenta of the charged leptons and the missing transverse momentum (c.f. Eq. (6.21)) for two different mass ranges. On the left, where we entirely omitted the dominating $\text{t}\bar{\text{t}}+\text{jets}$ contribution, we observe a prominent peak, which is reminiscent of the Higgs-boson resonance at $M_{\text{WW}} = M_{\text{H}}$ and therefore only appears in the EW-signal contribution. In contrast to the sharp peak in M_{ZZ} shown on the l.h.s. of Fig. 6.17 for the related $\text{ZZ}jj$ -process, the peak in the transverse mass is clearly smeared out towards lower scales, since the longitudinal component remains unobserved in $M_{\text{T}_{\text{WW}}}$. Above the W-pair production threshold of $M_{\text{WW}} = 2M_{\text{W}} \sim 160 \text{ GeV}$ we notice a slight decrease of the signal as well as the background contribution. On the r.h.s. we show the same observable, now in the high-energy region, where the steep decrease of the dominating $\text{t}\bar{\text{t}} + \text{jets}$ contribution towards larger invariant masses is plainly visible, which finally allows to study the VBS signal contribution in a cleaner environment.

By applying a cut on the transverse mass of the gauge-boson system, the dominant $\text{t}\bar{\text{t}} + \text{jets}$ contribution can finally be drastically reduced. In the second row of Tab. 6.5 we list the resulting cross sections obtained by applying the cut

$$M_{\text{T}_{\text{WW}}} > M_{\text{T}_{\text{WW}}}^{\text{min}} = 1 \text{ TeV}, \quad (6.29)$$

additionally to the former VBS setup, which results in a S/B -ratio of 0.8. The obtained signal cross section of 3.6 fb is still large enough for a dedicated analysis, and even slightly more stringent cuts on the transverse diboson mass to further improve on the S/B -ratio might be possible. In Fig. 6.20 we show the invariant mass and rapidity separation of the two tagging jets, where all the cuts mentioned above have been applied. While the genuine QCD-background contribution is well suppressed by the applied cuts, the $\text{t}\bar{\text{t}} + \text{jets}$ background dominates the EW VBS signal up to invariant dijet masses of about 7 TeV and jet-rapidity separations as large as 8.

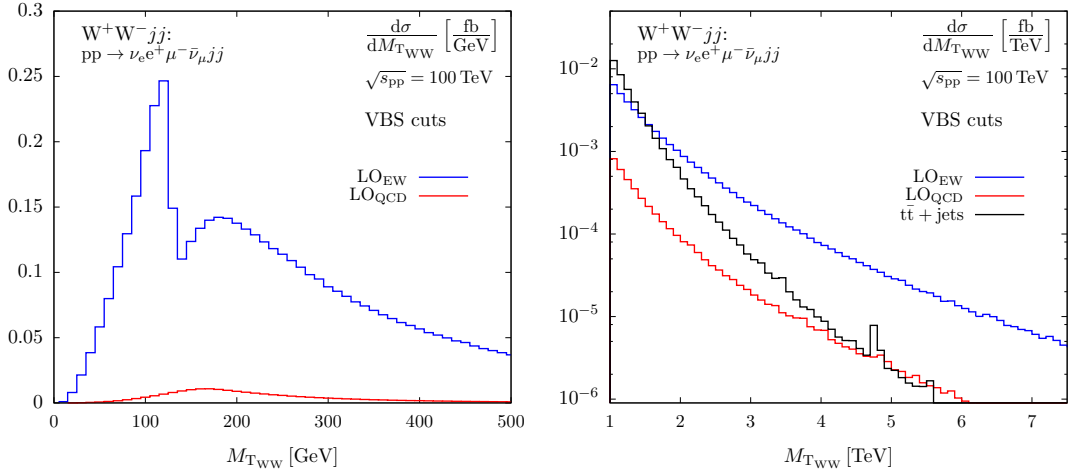


Figure 6.19.: Transverse-mass distribution of the gauge-boson system for two different plot ranges for the EW-induced (blue line), QCD-induced (red line) and $t\bar{t}$ +jets (black line, only r.h.s.) contributions to $pp \rightarrow \nu_e e^+ \mu^- \bar{\nu}_\mu jj$, within our VBS selection criteria defined by the default cuts of Eqs. (6.13)–(6.17), the process-specific cuts of Eq. (6.28), as well as the realistic b-jet veto and the central-jet veto of Eq. (6.27) for the $t\bar{t}$ +jets contribution.

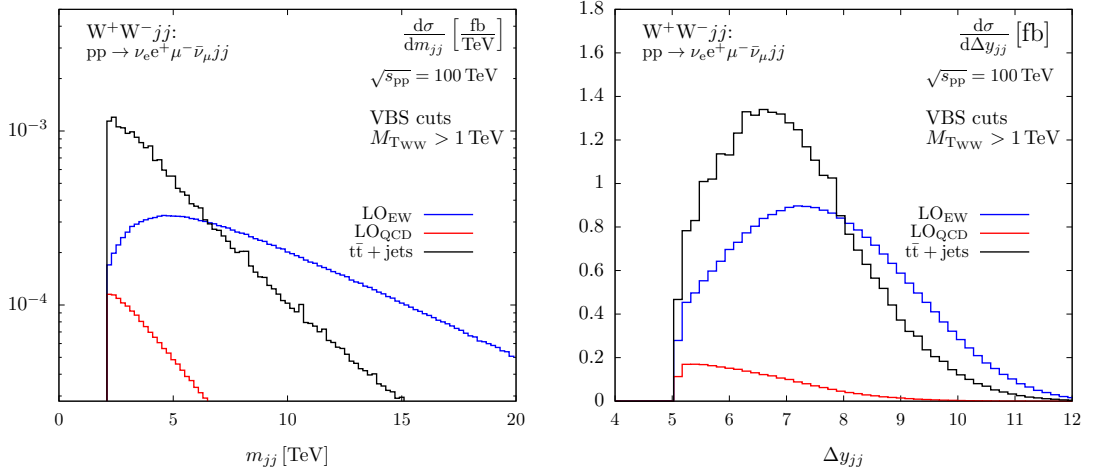


Figure 6.20.: Invariant mass (l.h.s.) and rapidity separation (r.h.s.) of the two tagging jets for the EW-induced (blue line) QCD-induced (red line) and $t\bar{t}$ +jets (black line) contributions to $pp \rightarrow \nu_e e^+ \mu^- \bar{\nu}_\mu jj$, within our constrained VBS selection criteria defined by the default cuts of Eqs. (6.13)–(6.17), the process-specific cuts of Eq. (6.28), the additional $M_{T_{WW}}$ -cut of Eq. (6.29), as well as the realistic b-jet veto and the central-jet veto of Eq. (6.27) for the $t\bar{t}$ +jets contribution.

FCC W^+jj	σ_{EW} [fb]	σ_{QCD} [fb]	S/B
VBF I (Eq. (6.30))	6980.1(8)	41324(10)	0.17
VBF II (Eq. (6.32))	1488.1(4)	1227.8(8)	1.21

Table 6.6.: Cross sections for the EW-induced W^+jj production processes together with the irreducible QCD background and the signal-to-background ratio, S/B , within our two different VBF-cut scenarios discussed in the text. The numbers in parentheses represent the Monte Carlo uncertainty on the last given digit.

Although more stringent cut on the invariant dijet mass or the transverse mass of the lepton system would definitely help to further improve on the S/B ratio, the dedicated study of the W^+W^-jj process via VBS would benefit most from additional techniques to suppress the $t\bar{t} + \text{jets}$ background, which do not further diminish the signal contribution. Since an improvement of the b-tagging efficiencies of Tab. 6.4 will almost certainly be achieved until the FCC starts its operation, we are very confident that at such a machine also the same-sign W-boson pair production process via VBS will be subject to precise investigations.

6.3.5. Single Gauge-Boson Production via VBF

The genuine QCD-background contributions to single gauge-boson production via VBF are much larger compared to the gauge-boson pair production processes via VBS discussed so far. In order to yield sufficiently large S/B ratios to investigate the VBF process at a future FCC, the techniques applied so far have to be slightly modified. In the following we consider the representative e^-e^+jj and $\nu_e e^+jj$ final states for the two VBF processes Zjj and W^+jj , respectively.

Extending our default cut setup of Eqs. (6.13)–(6.18) by the two typical VBF-specific cuts on the dijet system

$$m_{jj} > 2000 \text{ GeV}, \quad \Delta y_{jj} > 5, \quad (6.30)$$

the QCD-background contributions still dominate both considered VBF-signal processes by roughly a factor of five. The corresponding cross sections and the S/B ratio are given in Tabs. 6.6 and 6.7 for the W^+jj and Zjj process, respectively, where we refer to this setup as VBF I.

In Fig. 6.21 we representatively show the two dijet observables for the W^+jj process within this cut setup. Although simply raising the m_{jj} -cut value would definitely slightly improve on the poor S/B ratio, the QCD-induced contribution would still dominate the cross section at least up to a cut value of $m_{jj}^{\text{cut}} = 12 \text{ TeV}$. In order to further improve on the S/B ratio without losing also most of the signal, we rather

FCC Zjj	σ_{EW} [fb]	σ_{QCD} [fb]	S/B
VBF I (Eq. (6.30))	1079.5(3)	5164(1)	0.21
VBF II (Eq. (6.32))	154.4(1)	138.0(1)	1.12

Table 6.7.: Cross sections for the EW-induced Zjj production processes together with the irreducible QCD background and the signal-to-background ratio, S/B , within our two different VBF-cut scenarios discussed in the text. The numbers in parentheses represent the Monte Carlo uncertainty on the last given digit.

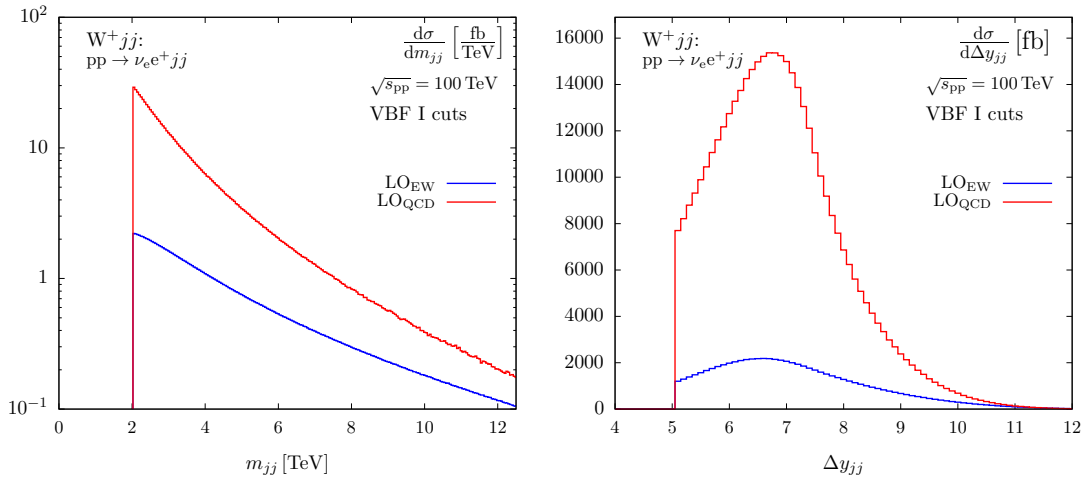


Figure 6.21.: Invariant mass (l.h.s.) and rapidity separation (r.h.s.) of the two tagging jets for the EW-induced (blue line) and QCD-induced (red line) contributions to $pp \rightarrow \nu_e e^+ jj$, within our VBF I cut setup, defined by the default selection cuts of Eqs. (6.13)–(6.17) and Eq. (6.30).

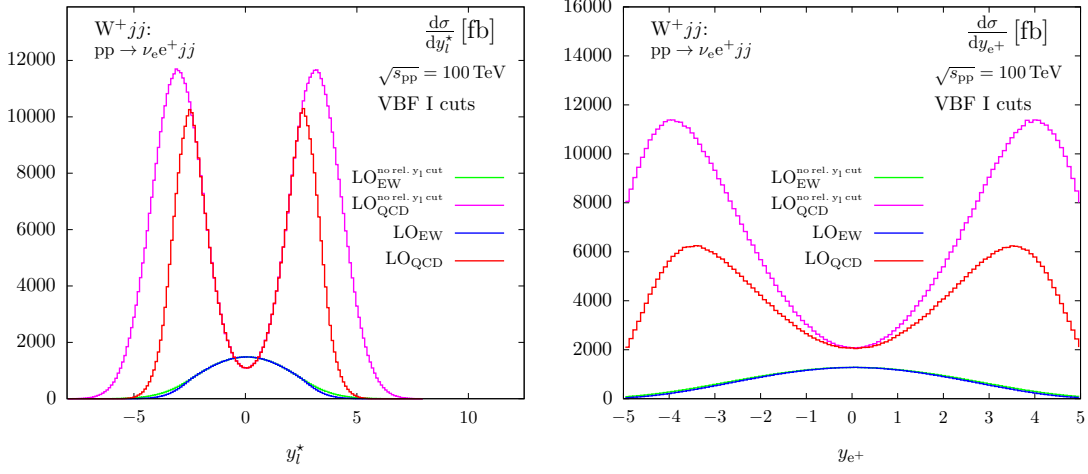


Figure 6.22.: Distribution of the y_l^* variable (l.h.s.) and rapidity distribution of the positron (r.h.s.) for the EW-induced and QCD-induced contributions to $pp \rightarrow \nu_e e^+ jj$, within the selection cuts of Eqs. (6.13)–(6.16) and Eq. (6.30), without (green and purple line) and with (blue and red line) the lepton rapidity-gap cut of Eq. (6.17).

consider other distributions, that might reveal a distinct difference between the EW-induced and the QCD-induced contribution. A particularly important cut for the QCD-suppression is for example the already applied cut on the lepton rapidity relative to the tagging jets, Eq. (6.17), since the QCD-background typically features leptons that are not located in between the tagging jets. We illustrate the impact of this cut in Fig. 6.22 by means of the y_l^* variable on the l.h.s., which is defined as

$$y_l^* = y_l - \frac{y_{j_1}^{\text{tag}} + y_{j_2}^{\text{tag}}}{2}, \quad (6.31)$$

giving the relative position of the charged lepton with respect to the two tagging jets, and the rapidity distribution of the positron on the r.h.s.. In both plots we show the EW- and QCD-induced contributions without (green and purple line) and with (blue and red line) the cut of Eq. (6.17). While the EW-induced contribution, that is mainly located around small values in both distributions, loses only $\sim 5\%$, the cut has a large impact on the QCD-background contribution, reducing its contribution by 40%.

By further restricting the lepton(s) to the central rapidity region and additionally slightly amplifying our VBF I cut setup, a considerable improvement of the S/B ratio can be effected. Therefore, we define the selection criteria VBF II by supplementing the default cuts of Eqs. (6.13)–(6.18) by

$$m_{jj} > 3000 \text{ GeV}, \quad \Delta y_{jj} > 6, \quad |y_l| \leq 1. \quad (6.32)$$

The integrated cross sections and the S/B ratios obtained by imposing these more severe cuts are also given in Tabs. 6.6 and 6.7. Considering Fig. 6.23, which shows

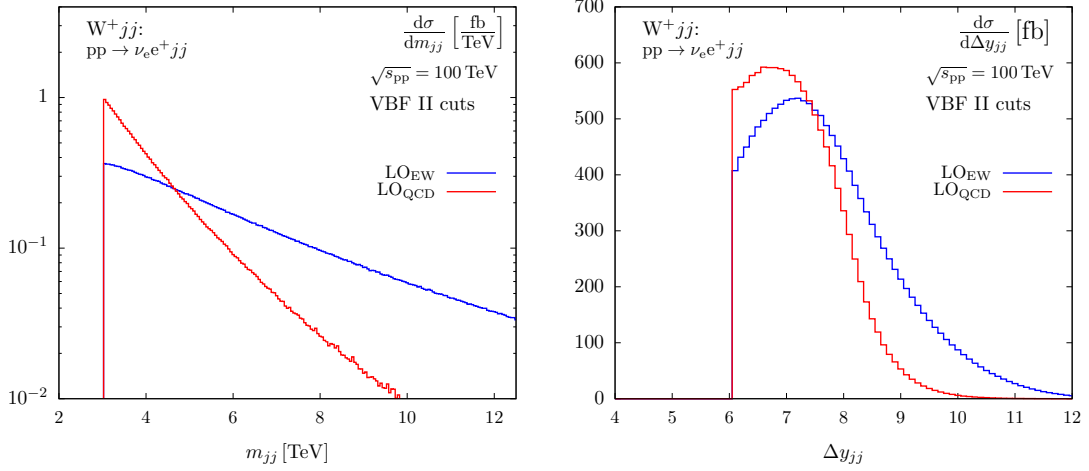


Figure 6.23.: Invariant mass (l.h.s.) and rapidity separation (r.h.s.) of the two tagging jets for the EW-induced (blue line) and QCD-induced (red line) contributions to $pp \rightarrow \nu_e e^+ jj$, within our VBF II cut setup, defined by the default selection cuts of Eqs. (6.13)–(6.17) and Eq. (6.32).

the distributions of the resulting invariant dijet mass and jet-rapidity separation, we notice that even higher S/B ratios can now again be easily achieved by raising the m_{jj} -cut towards higher energy scales, as the corresponding distribution shows a much steeper decrease of the QCD-induced contribution than in the VBF I cut setup, shown in Fig. 6.21. Even more severe cuts on the jet-rapidity separation, on the other hand, would further diminish the EW-contribution unnecessarily, without significantly improving on the S/B ratio.

Note, however, that even though the application of the VBF II cuts reduces the total cross section of both considered VBF processes by roughly 95 % with respect to the looser VBF I cuts of Eq. (6.30), the remaining cross sections are still much larger than the ones obtained for the VBS processes in the previous sections. Figure 6.24 clearly indicates that even after the application of much more severe cuts on the invariant dijet mass, to further improve on the S/B ratio, the FCC would be capable to deliver a sufficient amount of events to precisely study the details of VBF processes.

6.4. Summary and Conclusions

Studying VBS reactions provides direct insight into the consequences of EWSB in the SM and is therefore of utter importance in present and upcoming searches for new physics entering via the weak sector. Unfortunately, taking the couplings to production and decay fermions into account, the lowest possible order to study VBS is already via processes of $\mathcal{O}(\alpha^6)$, which consequently provide relatively small cross sections. More-

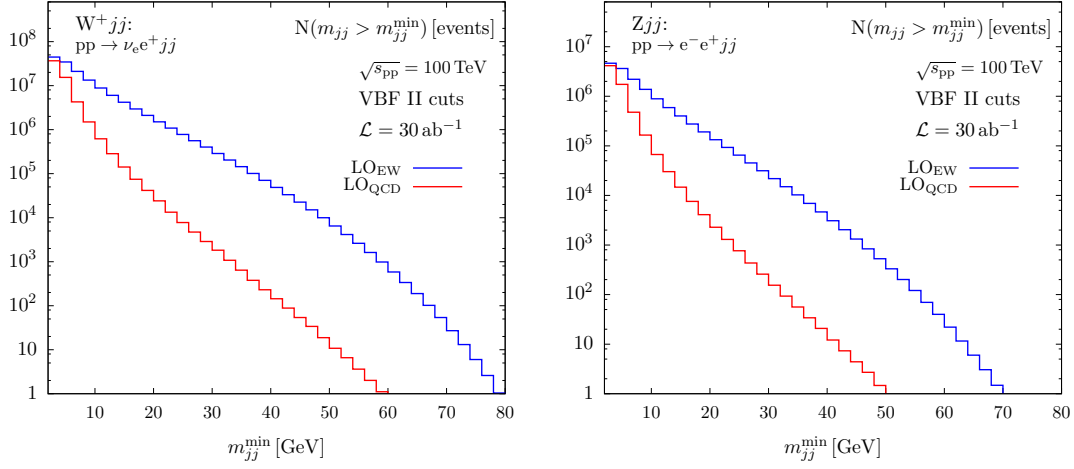


Figure 6.24.: Total number of events (N) produced with $m_{jj} > m_{jj}^{\min}$ for the EW-induced (blue line) and QCD-induced (red line) contributions to $pp \rightarrow \nu_e e^+ jj$ (l.h.s.) and $pp \rightarrow e^- e^+ jj$ (r.h.s.), within the cut setup VBF II, comprising the selection cuts of Eqs. (6.13)–(6.18), and Eq. (6.32). An integrated luminosity of 30 ab^{-1} is assumed.

over, at hadron colliders additional background contributions of the order $\alpha_s^2 \alpha^4$ have to be taken into account which generally lead to much larger cross sections than the purely EW contribution.

In this chapter we demonstrated that a future proton-proton collider operating at a c.m. energy of 100 TeV would provide excellent opportunities for detailed studies of the different VBS reactions. For each of the four VBS process classes $W^\pm W^\pm jj$, $W^\pm Z jj$, $ZZ jj$, and $W^+ W^- jj$ we discussed one representative final state in detail and pointed out how dedicated event-selection criteria can be used to efficiently suppress the considered background contributions. A particular role in the suppression of background contributions is played by the cuts on the dijet-system, as the final-state jets feature entirely different kinematic properties for both production modes. While the final-state jets of the VBS signal contribution are generally widely separated in rapidity and exhibit large invariant dijet masses, the major part of the-QCD background processes features much closer final-state jets leading to small invariant dijet masses. Exploiting these facts the signal-to-background ratios of all process classes have been considerably improved.

The same-sign W-boson pair production process via VBS is of particular interest, as this process possesses by far the cleanest signal. Due to the charge structure, the EW contribution dominates the QCD background already at the fully inclusive level, such that even comparably loose additional VBS cuts drastically reduce the background, while the signal contribution is only marginally affected. Basically over the entire remaining phase space, the VBS process dominates the cross section and could therefore easily be studied by means of several differential distributions.

For two of the process classes, $W^\pm Zjj$ and $ZZjj$, we observed in principle a rather similar behaviour. We demonstrated how the specific application of the additional cuts on the invariant dijet mass and the rapidity separation of the jets affect the resulting cross-section contributions and the obtained signal-to-background ratios. By means of the invariant di-boson mass, we have shown that both processes exhibit perfect possibilities to search for new physics effects in the weak sector, that would directly affect these distributions.

The last VBS process we investigated was the opposite-sign W-boson pair production process via VBS, which is plagued by exceptionally large QCD backgrounds due to top-quark pair production. Our analyses incorporate this process with up to two additional light jets, including all off-shell contributions of the top quarks and the W bosons. By applying realistic b-tagging efficiencies and an additional cut on contributions featuring more than two detected final-state jets, we demonstrated how this a priori overwhelming $t\bar{t}$ background can be reduced to the same size as the signal process, without decreasing the latter. Upcoming improvements on b-tagging efficiencies will certainly help to further diminish the top background and, thus, allow for dedicated studies of opposite-sign W-boson production via VBS.

In the case of VBF processes featuring single vector bosons the effective suppression of the genuine QCD background is much more involved, since the dijet systems of both production modes show rather similar kinematic patterns. For the particular processes W^+jj and Zjj we demonstrated that already quite stringent cuts have to be applied to yield signal-to-background ratios slightly larger than one. However, the enormous cross section of these processes at the FCC would still allow for dedicated investigations of the VBF process at such very constrained phase spaces.

From our results we can definitely approve the excellent opportunities of a future high-energy proton-proton collider to explore the details of VBS. To fully exploit the capabilities of the FCC, precise measurement of high-energetic final-state jets at least up to rapidities as large as ± 5 should be realizable. For the optimal balance between higher signal purity and a sufficiently large signal cross section in the fiducial phase space further studies will have to be performed when more details on the exact detector setup and differential measurement efficiencies are known. Moreover, those subsequent studies should additionally include the effects of higher-order corrections in QCD as well as in the EW theory, to reach the accuracy needed to adequately describe the future measurements at the FCC.

Chapter 7

Summary and Outlook

With the experimental observation of a SM-like Higgs boson in 2012 at the LHC, the field of particle physics has definitely entered a new era. Concluding a decades-long search for the last missing piece of the SM, this great achievement finally completed the particle spectrum predicted by the theory and confirmed the realisation of EWSB via the Higgs mechanism. Now, two of the main prospects of particle physics are to further reveal the very details of this involved mechanism and eventually—maybe even simultaneously—find the first signs of new physics at high-energy colliders.

Studying purely EW processes comprising weak gauge bosons at hadron colliders provides particularly promising means to accomplish these purposes. On the one hand, hadron colliders probe a wide range of energy scales, reaching deep into the TeV regime, and on the other hand processes containing several weak bosons are exceptionally sensitive to the exact realisation of EWSB. Moreover, if purely leptonic decays of the weak bosons are considered, these processes lead to fairly clean signatures in the detector, allowing for very precise experimental measurements. In order to detect an unforeseen and presumably very tiny signal above a large SM background, however, precisely knowing the latter is of utter importance.

We commenced this thesis with a detailed outline of the SM and the basic concepts that are required to perform theoretical predictions for hadron collider processes. Subsequently, the second part comprised the discussion of two important phenomenological applications of this theoretical foundation. One main goal of this work was to provide theoretical predictions at the highest possible accuracy for the purely EW W -boson pair production process at the LHC. Including the trilinear weak gauge-boson interaction at the lowest order that is experimentally accessible, this process is particularly suitable to further challenge the weak sector of the SM at the LHC. Since the dominant source of theoretical uncertainties at hadron colliders is genuinely associated to the omnipresent strong sector of the SM, in the last years a huge effort was put into the calculation of higher-order QCD corrections with the result that since very recently this process is known to the next-to-next-to-leading order QCD in a fully differential form.

Due to the involved EW structure of the W -boson pair production process, however, also corrections in the EW interaction play a crucial role in upcoming precision analyses. In Chap. 5 we presented the first calculation of the full EW corrections to the hadronic process $pp \rightarrow W^+W^- \rightarrow 4 \text{ leptons}$. After a detailed outline of the calculation, we have shown the effect of the EW corrections on several differential distributions for realistic

event-selection setups. Particularly at high energy scales, where new-physics searches are commonly performed, the impact of these corrections could easily be misinterpreted as first signs of new physics, if they are not properly included in the experimental analysis. In addition, we discussed the improvement compared to a former calculation applying the so-called double-pole approximation. Here, we observed the expected deviations in peculiar phase-space regions, while for integrated results the validity of the approximation has been ascertained.

Subsequently, in Chap. 6, we turned to the genuine $2 \rightarrow 2$ scattering reaction of weak gauge bosons. In principle, these VBS processes provide at least equally promising means to examine the SM and to search for new physics in the EW sector as the formerly discussed W-pair production process. Unfortunately, the much lower cross sections of the experimentally accessible states hardly allow for detailed differential analyses at the LHC. Moreover, we have also discussed how large QCD-induced background contributions additionally impede the extraction of the signal of interest. For VBS reactions, we therefore performed a dedicated signal-to-background analysis, where we investigated the opportunities at a future high-energy hadron collider operating at 100 TeV. For all process classes we devised process-specific selection criteria that drastically reduce the otherwise overwhelming QCD backgrounds and therefore prospectively facilitate precise experimental measurements of the purely EW contributions.

In this second phenomenological study we have revealed the great potential of a future high-energy hadron collider to observe BSM effects in VBS processes, but nevertheless we still hope for a detection of first signs of new physics in a not-so-distant future. The enormous amount of data presently recorded in LHC-Run II and its much deeper energy reach, that will soon allow for precision studies of many processes at yet unprecedented energy scales, may perhaps lead to some unforeseen surprises. Additionally, for most of the processes of interest the proper combination of accurate NLO EW corrections and state-of-the-art predictions of the QCD effects is already available, such that also from the theoretical side a mandatory step for a qualified interpretation of the upcoming data is now close to be completed.

We surely have very exiting times ahead of us, and it might even well be possible that with the first observation of BSM physics the LHC will be once more responsible for the beginning of new era of particle physics.

Appendices

Appendix A

Group Theory

Since group theory builds the footing of the SM, we give some basic definitions and clarify the notation in this appendix. However, we will only mention the aspects needed for the formulation of the SM, such that we refer the reader to Refs. [144] and [145] for a more rigorous treatment of the subject. After a short general introduction, we first discuss the concept of gauge theories and the gauge groups of the SM in App. A.1 and then the space-time symmetries in App. A.2.

A group is a mathematical set of objects (\mathcal{G}) with a prescription (\circ , group multiplication) under which the set is closed

$$f, g \in \mathcal{G} : f \circ g = h \in \mathcal{G}. \quad (\text{A.1})$$

This group multiplication has to be associative ($(f \circ g) \circ h = f \circ (g \circ h)$) and an unique identity element ($e : g \circ e = e \circ g = g$) as well as the inverse element ($g^{-1} : g \circ g^{-1} = g^{-1} \circ g = e$) for every element g must be part of the set. We call a group *Abelian* if the group multiplication is commutative ($f \circ g = g \circ f$) for every pair of elements of the group, otherwise *non-Abelian*. As representation (R) of a group we denote a mapping (\mathcal{D}) of the elements of \mathcal{G} onto a set of linear operators (for finite dimensional groups we can speak of matrices), that respects the group multiplication, i.e.

$$\mathcal{D}(g)\mathcal{D}(f) = \mathcal{D}(g \circ f). \quad (\text{A.2})$$

We call a representation unitary, if all $\mathcal{D}(g)$ are unitary operators ($\mathcal{O}^\dagger = \mathcal{O}^{-1}$) and irreducible, if it cannot be written as a direct sum of representations of a lower dimension.

A (finite dimensional) *Lie group* is a group where all elements of the group can be parametrized by a set of n continuous parameters $\omega = (\omega_1, \dots, \omega_n)$. The parametrization is chosen such that $g(0, \dots, 0)$ corresponds to the unity element, which obviously also has to hold in any representation, $\mathcal{D}_R(0, \dots, 0) = \mathbb{1}$. For elements (infinitely) close to the identity the parameters are also (infinitely) close to zero, such that for a group element in this region a Taylor expansion of the form

$$\mathcal{D}_R(d\omega) = \mathbb{1} + i d\omega^a X_R^a + \dots, \quad (\text{A.3})$$

holds in every representation, where

$$X_R^i = -i \frac{\partial}{\partial \omega_i} \mathcal{D}_R(\omega_1, \dots, \omega_n) |_{(\omega)=(0, \dots, 0)}, \quad (\text{A.4})$$

are the generators of the group in a given representation. The inclusion of “i” in the definition of Eq. (A.4) ensures that unitary representations are generated by hermitian operators. In every representation, the X_R have to fulfil the commutator relation (Lie algebra)

$$[X_R^a, X_R^b] = X_R^a X_R^b - X_R^b X_R^a = i f_{abc} X_R^c, \quad (\text{A.5})$$

with the structure constants f_{abc} . Equation (A.5) holds independently of the representation, such that the structure constants contain all information about the group multiplication, and therefore uniquely define the group. For groups with unitary representations, on which we are mainly interested, one can show that the structure constants are always real. In a given representation R every group element of a Lie group can be reached by consecutively applying infinitesimal transformations of the form of Eq. (A.3) and respecting the Lie algebra (Eq. (A.5)), which can be written as

$$\mathcal{D}_R(\omega) = \exp(i\omega^a X_R^a). \quad (\text{A.6})$$

Furthermore, the structure of Lie algebras allows for every representation to define the (quadratic) *Casimir operator*, which commutes with all elements of the Lie algebra. Due to Schur’s lemma, the Casimir operators in irreducible representations are proportional to the unit matrix in the respective dimension n_R of the representation R .

A.1. Gauge Theories

Given a Lagrangian $\mathcal{L}(\Phi, \partial_\mu \Phi)$ that only depends on an arbitrary field $\Phi(x)$ and its derivative $\partial_\mu \Phi(x)$. Let $\Phi(x)$ transform under a specific irreducible representation of the Lie group (\mathcal{G}),

$$\Phi \xrightarrow{\mathcal{G}} \Phi' = U(\omega)\Phi, \quad U(\omega) = \exp(-ig\omega^a t_R^a), \quad (\text{A.7})$$

where $\omega = (\omega^a)$ denotes the (spacetime-independent) group parameters and t_R^a are the generators of \mathcal{G} in the representation under which Φ transforms. For conventional reasons, with respect to Eq. (A.6) the additional factor of $-g$ has been introduced, where g will later be identified as the coupling strength. The transformation $U(\omega)$ is called a *global gauge symmetry*, if it leaves the Lagrangian \mathcal{L} invariant¹.

Having constructed a Lagrangian that exhibits certain global symmetries it is straight forward to promote this symmetry to a *local gauge symmetry*, that holds at every individual space-time point. In this way, interactions among the fields via the exchange of gauge bosons can be brought to the theory in a very elegant and fundamental way. The difference between a global and a local gauge symmetry is, that the group parameters of the latter are space-time dependent, $\omega = \omega(x)$. This obviously spoils the

¹More precisely, the condition has to be posed on the action (Eq. (2.1)), but as internal symmetries per definition leave the measure of the Minkowski space d^4x invariant, there is no difference in the argumentation.

transformation properties of the terms involving derivatives,

$$\partial_\mu \Phi(x) \xrightarrow{\mathcal{G}} \partial_\mu \Phi'(x) = \partial_\mu [U(\omega) \Phi(x)] \neq U(\omega(x)) \partial_\mu \Phi(x), \quad (\text{A.8})$$

such that a Lagrangian depending only on Φ and $\partial_\mu \Phi$ cannot stay invariant. However, the invariance can be retrieved also locally by promoting the derivative to the so-called *covariant derivative*

$$\partial_\mu \longrightarrow D_\mu = \partial_\mu + ig \mathcal{A}_\mu(x), \quad \mathcal{A}_\mu(x) := A_\mu^a(x) t_R^a, \quad (\text{A.9})$$

which introduces as many *gauge fields* $A_\mu^a(\mathbf{x})$ to the theory, as there are generators in the corresponding Lie algebra. By definition, the gauge fields show exactly the transformation properties under \mathcal{G} to compensate for the additional terms in Eq. (A.8), namely

$$\mathcal{A}_\mu(x) \xrightarrow{\mathcal{G}} \mathcal{A}'_\mu(x) = U(\omega(x)) \mathcal{A}_\mu(x) U^\dagger(\omega(x)) - \frac{i}{g} U(\omega(x)) (\partial_\mu U^\dagger(\omega(x))). \quad (\text{A.10})$$

Recalculating Eq. (A.8), now with the covariant derivative D_μ instead of ∂_μ , yields

$$D_\mu \Phi(x) \xrightarrow{\mathcal{G}} D'_\mu \Phi'(x) = D'_\mu (U(\omega(x)) \Phi(x)) = U(\omega(x)) [D_\mu \Phi(x)], \quad (\text{A.11})$$

which makes the Lagrangian $\mathcal{L}(\Phi, D_\mu \Phi)$, constructed from a globally invariant Lagrangian, also invariant under local gauge transformations. Moreover, we introduced interaction to the former non-interacting theory, which is mediated through the exchange of the gauge fields. Also, the term of the Lagrangian that is responsible for the dynamics of the gauge fields therefore directly follows from the definition of the covariant derivative. The *field-strength tensor* is defined as

$$\mathcal{F}_{\mu\nu} := -\frac{i}{g} [D_\mu, D_\nu], \quad (\text{A.12})$$

and shows the following transformation properties under \mathcal{G} ,

$$\mathcal{F}_{\mu\nu} \xrightarrow{\mathcal{G}} \mathcal{F}'_{\mu\nu} = U(\omega(x)) \mathcal{F}_{\mu\nu} U^\dagger(\omega(x)), \quad (\text{A.13})$$

such that

$$-\frac{1}{2} \text{Tr}[\mathcal{F}_{\mu\nu} \mathcal{F}^{\mu\nu}] = -\frac{T_R}{2} F_{\mu\nu}^a F^{a,\mu\nu} = \mathcal{L}_{\text{Gauge}}, \quad (\text{A.14})$$

results in a gauge invariant Lagrangian, that suffices all requirements discussed in Chap. 2 to be part of the SM Lagrangian. In Eq. (A.14) the components of $\mathcal{F}_{\mu\nu} = F_{\mu\nu}^a t_F^a$ read

$$F_{\mu\nu}^a = \partial_\mu A_\nu^a - \partial_\nu A_\mu^a - g f^{abc} A_\mu^b A_\nu^c, \quad (\text{A.15})$$

with the structure constants f^{abc} of the underlying gauge group. It is worth mentioning, that for non-Abelian symmetry groups ($f^{abc} \neq 0$) the inclusion of a kinetic term for

²The generators t_R^a are normalized according to Eq. (A.16).

the gauge bosons automatically yields self interaction among them. Such field theories play a crucial role in the SM and are generally called *Yang-Mills theories*.

The SM ($= \text{SU}(3)_C \times \text{SU}(2)_W \times \text{U}(1)_Y$) consists of two special unitary groups ($\text{SU}(N)$) and one unitary group ($\text{U}(1)_Y$). $\text{U}(1)_Y$ is a one dimensional Abelian group, depending on one real parameter. $\text{SU}(N)$ groups are formed by the unitary $N \times N$ -matrices with determinant equals 1 and generally the dimension of these non-Abelian groups reads $n_G = N^2 - 1$, and, thus, $\text{SU}(2)_W$ is a three dimensional and $\text{SU}(3)_C$ an eight dimensional group. In every representation of the $\text{SU}(N)$ groups one can choose the generators in such a way that they are normalized according to

$$\text{Tr}[t_R^a t_R^b] = T_R \delta^{ab}, \quad (\text{A.16})$$

with a positive constant T_R , the *Dynkin index*. For both $\text{SU}(N)$ groups appearing in the SM we choose in the fundamental representation $T_F = \frac{1}{2}$, such that the generators read

$$I_Y^i := t_F^i(\text{SU}(2)) = \frac{\sigma^i}{2}, \quad i = 1, \dots, 3, \quad (\text{A.17})$$

$$T^a := t_F^a(\text{SU}(3)) = \frac{\lambda^a}{2}, \quad a = 1, \dots, 8, \quad (\text{A.18})$$

with the three *Pauli matrices*,

$$\sigma_1 = \begin{pmatrix} 0 & 1 \\ 1 & 0 \end{pmatrix}, \quad \sigma_2 = \begin{pmatrix} 0 & -i \\ i & 0 \end{pmatrix}, \quad \sigma_3 = \begin{pmatrix} 1 & 0 \\ 0 & -1 \end{pmatrix}, \quad (\text{A.19})$$

and the eight *Gell-Mann matrices*,

$$\begin{aligned} \lambda^1 &= \begin{pmatrix} 0 & 1 & 0 \\ 1 & 0 & 0 \\ 0 & 0 & 0 \end{pmatrix}, & \lambda^2 &= \begin{pmatrix} 0 & -i & 0 \\ i & 0 & 0 \\ 0 & 0 & 0 \end{pmatrix}, & \lambda^3 &= \begin{pmatrix} 1 & 0 & 0 \\ 0 & -1 & 0 \\ 0 & 0 & 0 \end{pmatrix}, \\ \lambda^4 &= \begin{pmatrix} 0 & 0 & 1 \\ 0 & 0 & 0 \\ 1 & 0 & 0 \end{pmatrix}, & \lambda^5 &= \begin{pmatrix} 0 & 0 & -i \\ 0 & 0 & 0 \\ i & 0 & 0 \end{pmatrix}, & \lambda^6 &= \begin{pmatrix} 0 & 0 & 0 \\ 0 & 0 & 1 \\ 0 & 1 & 0 \end{pmatrix}, \\ \lambda^7 &= \begin{pmatrix} 0 & 0 & 0 \\ 0 & 0 & -i \\ 0 & i & 0 \end{pmatrix}, & \lambda^8 &= \frac{1}{\sqrt{3}} \begin{pmatrix} 1 & 0 & 0 \\ 0 & 1 & 0 \\ 0 & 0 & -2 \end{pmatrix}, \end{aligned} \quad (\text{A.20})$$

respectively. The generators of the adjoint representation are given by the structure constants f^{abc} times the imaginary unit:

$$(t_A^b)_{ac} = i f^{abc}, \quad a, b, c = 1, \dots, n_G \quad (\text{A.21})$$

i.e. the dimension of the adjoint representation is always the same as the dimension of the group. Usually, the structure constants of the $\text{SU}(2)_W$ group are denoted by

ϵ^{ijk} , whereas the general symbol f^{abc} is also used to denote the structure constants of $SU(3)_C$. Finally, the Casimir operators of the SM gauge groups are given by

$$\sum_{j=1}^{n_R} t_R^j t_R^j = C_R \mathbb{1}_{n_R \times n_R}, \quad (\text{A.22})$$

where the constants C_R in the fundamental and adjoint representation read,

$$SU(3) : C_F = \frac{4}{3}, \quad C_A = 3, \quad (\text{A.23})$$

$$SU(2) : C_F = \frac{3}{4}, \quad C_A = 2, \quad (\text{A.24})$$

$$U(1) : C_F = 1, \quad C_A = 0. \quad (\text{A.25})$$

A.2. Space-time Symmetries

In this appendix some features of the Lorentz and Poincaré group, their algebras, and their representations are collected. The proceeding closely follows Chap. 10 of Ref. [145], which is also recommended for further details.

The proper orthochronous Lorentz group $L_+^{\uparrow 3}$ is defined as the set of Lorentz transformations Λ with $\Lambda^0_0 \geq 0$ and $\det \Lambda = 1$ that leave the Minkowski metric $g = \text{diag}(1, -1, -1, -1)$ invariant, $\Lambda^\top g \Lambda = g$. This constraint fixes ten of the 16 parameters of the 4×4 matrix Λ , such that six free parameters remain to characterize every proper orthochronous Lorentz transformation. The most convenient and illustrative parametrization distinguishes between three rotations (R_i) in the spatial dimensions of the Minkowski space and three boosts along the spatial coordinate axes (L_i),

$$(R_i)^\mu_\nu = \begin{pmatrix} 1 & 0 & 0 & 0 \\ 0 & & & \\ 0 & (R_i)^k_l & & \\ 0 & & & \end{pmatrix}, \quad (L_1)^\mu_\nu = \begin{pmatrix} \cosh \xi & \sinh \xi & 0 & 0 \\ \sinh \xi & \cosh \xi & 0 & 0 \\ 0 & 0 & 1 & 0 \\ 0 & 0 & 0 & 1 \end{pmatrix}, \quad (\text{A.26})$$

where $(R_i)^k_l$ denotes the usual 3×3 rotation matrices and the boost along the x -axis (L_1) was chosen exemplary. The boosts are parametrized by the boost parameter (*rapidity*) $\xi = \tanh^{-1}(v/c)$, where v/c is the relative velocity (with respect to the speed of light) between the coordinate systems.

The three rotations build the non-trivial subgroup $SO(3)$, while the three independent boosts are one-parameter subgroups. Note that since the boost parameters ξ are unbounded, the Lorentz group is a non-compact group. Due to a general principle of

³Often referred to as the Lorentz group. However, the latter formally consists of the set $L_+^{\uparrow}, L_-^{\uparrow}, L_+^{\downarrow}$, and L_-^{\downarrow} , therefore additionally including the parity transformation ($\mathcal{P} = \text{diag}(1, -1, -1, -1)$), the time-reversal transformation ($\mathcal{T} = \text{diag}(-1, 1, 1, 1)$), and the combination \mathcal{PT} , respectively.

group theory, the finite dimensional irreducible representations of the Lorentz group can therefore not be unitary representations. Since, on the other hand, the symmetry transformations on the space of physical states must be realized by unitary operators, we conclude, that the physical states cannot be represented by the finite dimensional representations of the Lorentz group, but, if ever, they are represented by the infinite-dimensional representations. However, studying the finite-dimensional representations will provide the necessary starting point to classify the transformations of the fields that govern the particles' dynamics, while the infinite-dimensional representations can subsequently be constructed by the so-called method of the induced representation.

Every proper orthochronous Lorentz transformation can be expressed as

$$\Lambda(\omega) = \exp\left(-\frac{i}{2}\omega_{\mu\nu}J^{\mu\nu}\right), \quad (\text{A.27})$$

with the generators of the Lorentz transformations, $J^{\mu\nu}$, and a totally anti-symmetric tensor, $\omega_{\mu\nu}$. The generators fulfil the Lie algebra of the Lorentz group,

$$[J_{\mu\nu}, J_{\rho\sigma}] = i(J_{\rho\nu}g_{\mu\sigma} - J_{\sigma\nu}g_{\mu\lambda} + J_{\mu\rho}g_{\nu\sigma} - J_{\mu\sigma}g_{\nu\lambda}). \quad (\text{A.28})$$

Further one separately defines the generators of the rotations (J_i) and boosts (K_i),

$$J_i = \frac{1}{2}\epsilon^{ijk}J_{jk}, \quad K_i = J_{i0}, \quad i = 1, 2, 3, \quad (\text{A.29})$$

and finds that the generators J_i are hermitian, whereas the K_i are anti-hermitian. However, the two linearly independent combinations

$$T_i^{1,2} = \frac{1}{2}(J_i \pm iK_i), \quad i = 1, 2, 3, \quad (\text{A.30})$$

yield two hermitian generators. They separately fulfil the $\text{su}(2)$ Lie algebra,

$$[T_i^a, T_j^b] = i\epsilon^{ijk}T_k^a\delta_{ab}, \quad i = 1, 2, 3 \quad a, b = 1, 2, \quad (\text{A.31})$$

which therefore defines the Lie algebra of the direct product of two independent $\text{SU}(2)$ groups, $\text{SU}(2) \times \text{SU}(2)$. The irreducible representations of two groups that share the same Lie algebra, however, can be classified in the same way, which means that every product of two fundamental representations of $\text{SU}(2)$ yields a representation of the Lorentz group.

Denoting the two-dimensional fundamental representation of $\text{SU}(2)$ by $D(\frac{1}{2})$, the two fundamental representations of the Lorentz group follow to be

$$D\left(\frac{1}{2}, 0\right), \quad D\left(0, \frac{1}{2}\right), \quad (\text{A.32})$$

which are called right-handed fundamental representation and left-handed fundamental representation, respectively. The notation is defined in such a way, that in the right-handed fundamental representation the generators T^1 of the first $\text{SU}(2)$ are chosen in the

fundamental representation and T^2 in the trivial representation ($T_i^2 = 0$), while for the left-handed fundamental representation the opposite is true. All fields appearing in the SM transform in one of the representations $D(0, 0)$, $D(\frac{1}{2}, 0)$, $D(0, \frac{1}{2})$, $D(\frac{1}{2}, 0) \oplus D(0, \frac{1}{2})$, and $D(\frac{1}{2}, \frac{1}{2})$, which are denoted as scalar fields, right-handed and left-handed Weyl-spinors, Dirac spinors and vector fields, respectively.

Note, however, that even though the Lorentz group and $SU(2) \times SU(2)$ share the same Lie algebra, unitary representations of $SU(2) \times SU(2)$ cannot be unitary representations of the Lorentz group due to the “i” in the definition of the generators $T_i^{1,2}$ in Eq. (A.30).

The proper orthochronous Poincaré group $P_+^{\uparrow 4}$ is a generalization of the Lorentz group by additionally including four-dimensional translations. It is defined as the group of transformations

$$g(a, \Lambda) : x^\mu \rightarrow x'^\mu = \Lambda^\mu_\nu x^\nu + a^\mu, \quad (\text{A.33})$$

where Λ^μ_ν is a (proper orthochronous) Lorentz transformation and a^μ a four-dimensional translation. The group multiplication law reads

$$g(a, \Lambda)g(a', \Lambda') = g(\Lambda a' + a, \Lambda \Lambda'). \quad (\text{A.34})$$

Every (proper orthochronous) Poincaré transformation can be expressed as

$$g(a, \Lambda) = \exp\left(-\frac{i}{2}\omega_{\mu\nu}J^{\mu\nu} + ia_\mu P^\mu\right), \quad (\text{A.35})$$

where $J^{\mu\nu}$ are the generators of the Lorentz group, satisfying the commutator relation Eq. (A.28), and the four generators of the translation are called P_μ , which form an Abelian group

$$[P_\mu, P_\nu] = 0. \quad (\text{A.36})$$

The generators of the translations and of the Lorentz group are connected by the relation

$$[P_\mu, J_{\nu\rho}] = i(P_\nu g_{\mu\rho} - P_\rho g_{\mu\nu}), \quad (\text{A.37})$$

which, together with Eq. (A.28) and Eq. (A.36) defines the Poincaré algebra.

The irreducible representations of the Poincaré group can be characterised by means of the eigenvalues of the two Casimir operators, P^2 and W^2 , where

$$W_\mu = -\frac{1}{2}\epsilon_{\mu\nu\rho\sigma}P^\nu J^{\rho\sigma}, \quad (\text{A.38})$$

is the *Pauli-Lubanski vector*. According to Schurs lemma, in irreducible representations the Casimir operators are proportional to the unit matrix of the respective dimension of the representation and read

$$P^2 = m^2 \mathbb{1}, \quad (\text{A.39})$$

$$W^2 = -m^2 s(s+1) \mathbb{1} \quad s = 0, \frac{1}{2}, 1, \dots, \quad (\text{A.40})$$

where we call the eigenvalues mass and spin of the respective irreducible representation.

⁴As for the Lorentz group, also this group is often referred to as the Poincaré group.

Appendix B

Kinematics and Scattering

In this appendix we present the complete formula connecting the squared matrix element to the cross section and give some useful kinematic relations for hadron collider physics.

$2 \rightarrow n$ scattering reactions

In order to calculate the cross section, σ , of a certain scattering process of elementary particles into the particular final state F , $ab \rightarrow F$, the summed and averaged squared matrix element,

$$\langle |\mathcal{M}_{ab \rightarrow F}|^2 \rangle = \frac{1}{n(f_a)n(f_b)} \sum_{f_a, f_b, f_F} |\mathcal{M}_{ab \rightarrow F}|^2, \quad (\text{B.1})$$

needs to be integrated over the phase space depending on the respective process. Here, the sum extends all initial- and final-state degrees of freedom (f), such as colour and helicity, and the additional division by their quantity in the initial state $n(f_a)$ and $n(f_b)$ results in the respective average.

For a $2 \rightarrow n$ process the general cross section formula reads

$$\sigma = \int d\sigma = \int \frac{\langle |\mathcal{M}^{2 \rightarrow n}(p_i; p_f)|^2 \rangle}{F(p_i) \cdot S_n(f)} \Theta_{\text{cut}}(\Phi_n) d\Phi_n(p_i; p_f), \quad (\text{B.2})$$

with the flux factor $F(p_i)$, the symmetry factor for the final-state particles $S_n(f)$, the cut function $\Theta_{\text{cut}}(\Phi_n)$, and the n -particle phase space $d\Phi_n(p_i; p_f)$. In general, the flux factor depends on the momenta and masses of the two initial-state particles, but for massless initial-state particles (a and b), which we exclusively treat in this work, it reduces to a simple function of the c.m. energy,

$$F(p_a, p_b) = 4\sqrt{(p_a \cdot p_b)^2 - m_a^2 m_b^2} \xrightarrow{(m_a=m_b=0)} 4p_a \cdot p_b = 2s. \quad (\text{B.3})$$

The final-state symmetry factor simply reads $S_n = n_i!$ for every set of n_i identical particles in the final state. The cut function $\Theta_{\text{cut}}(\Phi_n)$ contains all phase-space cuts on the final-state momenta leading to the particular fiducial phase space. Moreover, a possible recombination of final-state particles to collinear-safe objects as well as the

filling of the desired histograms is implemented via this function. Finally, the n -particle phase space generally can be transformed to the form

$$\begin{aligned} d\Phi_n(p_a, p_b; p_n) &= \prod_{i=1}^n \left(\frac{d^3 \mathbf{p}_i}{(2\pi)^3 2p_i^0} \right) (2\pi)^4 \delta^{(4)} \left(p_a + p_b - \sum_{j=1}^n p_j \right) \Big|_{p_i^0 = \sqrt{\mathbf{p}_i^2 + m_i^2}} \\ &= \frac{1}{(2\pi)^{3n-4}} \prod_{i=1}^n \left(\frac{d^3 \mathbf{p}_i}{2p_i^0} \right) \delta^{(4)} \left(p_a + p_b - \sum_{j=1}^n p_j \right) \Big|_{p_i^0 = \sqrt{\mathbf{p}_i^2 + m_i^2}} . \end{aligned} \quad (\text{B.4})$$

Kinematics

From special relativity it is known that the four-momentum p^μ of a particle of mass m and with three-momentum \mathbf{p} is given by

$$p^\mu = (E, |\mathbf{p}| \sin \theta \cos \varphi, |\mathbf{p}| \sin \theta \sin \varphi, |\mathbf{p}| \cos \theta) , \quad (\text{B.5})$$

where E denotes the energy of the particle $E = \sqrt{\mathbf{p}^2 + m^2}$ and the three-momentum is given in the usual spherical coordinates θ , φ , and the modulus of three-momentum $|\mathbf{p}|$.

$2 \rightarrow n$ scattering processes are most conveniently parametrized in the centre-of-mass system (c.m.s.) of the reaction with the beam line in the direction of the z -axis, which implies $\theta = 0$ and no φ dependence of the momenta of the incoming particles. However, at hadron colliders we need to distinguish between two such frames. The first is the laboratory frame (lab) where the colliding hadrons (H_1, H_2) have the four-momenta

$$p_{H_1}^\mu = (E_B, 0, 0, E_B) , \quad p_{H_2}^\mu = (E_B, 0, 0, -E_B) , \quad (\text{B.6})$$

where E_B denotes the beam energy. In this system the c.m. energy is twice the beam energy $E_{\text{lab}} = 2E_B = \sqrt{s_{\text{HH}}}$. The second c.m.s. involved is the partonic c.m.s. (pcms) of the colliding partons (a, b),

$$p_a^\mu = (E, 0, 0, E) \quad \text{and} \quad p_b^\mu = (E, 0, 0, -E) . \quad (\text{B.7})$$

The pcms is connected to the partonic reaction in the laboratory frame via a boost along the z -axis. If the partons carry the respective momentum fractions ξ_1 and ξ_2 of the hadrons

$$p_{a,\text{lab}}^\mu = \xi_1 p_{H_1}^\mu = \xi_1 (E_B, 0, 0, E_B) , \quad p_{b,\text{lab}}^\mu = \xi_2 p_{H_2}^\mu = \xi_2 (E_B, 0, 0, -E_B) , \quad (\text{B.8})$$

the boost that transforms the momenta of Eq. (B.8) to the form Eq. (B.7) reads

$$(L_3)^\mu_\nu = \begin{pmatrix} \cosh \xi & 0 & 0 & \sinh \xi \\ 0 & 1 & 0 & 0 \\ 0 & 0 & 1 & 0 \\ \sinh \xi & 0 & 0 & \cosh \xi \end{pmatrix} , \quad \xi = \frac{1}{2} \ln \left(\frac{\xi_1}{\xi_2} \right) . \quad (\text{B.9})$$

and for the involved energies the following equation holds,

$$\begin{aligned}\sqrt{\hat{s}} &= E_{\text{pcms}} = 2E = \sqrt{(p_a + p_b)^2} \\ &= \sqrt{(p_{a,\text{lab}} + p_{b,\text{lab}})^2} = \sqrt{\xi_1 \xi_2 E_{\text{lab}}} = \sqrt{\tau s_{\text{HH}}},\end{aligned}\quad (\text{B.10})$$

where we introduced the variable

$$\tau = \xi_1 \xi_2 = \frac{\hat{s}}{s_{\text{HH}}}, \quad (\text{B.11})$$

which is often used for parametrizing the convolution with the PDFs.

Since the final-state phase space is parametrized in the pcms, but cuts and the resulting observables are defined in the laboratory frame, it is convenient to parametrize the four-momenta in variables that show simple transformation properties under the boost defined in Eq. (B.9):

$$\text{transverse momentum :} \quad p_T = \sqrt{(p^1)^2 + (p^2)^2}, \quad (\text{B.12})$$

$$\text{rapidity :} \quad y = \frac{1}{2} \ln \left(\frac{E + p^3}{E - p^3} \right), \quad (\text{B.13})$$

$$\text{transverse mass :} \quad m_T = \sqrt{p_T^2 + m^2} \xrightarrow{m \rightarrow 0} p_T, \quad (\text{B.14})$$

In these variables, the four-momentum of Eq. (B.5) shows the following transformation property under the boost defined in Eq. (B.9)

$$p^\mu = \begin{pmatrix} m_T \cosh y \\ p_T \sin \varphi \\ p_T \cos \varphi \\ m_T \sinh y \end{pmatrix} \xrightarrow{L_3} \begin{pmatrix} m_T \cosh(y + \xi) \\ p_T \sin \varphi \\ p_T \cos \varphi \\ m_T \sinh(y + \xi) \end{pmatrix} \xrightarrow{m \rightarrow 0} p_T \begin{pmatrix} \cosh(y + \xi) \\ \sin \varphi \\ \cos \varphi \\ \sinh(y + \xi) \end{pmatrix}, \quad (\text{B.15})$$

i.e. in order to transform between pcms and lab frame, depending on the direction, only the rapidities have to be summed or subtracted. In experiments the usage of the pseudorapidity variable,

$$\eta = -\ln \left(\tan \frac{\theta}{2} \right) \xrightarrow{m \rightarrow 0} y, \quad (\text{B.16})$$

is preferred, since θ is the angle from the beam pipe and therefore directly measurable. However, as indicated, for massless particles there is no difference between the pseudorapidity and the rapidity.

Appendix C

Feynman Rules

In this appendix we list the Feynman rules necessary for the computation of any invariant matrix element \mathcal{M}_{fi} including the physical particles of the SM. The assignments are given in the Weyl-van der Waerden (WvdW) spinor-formalism, worked out in Ref. [93], which we used for the calculation presented in Chap. 5. In particular, in Tabs. C.1, C.2, C.3, and C.5 we explicitly list the assignments for all SM physical particles in the 't Hooft–Feynman gauge, $\xi_a = 1$ (c.f. Sec. 2.1.5). For a complete list, including would-be Goldstone bosons, ghost fields and counterterms, we refer the reader to the appendix of Ref. [14].

For the computation of the invariant matrix element \mathcal{M}_{fi} for a specific process $f \rightarrow i$ it is necessary to:

- draw all relevant Feynman graphs for the reaction of interest (determines sort and number of external lines) in the respective order (determines number of loops).
- assign the factors for external particles (Tab. C.1), vertices (Tabs. C.2, C.3) and propagators (Tab. C.5), while respecting momentum conservation at each vertex.
- integrate over all (n-dimensional) loop momenta k_l with the measure $\int \frac{d^n k_l}{(2\pi)^n}$ and assign factors of (-1) for each closed fermion and ghost loop.
- split off a global factor of the imaginary unit i , include a symmetry factor to respect possible permutations of internal fields, and assign relative algebraic signs to graphs that are connected by permuting only external fermion lines.

In Tabs. C.4, C.6, and C.7 we list the coupling assignments for the different particles of the electroweak sector. The sine and cosine of the weak mixing angle θ_w are defined in Eq. (2.26) and are denoted by s_w and c_w , respectively. In Tab. C.4, where we list the particular chiral couplings $C_{\bar{f}_i f_j}^\pm$, we use the following abbreviations in the assignment of the $Z\bar{f}f$ vertex,

$$g_f^+ = -\frac{\sin \theta_w}{\cos \theta_w} Q_f, \quad g_f^- = \frac{I_{W,f}^3 - \sin^2 \theta_w Q_f}{\sin \theta_w \cos \theta_w}. \quad (\text{C.1})$$

Note that whereas in Tabs. C.3 and C.5 the labels i and j belong to the fundamental representation of the colour group $SU(3)_C$, in Tabs. C.2 and C.4, for convenience, we use the same symbols for flavour assignments. However, since in the latter case QCD is of no relevance, this should not lead to any confusion.

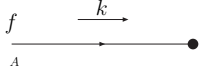
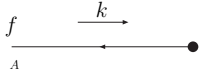
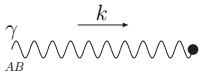
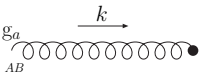
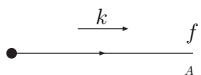
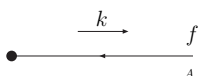
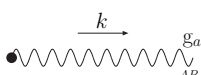
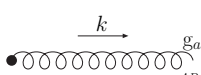
Particle	Expression	Diagram
incoming fermion	$\Psi_\sigma(k) \stackrel{m_f=0}{=} \begin{cases} \begin{pmatrix} k^A \\ 0 \end{pmatrix} & \sigma = R \\ \begin{pmatrix} 0 \\ k^A \end{pmatrix} & \sigma = L \end{cases}$	
incoming anti-fermion	$\bar{\Psi}_\sigma(k) \stackrel{m_f=0}{=} \begin{cases} (k^A, 0) & \sigma = R \\ (0, k^A) & \sigma = L \end{cases}$	
incoming photon	$\varepsilon_{\lambda, \dot{A}B}^\gamma(k) = \begin{cases} \frac{\sqrt{2}g_{+, \dot{A}}k_B}{\langle g+k \rangle^*} & \lambda = + \\ \frac{\sqrt{2}k_{\dot{A}}g_{-, B}}{\langle g-k \rangle} & \lambda = - \end{cases}$	
incoming gluon	$\varepsilon_{\lambda, \dot{A}B}^{g_a}(k) = \begin{cases} \frac{\sqrt{2}g_{+, \dot{A}}k_B}{\langle g+k \rangle^*} & \lambda = + \\ \frac{\sqrt{2}k_{\dot{A}}g_{-, B}}{\langle g-k \rangle} & \lambda = - \end{cases}$	
outgoing fermion	$\bar{\Psi}_\sigma(k) \stackrel{m_f=0}{=} \begin{cases} (0, k^A) & \sigma = R \\ (k^A, 0) & \sigma = L \end{cases}$	
outgoing anti-fermion	$\Psi_\sigma(k) \stackrel{m_f=0}{=} \begin{cases} \begin{pmatrix} 0 \\ k^A \end{pmatrix} & \sigma = R \\ \begin{pmatrix} k^A \\ 0 \end{pmatrix} & \sigma = L \end{cases}$	
outgoing photon	$\varepsilon_{\lambda, \dot{A}B}^{*\gamma}(k) = \begin{cases} \frac{\sqrt{2}k_{\dot{A}}g_{+, B}}{\langle g+k \rangle} & \lambda = + \\ \frac{\sqrt{2}g_{-, \dot{A}}k_B}{\langle g-k \rangle^*} & \lambda = - \end{cases}$	
outgoing gluon	$\varepsilon_{\lambda, \dot{A}B}^{*g_a}(k) = \begin{cases} \frac{\sqrt{2}k_{\dot{A}}g_{+, B}}{\langle g+k \rangle} & \lambda = + \\ \frac{\sqrt{2}g_{-, \dot{A}}k_B}{\langle g-k \rangle^*} & \lambda = - \end{cases}$	

Table C.1.: Feynman rules for (massless) external particles in the WvdW formalism.

Vertex	Expression	Diagram
fermion–boson	$ie \begin{pmatrix} 0 & C_{\sqrt{f_i f_j}}^- \delta_A^D \delta_B^{\dot{C}} \\ C_{\sqrt{f_i f_j}}^+ \epsilon^{\dot{A}C} \epsilon^{BD} & 0 \end{pmatrix}$	
fermion–Higgs	$\frac{-ie}{2s_W} \frac{m_{f_j}}{M_W} \begin{pmatrix} \delta_A^B & 0 \\ 0 & \delta_B^{\dot{A}} \end{pmatrix}$	
boson–Higgs	$-2ie \epsilon_{\dot{A}C} \epsilon^{BD} C_{V_1 V_2 H}$	
3-bosons	$\frac{i}{4} e C_{V_1 V_2 V_3} \left\{ \begin{aligned} &\epsilon^{\dot{A}C} \epsilon^{BD} (K_1 - K_2)^{\dot{E}F} \\ &+ \epsilon^{\dot{C}E} \epsilon^{DF} (K_2 - K_3)^{\dot{A}B} \\ &+ \epsilon^{\dot{A}E} \epsilon^{BF} (K_3 - K_1)^{\dot{C}D} \end{aligned} \right\}$	
3-Higgs	$-ie \frac{3}{2s_W} \frac{M_H^2}{M_W}$	
4-bosons	$\frac{ie^2}{4} C_{V_1 V_2 V_3 V_4} \left\{ \begin{aligned} &2 \epsilon^{\dot{A}C} \epsilon^{BD} \epsilon^{\dot{E}G} \epsilon^{FH} \\ &- \epsilon^{\dot{A}E} \epsilon^{BF} \epsilon^{\dot{C}G} \epsilon^{DH} \\ &- \epsilon^{\dot{A}G} \epsilon^{BH} \epsilon^{\dot{C}E} \epsilon^{DF} \end{aligned} \right\}$	
4-Higgs	$-ie^2 \frac{3}{4s_W^2} \frac{M_H^2}{M_W^2}$	
2-Higgs– 2-bosons	$-2ie^2 \epsilon_{\dot{A}C} \epsilon^{BD} C_{HHV_1 V_2}$	

Table C.2.: Feynman rules for EW vertices in the WvdW formalism. The particular values for the couplings are given in Tabs. C.4, C.6, and C.7, respectively.

Vertex	Expression	Diagram
quark–gluon	$-ig_s T_{ij}^c \begin{pmatrix} 0 & \delta_A^D \delta_B^C \\ \epsilon^{\dot{A}\dot{C}} \epsilon^{BD} & 0 \end{pmatrix}$	
3-gluon	$\frac{-g_s}{4} f^{abc} \left\{ \begin{aligned} &\epsilon^{\dot{A}\dot{C}} \epsilon^{BD} (K_1 - K_2) \dot{E}F \\ &+ \epsilon^{\dot{C}\dot{E}} \epsilon^{DF} (K_2 - K_3) \dot{A}B \\ &+ \epsilon^{\dot{A}\dot{E}} \epsilon^{BF} (K_3 - K_1) \dot{C}D \end{aligned} \right\}$	
4-gluon	$\frac{ig_s^2}{4} \left\{ \begin{aligned} &\epsilon^{\dot{A}\dot{E}} \epsilon^{BF} \epsilon^{\dot{C}\dot{G}} \epsilon^{DH} [f^{ace} f^{bde} - 2f^{ade} f^{bce}] \\ &+ \epsilon^{\dot{A}\dot{G}} \epsilon^{BH} \epsilon^{\dot{C}\dot{E}} \epsilon^{DF} [f^{ade} f^{bce} - 2f^{ace} f^{bde}] \\ &+ \epsilon^{\dot{A}\dot{C}} \epsilon^{BD} \epsilon^{\dot{E}\dot{G}} \epsilon^{FH} [f^{ace} f^{bde} + f^{ade} f^{bce}] \end{aligned} \right\}$	

Table C.3.: Feynman rules for QCD vertices in the WvdW formalism.

$C_{\sqrt{f}i f_j}^{\pm}$	$C_{\gamma f i f_j}^{\pm}$	$C_{Z f i f_j}^{\pm}$	$C_{W^+ \bar{u}_i d_j}^{\pm}$	$C_{W^+ \bar{\nu}_i l_j}^{\pm}$	$C_{W^- \bar{d}_i u_j}^{\pm}$	$C_{W^- \bar{l}_i \nu_j}^{\pm}$
C^-	$-Q_f \delta_{ij}$	$g_f^- \delta_{ij}$	$\frac{1}{\sqrt{2} s_W} \mathbf{V}_{ij}$	$\frac{1}{\sqrt{2} s_W} \delta_{ij}$	$\frac{1}{\sqrt{2} s_W} \mathbf{V}_{ij}^\dagger$	$\frac{1}{\sqrt{2} s_W} \delta_{ij}$
C^+	$-Q_f \delta_{ij}$	$g_f^+ \delta_{ij}$	0	0	0	0

Table C.4.: Coupling assignments for $V f \bar{f}$ couplings.

Propagator	Expression	Diagram
fermion	$\frac{i\delta_{ij}}{k^2 - m_f^2} \begin{pmatrix} m_f \delta_A^B & K_{A\dot{B}} \\ K^{\dot{A}B} & m_f \delta_{\dot{B}}^A \end{pmatrix}$	
gluon	$\frac{-2i\epsilon_{\dot{A}\dot{C}}\epsilon_{BD}\delta_{ab}}{k^2}$	
EW gauge boson	$\frac{-2i\epsilon_{\dot{A}\dot{C}}\epsilon_{BD}}{k^2 - M_V^2}$	
Higgs boson	$\frac{i}{k^2 - M_H^2}$	

Table C.5.: Feynman rules for the propagators in the WvdW formalism.

$$\frac{C_{P_1 P_2 P_3}}{\quad} \parallel \begin{array}{cccc} C_{W^+W^-H} & C_{ZZH} & C_{W^+W^-A} & C_{W^+W^-Z} \\ \frac{1}{s_W} M_W & \frac{1}{c_W^2 s_W} M_W & 1 & \frac{c_W}{s_W} \end{array}$$

Table C.6.: Non-zero coupling assignments for three electroweak boson couplings.

$$\frac{C_{P_1 P_2 P_3 P_4}}{\quad} \parallel \begin{array}{cccccc} C_{W^+W^-ZZ} & C_{W^+W^-AZ} & C_{W^+W^-AA} & C_{W^+W^+W^-W^-} & C_{HHZZ} & C_{HHW^+W^-} \\ -\frac{c_W^2}{s_W^2} & \frac{c_W}{s_W} & -1 & \frac{1}{s_W^2} & \frac{1}{2c_W^2 s_W^2} & \frac{1}{2s_W^2} \end{array}$$

Table C.7.: Non-zero coupling assignments for four electroweak boson couplings.

Bibliography

- [1] M. Gell-Mann, *A Schematic Model of Baryons and Mesons*, Phys. Lett. **8** (1964) 214; H. Fritzsch, M. Gell-Mann and H. Leutwyler, *Advantages of the Color Octet Gluon Picture*, Phys. Lett. **B47** (1973) 365.
- [2] S. Glashow, J. Iliopoulos and L. Maiani, *Weak Interactions with Lepton-Hadron Symmetry*, Phys.Rev. **D2** (1970) 1285; S. Weinberg, *A Model of Leptons*, Phys.Rev.Lett. **19** (1967) 1264; A. Salam, *Weak and Electromagnetic Interactions*, Conf.Proc. **C680519** (1968) 367.
- [3] F. Englert and R. Brout, *Broken Symmetry and the Mass of Gauge Vector Mesons*, Phys. Rev. Lett. **13** (1964) 321; P. W. Higgs, *Broken Symmetries and the Masses of Gauge Bosons*, Phys.Rev.Lett. **13** (1964) 508; G. Guralnik, C. Hagen and T. Kibble, *Global Conservation Laws and Massless Particles*, Phys.Rev.Lett. **13** (1964) 585.
- [4] UA1 collaboration, *Experimental Observation of Isolated Large Transverse Energy Electrons with Associated Missing Energy at $s^{1/2} = 540$ -GeV*, Phys. Lett. **B122** (1983) 103; UA2 collaboration, *Observation of Single Isolated Electrons of High Transverse Momentum in Events with Missing Transverse Energy at the CERN anti-p p Collider*, Phys. Lett. **B122** (1983) 476; UA1 collaboration, *Experimental Observation of Lepton Pairs of Invariant Mass Around 95-GeV/c² at the CERN SPS Collider*, Phys. Lett. **B126** (1983) 398; UA2 collaboration, *Evidence for $Z^0 \rightarrow e^+e^-$ at the CERN anti-p p Collider*, Phys. Lett. **B129** (1983) 130.
- [5] ATLAS collaboration, *Observation of a new particle in the search for the Standard Model Higgs boson with the ATLAS detector at the LHC*, Phys.Lett. **B716** (2012) 1, [[arXiv:1207.7214](https://arxiv.org/abs/1207.7214) [hep-ex]].
- [6] CMS collaboration, *Observation of a new boson at a mass of 125 GeV with the CMS experiment at the LHC*, Phys.Lett. **B716** (2012) 30, [[arXiv:1207.7235](https://arxiv.org/abs/1207.7235) [hep-ex]].
- [7] ATLAS, CMS collaboration, *Combined Measurement of the Higgs Boson Mass in pp Collisions at $\sqrt{s} = 7$ and 8 TeV with the ATLAS and CMS Experiments*, Phys. Rev. Lett. **114** (2015) 191803, [[arXiv:1503.07589](https://arxiv.org/abs/1503.07589) [hep-ex]]; ATLAS collaboration, *Study of the spin and parity of the Higgs boson in HVV decays with the*

- ATLAS detector*, ATLAS Note **008** (2015); ATLAS, CMS collaboration, *Measurements of the Higgs boson production and decay rates and constraints on its couplings from a combined ATLAS and CMS analysis of the LHC pp collision data at $\sqrt{s} = 7$ and 8 TeV*, JHEP **08** (2016) 045, [[arXiv:1606.02266](#) [hep-ex]].
- [8] ATLAS collaboration, *Search for resonances decaying to photon pairs in 3.2 fb^{-1} of pp collisions at $\sqrt{s} = 13 \text{ TeV}$ with the ATLAS detector*, ATLAS Note **081** (2015).
- [9] CMS collaboration, *Search for new physics in high mass diphoton events in proton-proton collisions at 13TeV*, CMS-PAS-EXO **004** (2015).
- [10] ATLAS collaboration, *Search for resonances in diphoton events at $\sqrt{s}=13 \text{ TeV}$ with the ATLAS detector*, JHEP **09** (2016) 001, [[arXiv:1606.03833](#) [hep-ex]]; CMS collaboration, *Search for Resonant Production of High-Mass Photon Pairs in Proton-Proton Collisions at $\sqrt{s} = 8$ and 13 TeV*, Phys. Rev. Lett. **117** (2016) 051802, [[arXiv:1606.04093](#) [hep-ex]].
- [11] B. Biedermann, M. Billoni, A. Denner, S. Dittmaier, L. Hofer, B. Jäger and L. Salfelder, *Next-to-leading-order electroweak corrections to $pp \rightarrow W^+W^- \rightarrow 4$ leptons at the LHC*, JHEP **06** (2016) 065, [[arXiv:1605.03419](#) [hep-ph]].
- [12] M. Billoni, S. Dittmaier, B. Jäger and C. Speckner, *Next-to-leading order electroweak corrections to $pp \rightarrow W+W^- \rightarrow 4$ leptons at the LHC in double-pole approximation*, JHEP **12** (2013) 043, [[arXiv:1310.1564](#) [hep-ph]].
- [13] M. E. Peskin and D. V. Schroeder, *An Introduction to quantum field theory*, Addison-Wesley Publishing Company, 1995.
- [14] M. Böhm, A. Denner and H. Joos, *Gauge theories of the strong and electroweak interaction*, Teubner, 2001.
- [15] M. Maggiore, *A Modern introduction to quantum field theory*, Oxford University Press, 2005.
- [16] M. D. Schwartz, *Quantum Field Theory and the Standard Model*, Cambridge University Press, 2013.
- [17] F. Dyson, *The S matrix in quantum electrodynamics*, Phys.Rev. **75** (1949) 1736.
- [18] R. Feynman, *Mathematical formulation of the quantum theory of electromagnetic interaction*, Phys.Rev. **80** (1950) 440.
- [19] L. Faddeev and V. Popov, *Feynman Diagrams for the Yang-Mills Field*, Phys.Lett. **B25** (1967) 29.
- [20] L. Salfelder, *Predictions for 4 Lepton + 2 Jet Production at the LHC*, Diploma thesis, Albert-Ludwigs-Universität Freiburg, 2013, unpublished.

- [21] C. Wu, E. Ambler, R. Hayward, D. Hoppes and R. Hudson, *Experimental test of parity conservation in beta decay*, Phys.Rev. **105** (1957) 1413.
- [22] N. Cabibbo, *Unitary Symmetry and Leptonic Decays*, Phys.Rev.Lett. **10** (1963) 531; M. Kobayashi and T. Maskawa, *CP Violation in the Renormalizable Theory of Weak Interaction*, Prog.Theor.Phys. **49** (1973) 652.
- [23] H. Lehmann, K. Symanzik and W. Zimmermann, *On the formulation of quantized field theories*, Nuovo Cim. **1** (1955) 205.
- [24] H. M. Georgi, S. L. Glashow, M. E. Machacek and D. V. Nanopoulos, *Higgs Bosons from Two Gluon Annihilation in Proton Proton Collisions*, Phys. Rev. Lett. **40** (1978) 692.
- [25] F. Bloch and A. Nordsieck, *Note on the Radiation Field of the electron*, Phys. Rev. **52** (1937) 54.
- [26] W. Pauli and F. Villars, *On the Invariant regularization in relativistic quantum theory*, Rev. Mod. Phys. **21** (1949) 434.
- [27] G. 't Hooft, *Lattice regularization of gauge theories without loss of chiral symmetry*, Phys. Lett. **B349** (1995) 491, [[arXiv:hep-th/9411228](#) [hep-th]].
- [28] R. Pittau, *A four-dimensional approach to quantum field theories*, JHEP **11** (2012) 151, [[arXiv:1208.5457](#) [hep-ph]].
- [29] G. 't Hooft and M. J. G. Veltman, *Regularization and Renormalization of Gauge Fields*, Nucl. Phys. **B44** (1972) 189; C. G. Bollini and J. J. Giambiagi, *Dimensional Renormalization: The Number of Dimensions as a Regularizing Parameter*, Nuovo Cim. **B12** (1972) 20.
- [30] G. 't Hooft, *Renormalization of Massless Yang-Mills Fields*, Nucl. Phys. **B33** (1971) 173; G. 't Hooft, *Renormalizable Lagrangians for Massive Yang-Mills Fields*, Nucl. Phys. **B35** (1971) 167.
- [31] A. Denner, *Techniques for calculation of electroweak radiative corrections at the one loop level and results for W physics at LEP-200*, Fortsch.Phys. **41** (1993) 307, [[arXiv:0709.1075](#) [hep-ph]].
- [32] D. Ross and J. Taylor, *Renormalization of a unified theory of weak and electromagnetic interactions*, Nucl.Phys. **B51** (1973) 125 .
- [33] A. Denner and T. Sack, *Renormalization of the Quark Mixing Matrix*, Nucl. Phys. **B347** (1990) 203.
- [34] E. N. Argyres, W. Beenakker, G. J. van Oldenborgh, A. Denner, S. Dittmaier, J. Hoogland, R. Kleiss, C. G. Papadopoulos and G. Passarino, *Stable calculations*

- for unstable particles: *Restoring gauge invariance*, Phys. Lett. **B358** (1995) 339, [arXiv:hep-ph/9507216 [hep-ph]].
- [35] A. Denner, S. Dittmaier, M. Roth and D. Wackerroth, *Predictions for all processes $e^+e^- \rightarrow 4$ fermions + γ* , Nucl. Phys. **B560** (1999) 33, [arXiv:hep-ph/9904472 [hep-ph]].
- [36] A. Denner, S. Dittmaier, M. Roth and L. H. Wieders, *Electroweak corrections to charged-current $e^+e^- \rightarrow 4$ fermion processes: Technical details and further results*, Nucl. Phys. **B724** (2005) 247, [arXiv:hep-ph/0505042 [hep-ph]], [Erratum: Nucl. Phys. **B854**, 504(2012)].
- [37] A. Denner and S. Dittmaier, *The Complex-mass scheme for perturbative calculations with unstable particles*, Nucl. Phys. Proc. Suppl. **160** (2006) 22, [arXiv:hep-ph/0605312 [hep-ph]].
- [38] W. A. Bardeen, A. J. Buras, D. W. Duke and T. Muta, *Deep Inelastic Scattering Beyond the Leading Order in Asymptotically Free Gauge Theories*, Phys. Rev. **D18** (1978) 3998.
- [39] G. 't Hooft, *Dimensional regularization and the renormalization group*, Nucl. Phys. **B61** (1973) 455.
- [40] J. C. Collins, *Renormalization*, Cambridge Monographs on Mathematical Physics, vol. 26, Cambridge University Press, Cambridge, 1986.
- [41] T. Kinoshita, *Mass singularities of Feynman amplitudes*, J. Math. Phys. **3** (1962) 650; T. D. Lee and M. Nauenberg, *Degenerate Systems and Mass Singularities*, Phys. Rev. **133** (1964) B1549, [25(1964)].
- [42] C. Weiser, *A combined secondary vertex based B-tagging algorithm in CMS*, CMS Note **014** (2006).
- [43] V. V. Sudakov, *Vertex parts at very high-energies in quantum electrodynamics*, Sov. Phys. JETP **3** (1956) 65, [Zh. Eksp. Teor. Fiz. **30**, 87(1956)].
- [44] M. A. Nowak, M. Praszalowicz and W. Slominski, *A Practical Guide to the Next-to-leading Order of the Perturbation Expansion*, Annals Phys. **166** (1986) 443.
- [45] R. K. Ellis, D. A. Ross and A. E. Terrano, *The Perturbative Calculation of Jet Structure in e^+e^- Annihilation*, Nucl. Phys. **B178** (1981) 421; S. D. Ellis, Z. Kunszt and D. E. Soper, *The One Jet Inclusive Cross-Section at Order α_s^{*3} . 1. Gluons Only*, Phys. Rev. **D40** (1989) 2188; M. L. Mangano, P. Nason and G. Ridolfi, *Heavy quark correlations in hadron collisions at next-to-leading order*, Nucl. Phys. **B373** (1992) 295; Z. Kunszt and D. E. Soper, *Calculation of jet cross-sections in hadron collisions at order α_s^{*3}* , Phys. Rev. **D46** (1992) 192; S. Frixione, Z. Kunszt and A. Signer,

- Three jet cross-sections to next-to-leading order*, Nucl. Phys. **B467** (1996) 399, [arXiv:hep-ph/9512328 [hep-ph]]; Z. Nagy and Z. Trocsanyi, *Calculation of QCD jet cross-sections at next-to-leading order*, Nucl. Phys. **B486** (1997) 189, [arXiv:hep-ph/9610498 [hep-ph]]; J. M. Campbell, M. A. Cullen and E. W. N. Glover, *Four jet event shapes in electron - positron annihilation*, Eur. Phys. J. **C9** (1999) 245, [arXiv:hep-ph/9809429 [hep-ph]].
- [46] S. Catani and M. H. Seymour, *The Dipole formalism for the calculation of QCD jet cross-sections at next-to-leading order*, Phys. Lett. **B378** (1996) 287, [arXiv:hep-ph/9602277 [hep-ph]].
- [47] S. Catani and M. H. Seymour, *A General algorithm for calculating jet cross-sections in NLO QCD*, Nucl. Phys. **B485** (1997) 291, [arXiv:hep-ph/9605323 [hep-ph]], [Erratum: Nucl. Phys. **B510**,503(1998)].
- [48] D. A. Kosower, *Antenna factorization of gauge theory amplitudes*, Phys. Rev. **D57** (1998) 5410, [arXiv:hep-ph/9710213 [hep-ph]]; D. A. Kosower, *Antenna factorization in strongly ordered limits*, Phys. Rev. **D71** (2005) 045016, [arXiv:hep-ph/0311272 [hep-ph]].
- [49] L. Phaf and S. Weinzierl, *Dipole formalism with heavy fermions*, JHEP **04** (2001) 006, [arXiv:hep-ph/0102207 [hep-ph]].
- [50] S. Catani, S. Dittmaier, M. H. Seymour and Z. Trocsanyi, *The Dipole formalism for next-to-leading order QCD calculations with massive partons*, Nucl. Phys. **B627** (2002) 189, [arXiv:hep-ph/0201036 [hep-ph]].
- [51] S. Dittmaier, *A General approach to photon radiation off fermions*, Nucl. Phys. **B565** (2000) 69, [arXiv:hep-ph/9904440 [hep-ph]].
- [52] S. Dittmaier, A. Kabelschacht and T. Kasprzik, *Polarized QED splittings of massive fermions and dipole subtraction for non-collinear-safe observables*, Nucl. Phys. **B800** (2008) 146, [arXiv:0802.1405 [hep-ph]].
- [53] R. P. Feynman, *Very high-energy collisions of hadrons*, Phys. Rev. Lett. **23** (1969) 1415; J. D. Bjorken and E. A. Paschos, *Inelastic Electron Proton and gamma Proton Scattering, and the Structure of the Nucleon*, Phys. Rev. **185** (1969) 1975.
- [54] V. N. Gribov and L. N. Lipatov, *Deep inelastic e p scattering in perturbation theory*, Sov. J. Nucl. Phys. **15** (1972) 438, [Yad. Fiz.15,781(1972)]; V. N. Gribov and L. N. Lipatov, *e+ e- pair annihilation and deep inelastic e p scattering in perturbation theory*, Sov. J. Nucl. Phys. **15** (1972) 675, [Yad. Fiz.15,1218(1972)]; L. N. Lipatov, *The parton model and perturbation theory*, Sov. J. Nucl. Phys. **20** (1975) 94, [Yad. Fiz.20,181(1974)]; G. Altarelli and G. Parisi, *Asymptotic Freedom in Parton Language*,

- Nucl. Phys. **B126** (1977) 298; Y. L. Dokshitzer, *Calculation of the Structure Functions for Deep Inelastic Scattering and e^+e^- Annihilation by Perturbation Theory in Quantum Chromodynamics.*, Sov. Phys. JETP **46** (1977) 641, [Zh. Eksp. Teor. Fiz.73,1216(1977)].
- [55] NNPDF collaboration, *Parton distributions with QED corrections*, Nucl. Phys. **B877** (2013) 290, [arXiv:1308.0598 [hep-ph]].
- [56] S. Dittmaier and M. Huber, *Radiative corrections to the neutral-current Drell-Yan process in the Standard Model and its minimal supersymmetric extension*, JHEP **01** (2010) 060, [arXiv:0911.2329 [hep-ph]].
- [57] D. de Florian, G. F. R. Sborlini and G. Rodrigo, *Two-loop QED corrections to the Altarelli-Parisi splitting functions*, JHEP **10** (2016) 056, [arXiv:1606.02887 [hep-ph]].
- [58] G. Passarino and M. J. G. Veltman, *One Loop Corrections for e^+e^- Annihilation Into $\mu^+\mu^-$ in the Weinberg Model*, Nucl. Phys. **B160** (1979) 151.
- [59] A. Denner, S. Dittmaier and L. Hofer, *COLLIER - A fortran-library for one-loop integrals*, PoS **LL2014** (2014) 071, [arXiv:1407.0087 [hep-ph]]; A. Denner, S. Dittmaier and L. Hofer, *Collier: a fortran-based Complex One-Loop Library in Extended Regularizations*, arXiv:1604.06792 [hep-ph].
- [60] A. Denner and S. Dittmaier, *Reduction of one loop tensor five point integrals*, Nucl. Phys. **B658** (2003) 175, [arXiv:hep-ph/0212259 [hep-ph]]; A. Denner and S. Dittmaier, *Reduction schemes for one-loop tensor integrals*, Nucl. Phys. **B734** (2006) 62, [arXiv:hep-ph/0509141 [hep-ph]].
- [61] A. Denner and S. Dittmaier, *Scalar one-loop 4-point integrals*, Nucl. Phys. **B844** (2011) 199, [arXiv:1005.2076 [hep-ph]].
- [62] J. Ohnemus, *An Order α^{-s} calculation of hadronic W^-W^+ production*, Phys. Rev. **D44** (1991) 1403; S. Frixione, *A Next-to-leading order calculation of the cross-section for the production of W^+W^- pairs in hadronic collisions*, Nucl. Phys. **B410** (1993) 280.
- [63] U. Baur, T. Han and J. Ohnemus, *QCD corrections and nonstandard three vector boson couplings in W^+W^- production at hadron colliders*, Phys. Rev. **D53** (1996) 1098, [arXiv:hep-ph/9507336 [hep-ph]].
- [64] L. J. Dixon, Z. Kunszt and A. Signer, *Helicity amplitudes for $O(\alpha^{-s})$ production of W^+W^- , $W^\pm Z$, ZZ , $W^\pm\gamma$, or $Z\gamma$ pairs at hadron colliders*, Nucl. Phys. **B531** (1998) 3, [arXiv:hep-ph/9803250 [hep-ph]].
- [65] J. M. Campbell and R. K. Ellis, *An Update on vector boson pair production at hadron colliders*, Phys. Rev. **D60** (1999) 113006, [arXiv:hep-ph/9905386 [hep-ph]].

- [66] T. Gehrmann, M. Grazzini, S. Kallweit, P. Maierhöfer, A. von Manteuffel, S. Pozzorini, D. Rathlev and L. Tancredi, *W^+W^- Production at Hadron Colliders in Next to Next to Leading Order QCD*, Phys. Rev. Lett. **113** (2014) 212001, [arXiv:1408.5243 [hep-ph]].
- [67] S. Frixione and B. R. Webber, *Matching NLO QCD computations and parton shower simulations*, JHEP **06** (2002) 029, [arXiv:hep-ph/0204244 [hep-ph]].
- [68] K. Hamilton, *A positive-weight next-to-leading order simulation of weak boson pair production*, JHEP **01** (2011) 009, [arXiv:1009.5391 [hep-ph]]; S. Hoche, F. Krauss, M. Schonherr and F. Siegert, *Automating the POWHEG method in Sherpa*, JHEP **04** (2011) 024, [arXiv:1008.5399 [hep-ph]]; T. Melia, P. Nason, R. Rontsch and G. Zanderighi, *$W+W^-$, WZ and ZZ production in the POWHEG BOX*, JHEP **11** (2011) 078, [arXiv:1107.5051 [hep-ph]]; R. Frederix, S. Frixione, V. Hirschi, F. Maltoni, R. Pittau and P. Torrielli, *Four-lepton production at hadron colliders: aMC@NLO predictions with theoretical uncertainties*, JHEP **02** (2012) 099, [arXiv:1110.4738 [hep-ph]]; P. Nason and G. Zanderighi, *W^+W^- , WZ and ZZ production in the POWHEG-BOX-V2*, Eur. Phys. J. **C74** (2014) 2702, [arXiv:1311.1365 [hep-ph]].
- [69] M. Grazzini, *Soft-gluon effects in WW production at hadron colliders*, JHEP **01** (2006) 095, [arXiv:hep-ph/0510337 [hep-ph]]; S. Dawson, I. M. Lewis and M. Zeng, *Threshold resummed and approximate next-to-next-to-leading order results for W^+W^- pair production at the LHC*, Phys. Rev. **D88** (2013) 054028, [1307.3249]; Y. Wang, C. S. Li, Z. L. Liu, D. Y. Shao and H. T. Li, *Transverse-Momentum Resummation for Gauge Boson Pair Production at the Hadron Collider*, Phys. Rev. **D88** (2013) 114017, [1307.7520].
- [70] D. A. Dicus, C. Kao and W. W. Repko, *Gluon Production of Gauge Bosons*, Phys. Rev. **D36** (1987) 1570; E. W. N. Glover and J. J. van der Bij, *VECTOR BOSON PAIR PRODUCTION VIA GLUON FUSION*, Phys. Lett. **B219** (1989) 488.
- [71] T. Binoth, M. Ciccolini, N. Kauer and M. Kramer, *Gluon-induced WW background to Higgs boson searches at the LHC*, JHEP **03** (2005) 065, [arXiv:hep-ph/0503094 [hep-ph]]; T. Binoth, M. Ciccolini, N. Kauer and M. Kramer, *Gluon-induced W -boson pair production at the LHC*, JHEP **12** (2006) 046, [arXiv:hep-ph/0611170 [hep-ph]].
- [72] T. Melia, K. Melnikov, R. Rontsch, M. Schulze and G. Zanderighi, *Gluon fusion contribution to $W+W^- + jet$ production*, JHEP **08** (2012) 115, [arXiv:1205.6987 [hep-ph]].
- [73] J. Bellm, S. Gieseke, N. Greiner, G. Heinrich, S. Platzer, C. Reuschle and J. F. von Soden-Fraunhofen, *Anomalous coupling, top-mass and parton-shower effects in W^+W^- production*, arXiv:1602.05141 [hep-ph].

- [74] G. Chachamis, M. Czakon and D. Eiras, *W Pair Production at the LHC. I. Two-loop Corrections in the High Energy Limit*, JHEP **12** (2008) 003, [arXiv:0802.4028 [hep-ph]].
- [75] M. Grazzini, S. Kallweit, S. Pozzorini, D. Rathlev and M. Wiesemann, *W⁺W⁻ production at the LHC: fiducial cross sections and distributions in NNLO QCD*, arXiv:1605.02716 [hep-ph].
- [76] F. Caola, K. Melnikov, R. Röntsch and L. Tancredi, *QCD corrections to W⁺W⁻ production through gluon fusion*, Phys. Lett. **B754** (2016) 275, [arXiv:1511.08617 [hep-ph]]; F. Caola, M. Dowling, K. Melnikov, R. Röntsch and L. Tancredi, *QCD corrections to vector boson pair production in gluon fusion including interference effects with off-shell Higgs at the LHC*, arXiv:1605.04610 [hep-ph].
- [77] ATLAS collaboration, *Measurement of W⁺W⁻ production in pp collisions at $\sqrt{s} = 7$ TeV with the ATLAS detector and limits on anomalous WWZ and WW γ couplings*, Phys. Rev. **D87** (2013) 112001, [arXiv:1210.2979 [hep-ex]], [Erratum: Phys. Rev.D88,no.7,079906(2013)]; ATLAS collaboration, *Measurement of the WW + WZ cross section and limits on anomalous triple gauge couplings using final states with one lepton, missing transverse momentum, and two jets with the ATLAS detector at $\sqrt{s} = 7$ TeV*, JHEP **01** (2015) 049, [arXiv:1410.7238 [hep-ex]]; ATLAS collaboration, *Measurement of the W⁺W⁻ production cross section in proton-proton collisions at $\sqrt{s} = 8$ TeV with the ATLAS detector*, ATLAS Note **033** (2014).
- [78] CMS collaboration, *Measurement of the W⁺W⁻ Cross section in pp Collisions at $\sqrt{s} = 7$ TeV and Limits on Anomalous WW γ and WWZ couplings*, Eur. Phys. J. **C73** (2013) 1, [arXiv:1306.1126 [hep-ex]]; CMS collaboration, *Measurement of the W⁺W⁻ cross section in pp collisions at $\sqrt{s} = 8$ TeV and limits on anomalous gauge couplings*, arXiv:1507.03268 [hep-ex].
- [79] P. F. Monni and G. Zanderighi, *On the excess in the inclusive W⁺W⁻ \rightarrow l⁺l⁻ $\nu\bar{\nu}$ cross section*, JHEP **05** (2015) 013, [arXiv:1410.4745 [hep-ph]].
- [80] ATLAS collaboration, *Measurement of the W⁺W⁻ production cross section in pp collisions at a centre-of-mass energy of $\sqrt{s} = 13$ TeV with the ATLAS experiment*, ATLAS Note **090** (2016).
- [81] CMS collaboration, *Measurement of the WW cross section pp collisions at $\sqrt{s}=13$ TeV*, CMS Physics Analysis Summary **006** (2016).
- [82] A. Denner and S. Pozzorini, *One loop leading logarithms in electroweak radiative corrections. 1. Results*, Eur. Phys. J. **C18** (2001) 461, [arXiv:hep-ph/0010201 [hep-ph]]; S. Pozzorini, *Electroweak radiative corrections at high-energies*, Ph.D. thesis, Zürich U., Inst. Math., 2001, arXiv:hep-ph/0201077 [hep-ph].

- [83] E. Accomando, A. Denner and A. Kaiser, *Logarithmic electroweak corrections to gauge-boson pair production at the LHC*, Nucl. Phys. **B706** (2005) 325, [[arXiv:hep-ph/0409247 \[hep-ph\]](#)]; E. Accomando and A. Kaiser, *Electroweak corrections and anomalous triple gauge-boson couplings in W^+W^- and $W^\pm Z$ production at the LHC*, Phys. Rev. **D73** (2006) 093006, [[arXiv:hep-ph/0511088 \[hep-ph\]](#)].
- [84] J. H. Kühn, F. Metzler, A. A. Penin and S. Uccirati, *Next-to-Next-to-Leading Electroweak Logarithms for W -Pair Production at LHC*, JHEP **06** (2011) 143, [[arXiv:1101.2563 \[hep-ph\]](#)].
- [85] A. Bierweiler, T. Kasprzik, J. H. Kühn and S. Uccirati, *Electroweak corrections to W -boson pair production at the LHC*, JHEP **11** (2012) 093, [[arXiv:1208.3147 \[hep-ph\]](#)]; A. Bierweiler, T. Kasprzik and J. H. Kühn, *Vector-boson pair production at the LHC to $\mathcal{O}(\alpha^3)$ accuracy*, JHEP **12** (2013) 071, [[arXiv:1305.5402 \[hep-ph\]](#)].
- [86] J. Baglio, L. D. Ninh and M. M. Weber, *Massive gauge boson pair production at the LHC: a next-to-leading order story*, Phys. Rev. **D88** (2013) 113005, [[1307.4331](#)].
- [87] L. A. Harland-Lang, V. A. Khoze and M. G. Ryskin, *Photon-initiated processes at high mass*, [arXiv:1607.04635 \[hep-ph\]](#).
- [88] A. Manohar, P. Nason, G. P. Salam and G. Zanderighi, *How bright is the proton? A precise determination of the photon PDF*, [arXiv:1607.04266 \[hep-ph\]](#).
- [89] A. Denner, S. Dittmaier, M. Roth and L. H. Wieders, *Complete electroweak $O(\alpha)$ corrections to charged-current $e^+e^- \rightarrow 4$ fermion processes*, Phys. Lett. **B612** (2005) 223, [[arXiv:hep-ph/0502063 \[hep-ph\]](#)], [Erratum: Phys. Lett. **B704**,667(2011)].
- [90] A. Denner, S. Dittmaier, M. Roth and D. Wackeroth, *$O(\alpha)$ corrections to $e^+e^- \rightarrow WW \rightarrow$ four fermions ($+\gamma$): First numerical results from RACOON W* , Phys. Lett. **B475** (2000) 127, [[arXiv:hep-ph/9912261 \[hep-ph\]](#)].
- [91] A. Denner, S. Dittmaier, M. Roth and D. Wackeroth, *Electroweak radiative corrections to $e^+e^- \rightarrow WW \rightarrow 4$ fermions in double pole approximation: The RACOONWW approach*, Nucl. Phys. **B587** (2000) 67, [[arXiv:hep-ph/0006307 \[hep-ph\]](#)].
- [92] A. Denner, S. Dittmaier, M. Roth and D. Wackeroth, *RACOONWW1.3: A Monte Carlo program for four fermion production at e^+e^- colliders*, Comput. Phys. Commun. **153** (2003) 462, [[arXiv:hep-ph/0209330 \[hep-ph\]](#)].
- [93] S. Dittmaier, *Weyl-van der Waerden formalism for helicity amplitudes of massive particles*, Phys. Rev. **D59** (1998) 016007, [[arXiv:hep-ph/9805445 \[hep-ph\]](#)].

- [94] A. Bredenstein, S. Dittmaier and M. Roth, *Four-fermion production at gamma gamma colliders. 1. Lowest-order predictions and anomalous couplings*, Eur. Phys. J. **C36** (2004) 341, [[arXiv:hep-ph/0405169](#) [hep-ph]].
- [95] A. Bredenstein, S. Dittmaier and M. Roth, *Four-fermion production at gamma gamma colliders. 2. Radiative corrections in double-pole approximation*, Eur. Phys. J. **C44** (2005) 27, [[arXiv:hep-ph/0506005](#) [hep-ph]].
- [96] J. Küblbeck, M. Bohm and A. Denner, *Feyn Arts: Computer Algebraic Generation of Feynman Graphs and Amplitudes*, Comput. Phys. Commun. **60** (1990) 165; T. Hahn, *Generating Feynman diagrams and amplitudes with FeynArts 3*, Comput. Phys. Commun. **140** (2001) 418, [[arXiv:hep-ph/0012260](#) [hep-ph]].
- [97] W. Beenakker, F. A. Berends and A. P. Chapovsky, *Radiative corrections to pair production of unstable particles: results for $e^+e^- \rightarrow \ell^+\ell^-$ four fermions*, Nucl. Phys. **B548** (1999) 3, [[arXiv:hep-ph/9811481](#) [hep-ph]].
- [98] S. Jadach, W. Placzek, M. Skrzypek, B. F. L. Ward and Z. Was, *Final state radiative effects for the exact $O(\alpha)$ YFS exponentiated (un)stable W^+W^- production at and beyond LEP-2 energies*, Phys. Rev. **D61** (2000) 113010, [[arXiv:hep-ph/9907436](#) [hep-ph]].
- [99] S. Dittmaier and C. Schwan, *Non-factorizable photonic corrections to resonant production and decay of many unstable particles*, Eur. Phys. J. **C76** (2016) 144, [[arXiv:1511.01698](#) [hep-ph]].
- [100] S. Dittmaier, M. Bohm and A. Denner, *Improved Born approximation for $e^+e^- \rightarrow W^+W^-$ in the LEP200 energy region*, Nucl. Phys. **B376** (1992) 29, [Erratum: Nucl. Phys. **B391**,483(1993)].
- [101] A. Denner, S. Dittmaier, M. Roth and D. Wackerroth, *Off-shell W pair production: Universal versus nonuniversal corrections*, Proceedings RADCOR **2000** (2001), [[arXiv:hep-ph/0101257](#) [hep-ph]].
- [102] S. Actis, A. Denner, L. Hofer, A. Scharf and S. Uccirati, *Recursive generation of one-loop amplitudes in the Standard Model*, JHEP **04** (2013) 037, [[arXiv:1211.6316](#) [hep-ph]].
- [103] J. Alwall, M. Herquet, F. Maltoni, O. Mattelaer and T. Stelzer, *MadGraph 5 : Going Beyond*, JHEP **06** (2011) 128, [[arXiv:1106.0522](#) [hep-ph]].
- [104] Particle Data Group collaboration, *Review of Particle Physics (RPP)*, Phys. Rev. **D86** (2012) 010001.
- [105] D. Yu. Bardin, A. Leike, T. Riemann and M. Sachwitz, *Energy Dependent Width Effects in e^+e^- Annihilation Near the Z Boson Pole*, Phys. Lett. **B206** (1988) 539.

- [106] K. P. O. Diener, S. Dittmaier and W. Hollik, *Electroweak higher-order effects and theoretical uncertainties in deep-inelastic neutrino scattering*, Phys. Rev. **D72** (2005) 093002, [[arXiv:hep-ph/0509084](#) [hep-ph]].
- [107] ATLAS collaboration, *Measurement of the transverse momentum distribution of Z/γ^* bosons in proton–proton collisions at $\sqrt{s}=7$ TeV with the ATLAS detector*, Phys. Lett. **B705** (2011) 415, [[arXiv:1107.2381](#) [hep-ex]].
- [108] ATLAS collaboration, *Observation and measurement of Higgs boson decays to WW^* with the ATLAS detector*, Phys. Rev. **D92** (2015) 012006, [[arXiv:1412.2641](#) [hep-ex]].
- [109] CMS collaboration, *Measurement of Higgs boson production and properties in the WW decay channel with leptonic final states*, JHEP **01** (2014) 096, [[arXiv:1312.1129](#) [hep-ex]].
- [110] M. Rubin, G. P. Salam and S. Sapeta, *Giant QCD K-factors beyond NLO*, JHEP **09** (2010) 084, [[arXiv:1006.2144](#) [hep-ph]].
- [111] ATLAS collaboration, *Search for the Standard Model Higgs boson in the $H \rightarrow WW^{(*)} \rightarrow l\nu l\nu$ decay mode with 4.7 fb^{-1} of ATLAS data at $\sqrt{s} = 7\text{ TeV}$* , Phys. Lett. **B716** (2012) 62, [[arXiv:1206.0756](#) [hep-ex]].
- [112] B. Biedermann, A. Denner, S. Dittmaier, L. Hofer and B. Jäger, *Electroweak corrections to $pp \rightarrow \mu^+\mu^-e^+e^- + X$ at the LHC: a Higgs background study*, Phys. Rev. Lett. **116** (2016) 161803, [[arXiv:1601.07787](#) [hep-ph]]; B. Biedermann, A. Denner, S. Dittmaier, L. Hofer and B. Jäger, *Next-to-leading-order electroweak corrections to the production of four charged leptons at the LHC*, [arXiv:1611.05338](#) [hep-ph].
- [113] M. L. Mangano et al., *Physics at a 100 TeV pp collider: Standard Model processes*, [arXiv:1607.01831](#) [hep-ph].
- [114] B. Jäger, L. Salfelder, M. Worek and D. Zeppenfeld, *Physics Opportunities for Vector-Boson Scattering at a Future 100 TeV Hadron Collider*, in preparation.
- [115] F. Campanario, M. Kerner, L. D. Ninh and D. Zeppenfeld, *Next-to-leading order QCD corrections to W^+W^+ and W^-W^- production in association with two jets*, Phys. Rev. **D89** (2014) 054009, [[arXiv:1311.6738](#) [hep-ph]].
- [116] ATLAS collaboration, *Evidence for Electroweak Production of $W^\pm W^\pm jj$ in pp Collisions at $\sqrt{s} = 8$ TeV with the ATLAS Detector*, Phys. Rev. Lett. **113** (2014) 141803, [[arXiv:1405.6241](#) [hep-ex]]; ATLAS collaboration, *Measurement of $W^\pm W^\pm$ vector-boson scattering and limits on anomalous quartic gauge couplings with the ATLAS detector*, [arXiv:1611.02428](#) [hep-ex].

- [117] ATLAS collaboration, *Measurements of $W^\pm Z$ production cross sections in pp collisions at $\sqrt{s} = 8$ TeV with the ATLAS detector and limits on anomalous gauge boson self-couplings*, Phys. Rev. **D93** (2016) 092004, [arXiv:1603.02151 [hep-ex]].
- [118] ATLAS collaboration, *Search for anomalous electroweak production of WW/WZ in association with a high-mass dijet system in pp collisions at $\sqrt{s} = 8$ TeV with the ATLAS detector*, arXiv:1609.05122 [hep-ex].
- [119] CMS collaboration, *Study of vector boson scattering and search for new physics in events with two same-sign leptons and two jets*, Phys. Rev. Lett. **114** (2015) 051801, [arXiv:1410.6315 [hep-ex]].
- [120] B. Biedermann, A. Denner and M. Pellen, *Large electroweak corrections to vector-boson scattering at the Large Hadron Collider*, arXiv:1611.02951 [hep-ph].
- [121] M. Benedikt and F. Zimmermann, *Future Circular Colliders*.
- [122] J. Tang et al., *Concept for a Future Super Proton-Proton Collider*, arXiv:1507.03224 [physics.acc-ph].
- [123] R. Contino et al., *Physics at a 100 TeV pp collider: Higgs and EW symmetry breaking studies*, arXiv:1606.09408 [hep-ph].
- [124] T. Golling et al., *Physics at a 100 TeV pp collider: beyond the Standard Model phenomena*, arXiv:1606.00947 [hep-ph].
- [125] K. Arnold et al., *VBFNLO: A Parton level Monte Carlo for processes with electroweak bosons*, Comput. Phys. Commun. **180** (2009) 1661, [arXiv:0811.4559 [hep-ph]]; K. Arnold et al., *VBFNLO: A Parton Level Monte Carlo for Processes with Electroweak Bosons – Manual for Version 2.7.0*, arXiv:1107.4038v3 [hep-ph]; J. Baglio et al., *Release Note - VBFNLO 2.7.0*, arXiv:1404.3940 [hep-ph].
- [126] B. Jäger, C. Oleari and D. Zeppenfeld, *Next-to-leading order QCD corrections to $W+W^-$ production via vector-boson fusion*, JHEP **07** (2006) 015, [arXiv:hep-ph/0603177 [hep-ph]].
- [127] B. Jäger, C. Oleari and D. Zeppenfeld, *Next-to-leading order QCD corrections to Z boson pair production via vector-boson fusion*, Phys. Rev. **D73** (2006) 113006, [arXiv:hep-ph/0604200 [hep-ph]].
- [128] G. Bozzi, B. Jäger, C. Oleari and D. Zeppenfeld, *Next-to-leading order QCD corrections to $W+Z$ and $W-Z$ production via vector-boson fusion*, Phys. Rev. **D75** (2007) 073004, [arXiv:hep-ph/0701105 [hep-ph]].

- [129] B. Jäger, C. Oleari and D. Zeppenfeld, *Next-to-leading order QCD corrections to $W^+ W^+ jj$ and $W^- W^- jj$ production via weak-boson fusion*, Phys. Rev. **D80** (2009) 034022, [arXiv:0907.0580 [hep-ph]].
- [130] F. Campanario, M. Kerner, L. D. Ninh and D. Zeppenfeld, *WZ Production in Association with Two Jets at Next-to-Leading Order in QCD*, Phys. Rev. Lett. **111** (2013) 052003, [arXiv:1305.1623 [hep-ph]].
- [131] F. Campanario, M. Kerner, L. D. Ninh and D. Zeppenfeld, *Next-to-leading order QCD corrections to ZZ production in association with two jets*, JHEP **07** (2014) 148, [arXiv:1405.3972 [hep-ph]].
- [132] M. Rauch, *Vector-Boson Fusion and Vector-Boson Scattering*, arXiv:1610.08420 [hep-ph].
- [133] M. Ciccolini, A. Denner and S. Dittmaier, *Electroweak and QCD corrections to Higgs production via vector-boson fusion at the LHC*, Phys. Rev. **D77** (2008) 013002, [arXiv:0710.4749 [hep-ph]].
- [134] M. Czakon, C. G. Papadopoulos and M. Worek, *Polarizing the Dipoles*, JHEP **08** (2009) 085, [arXiv:0905.0883 [hep-ph]].
- [135] C. Oleari and D. Zeppenfeld, *QCD corrections to electroweak $\nu(l) jj$ and $l+l-j$ production*, Phys. Rev. **D69** (2004) 093004, [arXiv:hep-ph/0310156 [hep-ph]].
- [136] L. A. Harland-Lang, A. D. Martin, P. Motylinski and R. S. Thorne, *Parton distributions in the LHC era: MMHT 2014 PDFs*, Eur. Phys. J. **C75** (2015) 204, [arXiv:1412.3989 [hep-ph]].
- [137] A. Buckley, J. Ferrando, S. Lloyd, K. Nordström, B. Page, M. Rüfenacht, M. Schönherr and G. Watt, *LHAPDF6: parton density access in the LHC precision era*, Eur. Phys. J. **C75** (2015) 132, [arXiv:1412.7420 [hep-ph]].
- [138] A. D. Martin, W. J. Stirling, R. S. Thorne and G. Watt, *Heavy-quark mass dependence in global PDF analyses and 3- and 4-flavour parton distributions*, Eur. Phys. J. **C70** (2010) 51, [arXiv:1007.2624 [hep-ph]].
- [139] M. Cacciari, G. P. Salam and G. Soyez, *The Anti- $k(t)$ jet clustering algorithm*, JHEP **04** (2008) 063, [arXiv:0802.1189 [hep-ph]].
- [140] B. Jäger and G. Zanderighi, *NLO corrections to electroweak and QCD production of W^+W^+ plus two jets in the POWHEGBOX*, JHEP **11** (2011) 055, [arXiv:1108.0864 [hep-ph]].
- [141] ATLAS collaboration, *Search for the Higgs boson in the $H \rightarrow WW \rightarrow l\nu jj$ decay channel at $\sqrt{s} = 7$ TeV with the ATLAS detector*, Phys. Lett. **B718** (2012) 391, [arXiv:1206.6074 [hep-ex]].

-
- [142] C. Englert, B. Jäger, M. Worek and D. Zeppenfeld, *Observing Strongly Interacting Vector Boson Systems at the CERN Large Hadron Collider*, Phys. Rev. **D80** (2009) 035027, [[arXiv:0810.4861](#) [hep-ph]].
- [143] B. Jäger, F. Schissler and D. Zeppenfeld, *Parton-shower effects on Higgs boson production via vector-boson fusion in association with three jets*, JHEP **07** (2014) 125, [[arXiv:1405.6950](#) [hep-ph]].
- [144] H. Georgi, *Lie Algebra in Particle Physics. From Isospin to Unified Theories*, vol. 2, Westview Press, 1999.
- [145] W. Tung, *Group Theory in Physics*, World Scientific, 1985.

List of Publications

- [1] *Next-to-leading-order electroweak corrections to $pp \rightarrow W^+W^- \rightarrow 4$ leptons at the LHC*, B. Biedermann, M. Billoni, A. Denner, S. Dittmaier, L. Hofer, B. Jäger, and L. Salfelder, *JHEP* **06** (2016) 065, [arXiv:1605.03419](#)[hep-ph]
- [2] *Physics at a 100 TeV pp collider: Standard Model processes*, M. Mangano and others, [arXiv:1607.01831](#)[hep-ph]
- [3] *Electroweak corrections to gauge-boson pair production processes at the LHC including leptonic W/Z decays* B. Biedermann, M. Billoni, A. Denner, S. Dittmaier, L. Hofer, B. Jäger, and L. Salfelder, *PoS LL2016* (2016) 018
- [4] *Physics Opportunities for Vector-Boson Scattering at a Future 100 TeV Hadron Collider*, B. Jäger, L. Salfelder, M. Worek, D. Zeppenfeld, **in preparation**

Acknowledgements

First and foremost, I want to thank my supervisor Barbara Jäger for giving me the opportunity to perform my PhD studies on this interesting topic under her profound guidance. I was able to benefit a lot from her broad expertise in the field of collider phenomenology and particularly appreciated her support and encouragements to present my work at workshops and conferences.

I am grateful to Werner Vogelsang for his interest in this work and for providing the second appraisal of the thesis.

I want to thank my collaborators Benedikt Biedermann, Marina Billoni, Ansgar Denner, Stefan Dittmaier, Lars Hofer, Malgorzata Worek, and Dieter Zeppenfeld for the fruitful cooperations during my PhD time. Special thanks go to Benedikt, Marina, and Malgorzata for many helpful discussions and the countless hours spent on the numerical comparison of the code.

Moreover, I thank the entire seventh floor for the warm welcome after we moved to Tübingen and for maintaining such a great working environment. In this respect I owe special thanks to Patriz Hinderer, Tom Kaufmann, and Martin Lambertsen, who quickly became true friends of mine and made the time in, around, and between Tübingen and Stuttgart very enjoyable and less annoying, respectively ;). I also want to thank Ingrid Estiry for her support in all organisational issues.

I enjoyed a lot sharing the office with Matthias Kesenheimer for the last two+ years and want to thank him for the nice working atmosphere and many physics/non-physics related conversations. In quite the same way I am obliged to all present and former members of our research group, Julien Baglio, Marina Billoni, Christoph Borschensky, Gabriele Coniglio, Junya Nakamura, Robin Sellnow, Juraj Streicher, Anton Stoyanov, and Stephan Thier. In particular, I am grateful to Christoph, Julien, and Martin for proofreading parts of the manuscript and the Latex-support.

I also want to thank Marco Stratmann for many enlightening conversations that by no means were only restricted to pQCD and computer-related topics.

Last but not least, I want to express my deepest gratitude to my entire family for their continuous support and encouragement during my whole studies that would not have been possible without them. I am particularly indebted to Katharina for her assistance and her patience, especially in the last steps of this work.